



# **Advances in Printing and Media Technology**

**Vol. XLIII(III)**

*Edited by Patrick Gane  
Associate editor: Cathy Ridgway*

Darmstadt  
MMXVI

**Advances in Printing and Media Technology**  
Proceedings of the 43<sup>rd</sup> International Research Conference of **iarigai**  
Toronto, Canada, August 2016

Published by the International Association of  
Research Organizations for the Information,  
Media and Graphic Arts Industries  
Darmstadt, Germany, 2016

Edited by Patrick Gane, Aalto, Finland

Scientific Committee

Ian Baitz (Toronto, Canada)  
Anne Blayo (Grenoble, France)  
Roger Bollström (Oftringen, Switzerland)  
Edgar Dörsam (Darmstadt, Germany)  
Malin Edvardsson (Gothenburg, Sweden)  
Nils Enlund (Helsinki, Finland)  
Wolfgang Faigle (Stuttgart, Germany)  
Patrick Gane (Helsinki, Finland)  
Philip Gerstner (Helsinki, Finland)  
Gorazd Golob (Ljubljana, Slovenia)  
Martin Habekost (Toronto, Canada)  
Gunter Hübner (Stuttgart, Germany)  
Eifion Jewell (Swansea, UK)  
John Kettle (Espoo, Finland)  
Yuri Kuznetsov (St. Petersburg, Russian Federation)  
Magnus Lestelius (Karlstad, Sweden)  
Branka Lozo (Zagreb, Croatia)  
Mladen Lovreček (Zagreb, Croatia)  
Natalia Lumby (Toronto, Canada)  
Thomas Mejtoft (Umeå, Sweden)  
Erzsebet Novotny (Budapest, Hungary)  
Anastasios Politis (Athens, Greece)  
Anayath Rajendrakumar (Bhiwani, Haryana, India)  
Anu Seisto (Espoo, Finland)  
Chris Smyth (Toronto, Canada)  
Tomas Syrový (Pardubice, Czech Republic)  
Dan Thomas (Swansea, UK)  
Martti Toivakka (Åbo/Turku, Finland)  
Renke Wilken (Munich, Germany)  
Scott Williams (Rochester, USA)  
Li Yang (Stockholm, Sweden)

The facts published in this book are obtained from sources believed to be reliable. However, publishers can accept no legal liability for the contents of papers, nor for any information contained therein, nor for conclusions drawn by any party from it.

No part of this publication may be reproduced, stored in a retrieval system or transmitted in any form or by any means of electronic, mechanical, photocopying, recording or otherwise without the prior written permission of the publisher.

*Online edition*

**ISBN 978-3-9870704-6-4**

**ISSN 2409-4021**

Copyright © **iarigai** 2016

# Contents

## Preface

The Print Media Research Center, together with the School of Graphic Communications Management at Ryerson University in Toronto, Canada is thrilled to host the 43 <sup>rd</sup> annual <b>iarigai</b> conference <i>Natalia Lumby</i>	1
---	---

## 1 – Printed Functionality

From Biological Molecules to Industrial Printed Products: the challenges facing new functional printed applications development <i>Michael Pruneau, Éric Athlan, Laurent Desfontaines, Christiane Lecomte, Michel Martineau and Chloé Bois</i>	3
New Fabrication Approach for Low Cost RFID Tags <i>Lorenzo Pirrami, Danilo Demarchi, Marco Mazza, Fritz Bircher</i>	13
Fabricating a Flexible Thin Film Humidity Sensor: minimum viable product <i>Maksim Korobkin, Jiayuan Yin, Aarne Klemetti</i>	21

## 2 – Printed Functionality

Spot Application of a Transparent Nanoclay Layer to Provide Post-print Laser Marking Functionality on High Brightness 100 % Calcium Carbonate Coatings <i>Roger Bollström, Patrick Gane</i>	33
Reaction Platforms for Enzymatic Testing <i>Eveliina Jutila, Risto Koivunen, Roger Bollström, Tiina Sikanen and Patrick Gane</i>	39
Improving Run-time Stability with Aerosol Jet Printing Using a Solvent Add-back Bubbler <i>Arjun Wadhwa, Denis Cormier, Scott Williams</i>	49

## 3 – Colour

Optimized inking for cardboard food packaging <i>Fons Put</i>	57
Colour Management of Tablet Devices <i>Daniel Langsford, Reem El Asaleh, Richard Adams</i>	65
Microscale halftone dots analysis: A spatial threshold evaluation method <i>Louis Vallat-Evrard, Lionel Chagas, Raphaël Passas, Nadège Reverdy-Bruas</i>	71

## 4 – Design

A Case of Beer: A study to determine if the visual design elements of Ontario craft beer packaging communicate their unique flavour profiles <i>Diana Varma</i>	81
Why most Brand Manuals fail when it comes to defining Brand Colors; And how to determine acceptable Color Deviations for specific Brand Colors <i>Michael Abildgaard Pedersen</i>	91

## 5 – Printing Materials

Influence of drying temperature on inkjet printed droplets and lines morphology by using silver nanoparticles based ink: relation with electrical performances <i>Vincent Faure, Aurore Denneulin, Yahya Rharbi, Albert Magnin, Anne Blayo</i>	101
Influence of the Background Color on the Quality of Embossed Holograms <i>Pauline Brumm, Edgar Dörsam, Duy Linh Nguyen, Martin Schmitt-Lewen</i>	111
TiO <sub>2</sub> nanostructures for dye-sensitized solar cells (DSSCs) on a glass substrate <i>Jarkko J. Saarinen, Roger Bollström, Björn Törngren, Janne Haapanen, Tommi Kääriäinen, Steven M. George, Jyrki M. Mäkelä, and Martti Toivakka</i>	121

## 6 – Manufacturing and 3D Printing

Challenges in the Fabrication of Optimized Microstructures via Fused Layer Modeling <i>Vinzenz Nienhaus, Daniel Laumann, Dieter Spiehl, Edgar Dörsam</i>	127
3D Printing of Model Polymeric Resins for Medical Applications <i>Azem Yahamed, Pavel Ikononov, Paul D. Fleming, Alexandra Pekarovicova and Peter Gustafson</i>	137
Inkjet Printed Polyelectrolyte Patterns for Analyte Separation on Microfluidic Paper-based Analytical Devices <i>Risto Koivunen, Eveliina Jutila, Roger Bollström, Patrick Gane</i>	143

<b>Index of authors</b>	153
-------------------------	-----

**The Print Media Research Center, together with the School of Graphic Communications Management at Ryerson University in Toronto, Canada is thrilled to host the 43<sup>rd</sup> annual iarigai conference**

*Natalia Lumby*  
Conference Chair

E-mail: [nlumby@ryerson.ca](mailto:nlumby@ryerson.ca)

The Print Media Research Centre (PMRC) is a Faculty-based Research Centre within the Faculty of Communication and Design at Ryerson University. The PMRC's Scholarly Research and Creative (SRC) agenda focuses on advancing the broad areas of premedia, printing and finishing on an international scale. The PMRC combines the SRC efforts of faculty in the School of Graphic Communications Management (GCM) and other collaborators within the university and internationally, with those of undergraduate and postgraduate students across the university and other institutions around the world. The PMRC forges short and long-term research partnerships with industry at local, national, and international levels. Funding from industry partners results in a one-of-a-kind print media research centre that establishes Ryerson University as the premiere print media research institution in Canada.

Ryerson is Canada's leader in innovative, career-focused education. Being located in the core of downtown Toronto, it is distinctly urban, with a focus on innovation and entrepreneurship. The roots of Ryerson University are in applied education, with the School of Graphic Communications Management being one of the original programs launching in 1948. As Canada's only degree program for the printing industries, we are serious about developing qualified graduates to move our industry forward.

Hosting the 43<sup>rd</sup> annual iarigai conference is an example of how our school fosters collaboration and innovation within our industry. The breadth of topics for the conference is a testament to the high level of expertise that is a part of the iarigai community. With industry's ability to print circuits, solar cells and 3D objects the applications are far reaching. Gathering international researchers from a dozen countries provides us with opportunities to learn from one another and create opportunities to collaborate to further the growth of this important industry.

In addition to covering topics new to the graphic arts, there is a great deal left to learn and discover about more traditional uses of print media. With the changing media landscape, print is constantly adjusting to respond to new demands. Printed advertisements often have to connect to digital counterparts, and the design we use today needs to reflect this new behavior. In addition, our ability to manufacture high quality images, with excellent colour accuracy both traditionally and digitally continues to improve. The topics covered include advancement in each of these critical areas.

We are also thrilled to have an excellent set of keynote speakers represented at the conference. Covering topics of colour, haptics and integration of audio content these speakers used their graphic arts industry knowledge to push our thinking beyond the page, while reminding us that the page persists to be critical tool in the media landscape.

Further, in addition to academic presentations, this conference also included a morning of industry focused workshop sessions. Challenging the Status Quo industry day featured several relevant workshops on topics, which include big data, e-mail communication and targeted marketing. In addition to workshops, iarigai in partnership with Ryerson delivered a Drupa update session. Attendees consisted of regular conference participants as well as industry guests.

In total the conference featured 17 academic presentations, representing the work of 63 researchers, 3 keynote presentations as well as 4 industry focused workshops. In addition to attending presentations conference goers were able to explore the majestic Niagara Falls, as well as visit the Mackenzie Printery Museum, which houses Canada's largest collection of operational antique presses.

On behalf of Ryerson I would like to thank you for your participation in this year's conference.

## From Biological Molecules to Industrial Printed Products: the challenges facing new functional printed applications development

*Michael Pruneau<sup>1</sup>, Éric Athlan<sup>1,2</sup>, Laurent Desfontaines<sup>2</sup>, Christiane Lecomte<sup>1,2</sup>, Michel Martineau<sup>2</sup> and Chloé Bois<sup>2</sup>*

<sup>1</sup> Collège Ahuntsic, 9155 Rue St-Hubert, Montréal, QC H2M 1Y8, CANADA

<sup>2</sup> ICI – Printability and Graphic Arts Institute, 999 Avenue Émile Journault, Montréal, QC H2M 2E2, CANADA

### Short Abstract

The biosensor strips are used as blood glucometer by diabetic patients worldwide. The strips convert an electrochemical signal of an enzymatic redox reaction that takes place in the presence of glucose into a digital signal. The price of these strips is a major parameter as the daily number of strips used by patients is significant and critical for monitoring their condition. To achieve a lower production cost the potential of conventional printing methods on industrial press using less expensive raw materials and paper substrate is investigated. ICI establishes the proof a concept of a fully printed biosensor device by flexography using commercially available inks and in-house carbon-based and enzymatic formulated inks. The control of the enzymatic activity during formulation optimization and printing is the core challenge faced in this project. Therefore, the influence of solvents and temperature on the enzymatic activity is investigated to formulate an ink which preserves the functionality of the biological material. Moreover, the required printability and electrical performances of silver and carbon-based conductive inks used as electrodes is achieved by superimposing multiple inks layers and specific drying conditions. Finally, fully printed functional devices on paper are obtained, which signal is proportionate to the glucose amount of several solutions mimicking diabetic blood ranges. Thereafter, the technical transfer of these results from lab-scale to industrial flexography printing press will demand formulation adaptation, substrate properties adaptation, device geometry optimization and characterization method development.

**Keywords:** functional printing, biosensors, ink formulation, industrialization, diabetes, printed electronics

### 1. Introduction

The enzymatic biosensors are widely used to diagnose particular diseases or as a monitoring tool of a biological marker for which they are made specifically. Combining reliability and ease of use, these devices provide quick solutions to the medical field. As diabetes continues to grow, Self-Monitoring Blood Glucose (SMBG) devices based on enzymatic biosensors for monitoring blood glucose levels are now widely used (Cardosi and Liu, 2012). These sensors have the distinction of being portable and reliable in addition to requiring a small volume of blood for analysis. Strips, which constitute the biosensor, are associated with a reader and display device. They transform the electrochemical signal into a digital signal. Diabetic patients must therefore undeniably use test strips to monitor their blood glucose levels and an average of three per day. The price of these stripes is significant. Hence, one of the challenges for this type of biosensor is the reduction of the strips production costs.

The strips that are found on the shelves of pharmacies are mainly produced on a polymeric substrate such as PolyEthyleneTerephthalate (PET). This method of manufacture in accordance with the use of ink based on noble metals (gold, platinum, etc.) greatly increases their selling price. To achieve a reasonable production cost and therefore a lower price for the consumers, one possible solution is the printing by conventional methods on industrial press using less expensive raw materials and paper substrates (Tudorache and Bala, 2007).

## 2. Objectives of the research

ICI objective is the development of an enzyme biosensor fully printable on paper that can be used for blood glucose monitoring for diabetic patients.

From the selection of the active materials to the proof of concept of the product, the challenges that are addressed are:

1. Reduction of the raw material cost
  - New conductive materials
  - Enzyme selection
  - Paper substrate
2. Functional inks formulation
  - Activity preservation
  - Conductive inks
3. Device manufacturing
  - Optimization of characterization methods
  - Printability of functional inks on paper
  - Industrial transfer

## 3. Research materials and methods

### 3.1 Biosensor devices design

The device which is developed is composed of three different types of inks. The steps and respective designs for each layer are detailed in the following Figure 1, Figure 2 and Figure 3. The dimension of the printed area is  $70 \times 90$  mm.

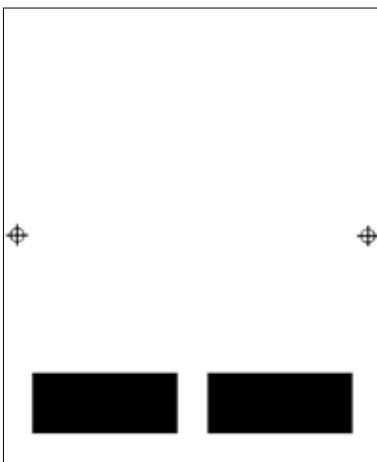


*Figure 1: Step 1: Enzymatic layer*

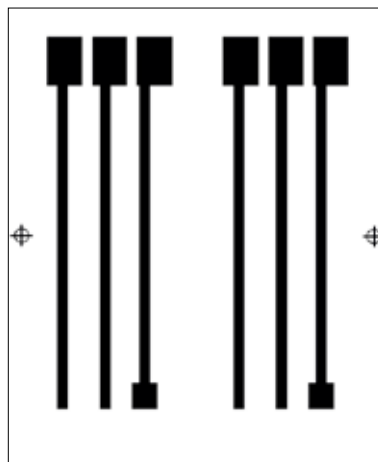


*Figure 2: Step 2: Current collectors and reference electrode*

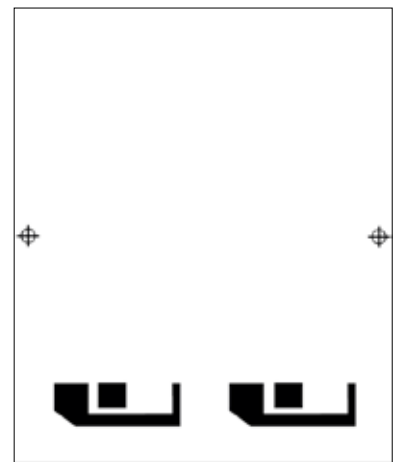


*Figure 3: Step 3: Working electrode and auxiliary electrode*

The original devices design requires three electrodes in order to perform current measurement using an ammeter (Rahman et al., 2010):

- a working electrode where the reaction occurs,
- an auxiliary electrode (for measuring the current generated),
- and finally a reference electrode that fixes the value potential throughout the process.



### 3.2 Enzymatic activity characterization

#### 3.2.1 Enzymatic solution

The enzyme selected for this application is the glucose oxidase (GOD or GOx). The glucose oxidase catalyzes the oxidation of glucose using oxygen as an electron acceptor (Heller and Feldman, 2008).

Glucose oxidase extracted from the fungus *Aspergillus Niger* (Tsuge et al., 1975) was purchased from Sigma (Cat# G0543). It was found that 0.05 U of the enzyme (in a volume of 5  $\mu$ l of 50 mM sodium acetate, pH = 5.1) was the smallest amount capable of completely digesting 5  $\mu$ l of 0.5 % glucose in 5 min at room temperature after drying the enzyme on a filter paper. This proportion was used for all experiments.

The steps followed to optimized the formulation of the complete active ink will be summarized in the results part of this abstract.

#### 3.2.2 Testing glucose solutions

In order to evaluate the enzymatic response, a glucose solution is: 0.5 %w/v glucose in 50 mM acetate buffer, pH = 5.1. Then, several glucose solutions are prepared to mimicking diabetic bloods from severe hypoglycemia (2 mmol·L<sup>-1</sup> glucose) to strong hyperglycemia (32 mmol·L<sup>-1</sup> glucose) (Higgins, 2013).

##### 3.2.2.1 Color scale

The enzyme solution is transferred onto a Whatman filter paper discs and dried at least 10 min before use at room temperature. The discs retain their full enzymatic activity for several months at room temperature.

Once the discs are dry, 5  $\mu$ l droplet of the solution at 0.5 % glucose in 50 mM sodium acetate is spotted on the discs and left to incubate for 5 min at room temperature. The reaction is stopped by transferring the filters to 500  $\mu$ l of 6 % O-Toluidine (in glacial acetic acid).

The O-toluidine is used for the determination of glucose in biological materials (Dubowski, 1962). This enzyme, in the presence of an aldose (a sugar containing an aldehyde function), leads to the condensation between the amine and the aldehyde function of the free glucose. The resulting complex is a green colour. The colour develops by boiling 5 min in a water bath at 100 °C.



*Figure 4: Color scale used to determine the percentage of enzyme activity  
(From left to right: 100 %, 75 %, 50 %, 25 % and 0 % of enzyme activity)*

Semi quantitative analysis are performed using comparisons of experimental samples to a visual colour scale as shown in Figure 4. Under experimental conditions, any glucose left after the 5 min incubation pe-

riod reflects a loss of enzyme activity. Various amounts of 0.5 % glucose are used to represent 100 % (no glucose), 75 %, 50 %, 25 % and 0 % (5  $\mu$ l of 0.5 % glucose) of the expected enzyme activity.

This method is used for characterized enzymatic activity in different drying conditions and solvents ratio in the solution.

### 3.3 Conductive inks

Silver and carbon-based inks are printed after the enzymatic ink, one of the challenges was to obtain a low resistance with drying time and temperature that do not drastically degrade the enzymatic ink activity.

#### 3.3.1 Silver-based ink

Several commercial silver ink samples suitable for flexography lab proofing were tested to determine which one appears to be suitable with the biosensor manufacturing process.

#### 3.3.2 Carbon-based ink

The two other electrodes were manufactured with a carbon ink. As the electrodes layers are in direct contact with the enzymatic layer, carbon was chosen for its chemical inertness during the oxidation-reduction occurring in the functional layer. In order to reach required conductivity, an in-house formulation with several ratio of graphite/carbon black are tested to find the optimum ratio.

### 3.4 Conductive inks and device current measurement

All electrical measurements are performed using a multimeter:

- An ammeter is used to measure the response of the printed enzymatic varnish with glucose solutions, the measurement accuracy is  $\pm 0.1 \mu\text{A}$ . For these pilot experiments, the negative electrode was connected to the reference electrode and the positive electrode was connected to the counter electrode.
- The electrical properties of the conductive inks are evaluated by resistance measurement with an ohmmeter. The distance of measure is set to 1 cm.

### 3.5 Substrate

Whatman lab filter paper was selected for its absorption and rigidity properties. The substrate influence on the enzymatic activity and its cost was not investigated at this state of the project.

### 3.6 Lab scale printing

The flexography printing tests were performed on a sheet-fed laboratory proofing device: the Flexiproof (Testing Machines Inc. TMI, New Castle, USA).

Similarly to the flexography printing unit, the system is composed of a flexography printing group that transfers the ink from the doctor blade, to the cells of anilox cylinder. The ink is deposited onto the plate's relief, which transfers the ink onto the substrate in the nip zone formed by the plate cylinder and the printing cylinder.

In the Flexiproof device, micrometric settings control the gap between:

- the anilox and the plate,
- the plate and the printing cylinder.

It modifies the ink transfer by adjusting the pressure in the nip zone.  
The selected anilox volume was  $18 \text{ cm}^3/\text{m}^2$  or 11.6 BCM.

#### 4. Summary of results

The results provided in this abstract focus on the impact of drying conditions and solvents on an in-house formulated enzymatic ink, and the lab-scale printing of a functional device acting as a glucometer biosensor.

##### 4.1 Formulation of the Enzyme ink

Enzymes are extremely sensitive constituents in all the surrounding physicochemical parameters. Therefore, glucose oxidase is first subjected to various physical and chemical stress in order to determine the limits of its use in the field of industrial printing and select suitable formulation solvents and resins.

##### 4.1.1 Thermal enzymatic activity

Industrial screen printing or flexographic inks require drying temperatures around  $100^\circ\text{C}$  and even more for a short time (a few seconds). At this step of the project, only lab-scale flexography is tested. Consequently, higher ranges of temperature and drying time can be investigated. Although such conditions of drying are not suitable for industrial printing, they are compatible with the commercial flexography conductive inks that are tested so far.

The enzyme ink is printed first, then carbon and silver inks are superimposed. It was therefore necessary to verify whether the enzyme could withstand high temperatures (up to  $120^\circ\text{C}$ ) for a long time (about several minutes). The objective was to define a temperature limit at which no loss of enzyme activity could be due to exposure to heat.

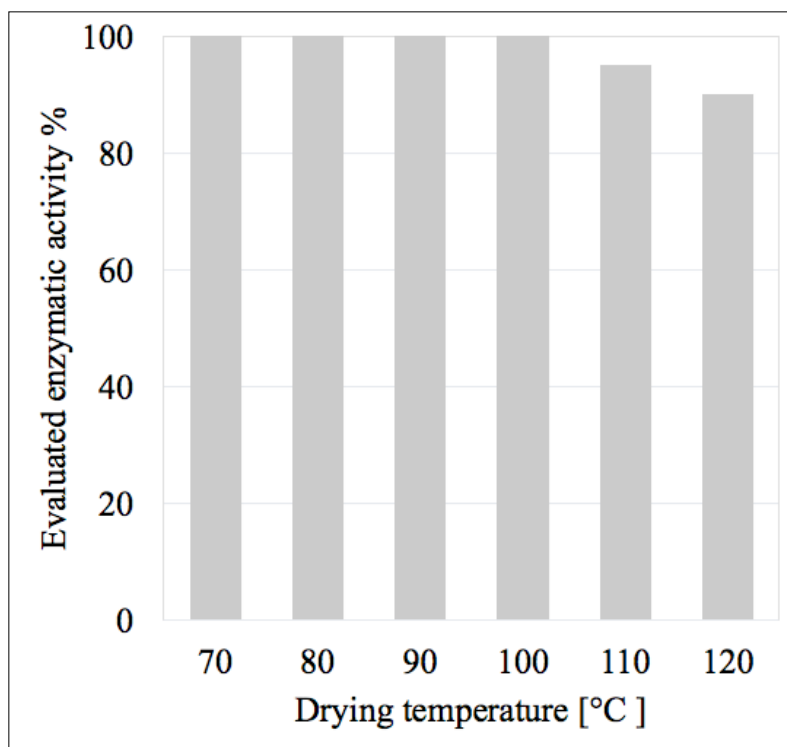


Figure 5: Enzymatic activities after imposing different temperatures for 5 minutes evaluated by comparison with the colour scale

The enzyme solution is transferred to filter paper discs and placed into a fixed temperature oven. After five minutes, the paper discs are removed from the oven, stored in room conditions. Glucose solution droplets are deposited to cover the enzymatic layer, then the colour response is visually evaluated within a minute after.

Figure 5 displays the colour-evaluated activity of the enzymatic ink layers when submitted to 70, 80, 90, 100, 110 and 120 °C for 5 minutes. The results demonstrate that the enzyme can withstand temperatures of 100 °C for 5 minutes without any loss of enzyme activity. On a separate experiment, a 20 min treatment at 100 °C had no apparent impact on the activity.

#### 4.1.2 Enzymatic activity in different solvents

The formulation of the varnish with the enzyme may contain a solvent to dissolve the resin portion. A volumetric ratio of the water in the solution of glucose has been replaced by solvent: n-propanol and ethyl acetate. The latter are two solvents commonly found in flexography and compatible with most of the selected resins for the formulation of inks used in this research.

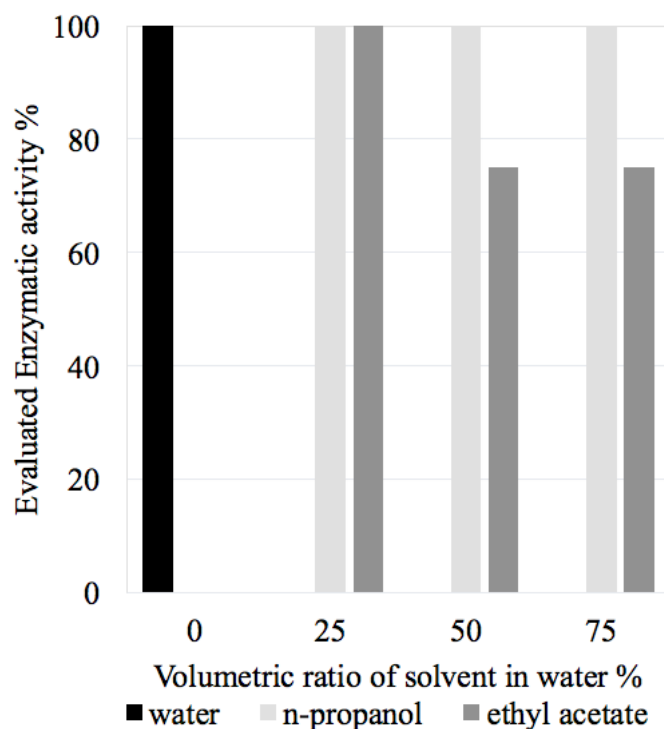


Figure 6: Enzymatic activities as a function of the volumetric ratio of solvents (water and n-propanol or water and ethyl acetate) compared to the water-based enzymatic solution evaluated by comparison with the colour scale

As shown in Figure 6, the enzyme was not affected by n-propanol at all concentration tested. Ethyl acetate reduces the activity by about 25 % at concentrations of 50 % and 75 %.

#### 4.1.3 Thermal enzymatic activity in different solvents

Since the printing of the biosensor requires the combination of drying conditions and solvents presence, various combinations of these parameters are investigated. The enzyme was prepared with different ratios buffer/solvent solution which have been subjected to several relevant temperatures. The results allow testing the limits of the enzyme cope with the increase in temperature when integrated with the solvent or observing a synergistic effect that greatly affect the activity of glucose oxidase.

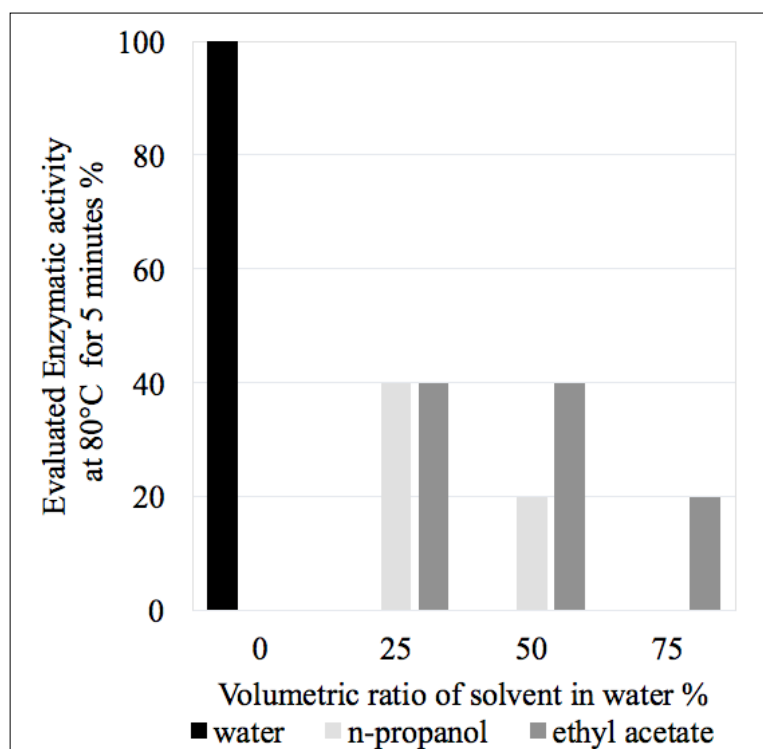


Figure 7: Enzymatic activities as a function of the ratio of solvents (water and n-propanol or water and ethyl acetate) compared to the water-based enzymatic solution at 80 °C for 5 minutes evaluated by comparison with the colour scale

The Figure 7 details the evaluated enzymatic response of solvent-containing solutions that are dried in a oven at 80 °C for 5 minutes. The combination of heat (5 min, 80 °C) and organic solvents leads to a drastic reduction of the enzymatic activity. Therefore, compared to the enzymatic activity in water, the enzymatic activity reaches 40 % in solutions with 25 % of N-propanol and ethyl acetate and 50 % of ethyl acetate, it reaches 20 % in solution with 50 % of N-propanol and 75 % of ethyl acetate, finally the enzymatic activity was undetected in solutions containing 75 % of N-propanol.

#### 4.1.4 Resin

According to the previous results, the strategy has to be revised: water-soluble resins were preferred for the formulation of the varnish containing the enzyme. Therefore, PolyVinylPyrrolidone (PVP K30) was tested. It offers proper viscosity (63 cp) and full enzyme activity at a 33 % w/v concentration. The use of such water-soluble binder allows the formulation of a water-based ink suitable for flexography lab-proofing. Moreover, Prussian blue was integrated as it acts as mediator for the reaction and as support for facilitating the registration during printing due to its colour.

#### 4.2 Device printing

The Flexiproof was used to transfer the silver and carbon-based inks and the enzymatic ink on the filter paper samples. As no significant printability issues were observed when printing the three inks, the optimization of the ink transfer focuses on achieving the required electrical performances required for this application.

Figure 8 highlights the appearance of a printed device. The manufacturing steps include:

- two layers of the enzymatic varnish, no drying step is applied,
- two layers of commercial silver-based ink, with drying at 100 °C for 5 minutes after each ink transfer, the measured resistance is below 2  $\Omega$ ,

- and three layers of carbon-based ink, with drying after the transfer of the three layer for 100 °C for 5 minutes, the measured resistance is about 1 k $\Omega$ .

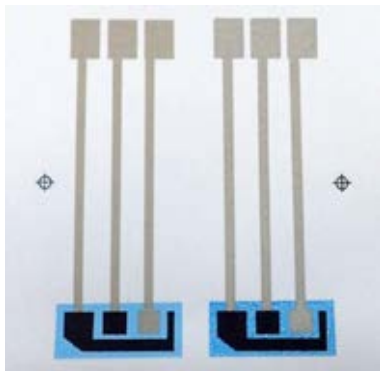


Figure 8: Printed devices; the enzymatic ink appears blue, the silver-based ink is grey and the carbon-based ink has a black appearance

#### 4.3 Biosensor functionality characterization

The last step was to check the functionality of the printed biosensor. The electrodes were connected to a simple electrical circuit for measuring the current and voltage during the reaction. Subsequently, several solutions having very different glucose concentrations, but remaining in the relevant field of the application (from 2 to 32 mmol·L<sup>-1</sup> glucose) are tested to establish the linearity of the signal. A volume of 20  $\mu$ L solution was deposited on the electrode surface and the test tap starts. The signal was measured every 10 seconds until the loss of a response, which indicates the end of the reaction. In Figure 9, current intensity values are reported for a fixed time at 2.5 minutes which corresponds to the maximum signal intensity about. The linearity of the device response confirms the proper functioning of the printed system.

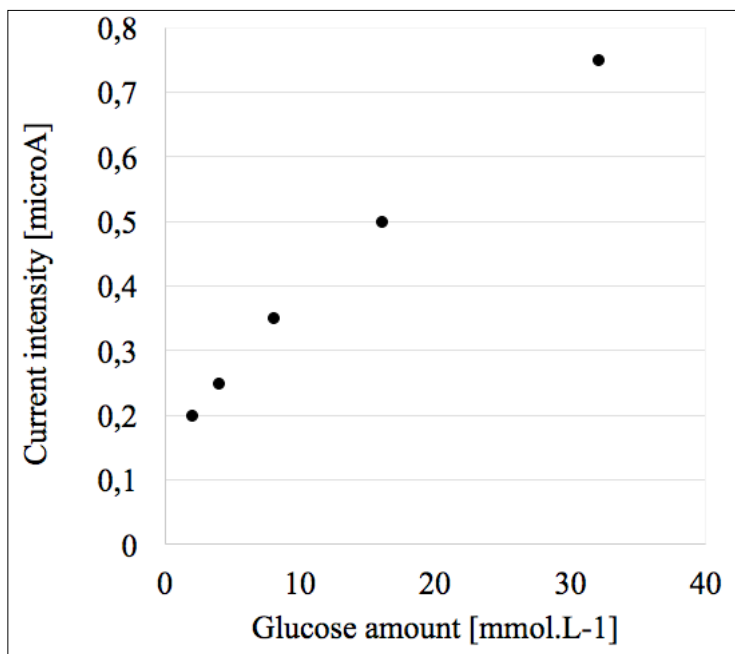


Figure 9: First trial of printed biosensor; intensity as a function of the glucose amount in a solution deposited on the device electrodes

The ammeter resolution is  $\pm 0.1 \mu$ A, which is not sufficient considering the resolution required for such an application. It will therefore be necessary to repeat the measurements with a nanoammeter.

## 5. Conclusion

This project establishes the proof of concept of an enzyme biosensor fully printable by flexography on paper that can be used for blood glucose monitoring for diabetic patients.

The study investigates the impact of different parameters on the enzymatic activity of the ink. First, the heating temperature demonstrated the degradation of the enzymatic color response to the glucose test solutions over 100 °C. Secondary, different ratios of two organic solvents (ethyl acetate and n-propanol) in water were tested. No strong activity reduction was noticed when the enzyme solution was introduced in the water-organic solvent solutions. However, after drying at 100 °C for 5 min, the enzymatic activity diminished drastically, which led to a change of the formulation strategy to favour water-soluble resins. Using such enzymatic ink and conductive inks, fully printed functional devices on filter paper were obtained using lab-scale flexography. The measured electrical signal was proportionate to the glucose amount of several solutions mimicking diabetic blood from 2 to 32 mmol·L<sup>-1</sup> glucose, which demonstrates the redox activity of a new enzymatic ink for flexography printing.

In order to go from the proof of concept to a prototype, numerous technological challenges should be addressed. First concerns are related to the formulation:

- carbon-based and enzyme inks fine-tuning,
- adaptation to large batches of ink production,
- industrial scale drying time.

Further investigations on the substrates are required:

- substrate properties selection and adaptation to the reader,
- inks and substrate printability assessment.

The current size of the device is about ten times the desired final product. Geometry optimization has to be done in order to fit with the harvested human blood samples that are only about a few microliters. Moreover, the strip design depends on the reader device.

Press management includes:

- prototyping,
- adequate printing supplies,
- and in-line characterization method development to ensure the reliability of the devices,
- compatible with medical applications requirements.

Moreover, a complete industrial ecosystem needs to be built if a valuable market is defined.

## Acknowledgement

This project was founded by the Programme d'Aide à la Recherche et au Transfert (PART) of the Ministère de l'Éducation et de l'Enseignement supérieur du Québec.

## References

- Cardosi, M. and. Liu, Z., 2012. Amperometric Glucose Sensors for Whole Blood Measurement Based on Dehydrogenase Enzymes. *INTECH, Chapter 13*.
- Dubowski, K. M., 1962. *An o-toluidine Method for Body-Fluid Glucose Determination*. Clinical Chemistry and Toxicology Laboratories, University of Florida Teaching Hospital and Clinics, USA, pp. 215–218.
- Heller, A. and Feldman, B., 2008. Electrochemical Glucose Sensors and Their Applications in Diabetes Management. *Chem. Rev.*, 108, pp. 2482–2505.
- Higgins, C., 2013. *Understanding Laboratory investigations: a guide for nurses, midwives and healthcare professionals, third edition*. Wiley-Blackwell, UK.
- Rahman, Md.M., Ahammad, A.J.S., Jin, J.-H., Ahn, S.J., Lee, J.-J., 2010. A comprehensive review of glucose biosensors based on nanostructured metal-oxides. (Open Access) *Sensors*, 10(5), pp.4855–4886.
- Tudorache, M. and Bala, C., 2007. Biosensors based on screen-printing technology, and their applications in environmental and food analysis. *Anal. Bioanal. Chem.*, 388, pp. 565–578.
- Tsuge, H., Natsuaki, O., Ohashi, K., 1975. Purification, properties, and molecular features of glucose oxidase from *Aspergillus niger*. *J. Biochem.* 78(4), pp.835–843.



## New Fabrication Approach for Low Cost RFID Tags

*Lorenzo Pirrami<sup>1</sup>, Danilo Demarchi<sup>1</sup>, Marco Mazza<sup>2</sup>, Fritz Bircher<sup>2</sup>*

<sup>1</sup>Department of Electronics and Telecommunications, Politecnico di Torino, Torino, Italy

<sup>2</sup>Institute for Printing, University of Applied Sciences Western Switzerland, Fribourg, Switzerland

E-mail: lorenzo.pirrami@polito.it; danilo.demarchi@polito.it; marco.mazza@hefr.ch; fritz.bircher@hefr.ch

### Short Abstract

The aim of this paper is to introduce the first step towards a new inkjet-based fabrication approach for low cost and high throughput radio frequency identification tags (RFID) as well as to demonstrate the feasibility of using double-surface radio frequency chips (RFIC) with a capacitive coupling instead of a direct contact (soldering) between the antenna coil and the chip itself. These RFICs can be delivered, using an inkjet-based process, onto one pad of an antenna coil instead to be precisely placed using flip-chip method. This will allow producing RFID tags only with printing steps, reducing considerably the assembly and hence the overall costs. Simulation results show that an optimization of the capacitive coupling between the chip and the antenna coil is possible and thanks to the boost of the quality factor of the tag, acceptable load voltages can be easily reached, even in unfavourable situations.

**Keywords:** RFID, inkjet printing, capacitive coupling, single chip delivering

## 1. Introduction and background

RFID technology is a well-established technology with billions pieces fabricated every year. The applications span from retail, to transportation, automotive, manufacturing, logistics, pharmaceutical, security, safety, etc. and the market is still in hunger for cheaper, large volume productions and increase the demand. In the HF, UHF and microwave frequency domain, tags are usually composed of an integrated circuit (IC) and an antenna; the fabrication of these two components is responsible for more than 50 % of the final cost. The remainder, are costs related to the assembly which are strongly dominated by the flip-chip step (more than 90 %) (Sarma, 2001; Swamy and Sarma 2003). Flip-chip is a widely used technique for interconnecting integrated circuits to external circuitry with solder bumps deposited on the chip pads. For example, a high-end FCM 10000 (Muehlbauer AG) flip chip assembly system can assemble approximately 9 500 chips per hour achieving a placement accuracy of 20  $\mu\text{m}$ . However, the assembly towards smaller chips, such as 100  $\mu\text{m}$  and less in lateral dimensions, becomes unfeasible because of unstable behavior in the atmosphere. In fact, in dry environments, the chips are negatively affected by electrostatic and the Van der Waals forces, which can cause them to either stick together, creating aggregated structures or fly apart. Precise positioning of the chips with small surface bumps onto external antenna metal terminals become also very difficult without trading off the speed. Furthermore, the fabrication of narrow space precise antenna patterns become also very difficult using either printing technologies or chemical etching methods.

### 1.1 State-of-the-art on micro-parts assembly processes

Many research projects have been done in order to reduce the overall costs and increase the assembly throughput of micro-components. The most promising techniques are the one based on the self-assembly processes which use the principle of minimum potential energy. These techniques are based on surface

tension and capillary forces (Park et al., 2014; Sato et al., 2003; Tsai et al., 2007; Zheng W. and Jacobs 2004; Srinivasan et al., 2001; Routa et al., 2013; Chang et al., 2012), mechanical shape recognition (Chang et al., 2012; Alien Technology Corporation, 1999), magnetic force (Perkins et al., 2002) and electrostatic force (Bohringer et al., 1998). Park et al. recently demonstrate the first implementation of a fluidic self-assembly machine, based on surface-tension-directed-self-assembly (Knuesel, 2010), capable of placing 15 k chips per hour using a 2.5 cm wide assembly region. Even though the above-mentioned technologies proved their competitiveness against the traditional fabrication process, in terms of efficiency and production rate, most of them have been demonstrated in favorable cases. In fact, Chang et al. pointed out the fact that the reported self-assembly methods have been applied in cases in which the densities of the receptor sites are very high and the spacing of the receptor sites and the size of the components are of the same magnitude. This, of course do not reflect the real case of an assembly of RFID tags where the size of the antenna can be several centimeters and the size of one RFID die is only few hundreds of micro-meters. Such difference in scale can reduce the efficiency of assembly process and to achieve a good fill rate, it requires either a huge number of components or a very long time. In order to cope to this limitations and deal with RFID chips, they proposed a hybrid technique (Chang et al., 2010; 2011; Saiola et al., 2008), which combine the two major branches of micro-handling: high speed and low-cost robotic micromanipulation for coarse positioning of multiple pads chip near the binding sites and droplet self-alignment for fine positioning.

Hitachi propose a new concept for RFID chip, called “ $\mu$ -chip” which consists in using one pad on the top of the chip and the back of the silicon die (bulk) acting as the second pad (Usami et al., 2003). With this approach, precise positioning to the antenna terminals is not necessary because there is only one connection on each surface. Moreover, the chip orientation can be arbitrary as long as one of the two contacts faces the landing pad. They also proposed a new water-based techniques for the double-surface radio frequency integrated circuits (RFICs). It is known that, when immersing microscopic objects in liquid, electrostatic and Van der Waals forces markedly decrease and the capillary forces become the dominant factor as the adhesive trigger between chips. In a first technique (Noda et al., 2009; Noda and Usami, 2008), the chips are kept dispersed in a liquid, and only a single chip is captured and manipulated using a micropipette. In a more recent technique (Noda et al., 2011), however, before their deposition onto the antenna, a micro-liter liquid droplet is dispensed onto a hydrophilic/hydrophobic patterned allowing a stress-free self-assembly process.

The advantages in using a double-surface RFIC clearly lead to an increasing of the fabrication rate. However, the fabrication process proposed by Hitachi is complicated and expansive, therefore, even if the assembly is easier than for traditional pick-and-place machines, the whole fabrication is less cost effective. Furthermore, the water-based techniques still suffer from the serial behaviour of the micropipette handling.

## 2. Materials and Methods

### 2.1 Printing of the antenna coil

The antenna coil has been inkjet-printed on polyethylene naphthalate (PEN – 125  $\mu$ m Teonex Q83 from DuPontTeijinFilms) substrate. The latter has been cleaned by immersion in isopropanol and deionized water and subsequently dried in an oven at 150 °C for 1 h. After that, the PEN foil has been plasma treated in order to modify its surface, resulting in an improvement of wettability for the conductive ink onto the substrate. The conductive ink (Sicrys I30EG-1 from PVNanoCell) is based on single-crystal silver nanoparticles (30 % by weight) in ethylene glycol (EG). A custom printer with a RICOH MH5440 printhead with 7 pL drop volume and native resolution of 150 dpi has been used. Two rows out of four were used to print the conductive layer in order to have a resolution of 300 dpi. Printing was performed with a custom

multipass algorithm (original image unravelled in four random images that recreate the original one when superposed) for improving layer homogeneity avoiding coalescence effects between drops. Our multipass algorithm randomizes the nozzles to be used in order to minimize the effects of malfunctioning nozzles.

## 2.2 Liquid phase single chip delivering concept

As shown in Figure 1(a), the idea of our new liquid phase single chip delivering concept is to fill a chip-reservoir with double-surface RFICs and a liquid solution (e.g. water or a dielectric ink) and singularizing them in order to enter the delivering channel one-by-one. A high frequency communication test will be performed before the delivering step in order to separate non-working RFICs from the working ones. The single chip detection will be done using a Charged Coupled Device (CCD) camera. The delivery will be performed by a piezoelement driven by a control logic which will be in turn driven by the information from the CCD camera in the region of interest (ROI). The RFICs will be delivered onto the antenna (printed before the delivering) encapsulated in the liquid solution and after landing, positioning of the chips will be performed by self-assembly. As shown in Figure 1 (c), the contact between the chip and the antenna will be purely capacitive increasing connection reliability (removing any soldering step) and allowing the production of RFID tags only with printing steps. In addition the RFIC will be protected against short circuits when printing the antenna bridge (top conductive layer).

Such approach will reduce considerably the assembly and hence the overall costs. Furthermore, this system is intended to be integrated in industrial inkjet printers for RFID fabrication as a specialized printhead. This will lead to very high throughput due to the high potential of parallelization (e.g: use a multi-channels, multi-printheads or a mix of both configurations).

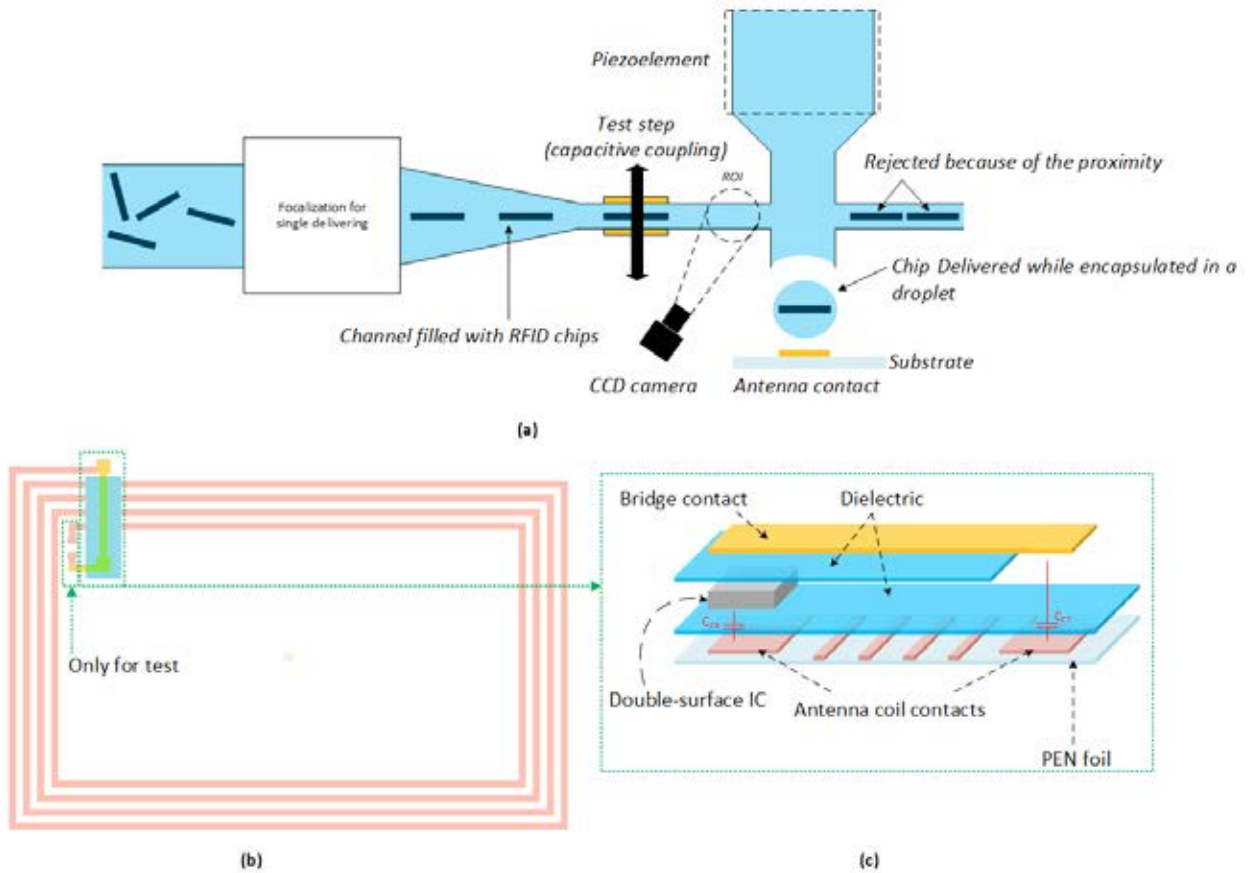


Figure 1: (a) Conceptual view of the new liquid phase single chip delivering approach; (b) Antenna coil with capacitive coupling; (c) Exploded view of the capacitive coupling with double-surface RFIC

### 3. Results and Discussion

#### 3.1 Capacitive coupling analysis

A typical RFID system can be separated into two parts: the reader and the tag. An equivalent electrical circuit is presented in Figure 2(a). In this model the reader is represented by a voltage source  $V_o$  with an internal resistance  $R_o$ . In order to deliver maximum power to the antenna, the impedance of the source has to be matched to the antenna impedance. The antenna can be modeled by an inductance  $L_1$  and a series resistance  $R_1$  in order to take ohmic losses into account. The tag antenna is modeled in the same way by an inductance  $L_2$  and a resistance  $R_2$ . In order to significantly improve the efficiency, the tag impedance is tuned to the resonance frequency by a capacitance  $C_2$ . The value can be calculated using the following equation:

$$C_2 = \frac{1}{(2\pi f_0)^2 L_2} - C_L = \frac{1}{\omega_0^2 L_2} - C_L \quad [1]$$

where  $f_0$  is the resonant frequency and  $C_L$  is the load capacitance. In Figure 2(b) is shown the modified electrical model considering the capacitive coupling introduced by our fabrication approach. The values of  $C_{CT}$  and  $C_{CB}$  can be estimated using the following equation:

$$C_{CT} = C_{CB} = \frac{A \epsilon_0 \epsilon_r}{d} \quad [2]$$

where,  $A$  is the effective coupling area which is equal to the chip surface,  $\epsilon_0$  is the vacuum permittivity,  $\epsilon_r$  is the relative dielectric constant of the dielectric layer and  $d$  is its thickness. The tag load is modeled by an impedance made up of a capacitor ( $C_L$ ) and a resistor ( $R_L$ ). The latter define the current consumption of the RFIC. A detailed analysis of the circuit shown in Figure 2(a) can be found in Finkenzeller (2010).

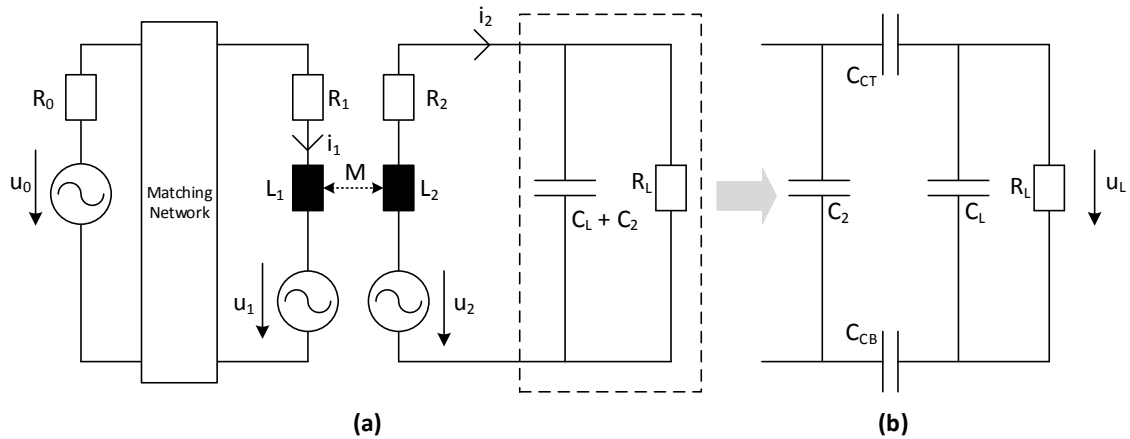


Figure 2: (a) Typical reader-tag electrical model; (b) Detail with the capacitive coupling

In a first step, we simulated the voltage on the load ( $u_L$ ) without capacitive coupling (direct contact from antenna to load). This voltage can be seen in Figure 3(a) (solid line) for a tag with properties as specified in Table 1. In a second step we simulated the voltage on the load considering the capacitive coupling and using the same numerical values. As shown in Figure 3(a) (dashed line), the load voltage is attenuated and the resonant frequency of the tag is slightly shifted toward higher frequencies. This is due to the additional capacitors in the circuit.

High frequency RFIDs require high value of the parallel capacitor  $C_2$  in order to reduce the resonant frequency. Such high values create a lower impedance path than the impedance of the coupling capacitors ( $C_{CT}$  and  $C_{CB}$ ). In fact, the available voltage at the chip level is strongly attenuated for small values of  $C_{CT}$  and  $C_{CB}$ . As shown in Figure 3(b), the frequency shift as well as the resulting attenuation become very small by increasing the values of  $C_{CT}$  and  $C_{CB}$ . This can be explained by the fact that the quality factor ( $Q$ ) is also low. In fact, as shown in Figure 4(a) and Figure 5(a), for the values given in Table 1,  $Q$  is less than 10.

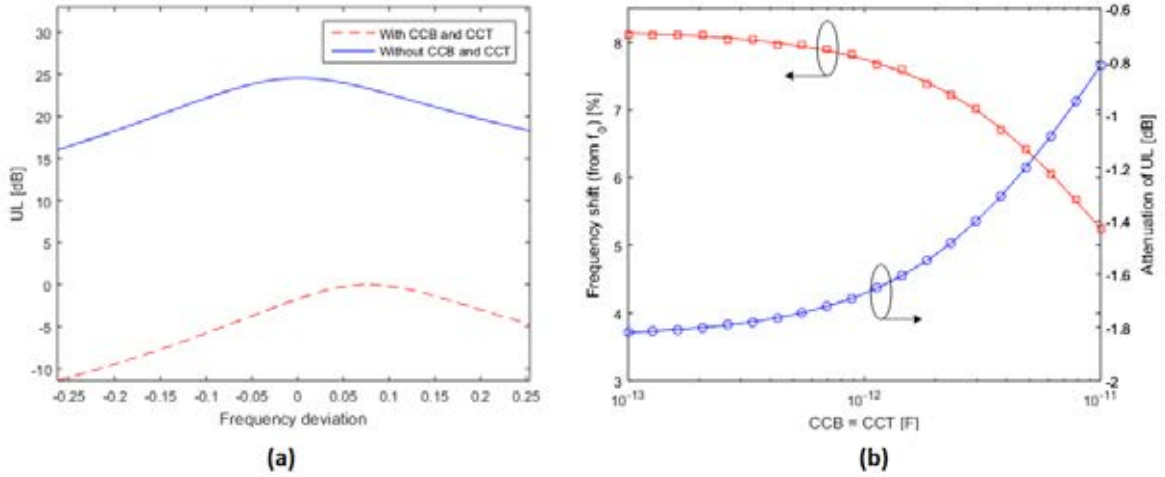


Figure 3: (a) Frequency behavior of the load voltage ( $\hat{U}_L$ ) around  $f_0$  with and without coupling capacitors ( $C_{CT}$  and  $C_{CB}$ ); (b) Left side: relative (to  $f_0$ ) frequency shift due to  $C_{CT}$  and  $C_{CB}$ . Right side: attenuation due to the frequency shift; the reader excitation frequency is kept constant at  $f_0$ ; the simulation has been carried out using the values of Table 1

One possibility for increasing  $Q$ , is to reduce the value of  $R_2$ , this can be done by stacking up more layers of the conductive ink, hence by increasing the thickness of the inductance  $L_2$ . Due to the capacitive coupling, for small  $R_2$ ,  $Q$  is boosted to higher values compared to the case without coupling. This is of a great interest since  $Q$  is directly related to the read range to be achieved. However, this solution has limitations as explained in section 2.1. Another solution to increase  $Q$  is to have larger value of  $L_2$ . However, in this case, the improvement is very limited.

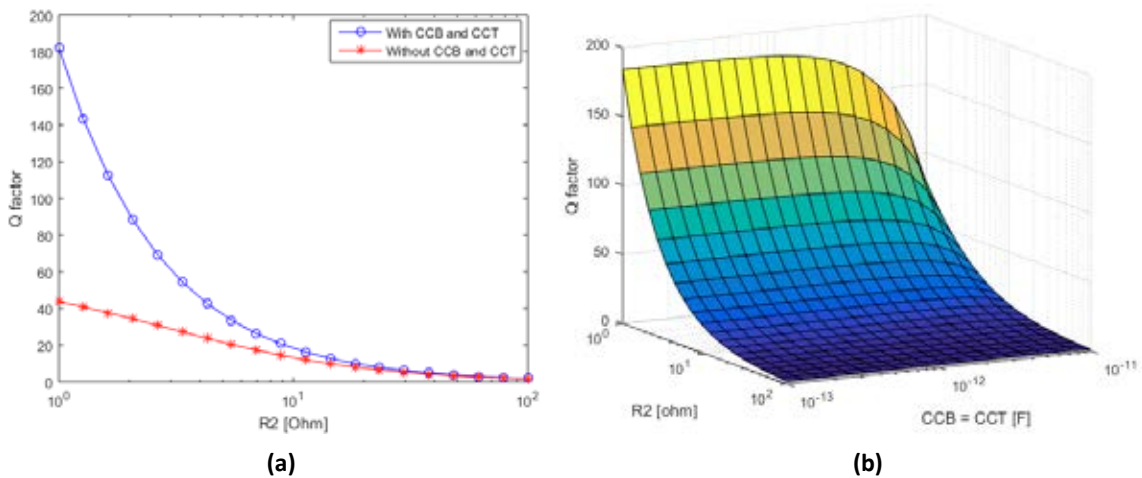


Figure 4: Improvement of the  $Q$  factor by reducing the value of  $R_2$ ; (a) simulation using the values of Table 1, and (b) evolution of the  $Q$  factor with  $C_{CT}$  and  $C_{CB}$  around 1pF; for coupling capacitors  $\geq 1$ pF, the  $Q$  factor is not significantly affected

An optimization for reducing the frequency shift, hence the related attenuation, can be done by adapting the value of  $C_2$  according to the value of the coupling capacitors.

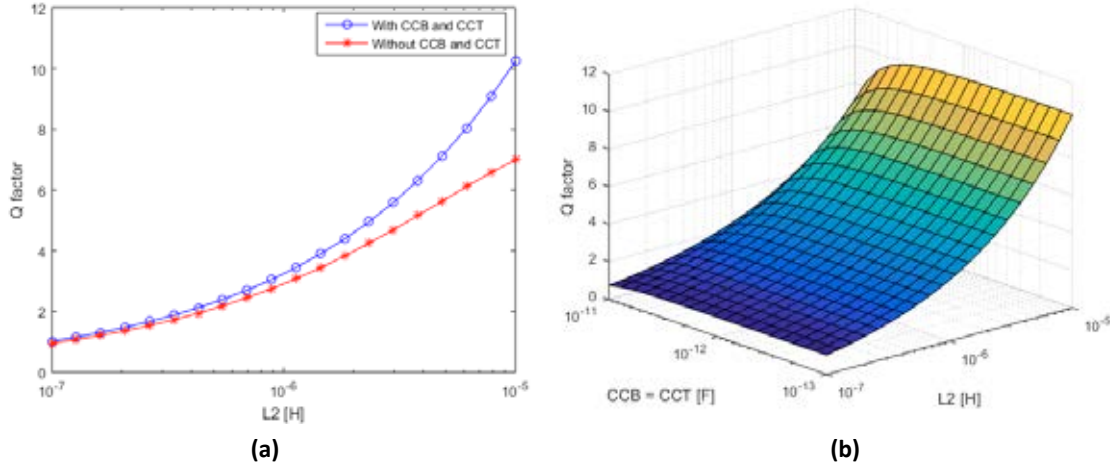


Figure 5: Improvement of the  $Q$  factor by increasing the value of  $L_2$ , (a) simulation using the values of Table 1 and (b) evolution of the  $Q$  factor with  $C_{CT}$  and  $C_{CB}$  around 1pF; for coupling capacitors  $\geq 1$ pF, the  $Q$  factor is not significantly affected

However, the advantage of tuning the tag to  $f_0$ , is counter balanced by a higher attenuation due to a higher value of  $C_2$  compared to the value given by equation 1. In addition, this optimization strongly depends on the ability of the fabrication process to have the desired dielectric thickness, especially for sub-micron values.

Table 1: Simulation parameters

Symbol	Description	Value	Unit
$f_0$	Resonant frequency	13.56	MHz
$k$	Coupling factor	0.05	–
$L_1$	Reader inductor <sup>b</sup>	2	$\mu\text{H}$
$L_2$	Tag inductor <sup>b</sup>	2	$\mu\text{H}$
$R_2$	$L_2$ internal resistance	40	$\Omega$
$R_L$	Load resistance <sup>a</sup>	10	$\text{k}\Omega$
$C_L$	Load capacitor <sup>a</sup>	10	pF
$C_2$	Tag parallel capacitor	59	pF
$C_{CT}$	“Top” coupling capacitor	1	pF
$C_{CB}$	“Bottom” coupling capacitor	1	pF
$\hat{I}_1$	Reader current	500	mA
$A$	Antenna dimension A	80	mm
$B$	Antenna dimension B	50	mm
$S$	Coupling surface	1	$\text{mm}^2$

### 3.2 Antenna coil fabrication

The optimization of the thickness of the conductive layer is fundamental for controlling ohmic losses, hence the quality factor of the antenna coil. The thickness can be controlled by stacking up several layers. We initially printed continuously each pass with the substrate heated up to 60 °C. As shown in Figure 6(d),



despite the multipass approach, we observed agglomerations of ink starting from the second layer. In this case it was difficult to control the thickness of the antenna coil. In addition, the ink start to spill onto the track of antenna coil. In order to cope with these limitations, we introduced a 60 s waiting time between each pass and the substrate temperature has been increased to 80 °C. In this way, each pass was pre-cured at 80 °C and the drops frozen quickly giving the topology shown in Figure 6(b) and (c). The profile was still not homogeneous; however, we had a much better control of the thickness.

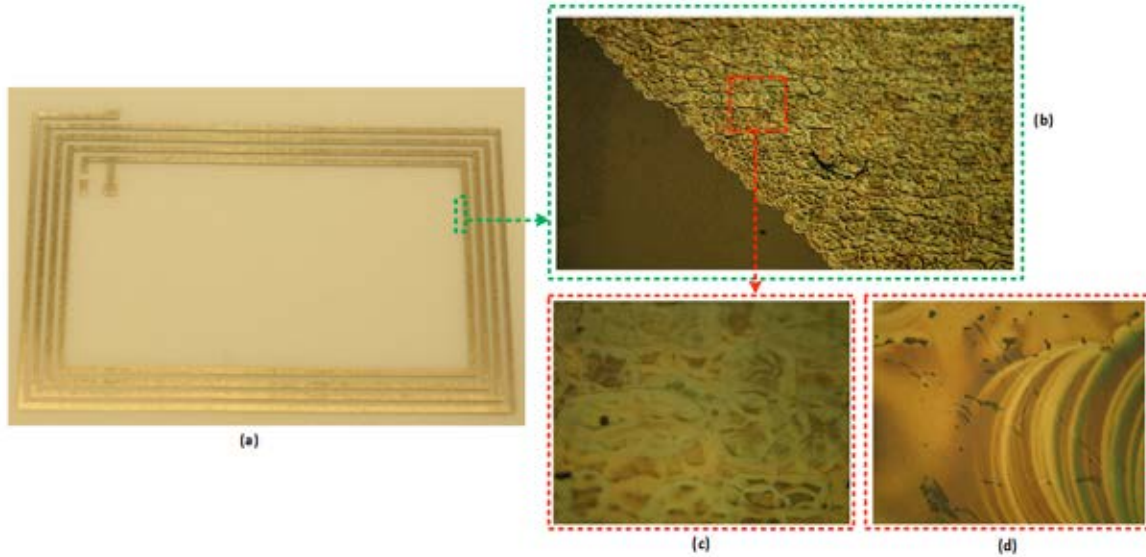


Figure 6: (a) Printed antenna coil; (b) Magnified ( $\times 100$ ) optical micrograph of the printed coil using the 60 s waiting time; (c) Zoom ( $\times 200$ ) with detail of the frozen drop; (d) Magnified ( $\times 50$ ) optical micrograph of the printed coil without waiting time

#### 4. Conclusions

New fabrication approaches are required to reduce the fabrication costs of passive RFID tags. Our proposition will allow a simple delivering method for double surface RFICs onto the antenna contacts using a capacitive coupling instead of direct contact (soldering). The capacitive coupling introduces an attenuation on the load voltage as well as a frequency deviation compared to the direct contact case. According to the simulation results, an optimization is required in order to maximize the voltage available for the RFIC. This optimization consists in decreasing as much as the printing process allows the thickness of the coupling capacitors in order to decrease the impedance at HF frequencies. Furthermore, the antenna coil resistance has to be decreased in order to boost the quality factor, hence increasing the load voltage as well as the reading range of the tag. However, the quality factor has to be defined in order to have sufficient bandwidth for the communication (e.g. NFC protocol).

#### References

- Alien Technology Corporation, 1999. *Fluidic Self Assembly, White Paper*.
- Bohringer, K.-F., Goldberg, K., Cohn, M., Howe, R. and Pisano, A., 1998. Parallel Microassembly with Electrostatic Force Fields. In: *Proc. IEEE Int. Conf. on Robotics and Automation*, 2, pp. 1204–1211.
- Chang, B., Jääskeläinen M., and Zhou Q., 2010. Hybrid Micro Assembly of Microchips on Segmented Patterns. In: *Proc. IEEE Int. Conf. on Automation Science and Engineering*, Toronto, Canada, pp. 15–20.

- Chang B., Routa, I., Sariola V. and Zhou Q., 2011. Self-alignment of RFID dies on four-pad patterns with water droplet for sparse self-assembly. *Journal of Micromechanics and Microengineering*, 21(9), p. 095024.
- Chang, B., Shah, A., Routa, I., Lipsanen, H. and Zhou, Q., 2012. Surface-tension driven self-assembly of microchips on hydrophobic receptor sites with water using forced wetting. *Applied Physics Letters*, 101(11), pp. 114105/1–5.
- Chang, B., Virta, A. and Zhou, Q., 2012. Hybrid Microassembly for Massively Parallel Assembly of Microchips with Water Mist. In: *Proc. IEEE Int. Conf. on Manipulation, Manufacturing and Measurement on the Nanoscale (3M-NANO)*, pp. 38–43.
- Finkenzeller, K., 2010. *RFID Handbook - Fundamentals and applications in contactless smart cards, radio frequency identification and near-field communication, Third edition*. Wiley.
- Knuesel R.J. and Jacobs H.O., 2010. Self-assembly of microscopic chiplets at a liquid–liquid–solid interface forming a flexible segmented monocrystalline solar cell. *PNAS*, 107(3), pp. 993–998.
- Park, S.-C., Fang, J., Biswas, S., Mozafari, M., Stauden, T. and Jacobs, H. O., 2014. A First Implementation of an Automated Reel-to-Reel Fluidic Self-Assembly Machine. *Advanced Materials*, 26(34), pp. 5942–5949.
- Noda, H. and Usami, M., 2008.  $0.075 \times 0.075 \text{ mm}^2$  Ultra-Small  $7.5 \text{ }\mu\text{m}$  Ultra-Thin RFID-Chip Mounting Technology. In: *Proc. IEEE 58<sup>th</sup> Electronic Components and Technology Conference*, pp. 366–370.
- Noda H., Usami, M. Sato, A. Terasaki S. and Ishizaka, H., 2009. Water-Based High-Volume Stress-Free Ultra-Thin Powder-Chip Method. In: *Proc. IEEE 59<sup>th</sup> Electronic Components and Technology Conference*, pp. 1506–1512.
- Noda H., Usami, M., Sato, A., Terasaki S. and Ishizaka, H., 2011. Self-aligned Positioning Technology to Connect Ultra-small RFID Powder-chip to an Antenna. In: *Proc. IEEE 61st Electronic Components and Technology Conference*, pp. 1009–1014.
- Perkins, J., Rumpler, J. and Fonstad, C.G., 2002. *Magnetically Assisted Self Assembly – A New Heterogeneous Integration Technique*, MIT Technical Report.
- Routa, I., Chang, B., Shah, A. and Zhou, Q., 2013. Surface Tension-Driven Self-Alignment of Microchips on Low-Precision Receptors. *Journal of Microelectromechanical Systems*, 23(4), pp. 819–828.
- Srinivasan, U., Liepmann, D. and Howe, R.T., 2001. Microstructure to Substrate Self-Assembly Using Capillary Forces. *Journal of Microelectromechanical Systems*, 10(1), pp. 17–24.
- Sarma, S., 2001. *Towards the 5¢ Tag, White Paper*. Cambridge, MA: Auto-ID Center.
- Swamy, G. and Sarma, S., 2003. *Manufacturing Cost Simulations for Low Cost RFID systems, White Paper*. Cambridge, MA: Auto-ID Center.
- Sato, K., Ito, K., Hata S. and Shimokohbe, A., 2003. Self-alignment of microparts using liquid surface tension—behavior of micropart and alignment characteristics. *Precision Engineering*, 27, pp. 42–50.
- Sariola, V., Zhou, Q., Laaß, R. and Koivo, H.N., 2008. Experimental study on droplet based hybrid microhandling using high speed camera. In: *Proc. IEEE/RSJ Int. Conf. on Intelligent Robots and Systems*, pp. 919–924.
- Tsai, C.G., Hsieh C.M. and Yeh, J.A., 2007. Self-alignment of microchips using surface tension and solid edge. *Sensors and Actuators: A Physical*, 139(1–2) pp. 343–349.
- Usami, M., Sato, A., Sameshima, K., Watanabe, K., Yoshigi H. and Imura, R., 2003. Powder LSI: an ultra small RF identification chip for individual recognition applications. In: *Solid-State Circuits Conference, Digest of Technical Papers. ISSCC IEEE International*, 1 pp. 398–501.
- Zheng W. and Jacobs, H.O., 2004. Shape-and-solder-directed self-assembly to package semiconductor device segments. *Applied Physics Letters*, 85(16), pp. 3635–3637.



## Fabricating a Flexible Thin Film Humidity Sensor: minimum viable product

*Maksim Korobkin, Jiayuan Yin, Aarne Klemetti*

Helsinki Metropolia University of Applied Sciences, PO Box 4070, FI-00079 Metropolia Finland, Vanha maantie 6, FI-02650 Espoo, Finland

E-mail: maksim.korobkin@metropolia.fi; jiayuan.yin@metropolia.fi; aarne.klemetti@metropolia.fi

### Short Abstract

In this applied research, the feasibility of using Carbon NanoBud (CNB®) depositions which is a hybrid of carbon nanotube (CNT) and fullerene, then being restructured as a sensor element, was proven and able to detect changes in absolute and relative humidity in room temperature environment in vitro and in vivo. In this investigation, the sensor element is fabricated to be of the capacitive kind. Carbon nanotube bundles were chosen because they can be used in flexible thin film structures. The humidity sensing functionality is demonstrated by a reversible change of the device capacitance, from a few to hundreds of pF, as the relative humidity level changes from 15 % to 99 % and over four decades of measurement frequencies starting from 100 Hz and ending in 100 kHz. Proofing was done taking humidity measurements in parallel from a position 1 cm distant. Then a climate controlled chamber was used to verify these findings with two individually fabricated sensors of later generations.

**Keywords:** carbon NanoBud (CNB®), capacitive sensor, hybrid media technology

### 1. Introduction and background

Since carbon nanotubes (CNTs) were created more than two decades ago (Iijima, 1991), they have been used as gas sensors due to their high surface area and ability to interact with gas, and, as a result, exhibit a change in electrical conductivity upon gas adsorption. What is more, these properties are manifest at room temperature, contributing to ease of use (Adjizan et al., 2014; Ricciaidella et al., 2015). CNTs can also conduct electricity, therefore they can additionally be utilized as capacitive sensors. We chose to study their properties in respect to humidity because humidity is one of the factors most contributing to aging of electronic circuit boards, mechanical systems and stationary structures. It changes the electrical characteristics, corrodes metallic surfaces, warps water sorbent materials and allows for fungi to grow wildly if left unattended, not to forget all the industrial manufacturing processes that require some humidity monitoring, such as on a printing press and in the whole value chain of the paper and board printing process.

New technological advantages also enable the supply of flexible smart systems (Reuss et al., 2015; Hackler et al., 2015). There have been a lot of studies dedicated to printed sensors, which, as well, continue to motivate the testing of new materials and processes for these purposes (Rivadeneyra et al., 2015; Islam et al., 2015).

Capacitive humidity sensors (CHSs) are broadly used because they have higher sensitivity and lower power dissipation than other humidity sensors (Kouda et al., 2008). Use of CNB® has not been investigated in such a manner prior to the work reported here.

The research questions in this study are:

- How to design, prepare, and test a flexible thin film humidity sensor with CNB®?
- What would be the plausible applications for this type of CHS?

## 2. Materials and Methods

The experimental measuring setup, which was designed in order to determine the feasibility of using CNB® to sense humidity, consisted of thin layer CNB® supplied by Canatu (Canatu Oy, Helsinki, Finland) deposited on polyethylene terephthalate (PET) substrate.

The sample specifications were constructed from proprietary non-densified CNB® depositions, with parameters only known in detail to Canatu. During the experiments we did not notice any significant variance in sample performance, with only occasional “faulty” sensor readings that gave exceptional capacitance and resistance values, and so easily identifiable. These we attributed to fabrication errors that happened during our processing or synthesizing of CNB®. We also noticed that the CNB® samples were deposited such that the random Moiré optical fringe pattern generating formations of the PET substrate was still visible due to the transparency and optical uniformity of deposition (Figure 1).



*Figure 1: Scan of CNT deposition at 300 dpi. The dark area is formed from deposited CNB®, and Moiré fringe formation is visible across the figure*

Deposited areas on the PET sheets were cut into an intersecting comb structure (Figure 2) using an automated cutting table to ensure uniform results with all sample sensors. The cutting table was chosen so that the process of fabrication could be replicated with minimum experimental error. Adobe Illustrator CC (AI) was used to produce the cutting pattern for this experiment.

After cutting, the samples were assembled on a support structure and laminated with Scotch® Transparent Tape (Figure 3), and contacts were coated with silver using a flex conductive pen (CircuitWorks® CW2900) to prevent further contamination of the CNTs and ensure reliable contact after multiple measurements. Silver-coating of contacts was also done because it was theorized that measurement clamps would otherwise scratch the contact surfaces rendering them useless after repetitive measurements. This, though, was not tested to the point of identifying the protective effect. Sensing elements were finally taped onto a CD holder to provide a rigid support structure. Sensing while the sensor element was twisted was not investigated in these experiments (Figure 4).



*Figure 2: Sample with comb structure*

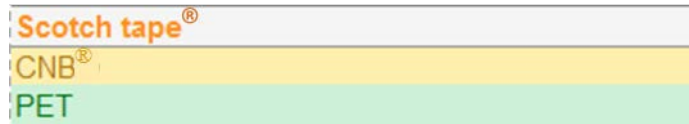


*Figure 3: Laminated sensor structure layout, with Scotch® Tape coating*



*Figure 4: Sensing element on a CD holder*

Preliminary measuring was performed by breathing onto a sensor element and pouring liquid substances on it, following the practice illustrated by Regoni et al. (2014). The measurement was confirmed by taking a reading from a proximity of 1 cm, using a sensor tag (CC2541 SensorTag Development Kit, Texas Instruments Incorporated), equipped with an integrated relative humidity (RH) sensor, according to the setup depicted in Figures 6 and 7. In the case of having an actual liquid on the sensor, a visual inspection was deemed sufficient. Sensor data were in the form of capacitance change between two sensing elements, and this change was measured using an RCL meter (Fluke PM6304 Programmable Automatic RCL Meter). Since the change in capacitance was the most important factor in determining the intended operation, variation of initial values of individual sensor elements was initially ignored. Later it was noticed that even though deposition thickness and Moiré pattern varied randomly, noticeable by variation in initial values, every sensor behaved essentially the same, as shown in Figure 5b. In this experiment, sensors were sub-

merged inside and outside a cold drink cup, which was made from polylactic acid (PLA) transparent plastic of thickness 0.4 mm, filled with distilled water (Figure 5a). The cup served a purpose to gauge sensitivity of the sensor; therefore, it was important to see what values would be reached while the sensor is experiencing different states of matter interaction. For both samples, as seen from the charts, generally both sensors behave the same way under same RH in the room at each data point. Biggest difference exists between being submerged half way and submerged inside the glass, respectively.



Figure 5a: Sensor was submerged inside and outside the cup

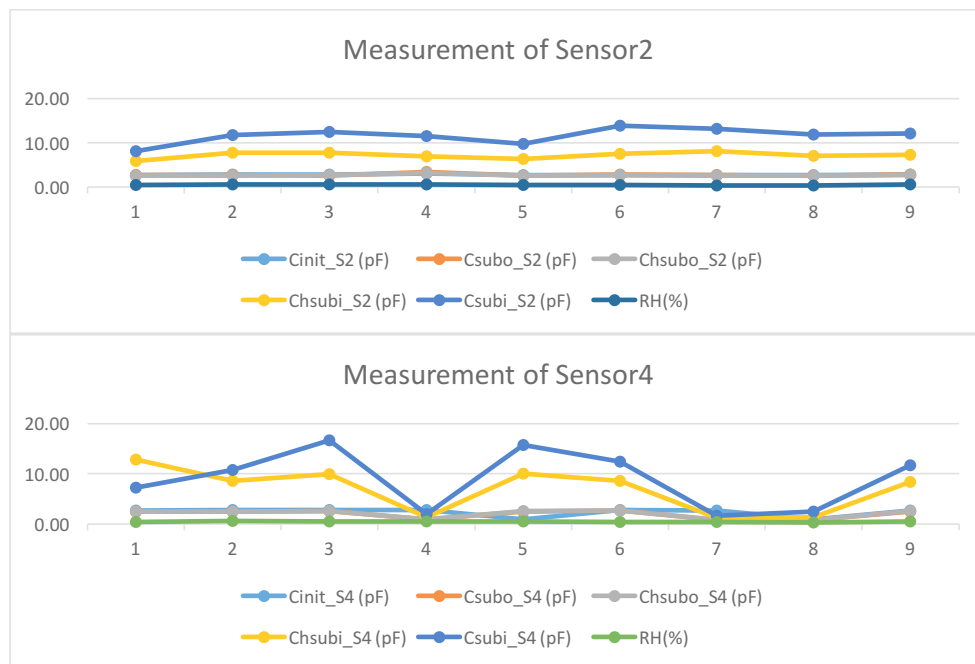


Figure 5b: States measured are init = initial; sub<sub>i</sub> = submerged inside Cups; sub<sub>o</sub> = submerged outside Cup; hsub<sub>i</sub> = half submerged Inside the Cup; hsub<sub>o</sub> = half submerged outside the Cup, where X axis shows measuring points with same parameters and timeframe, while in Y axis, number is the measurement, unit of which is marked in the legend

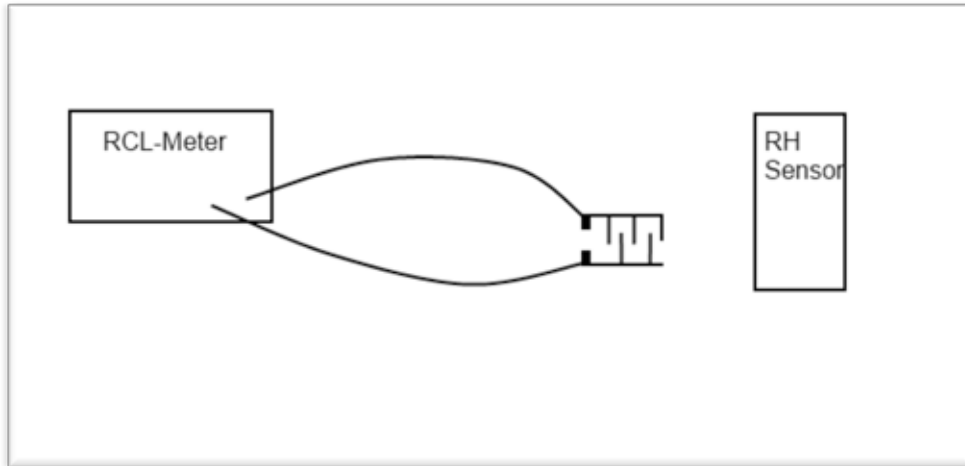


Figure 6: Sensor setup schematic



Figure 7: Sensor measurement setup

These experiments were confirmed in a climate chamber CTS (Temperature/Climatic Stress Screening Chamber, Model: CS-70/350-5) twice, each time with different samples but with the same setup. Samples were stored in an uncontrolled environment as it was deemed unnecessary to protect them because the tested medium was considered to be sufficiently sealed from external contaminants. Prevention of entering of contaminants, post-process, was ensured by lamination and hot-gluing the edges, thus preventing further contamination from interfering with the ongoing measurement (Figure 8 and 9). These experiments were performed under constant temperature, 25 °C and pressure, 1001.7 mBar, though they varied insignificantly when humidity in the chamber changed. The contamination of CNB® samples, that may have happened during the processing of the samples, at this stage of research, has no significance because to our current understanding it should only affect initial values of the samples, and not contribute to progressive change. This does not mean that some significant irregularities are in themselves insignificant, but we report this work only as the first stage of the applied research, and such factors are the next things to investigate when this part of the proof of principle research is done. Adsorption and absorption parameters of the coating were also left out of scope of this applied stage research.

Next we seized some opportunity to test our creation *in vivo* at the Teknologia 2015 exhibition in early October in Helsinki, which was a 3-day event where thousands of people handled this sensor as a capacitive switch for a voltage control of air cooling fans and LED lighting (Figure 10) by squeezing their fingers with different firmness around the sensor element. A month later we had the same setup driving just the



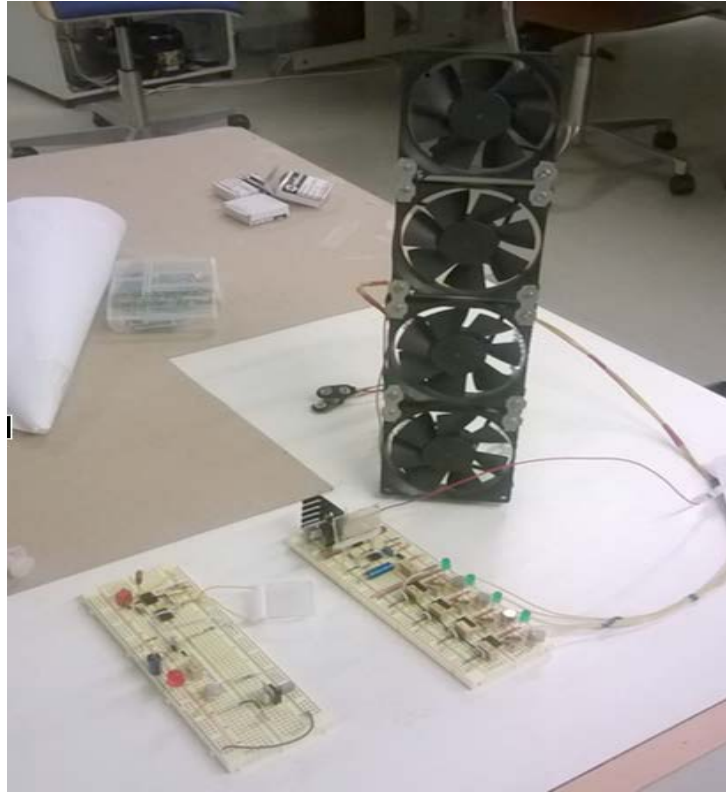
LEDs for a week in Shanghai NDIW15 (Nordic Design and Innovation Week) which was in the first week of November 2015, Figure 11.



Figure 8: Setup inside the CTS; sensor tag is placed next to the sample, with clamps that are sealed in low-density polyethylene (LDPE) to prevent interference from them



Figure 9: Data comparison of sensor tag, which is used as reference, and thermal couple imbedded in CTS



*Figure 10: Setup in Teknologia 2015 exhibition with indicators of fans and LEDs*



*Figure 11: Design and test in NDIW15, the harder you squeeze the more LEDs light up*

### 3. Results

#### 3.1 In vitro

Fabricated samples seem to possess similar initial capacitance characteristics within  $\pm 0.5$  pF range. The sensitivity of four different samples during measurements varied from  $\pm 0.09$  pF to  $\pm 0.10$  pF. Measurements yielded a positive result that was indicated by increased capacitance on the RCL meter, this change was recorded on camera in both sensors, commercial and fabricated alike.

First measurements that included ejecting liquid, here distilled water, from a syringe on top of the sensor (Figure 13) yielded interesting results. Namely, capacitance continued increasing as more liquid was added onto the sensor element until the whole area was covered. This revealed that the sensor can be used for different purposes, such wetted area measurement, though a further test would need to be devised based on these results.

When measurements were taken again a week later, it became apparent that something has happened to the CNB<sup>®</sup> structure over time. This was indicated by increased initial capacitance from 1.09 pF (at 44.9 % RH, ambient) to 1.40 pF (at 55.5 % RH, ambient). In spite of this unexpected change/contamination, the initially measured sensitivity did not significantly change.

Later tests in the CTS chamber confirmed the experimentation (Figures 12a and b), and sensors were able to measure humidity verifiably in range of 10–100 % RH at the defined temperature (Figure 9) and ambient pressure.

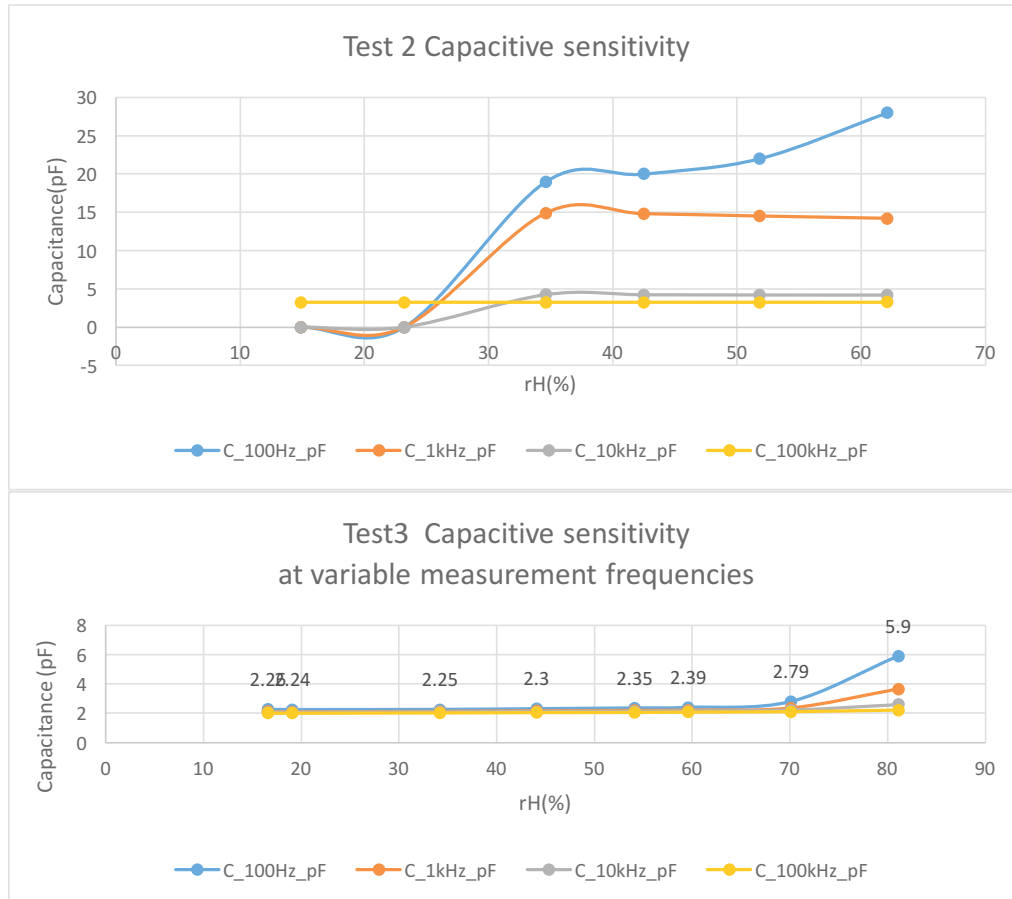


Figure 12a: Measurement from first CTS chamber testing



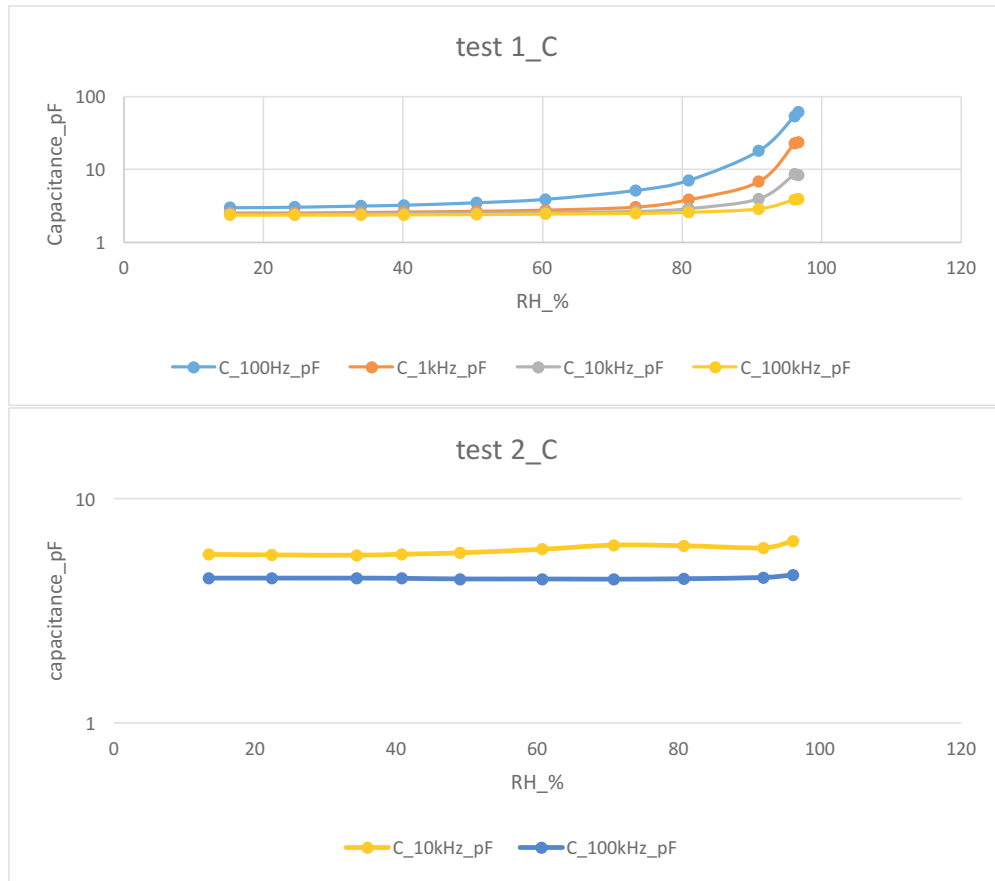


Figure 12b: Both sensors show the same trend in the second experiment in CTS chamber

When investigating for the effect of temperature drift, during the second measurement, the sensor initial values showed themselves to be surprisingly stable in the temperature range of 5–40 °C. For this experiment, humidity was set at 70 % RH to speed up the change in temperature inside the CTS chamber.

### 3.2 In vivo

During these experiments, durability of the packaging was the important factor. It was tested by letting the public twist, turn and squeeze the sensor constantly, only a few of the sensors stopped working due to mechanical failure when stressed excessively.

#### 4. Discussion

It was discovered (Figure 13) that in higher ambient humidity the sensor had developed extra capacitance. This change in initial values can also be contributed to the change in ambient relative humidity in the test environment, this was confirmed under controlled environment.



Figure 13: Measuring liquid surface dispersion measurability, using distilled water

During measurements with an aqueous liquid substance, it was noticed that when adding the liquid substance drop by drop ( $< 1$  ml/drop), the more liquid was added onto the sensor the bigger was the resulting capacitance of the measured sensor sample. It was concluded that the capacitance was modified by the liquid gradually covering the whole sensing area, suggesting that capacitive field is relatively large in the current construct. This effect was exploited in *in vivo* experiments as a pressure sensitive touch sensor application. Also it was reported that when humidity (in Shanghai) got too high (Figure 14), the experimental setup needed manual calibration so it would not consume power due to environmental factors triggering the hardware-logic.

#### Daily Weather History & Observations

2015	Lämpötila [°C]			Kastepiste [°C]			Ilmankosteus [%]			Sea Level Press. (hPa)			Näkyvyys (km)			Wind (km/h)			Precip. (mm)	Tapahtumat
merries	high	avg	low	high	avg	low	high	avg	low	high	avg	low	high	avg	low	high	avg	high	sum	
1	15	13	12	13	11	10	100	88	77	1028	1026	1024	10	7	4	21	10	-	0.00	Sadetta
2	18	14	10	10	7	3	94	65	37	1027	1026	1025	8	5	3	18	10	-	0.00	
3	20	14	9	12	10	7	93	71	46	1028	1027	1025	10	5	3	18	5	35	0.00	
4	20	18	15	18	15	11	94	83	68	1026	1024	1022	10	6	2	21	10	-	0.00	Sadetta
5	25	21	18	19	18	17	100	87	69	1023	1020	1019	10	6	1	14	6	-	0.00	Sadetta
6	26	23	20	21	20	19	94	87	69	1020	1018	1016	10	9	5	26	16	-	0.00	Sadetta
7	27	21	15	23	19	13	94	90	74	1019	1016	1014	10	6	3	26	14	-	0.00	Sadetta, Ukkosta

Source: The Weather Company, LLC

Figure 14: RH in Shanghai averaged 81.5% in the first week of November, where 'Lämpötila' means temperature, 'kastepiste' means dew point, 'ilmankosteus' means humidity, 'näkyvyys' means visibility, 'tapahtumat' means events, 'sadetta' means rain, and 'ukkosta' means thunder

Sensors were able to show measurable changes on both sides, front and back, according to working principles of a capacitor. It was also noticed that applying a different coating on each side produced varying sensitivity, also adding different materials on top of the coating attenuates the measuring magnetic field, reducing sensitivity considerably.

In *in vivo* experiments we found out that our weakest link in the design was the hot-glue that was meant as a suspender of the metallic connector legs. Hot glue is flexible and the connector was noticed to be too rigid for the purpose, this compromised adhesion between the two materials over time.

#### 4. Conclusions and future work

In this investigation the research hypothesis was answered, i.e. CNB<sup>®</sup> deposited on a PET substrate can produce a capacitive humidity sensor. Further testing of this sensor needs to be done in an automated manner, in order to approach industrial scale production and applications. For this purpose we have reduced the sensor electronics to an analogue low-pass filter to reduce the complexity needed. The future measurement setup will be: one sensor, one resistor and any conveniently available microcontroller with analogue input. For multiple simultaneous measurements a measuring matrix or multiplexing solution needs to be developed along with logging to a server.

The automated setup is going to be designed initially for monitoring the relative humidity conditions in a traditional printing lab, and monitor/visualize the effects of furniture and human interaction inside the lab.

#### Acknowledgments

Here we should like to thank people who helped to make all these events happen. A very special thank you to Ruslan Lagashkin, who built our first measuring circuit, which survived all that manhandling and logistics; Toni Spännäri, Jarmo Tuppurainen from Metropolia and Dr. Su Yunsheng from Tongji University for letting us use their facilities and equipment; Matti Hämäläinen from Digile Oy for providing the opportunity to test in Shanghai; Severi Tikkala and Eljas Linna from eloSpaces Oy, who helped the author survive when otherwise alone in China.

Obviously, the rest of the staff and students in Metropolia are also to receive the big thank you for helping us during these challenging times, especially:

- Kari Komulainen
- Sari Rintala
- Aino Hietala
- Jaana Kujala
- Viivi Leskinen
- Henrik Viluksela
- Matias Lackschewitz
- Mai Nguyen
- Khoi Luong Nguyen

#### References

- Adjizan, J., Leighrib, R., Koos, A.A., Suarez-Martinez, I, Crossley, A., Wagner, P., Grobert, N., Llobet, E. and Ewels, C.P., 2014. Boron- and nitrogen-doped multi-wall carbon nanotubes for gas detection. *Carbon*, 66, pp. 662–673.
- Hackler, D., Sime, D. and Wald, S., 2015. Enabling Electronics with Physically Flexible ICs and Hybrid Manufacturing. In: *Proceedings of the IEEE. Vol. 103, No. 4, April 2015*.
- Iijima, S., 1991. Helical microtubules of graphitic carbon. *Nature*, 354, pp.56–58.
- Islam, T., Mahboob, R. and Khan, S., A., 2015. Simple MOX Vapor Sensor on Polyimide Substrate for Measuring Humidity in ppm Level. *IEEE Sensors Journal*, 15(5), pp. 3004–3013.

Kouda, S., Dibi, Z. and Meddour, F., 2008. Modeling of a smart humidity sensor. *International Conference on Microelectronics*.

Planet Analog. ©2013. *UBM Tech: Planet Analog*. [online] Available at:

<[http://www.planetanalog.com/document.asp?doc\\_id=527490](http://www.planetanalog.com/document.asp?doc_id=527490)> [accessed 29 February 2016].

Reuss, R., Raupp, G. and Gnade B., eds., 2015. In: *Proceedings of the IEEE: Special Issue on Advanced Flexible Electronics for Sensing Applications, 103(4), April 2015*.

Ricciardella, F., Alfano, B., Loffredo, F., Villani, F., Polichetti, T., Miglietta, M., Massera, E. and Di Francia, G., 2015. Inkjet printed graphene-based chemiresistors for gas detection in environmental conditions. In: *2015 XVIII AISEM Annual Conference*, 4p.

Rigoni, F., Drera, G., Pagliara, S., Goldoni, A. and Sangaletti, L., 2014. High sensitivity, moisture selective, ammonia gas sensors based on single-walled carbon nanotubes functionalized with indium tin oxide nanoparticles. *Carbon*, 80, pp. 356–363.

Rivadeneyra, A., Salmerón, J.F., Palma, A.J., López-Villanueva, J.A., Agudo-Acemel, M. and Capitan-Vallvey, L.F., 2015. Comparative study of printed capacitive sensors. In: *10th Spanish Conference on Electron Devices (CDE)*.

Shanghai, 2016. *Tekijänoikeus, The Weather Company, LLC*. [online] Available at:

<[https://www.wunderground.com/history/airport/ZSSS/2015/11/1/WeeklyHistory.html?req\\_city=Shanghai&req\\_state=SH&req\\_statename=China&reqdb.zip=00000&reqdb.magic=1&reqdb.wmo=58362](https://www.wunderground.com/history/airport/ZSSS/2015/11/1/WeeklyHistory.html?req_city=Shanghai&req_state=SH&req_statename=China&reqdb.zip=00000&reqdb.magic=1&reqdb.wmo=58362)> [accessed 15 June 2016].

## Spot Application of a Transparent Nanoclay Layer to Provide Post-print Laser Marking Functionality on High Brightness 100 % Calcium Carbonate Coatings

Roger Bollström<sup>1</sup>, Patrick Gane<sup>1,2</sup>

<sup>1</sup> Omya International AG, Baslerstrasse 42, CH-4665 Oftringen, Switzerland

<sup>2</sup> Aalto University, School of Chemical Technology, Forest Products Technology, FI-00076 Aalto, Helsinki, Finland

E-mail: roger.bollstrom@omya.com; patrick.gane@omya.com

### Short Abstract

Laser marking is a widely used technique to form individualised identification, such as product numbering or 2D coding. The technique is based on ink removal via laser ablation, which requires local heating with a laser beam, i.e. the coating layer must absorb at the particular wavelength of the laser to provide the heat to vaporise the ink layer. Calcium carbonate shows a very low absorption at the wavelength peaks of the typical CO<sub>2</sub> lasers used, which has led to the need to incorporate a threshold amount of other minerals, however generally at the cost of losing natural brightness. Post application of an ultrathin nanoclay or nanosilica layer onto a high brightness calcium carbonate coating is shown to support laser ablation of offset ink with all the standard laser wavelengths, without compromising the optical appearance.

**Keywords:** laser marking, irradiation of coatings, light absorption, ink ablation, digital printing

### 1. Introduction and background

Product numbering or 2D coding can today be found on almost every package, to enable tracing or ease product handling, and in some cases, such as for medicine packaging, it may even be mandatory. A commonly used technique for applying the coding, as an alternative to printing, is laser marking. The technique is based on ink removal via laser ablation, i.e. local heating of the coating structure to such an extent that the overlaying ink is removed via vaporisation and/or discoloured by heat-induced oxidation. To enable local heating with a laser beam, the coating layer must absorb at the particular wavelength of the laser.

As a direct background work for this study we refer to an earlier publication (Gane et al., 2005), where a set of variously coated papers were tested for their ability to be patterned with exposure to laser irradiation. In that study a clear correlation between a high infrared absorbance and the laser marking threshold could be seen. Similar results were also recently reported by Hiorns et al. (2012), a study carried out on double coated board. The characteristic infra-red wavelengths of the typically used CO<sub>2</sub> lasing are 10.6 µm, 9.6 µm and 9.3 µm (Witteaman, 1987) (Figure 1A). Calcium carbonate shows a very low absorption until a peak at ca.11.4 µm, lying outside the intense laser peak region, which has led to the need to incorporate a threshold amount of other mineral pigment(s), such as kaolin, talc or silica to increase the absorbance at the lower wavelengths. It could be shown that with a higher absorbance, to mark satisfactorily required a significantly lower laser intensity per unit area, as shown in Figure 1B vs. Figure 1C, the pattern achieved with the same laser intensity was clearly better on the substrate with the increased absorbance. Kaolin could be shown to be the most efficient infrared absorbing mineral and the kaolin based coatings resulted in the best laser patternability. However, the drawback with kaolin, as a less bright mineral, compared to calcium carbonate is the resulting in a less white and thereby poorer visual appearance.

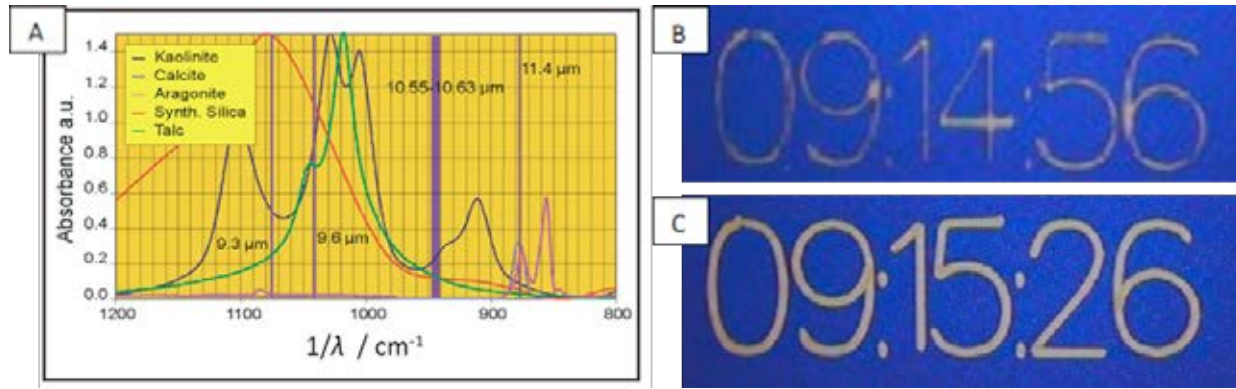


Figure 1: Absorbance spectra for different minerals versus standard laser wavelengths (A); Calcium carbonate, in both the calcite form as well as in the aragonite form show an extremely low absorbance in the wave numbers higher than 900 (wavelengths below 11  $\mu\text{m}$ ), this is indicated with the comparison in laser marking efficiency, with a laser having the wavelength of 10.6  $\mu\text{m}$ , tested on pure calcium carbonate (B) versus a blend with 80 pph calcium carbonate and 20 pph kaolin (C) – graphic taken from Gane et al. (2005).

In this study we introduce a novel concept for increasing the absorbance in the desired infrared region. Post application of an ultrathin nanoclay or nanosilica layer onto a high brightness pure calcium carbonate coating acts to support laser ablation without compromising the optical appearance. The layer thinness ensures a minimal path length for the light passing through the otherwise lower brightness material, with the nanoscale of the particles ensuring virtual transparency.

## 2. Materials and Methods

### 2.1 Pigment coated substrates

Sheets of impermeable SuperYUPO® (Yupo Corporation) carbonate pigment filled polypropylene film, formerly known as Synteape®, of 80  $\mu\text{m}$  thickness and 62  $\text{gm}^{-2}$  basis weight, were used as a base substrate for the coatings to ensure that no basesheet interference was occurring. The mineral pigments used for the coatings were ground calcium carbonate (GCC), Hydrocarb 90 ME (Omya International AG), and glossing kaolin, Hydragloss 90 EM (KaMin Performance Minerals LLC). As the binder in all the coatings, 10 pph, based on 100 parts by weight of pigment, of a styrene acrylic latex, Acronal S 728 (BASF Germany), was used. Each of the coating colours were coated to three different thicknesses with a K202 Control Coater (RK PrintCoat Instruments Ltd.) and dried under hot air, resulting in dry coating weights of 10, 45 and 90  $\text{gm}^{-2}$ . The respective coating formulations used are shown in Table 1.

Table 1: Substrate coating formulations.

GCC (pph)	Kaolin (pph)	Latex (pph)	Solids content (w/w %)	GCC (pph)
100	–	10	70	100
95	5	10	70	95
90	10	10	70	90
85	15	10	70	85
80	20	10	70	80
–	100	10	69	–

## 2.2 Nano-mineral dispersions

Two dispersions, one based on nanoclay and one based on nanosilica were prepared to be applied by spray coating. To ensure adequate wetting of the surface, the surface tension of the water based suspension was decreased by addition of ethanol. The nanoclay dispersion, based on bentonite, Optigel-CK (formerly Rockwood Additives GmbH (currently BYK-Chemie GmbH)), was prepared to a solids content of 2.1 w/w % in a 9 : 1 water : ethanol solution. The nanosilica dispersion, based on Sipernat® 350 silica (Evonik Industries), was prepared to a solids content of 2.5 w/w % also in a 9 : 1 ratio water : ethanol solution. As binder in both dispersions, 5 w/w % PVOH (BF05, Omya International AG), defined as weight per weight of the mineral, was used. To avoid agglomeration, potentially leading to nozzle clogging, the dispersions were stirred under sonication in a water bath.

## 2.3 Spray coating

Application of the nano-mineral dispersions, intended for creation of a thin infrared light absorbing layer, were applied with a handheld air brush (Sparmax SP-575), keeping ~25 cm distance from the substrate. The applied amount was approximately  $50 \text{ cm}^3\text{m}^{-2}$ , resulting when dried in a gravimetrically virtually immeasurably thin layer (calculated weight, based on a density of  $2.35 \text{ gcm}^{-3} : 0.25 \text{ gm}^{-2}$ ).

## 2.4 Absorbance spectra

The absorbance spectra of the samples were recorded with a Spectrum One™ FTIR spectrometer (PerkinElmer, Inc., USA). The attenuated total reflection (ATR) crystal was a 3-reflection diamond/zinc selenide crystal, and the scan speed  $0.2 \text{ cms}^{-1}$ .

## 2.5 Gloss and brightness

Brightness (R457) was measured with an Elrepho instrument according to the DIN 53145-1 standard, and the gloss (Tappi 75 °) with a Zehntner instrument according to the Tappi 75 EN ISO 8254-1 standard.

## 3. Results and Discussion

The absorbance for the coating structures was measured over the wavenumber range  $800$  to  $1\,200 \text{ cm}^{-1}$  ( $\lambda^{-1}$ ) (Figure 2). The standard lasers used are normally described in application based on their peak wavelength ( $\lambda$ ), i.e. a standard  $\text{CO}_2$  laser, for example, has major peaks at  $9.3 \text{ }\mu\text{m}$  and  $10.6 \text{ }\mu\text{m}$ , with a neighbouring peak at  $9.6 \text{ }\mu\text{m}$ , however other wavelengths may also be achieved with special optics by longitudinal lasing.

A normalisation of the absorbance, setting the maximum peak to 1.5, was made for all the infrared (IR) spectra. Calcium carbonate shows a negligible absorbance at wavenumbers greater than its peak value at  $872 \text{ cm}^{-1}$  ( $11.4 \text{ }\mu\text{m}$ ). For kaolin the main absorbance peaks are at  $1\,025 \text{ cm}^{-1}$  and  $1\,003 \text{ cm}^{-1}$ , where at the latter the pure kaolin coating shows its highest absorbance. Comparing the coatings, calcium carbonate blended with kaolin shows a systematic decrease at the kaolin specific wavenumber as the ratio of carbonate to clay increases. Similarly systematic is the decline in the absorbance at  $943 \text{ cm}^{-1}$ , as shown in Table 2.

The difference in absorbance as a function of coating colour thickness was also studied. In addition to the normal coating weight of  $10 \text{ gm}^{-2}$ , amounts as high as  $45 \text{ gm}^{-2}$  and even  $90 \text{ gm}^{-2}$ . As shown in Table 2, the increased coating weight, and thereby layer thickness, had no influence on the absorbance, which may be explained by the Beer-Lambert law as the thickness of these coating layers are far thicker ( $10\text{--}100 \text{ }\mu\text{m}$ ) than the penetration depth of the infrared radiation ( $0.5\text{--}1 \text{ }\mu\text{m}$ ).

Table 2: Absorbance at  $943\text{ cm}^{-1}$  for the coating colour formulations at different coating weights.

Coating colour formulation		Absorbance (scaled to max. 1.5) at $943\text{ cm}^{-1}$ ( $10.6\text{ }\mu\text{m}$ )		
GCC/pph	kaolin/pph	$10\text{ gm}^{-2}$	$45\text{ gm}^{-2}$	$90\text{ gm}^{-2}$
100	–	0.03	0.03	0.03
95	5	0.04	0.05	0.04
90	10	0.10	0.10	0.10
85	15	0.20	0.21	0.20
80	20	0.27	0.27	0.29
–	100	0.70	0.69	0.64

Post application of nanoclay or nanosilica via spray coating, to form an ultrathin layer on top of the pure calcium carbonate coating, increased the absorbance over the whole measured absorbance range, Figure 2. Both nanoclay and nanosilica showed broad absorbance peaks. Nanoclay resulted in a peak value at  $1\,006\text{ cm}^{-1}$ , the same wavenumber as one of the main peaks for the standard kaolin. With such a broad distribution then all the standard laser wavelengths are effectively covered. The peak value for the nanosilica is at  $1\,084\text{ cm}^{-1}$ , being almost optimal for the laser wavelength of  $9.3\text{ }\mu\text{m}$  and with good absorbance also for the  $9.6\text{ }\mu\text{m}$  laser. However, the absorbance decreases to a relatively low value at  $943\text{ cm}^{-1}$ , i.e. for a laser at  $10.6\text{ }\mu\text{m}$ . Based on the overall absorbance over the whole infrared range, one might therefore conclude that bentonite nanoclay provides the most universal layer, enabling use of all standard laser wavelengths.

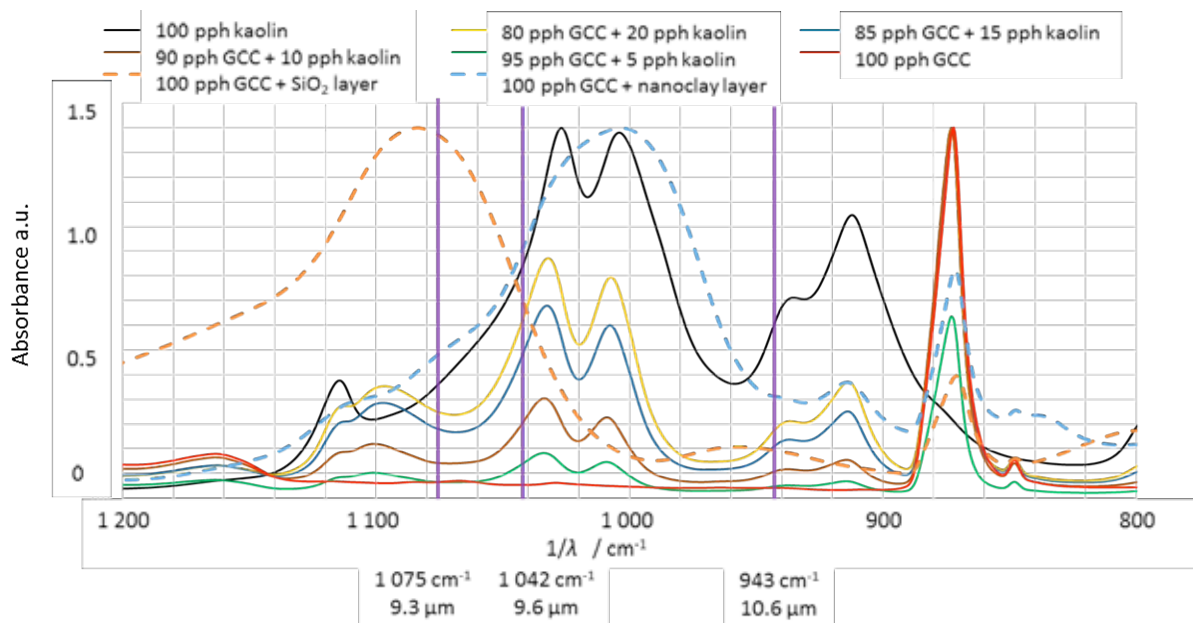


Figure 2: Absorption spectra for the substrates (coat weight  $10\text{ gm}^{-2}$ ); indicated with purple lines are the typical wavelength peaks for available  $\text{CO}_2$  lasers; the higher the absorbance at these particular wavelengths, the likelier is a successful laser patterning, according to Gane et al. (2005).

The limitation in respect to laser post print marking due to the mismatch in IR absorption with the commonly used laser wavelengths, led to the inability to use 100 % calcium carbonate coatings to achieve the brightness levels required without optical brightening aid (OBA), due to the ever-present required kaolin in the coating blend. This has more recently become a critical problem, since OBA is no longer desirable from a regulatory perspective in packaging, especially when considering food contact. Thereby, the demand for achieving higher brightness coatings “naturally” at ever lower cost is rapidly growing. The brightness of calcium carbonate is higher compared with kaolin, as is shown in Figure 3 for the test coatings, where the



pure calcium carbonate and the pure kaolin display the high and low extremities in brightness, 91.0 % and 81.8 %, respectively. As seen also in Figure 3, blending in kaolin in the calcium carbonate coating system-atically decreases the brightness as a function of the added amount.

In contrast to the pure carbonate and kaolin, and the blends between them, post application of the nano-mineral solutions by spray coating showed, interestingly, a slight increase in the brightness. Without conducting further detailed surface analyses this is most probably explained by the creation of an additional interface modifying the light scattering by multiple reflectance, i.e. a combination of diffuse and multiple reflectance across a boundary of slightly contrasting refractive index: calcium carbonate average index being  $\sim 1.66$  and that of bentonite being  $\sim 1.5$ . The same additional interface, however, results in a decreased gloss. From the literature we know that thin layers of bentonite and montmorillonite are essentially transparent (Ebina and Mizukami, 2007), being promoted for example as transparent barrier films. The observed brightness increase in our study may thereby be considered as a confirmation for the transparency, as the high brightness of the coating layer beneath it is transmitted through.

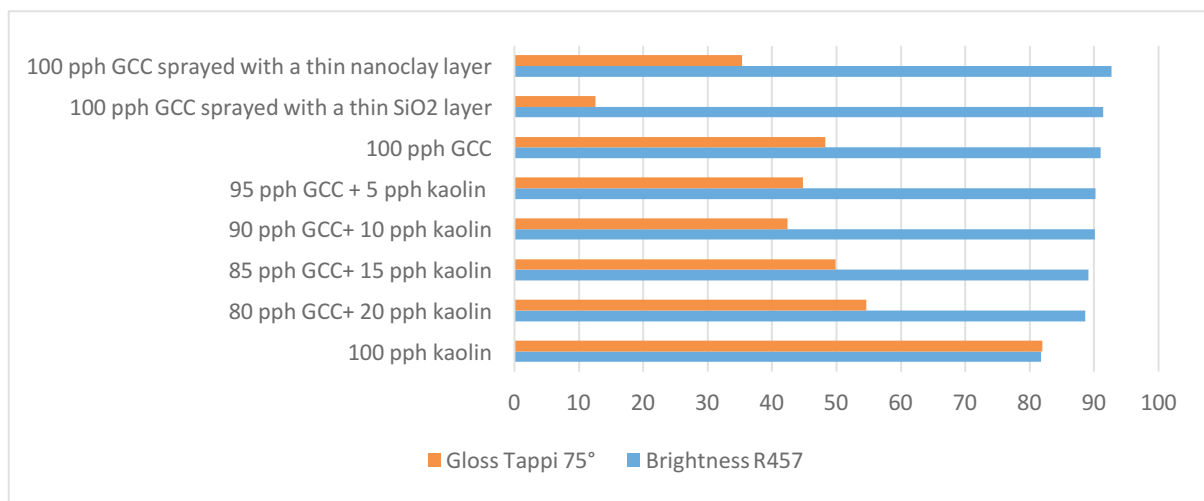


Figure 3: Gloss (Tappi 75°) and brightness (R457) for the different coated substrates.

Given the absorbance level match between pure kaolin and the calcium carbonate with the superposed nanoclay layer, we can conclude that the concept fits the criteria for excellent post-print laser marking. The advantages of applying the thin nanoclay coating are that in principle it could be applied only where the laser marking is actually required, making this a very low volume specific, speciality application, and thus in principle a low cost technical solution to achieving high natural brightness on 100 % calcium carbonate coated packaging paper board.

Further work will study the practicality of developing a spot specific application device for use either in converting or during printing. Additionally, post application to the already printed area will be researched, taking into consideration the surface energy requirement for satisfactory transfer.

#### 4. Conclusions

In this study we analysed and compared the absorbance in the infrared (IR) wavelength range for a set of coating structures; pure kaolin, various mixture ratios of kaolin with calcium carbonate and pure calcium carbonate. In correlation with what is already known from the literature, kaolin showed a clearly broader absorbance spectrum compared with calcium carbonate over the whole infrared region. As a novel concept, we introduce a post application via spray coating of a dispersion of nano-sized minerals, namely silica

and bentonite, with the target to achieve high enough absorbance to enable laser patterning. Both minerals show broad absorbance spectra, silica with its peak in the longer infrared wavelength area and bentonite/montmorillonite nanoclay in the mid-range. Post application of nanoclay or nanosilica on the pure calcium carbonate coating resulted in the required functional absorbance for all the standard CO<sub>2</sub> laser wavelengths. The measured absorbance of the calcium carbonate coated substrates with post added nanoclay or silica, were approximately the same as for the substrate coated with pure kaolin, however, the nanoclay layer applied on the 100 % calcium carbonate coating resulted in a significantly higher brightness.

The solution proposed of applying a thin layer of nanoclay to achieve post print laser markability, therefore, not only meets the IR absorbance requirements for good laser marking, but enables the paper board maker to achieve a new high level of brightness in those packaging fields where post print laser marking is required whilst remaining within the regulatory limitation pertaining to the use of optical brighteners.

### Acknowledgements

Jörg Nikas, Omya International AG, R&D Analytical Laboratory, Switzerland, is acknowledged for conducting the infrared absorbance measurements.

### References

- Ebina, T. and Mizukami, F., 2007. Flexible Transparent Clay Films with Heat-Resistant and High Gas Barrier Properties. *Advanced Materials*, 19, pp. 2450–2453.
- Gane, P.A.C., Buri, M., Spielmann, D.C., Neuenschwander B., Scheidiger H. and Bättig D., 2005. Mechanism of Post-Print Laser Marking on Coated Substrates: Factors Controlling Ink Ablation in the Application of High Brightness Calcium Carbonate. *Journal of Graphic Technology*, 1.
- Hiorns, A., Preston, J., Morgan, J. and Metters L., 2012. Laser marking of double coated board. *12<sup>th</sup> TAPPI Advanced Coating Fundamentals Symposium*, 10–12 September 2012, Atlanta, GA USA, .
- Wittman, W.J., 1987. *CO<sub>2</sub> Lasers*. Berlin Heidelberg: Springer Verlag, pp. 112–114.

## Reaction Platforms for Enzymatic Testing

*Eveliina Jutila<sup>1</sup>, Risto Koivunen<sup>1</sup>, Roger Bollström<sup>2</sup>, Tiina Sikanen<sup>3</sup> and Patrick Gane<sup>1,2</sup>*

<sup>1</sup> Aalto University, School of Chemical Technology, Department of Forest Products Technology, FI-00076 Aalto, Helsinki, Finland

<sup>2</sup> Omya International AG, Baslerstrasse 42, CH-4665 Oftringen, Switzerland

<sup>3</sup> Division of Pharmaceutical Chemistry and Technology, Faculty of Pharmacy, University of Helsinki, FI-00014 Helsinki, Finland

E-mail: [eveliina.jutila@aalto.fi](mailto:eveliina.jutila@aalto.fi); [risto.koivunen@aalto.fi](mailto:risto.koivunen@aalto.fi); [roger.bollstroem@omya.com](mailto:roger.bollstroem@omya.com); [tiina.sikanen@helsinki.fi](mailto:tiina.sikanen@helsinki.fi); [patrick.gane@omya.com](mailto:patrick.gane@omya.com)

### Short Abstract

The development of highly porous coating structures for reaction platforms, especially for enzymatic testing, is the focus of work presented here. Four types of coatings are formulated combining a highly porous form of pharmaceutical grade functionalised calcium carbonate (FCC) with two types of micro-fibrillated cellulose as binder (MFC A and MFC B), in which the fines content of MFC A and MFC B differ, MFC A having less freely dispersed film forming fines than MFC B. Additionally, two binder levels are adopted, namely 5 pph and 10 pph based on 100 pph by weight of FCC. Rod coating is used to meter the formulations onto an impermeable pigment filled polypropylene film. The coated substrate is then used as a base for hydrophobic patterning formed by printing each of two hydrophobic inks formulated based on polystyrene (PS) or alkyl ketene dimer (AKD), respectively. The study includes characterisation of the coating formulations, platform performance testing and design development at the stage prior to final application testing. The results show that the choice of binder as well as the binder amount has a significant effect on the porosity of the coatings, thus affecting the volume uptake and wetting capabilities of a test liquid in respect to a printed hydrophobic circular ring pattern. MFC A was seen to block/fill the inter-particle pores less than MFC B, though the volume uptake and evaporation times were greater for MFC B containing coatings, due to a slightly greater thickness of the coatings and the dependence of evaporation on diffusion and surface film flow rather than bulk flow. The results show inkjet-printing provides a convenient way to create patterns that can be easily adapted to suit the desired purposes depending on the functional properties of the coating. In future work, the suitability of the platforms will be tested using a model enzymatic reaction and ultimately developing a self-standing platform for enzymatic testing of pharmaceutical compounds.

**Keywords:** microfluidics, wicking, patterned coated paper, hydrophobic barriers, reaction platform

## 1. Introduction and background

Microfluidic paper-based analytical devices ( $\mu$ PADs) represent one of the most promising future applications in functional printing and a fast-growing new field in analytical chemistry. Patterned paper consisting of millimetre-sized hydrophobic channels offers a small, simple, low-cost, portable and self-standing platform for bioassays (Martinez et al., 2007), which already has been shown to be suitable for multiple applications, including blood type analysis (Khan et al., 2010), liver function assessment based on enzymatic markers (Vella et al., 2012) and detection of morphine (Teerinen et al., 2014).

Conventional analytical microfluidic devices consist of silicon glass or polymers such as polydimethylsiloxane (PDMS) (Iliescu et al., 2012). Both conventional and paper-based platforms enable the use of small volumes and diverse analyses, but compared with conventional microfluidic platforms, paper-based devices require no external pumps due to two main factors, the microcapillarity of the pore structure and the constant fluid evaporation for typical liquids, which function as a negative pressure pump, and provide for the use of simple detection methods, such as colorimetry (Yamada et al., 2015). Paper, as a material also offers many other advantages for microfluidics offering high surface-to-volume ratio enabling a greater capacity for bound analytes (for reaction and detection), and the ability to keep reagents active within the fluidised fibre network, and the white background is particularly suitable for colorimetric detection (Cate et al., 2015; Martinez, 2011). The majority of the researchers utilise cellulose-based chromatographic and filter papers, in which the sample wicks along cellulose fibres (Khan et al., 2010; Martinez et al., 2007, 2010).

Despite the attractiveness of paper it has some distinct disadvantages as a platform for analytical devices due to its fibrous and heterogeneous consistency, as well as the coarse scale of its pore structure. Depending on the method of detection, (i) the organic nature of the fibres and the generally high light absorbance may not be well suited optical measurements (Ellerbee et al., 2009), (ii) the wicking rate of paper is seldom completely uniform, depending on the channel dimensions and test conditions (Martinez, 2011), and as a consequence of the two abovementioned factors (iii) current paperfluidic devices have limitations in positional accuracy and analytical sensitivity (Liana et al., 2012). These disadvantages can be largely overcome by utilising highly porous coatings, which provide a more homogeneous surface, a finer and designable pore network structure, a primarily inorganic largely inert substrate. Further control can be provided by the choice and amount of binder (Jutila et al., 2015). It is possible to fabricate narrower, spatially better resolved channels, and so enable smaller volumes of sample to be applied, as well as provide better colour contrast during optical sensing, having a more pure white background.

Paper can be patterned in several ways utilising hydrophobic material including photolithography (Martinez et al., 2007), wax printing (Carrilho et al., 2009), flexographic printing (Olkkonen et al., 2010), inkjet printing (Koivunen et al., 2015), spraying (Nurak et al., 2013), stamping (de Taso Garcia et al., 2014) or alternatively by embossing or cutting (Thuvo et al., 2014). Printing-based fabrication methods are the most utilised methods nowadays, because they are simple, cost-effective, reproducible, and can be adapted for mass production. Furthermore, inkjet printing provides an efficient fabrication tool, because it can be used to both fabricate the hydrophobic barriers and to deposit reagents (Yamada et al., 2015). In this paper, we introduce a microfluidic reaction platform designed for enzymatic testing of pharmaceutical compounds, which has been fabricated utilising speciality coated substrates and inkjet printing.

## 2. Materials and Methods

The materials used in the coating formulations, the hydrophobic inks, pattern designing process and pigment coating characterisation methods are described in the following sections.

### 2.1 Coating Materials and Formulations

Table 1 shows the formulations and properties of the coatings which were used in the fabrication of a reaction platform for enzymatic testing of chemical actives. The chosen coating pigment is a highly porous form of pharmaceutical grade functionalised calcium carbonate (FCC) provided by Omya International AG, Oftringen, Switzerland.

Two types of micro-fibrillated cellulose (MFC A), a commercially available Arbocel MF-40-7 (J. Rettenmaier & Söhne GmbH + Co KG, Rosenberg, Germany), and a mechanically fibrillated carboxymethyl cellulose (CMC)

dispersed micro nanofibrillated cellulose (MFC B) (Omya International AG, Oftringen, Switzerland), were used as binders.

Sheets of impermeable SuperYUPO® (Yupo Corporation), known formerly as Synteape®, a pigment filled polypropylene film of 80 µm thickness and 62 gm<sup>-2</sup> basis weight, were used as a base substrate for the coatings.

Table 1: Coating colour formulations

Abbreviation	Pigment	Binder	Binder amount (pph)	Solids content (w/w %)
FCC + 5 pph MFC A	FCC	micro-fibrillated cellulose (commercial grade)	5	16.4
FCC + 10 pph MFC A	FCC	micro-fibrillated cellulose (commercial grade)	10	15.6
FCC + 5 pph MFC B	FCC	micro nanofibrillated cellulose (CMC dispersed)	5	7.8
FCC + 10 pph MFC B	FCC	micro nanofibrillated cellulose (CMC dispersed)	10	6.6

Coating colours were applied with a K202 Control Coater (RK PrintCoat Instruments Ltd.) employing two spirally wound rods, applying a 150 µm (MFC A containing coatings) and 400 µm (MFC B containing coatings) thick wet layer, respectively, with a speed setting of 6 m·min<sup>-1</sup> to achieve as thick coating layers as possible. The difference in wet layer thickness during application relates to the difference in solids content, with the aim in mind to achieve close to equivalent dry coating layer thickness in each case. The coatings were allowed to dry freely in the laboratory atmosphere. The dry thickness of the samples is presented in Table 1. Figure 1 displays scanning electron microscope (SEM) images of FCC in combination with 10 pph of both MFC binders, in which the greater film forming tendency of MFC B is clearly seen, indicating a greater degree of dispersed nanofibrillated fines.

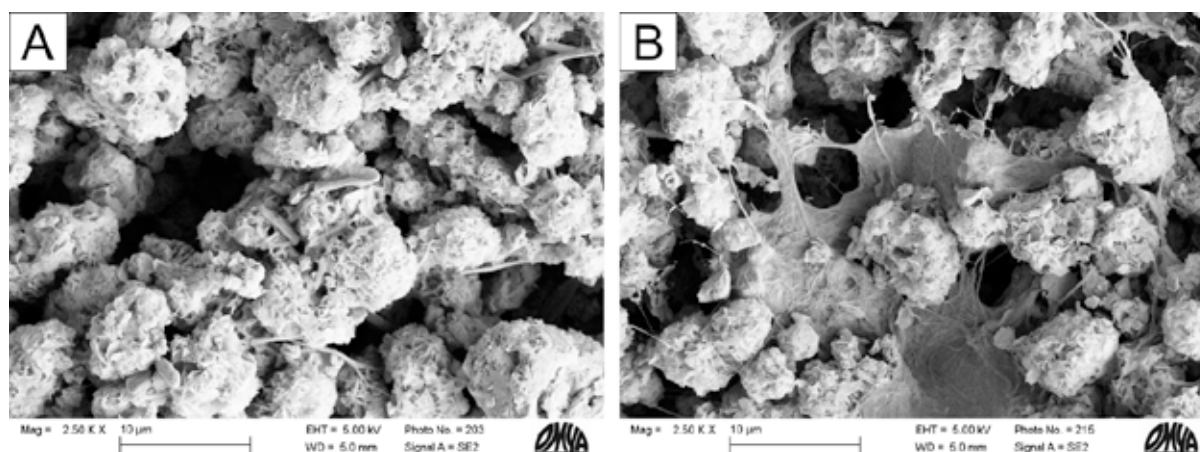


Figure 1: SEM images of a) FCC + 10 pph MFC A and b) FCC + 10 pph MFC B

## 2.2 Functional Inks and Printing

Two functional inks, PS ink and AKD ink, were prepared using two different hydrophobising agents, polystyrene, PS, (Sigma-Aldrich, St. Louis, USA, product code 331651) and alkyl ketene dimer, AKD, Basoplast 88 (BASF, Ludwigshafen, Germany), dissolved in p-xylene solvent (VWR, Vienna, Austria, product code 28984.292). The PS ink was coloured with Sudan Red G (Sigma-Aldrich, St. Louis, USA, prod-

uct code 17373), and the AKD ink was coloured with Blue 807 Dye (Kremer Pigmente GmbH, & Co. KG, Aichstetten, Germany, product number 94030) to enable clear visibility of the ink-applied areas. The inks were printed with a DMP-2831 research inkjet printer (Fujifilm Dimatix, Santa Clara, USA) employing DMC-11610 ink cartridges with ten picolitre nominal drop volume. The ink preparation process and printing details are described further in publications by Koivunen et al. (2015a; 2015b).

### 2.3 Pattern Design

Various pattern designs were printed and tested starting from printed circular rings with a width of 2 mm and a 5 mm inner diameter using both the PS and AKD inks, respectively. This ring cell pattern was then evolved into a design consisting of a possible reaction area with a ~5 mm diameter followed by a channel with a width of ~3 mm through which the end products of the reaction could be transported by the means of elution and liquid wicking. The actual dimensions of the patterns may vary slightly from the nominal dimensions due to the spreading of the hydrophobising agent and the colorant. Different concentration zones, adopting pattern features such as an arrowhead, circle and square shapes, were also printed at the end of the channel to investigate how end products could possibly be concentrated during localised evaporation for detection purposes. The additional patterning was also printed with both PS and AKD inks, respectively, and combination patterns were made. The full design is shown in the Results section in Figure 3.

### 2.4 Pigment Coating Characterisation Methods

The solids content of the coating slurries was determined with a Precisa HA 300 Moisture Balance (Precisa Gravimetrics AG, Dietikon, Switzerland). Coating weight was determined by measuring the weight of 5 × 5 cm pieces of the coated polypropylene film, using a Mettler AE260 analytical balance (Mettler-Toledo International Inc., Columbus, Ohio, the United States), and deducting the equivalent proportional basis weight of the film, measured from uncoated pieces of film. Five measurements were taken per coating. The total dry coating plus substrate thickness was measured with an SE250D micrometer (Lorentzen & Wettre, Kista, Sweden), having a 2 cm<sup>2</sup> measurement area spindle and measurement pressure of 100 kPa. The dry coating thickness was determined from the measured coated films by subtracting the nominal thickness, 80 µm, of the polypropylene film. Ten measurements were taken per coating.

Scanning electron micrographs (SEM) were obtained with a Sigma VP field emission scanning electron microscope (Carl Zeiss AG, Oberkochen, Germany). Coating pore volume was measured with an Autopore IV mercury intrusion porosimeter (Micromeritics, Norcross, USA) from coating samples dried in a petri dish (diameter 5.5 cm) in normal laboratory conditions.

### 2.5 Platform Performance Testing Methods

The maximum liquid volume uptake of each coating was determined by applying as high a volume of 100 mM Tris buffer solution (pH = 7.5) onto the ink-free interior of the AKD-printed rings (inner diameter ~5 mm) as could be delivered, using an adjustable volume pipette (Finnpipette, Thermo Fisher Scientific, USA), without leaving a film of water on the surface of the ring. Several such liquid loaded ring samples were tested to determine the specific volume uptake.

Evaporation (mass as a function of time) was studied to determine how long the interior of the AKD-printed rings stay wet. The measurement volumes applied ranged 1.0–1.8 µl corresponding to the previously measured volume uptake of the respective coating. The change in mass was recorded manually every 10 s with a Mettler Toledo MT5 microbalance in combination with Mettler Toledo Balance Link – DSC software. Three such evaporation rate measurements were made per coating. Standard paper testing conditions were not adhered to in this case, since the balance equipment used in the evaporation experiments

was situated in a laboratory with a temperature of 20 °C and relative humidity of approximately 28 %. As a reference, one experiment was also repeated using 1.0 µl buffer and a 20 × 20 mm glass substrate in the form of a microscope cover slip.

The additional pattern features were also tested by filling the AKD-printed channels, exemplified by an arrowhead, with 15 µl of the buffered water to see if the coating withstands large volumes of liquid, which could be used to elute the end products from the reaction area to the concentration zone. The introduction of an absorbent pad consisting of Whatman GF/F glass microfibre filter (GE Healthcare), aimed at keeping the reaction area wet for longer periods of time, was investigated. This was achieved by creating a pattern with an absorbent pad zone and testing the pad with and with pre-saturation and adding a few microlitres of water on top of the pad.

### 3. Results and Discussion

The findings from the experimental procedures are reported here, beginning with the characterisation of the coatings, followed by some examples of platform performance and discussion regarding the important features of the pattern design.

#### 3.1 Coating Properties

Table 2 presents the coat weight, thickness and specific pore volume distributions of the coatings. The value  $d^*$  represents the size at which the two pore size components of the discretely bimodal distribution are separated, i.e. the inter-particle and the intra-particle pore volumes, respectively, and  $d^{**}$  is the upper limit of the inter-particle pore volume region. The coating formulations were optimised in a way that a maximum solids content was achieved while still maintaining good “coatability”, meaning in effect that the solids content had to be lowered when more MFC was added, which is seen as a decrease in the coat weight values. Due to the different solids contents, two different rods were used in coating to achieve similar dry coating thicknesses between the coatings consisting of the two different MFC binders. The aim was to achieve as thick coating layers as possible with a single coating step to maximise the volume uptake within the hydrophobising patterns and thus to extend and elongate the wetting capabilities of the patterned coating.

*Table 2: Measured substrate properties for coatings including the total specific mercury intruded volumes into the samples over the diameter range 0.004–10 µm.*

Coating formulation	Coat weight (gm <sup>-2</sup> )	Thickness (dry) (µm)	Intra-particle volume: 0.004– $d^*$ (µm/cm <sup>3</sup> g <sup>-1</sup> )	Inter-particle volume: $d^*$ – $d^{**}$ (µm/cm <sup>3</sup> g <sup>-1</sup> )	$d^*$ (µm)	$d^{**}$ (µm)
FCC + 5 pph MFC A	37.1 ± 1.4	102 ± 7	0.98	1.17	0.64	3.50
FCC + 10 pph MFC A	33.8 ± 1.3	92 ± 3	0.95	1.10	0.64	3.50
FCC + 5 pph MFC B	43.3 ± 2.3	137 ± 11	0.92	1.26	0.51	3.50
FCC + 10 pph MFC B	33.6 ± 0.6	109 ± 6	0.86	1.05	0.51	2.80

As mentioned above, FCC compacts from the coating colours have a bimodal pore size distribution consisting of both intra-particle and inter-particle voids. The sample compacts were formed from equal volumes of coating samples dried in a petri dish. This is seen as two peaks in Figure 2, which shows the first derivative of the cumulative mercury porosimetry intrusion curves. The data are presented in terms of specific pore volume, i.e. the pore volume in a given size range per unit weight of the sample. The main peak in the pore size distribution between 1–3.1 µm represents the interparticle pore volume. The secondary peaks below 1 µm represents the intra-particle pore size distribution, i.e. the internal pore volume of the FCC

particles. The MFC binder amount was decreased from 10 pph to 5 pph, based on 100 parts by weight of pigment, to enhance the porosity of the coatings. The results show a clear increase in pore volume especially in the inter-particle region as the MFC portion is decreased. With smaller binder amounts, less fine pores are filled/blocked with MFC. More inter-particle pores are filled/blocked in the case of MFC B, as is also apparent when the SEM images of Figure 1 are examined. This effect reduces the permeability of the coating. The MFC B containing coatings are somewhat thicker than the MFC A coatings, a fact that also contributes, for example, to the volume uptake of the coating, as will be seen in the next section.

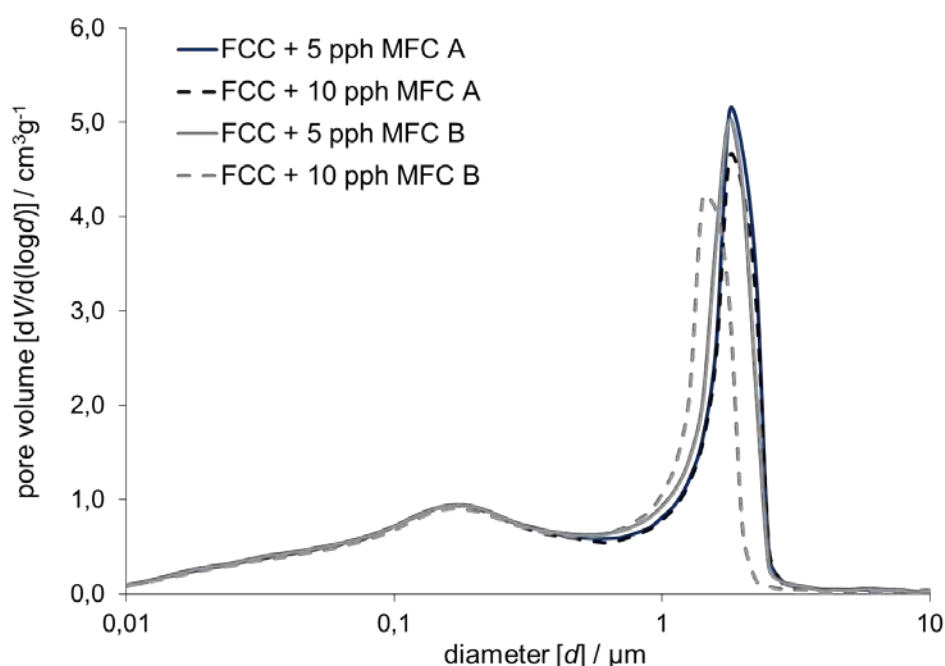


Figure 2: Pore size distribution of the coating formulations

### 3.2 Platform Performance

Table 3 presents the calculated volume uptake capacity, the measured volume uptake, the evaporation time and drying rate related to printed ring cell patterns with a nominal inner diameter of 5 mm. The actual diameter of the circles may vary due to spreading of the hydrophobising agent and its colorant. The intra-particle, inter-particle and total volume uptake were each calculated by multiplying the internal unprinted area of the circular ring cell, the coat weight of the given coating and the corresponding specific pore volume data from Table 2, and the values converted into microlitres. The measured volume uptake was experimentally determined by applying different volumes of water into the centre of the ring until a reflective liquid layer remaining on the surface was just apparent. The measured uptake volumes corresponding to each coating formulation were used in the evaporation rate experiments.

The calculated and measured volume uptake of the ring cells correlate quite well when 5 pph binder was used. The calculated values are slightly higher, because the actual diameter of the circles is probably slightly less than 5 mm due to the spreading of the hydrophobising agent. In the case of 10 pph MFC A, the calculated volume uptake is also somewhat higher than the experimental uptake, also for the abovementioned reasons. In the case of 10 pph MFC B, however, the measured volume uptake was greater than the calculated uptake, which is considered to be caused by the ability of the MFC in question to swell and absorb water. There might also be a small effect related to the difference in sample preparation for the porosimetry analysis, being a bulk dried sample, versus a thin coated layer, but such a systematic error would be expected to be seen for both MFC A and MFC B, which is not the case. Furthermore, the porosimetry data are truncated



at 10  $\mu\text{m}$  to remove any macroscopic effects, such as sample cracks, arising from the bulk drying sample preparation method.

*Table 3: Calculated and measured volume intake, evaporation time and drying rate of ring cell patterns with a nominal diameter of 5 mm.*

Coating formulation	Calculated intra particle volume uptake ( $\mu\text{l}$ )	Calculated inter particle volume uptake ( $\mu\text{l}$ )	Calculated total volume uptake ( $\mu\text{l}$ )	Measured volume uptake ( $\mu\text{l}$ )	Total sample evaporation time ( $\text{s}^*$ )	Drying rate ( $\text{s}\cdot\mu\text{l}^{-1*}$ )
FCC + 5 pph MFC A	0.71	0.85	1.56	1.50	$913 \pm 49$	$337 \pm 13$
FCC + 10 pph MFC A	0.63	0.73	1.36	1.00	$830 \pm 17$	$404 \pm 22$
FCC + 5 pph MFC B	0.78	1.07	1.85	1.80	$1\,060 \pm 87$	$345 \pm 16$
FCC + 10 pph MFC B	0.57	0.69	1.26	1.50	$967 \pm 65$	$376 \pm 32$

\*a total sample evaporation time of  $1\,727 \pm 99$  s and a drying rate  $695 \pm 47$   $\text{s}\cdot\mu\text{l}^{-1}$  were obtained on the glass substrate (in the form of a microscope glass cover slip)

The evaporation time data show that the ring cells stay wetted for approximately 15–18 minutes under the experimental conditions. The evaporation times correspond with the applied uptake liquid volumes. The longest times, therefore, were achieved with MFC B coatings followed by 5 pph MFC A and 10 pph MFC A, respectively. The drying rates were calculated from the slopes of the linear part of the evaporation curves ( $t = 200\text{--}600$  s). The density of the Tris buffer was assumed to be  $1\text{ gcm}^{-3}$ . The drying rate shows how many seconds it takes for one microlitre to evaporate. The results show that the drying rate is rather similar between the samples containing 5 pph of binder, MFC B providing a very slightly slower evaporation, but well within the standard deviation of the measurement. These rates correspond well with the porosimetric pore volume results presented in Table 2, when 5 pph MFC A and MFC B are compared. With the higher binder amount the difference in evaporation rate between the binders is more pronounced, though still borderline in respect to the standard deviation of the measurement, being slower in the case of MFC A. This is somewhat surprising since the inter-particle pore size, and hence permeability, is reduced (but not volume) in the case of MFC B when the dose is increased from 5 pph to 10 pph. However, if we consider the surface area increase presented by the inter-particle MFC matrix providing for the finer inter-particle pores at the same pore volume (Figure 1 and Table 2), and that evaporation is diffusion and film flow driven rather than bulk flow driven, the reduction in bulk permeability is probably compensated by the evaporative surface area increase.

As these coatings are to be used as reaction platforms for enzymatic testing, it is important that the reaction area stays wet under elevated temperatures, typically  $37\text{ }^{\circ}\text{C}$ , for extended periods of time, typically  $\sim 10$  min or more, for the reaction to take place. These results show that the evaporation time can be altered by changing the formulation of the coating and thus affecting the porosity, volume uptake and pore size-related internal surface area of the coating structure within the confines of the hydrophobising printed pattern. The evaporation time under heating, would of course require further testing. Since the deviation in the experimental evaporation rate data were relatively large in respect to the differences seen, a more macroscopic tool is probably needed to control the retained wetting. In this case we provided an absorbent pad pre-saturated with water and placed onto a designed absorbent pad zone so as to retain the wetted character of the system. This proved to be the more viable way to extend the wet time by providing replenishment of the water during evaporation.

A sufficient amount of binder is required to bind the pigment particles to each other and to the base substrate and, thus, to maintain the integrity of the coating. Elution experiments revealed that 5 pph MFC A is not sufficient when larger liquid amounts are applied onto the reaction channel (Figure 3). The coating separated from the base substrate and travelled with the eluent. This shows that finding an optimal coating formulation requires balancing coating integrity and absorption and wetting capabilities. In this respect, the fibrillated cellulose binder seems to provide a good compromise.

### 3.3 Pattern Design

Inkjet printing with hydrophobic inks provides a convenient pattern fabrication method, which allows patterns to be printed that are specifically designed for a given purpose. The pattern for future pharmaceutical active enzymatic testing evolved from a simple printed circular ring cell into a design with channels, concentration zones and an absorbent pad zone to counter evaporation. The coating properties, especially the porosity, permeability and thickness of the coating, affect not only the liquid dynamics of the microfluidic elements, but also the printing parameters required to achieve the boundary hydrophobisation. More details concerning the pattern printing have been published by Koivunen et al. (2015a; 2015b), and will be discussed further in future publications. Figure 3 shows some examples of test patterns.

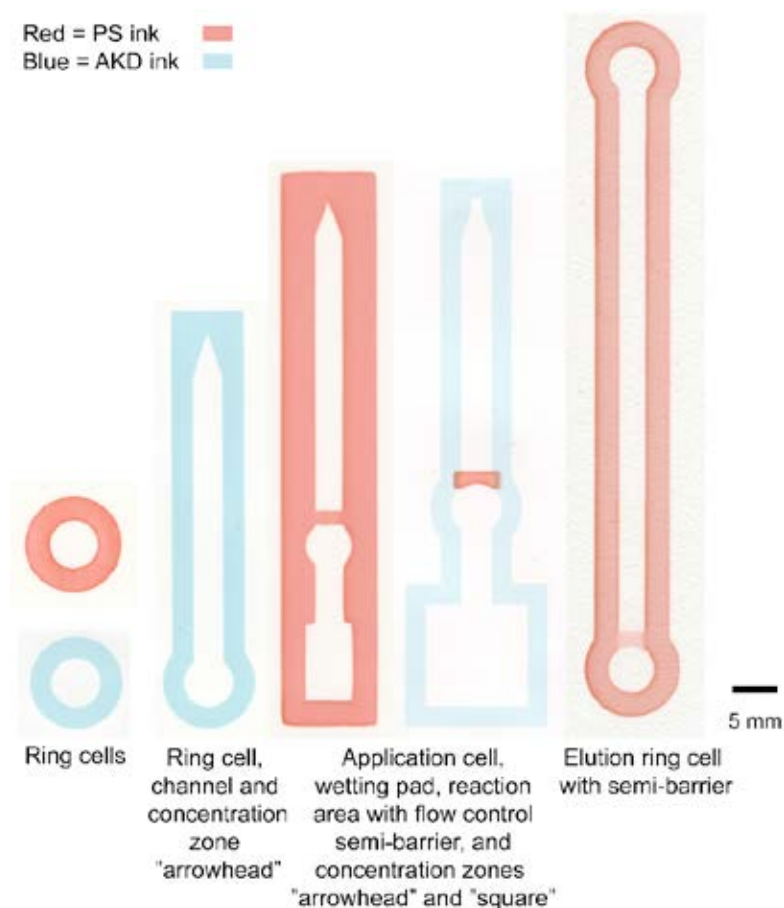


Figure 3: Examples of pattern design for reaction platforms for potential enzymatic reaction

Both PS and AKD inks provide reliable hydrophobic barriers, which are able to keep the test liquids inside the patterns and wicking channels. However, on the one hand, the AKD ink hydrophobises the coating more efficiently, and thus fewer printing layers and less time are required for printing with AKD than with PS, especially when employing thick coating layers. On the other hand, since PS does not hydrophobise the coating layer so efficiently, it can be used with higher sensitivity to control liquid flow momentarily when

used to form a semi-permeable or height controlled barrier. For example, in the case where an absorbent pad might be applied to keep the reaction area wet for a certain time, such a semi-barrier could be employed to prevent the liquid wicking through the whole channel, and after the reaction the end products could later be eluted with larger free flowing liquid volumes through the semi-barrier into the channel and to the concentration zone.

The circular ring cell patterns could also be used for reactions, but if some component used in the reaction disturbs the subsequent detection, for example in fluorescence detection, the design shown with a reaction area and a channel is preferably used instead. With this kind of design, the end products can be transported to the concentration zone rather quickly by eluting a few times. If the reaction area should stay wetted for longer periods of time, contact with an absorbent pad can be accommodated. Elution with this kind extended wetting design, however, takes much longer and larger eluting volumes are required, than with a design with no absorbent pad. The elution time can be modified by changing the dimensions, particularly the length of the channels between the absorbent pad zone and the reaction area, and between the semi-barrier and the concentration zone and in turn the concentration of the end products by altering the concentration zone geometry.

#### 4. Conclusions

FCC-based coatings in combination with inkjet-printed hydrophobic patterns could be used as reaction platforms, for example for enzymatic pharmaceutical actives testing. The results show that the coating formulations can be altered to enhance porosity and wetting capabilities of the coatings by utilising different types of microfibrillated and micro nanofibrillated cellulose as binder at different amounts, and that inkjet-printing provides a convenient way to create hydrophobised patterns that can easily be adapted to control aqueous microfluidics to suit a given desired purpose.

In future work, the feasibility of the developed platforms for carrying out *in vitro* drug metabolism assays will be tested using a model pharmaceutical agent enzyme reaction. This involves testing compatibility of the coating and ink components with the drug-metabolising enzyme(s), determining achievable detection limits and comparing them with detection limits achieved with other platforms, such as filter or chromatographic paper, finding a suitable heating method such as printed thin-film resistors, selecting an optimal detection method and ultimately developing a self-standing platform for such enzymatic testing.

#### Acknowledgements

Funding for the project was supported by Omya International AG (Juttila and Koivunen, Aalto University) and the European Research Council (project no. 311705. CUMTAS. Dr Sikanen, Helsinki University). Silvan Fischer (Omya International AG) is acknowledged for the SEM analysis and Cathy Ridgway (Omya International AG) for porosimetry.

#### References

- Carrilho, E., Martinez, A.W. and Whitesides, G.M., 2009. Understanding Wax Printing: A Simple Micropatterning Process for Paper-Based Microfluidics. *Analytical Chemistry*, 81(16), pp. 7091–7095.
- Cate, D.M., Adkins, J.A., Mettakoonpitak, J. and Henry, C.S., 2015. Recent Developments in Paper-Based Microfluidic Devices. *Analytical Chemistry*, 87(1), pp. 19–41.
- de Tarso Garcia, P., Cardoso, T.M.G., Garcia, C.D., Carrilho, E. and Coltro, W.K.T., 2014. A handheld Stamping Process to Fabricate Microfluidic Paper-based Analytical Devices with Chemically Modified Surface for Clinical Assays. *RSC Advances*, 4, pp. 37637–37644.

- Ellerbee, A.K., Phillips, S.T., Siegel, A.C., Mirica, K.A., Martinez, A.W., Stiehl, P., Jain, N., Prentiss, M. and Whitesides, G.M., 2009. Quantifying Colorimetric Assays in Paper-Based Microfluidic Devices by Measuring the Transmission of Light through Paper. *Analytical Chemistry*, 81(20), pp. 8447–8452.
- Iliescu, C., Taylor, H., Avram, M., Miao, J. and Franssila, S., 2012. A Practical Guide for the Fabrication of Microfluidic Devices using Glass and Silicon. *Biomicrofluidics*, 6(1), pp. 016505-1–16.
- Juttila, E., Koivunen, R. and Gane, P.A.C., 2015. Effect of Coating Pigment, Binder Type and Binder Amount on Planar Liquid Wicking on Coated Substrates. *Journal of Print and Media Technology Research*, 4(3), pp. 173–186.
- Khan, M.S., Thouas, G., Shen, W., Whyte, G. and Garnier, G., 2010. Paper Diagnostics for Instantaneous Blood Typing. *Analytical Chemistry*, 82(10), pp. 4158–4164.
- Koivunen, R., Juttila, E., and Gane, P.A.C., 2015a. Inkjet Printed Hydrophobic Microfluidic Channelling on Porous Substrates. *Journal of Print and Media Technology Research*, 4(1), .pp. 7–17.
- Koivunen, R., Juttila, E., Bollström, R. and Gane, P.A.C., 2015b. Inkjet-Printed Reaction Arrays on Pigment Coated Substrates. In: *Advances in Printing and Media Technology*, Vol. XLII(II), Ed. Gane, P.A.C. and Ridgway, C., International Association of Research Organizations for the Information, Media and Graphic Arts Industries, pp. 107–114.
- Liana, D.D., Raguse, B., Gooding, J.J. and Chow, E., 2012. Recent Advances in Paper-based Sensors. *Sensors*, 12(9), pp. 11505–11526.
- Martinez, A.W., 2011. Microfluidic Paper-based Analytical Devices: from POCKET to Paper-based ELISA. *Bioanalysis*, 3(23), pp. 2589–2592.
- Martinez, A.W., Phillips, S.T., Butte, M.J. and Whitesides, G.M., 2007. Patterned Paper as a Platform for Inexpensive, Low-volume, Portable Bioassays. *Angewandte Chemie International Edition*, 46(8), pp. 1318–1320.
- Martinez, A.W., Phillips, S.T., Whitesides, G.M. and Carilho, E., 2010. Diagnostics for the Developing World: Microfluidic Paper-based Analytical Devices. *Analytical Chemistry*, 82(1), pp. 3–10.
- Nurak, T., Praphairaksit, N. and Chailapakul, O., 2013. Fabrication of Paper-based Devices by Lacquer Spraying Method for the Determination of Nickel (II) ion in Waste Water. *Talanta*, 114, pp. 291–296.
- Olkkonen, J., Lehtinen, K. and Erho, T., 2010. Flexographically Printed Fluidic Structures in Paper. *Analytical Chemistry*, 82(24), pp. 10246–10250.
- Teerinen, T., Lappalainen, T. and Erho, T., 2014. A Paper-based Lateral Flow Assay for Morphine. *Analytical and Bioanalytical Chemistry*, 406(24), pp. 5955–5965.
- Thuo, M.M., Martinez, R.V., Lan, W.-J., Liu, X., Barber, J., Atkinson, M.B.J., Bandarage, D., Block, J-F. and Whitesides, G.M., 2014. Fabrication of Low-Cost Paper-Based Microfluidic Devices by Embossing or Cut-and-Stack Methods. *Chemistry of Materials*, 26(14), pp. 4230–4237.
- Vella, S.J., Beattie, P., Cademartiri, R., Laromaine, A., Martinez, A.W., Phillips, S.T., Mirica, K.A. and Whitesides, G.M., 2012. Measuring Markers of Liver Function Using a Micropatterned Paper Device Designed for Blood from a Fingertick. *Analytical Chemistry*, 84(6), pp. 2883–2891.
- Yamada, K., Henares, T.G., Suzuki, K. and Citterio, D., 2015. Paper-Based Inkjet-Printed Microfluidic Analytical Devices. *Angewandte Chemie International Edition*, 54(18), pp. 5294–5310.

## Improving Run-time Stability with Aerosol Jet Printing Using a Solvent Add-back Bubbler

Arjun Wadhwa<sup>1</sup>, Denis Cormier<sup>2</sup>, Scott Williams<sup>3</sup>

<sup>1</sup> Quest Integrated, LLC, 19823 58<sup>th</sup> Pl. South, Suite 200, Kent, WA 98032 (USA)

<sup>2</sup> Industrial and System Engineering, Rochester Institute of Technology, 81 Lomb Memorial Drive, Rochester, NY 14623 (USA)

<sup>3</sup> School of Chemistry and Materials Science, Rochester Institute of Technology, 85 Lomb Memorial Drive, Rochester, NY 14623 (USA)

E-mail: a.wadhwa@qi2.com; drceie@rit.edu; sawppr@rit.edu

### Short Abstract

Aerosol Jet printing is a non-contact process capable of printing on conformal and flexible surfaces. Aqueous or solvent nano-inks are pneumatically atomized under nitrogen. The atomizing gas flow through the atomization cup leads to evaporation and removal of volatile solvent(s). As the ink solid loading fraction increases with the loss of solvent during atomization, the rheological changes eventually lead to instabilities in print output. A potential solution to this problem is to moisten the incoming atomizing gas with a solvent add-back system. In this study, neat co-solvent solutions of ethanol and ethylene glycol at 85 : 15 and 30 : 70 mixing ratios were atomized using nitrogen flow rates ranging from 600 to 1000 ccm. It was observed that ethanol, being the more volatile solvent, was depleted from the neat solution at a much higher rate than ethylene glycol. When nitrogen gas was passed through a bubbler prior to atomization, an excessive amount of ethanol was returned to the neat solution. The solvent loss rate from an ethanol rich neat solution (80 %) was higher compared to an ethylene glycol rich neat solution. Perfecting the solvent add-back rate to an ink will enable longer print runs in a manufacturing environment.

**Keywords:** aerosol jet printing, direct write, ink stability

### 1. Introduction and background

Direct-write (DW) printing refers to a class of additive manufacturing processes in which inks or pastes are digitally deposited in any desired geometric pattern onto a substrate of interest. Substrate examples could include molded plastic parts, 3D printed parts, composite panels, etc. DW printing is rapidly gaining importance in several industries. For example, significant weight reductions are possible when electrical traces are printed onto or even within a non-planar component surface instead of using externally routed wires and connectors (Kessler, 2009). Printed antennas that conform to non-planar surfaces provide tremendous flexibility in location, number, and size of antennas (Deffenbaugh, 2013). A broad spectrum of electronic components such as ring oscillators (Ha, 2013), thin film transistors (Jones, 2010), and hydrogen sensors (Liu, 2012) can be printed directly on a wide-variety of substrates, regardless of whether or not the substrate is planar.

Whereas conventional lithography processes have much higher feature resolutions than current direct-write printing technologies, direct-write processes are able to deposit a much wider array of materials. Practically speaking, any nano-material that can be synthesized in ink form can be direct-write printed. For example, solid oxide fuel cells employing yttria-stabilized zirconia (YSZ) electrolyte layers and YSZ-nickel oxide composite anodes have been aerosol jet printed (Sukeshini, 2012). Specifically, aero-

sol jet printed poly(3-hexylthiophene) (P3HT) polymer semiconductor inks for use in printed transistors (Kim, 2013). Aerosol jet printing was also used to deposit biologically active inks (Grunwald, 2010). When used in printed electronics applications, direct-write processes are also attractive from an environmental perspective. Rather than plating copper, conductive inks (e.g. copper, silver, gold, etc.) can be selectively printed thereby minimizing material use and hazardous waste disposal.

For any relatively new manufacturing technology, the transition from a research and development environment to a production environment is largely dictated by factors such as cost, throughput, and process stability and repeatability. This paper specifically focuses on run-time printing stability on a production scale aerosol jet printing platform when using co-solvent blended ink systems that have, in many cases, vastly different boiling points or evaporation rates.

## 1.1 Aerosol Jet Printing

### 1.1.1 Process Fundamentals

Aerosol Jet (AJ) printing is a direct-write printing technique for depositing a pre-set pattern or layout (Hon, 2008). It is capable of producing fine pitch structures below 50  $\mu\text{m}$  using nano-ink suspensions with particle sizes up to a recommended maximum of approximately 700 nm and with a ink viscosity range from 0.7–2500 cP (Goth, 2011). The AJ process steps are illustrated in Figure 1. A fluid can be atomized in the reservoir either pneumatically with nitrogen gas or ultrasonically. The maximum wet droplet diameter is typically on the order of 2–5  $\mu\text{m}$  (Mahmud, 2010).

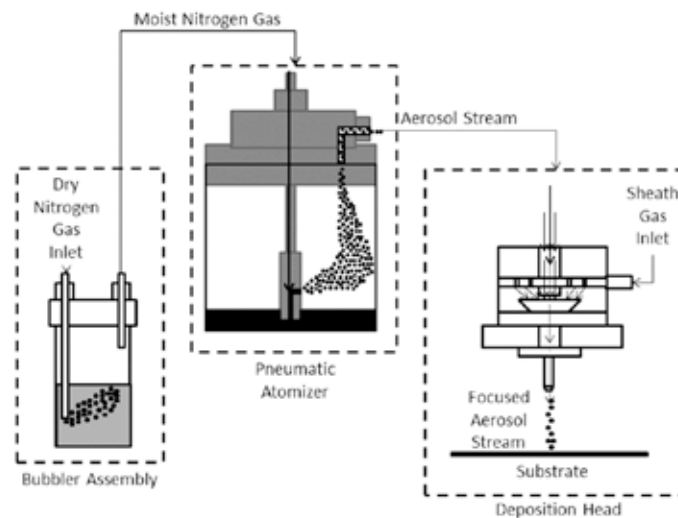


Figure 1: Schematic representation of the Aerosol Jet printing process.

Table 1. Aerosol jet printing process parameters

Process Parameter	Units	Recommended Range
Atomization Flow Rate	ccm	500–1200
Virtual Impactor Flow Rate	ccm	400–1100
Sheath Gas Flow Rate	ccm	30–100
Tube Heater Temperature	$^{\circ}\text{C}$	RT – 90
Platen Temperature	$^{\circ}\text{C}$	RT – 90
Nozzle Diameter	$\mu\text{m}$	100, 150, 200, 250, 300
Nozzle Stand-Off Distance	mm	3–10

Although AJ printing has been used for numerous interesting applications produced in very small quantities, the process as a manufacturing option has not been widely studied. Hoerber et al. studied the effect of process parameters (Table 1) on printed line width and thickness (Hoerber, 2011). They observed that the line width increased with increases in atomization and sheath flow rates. Also, line width and height increased when the number of print passes was increased. Conversely, line width decreased when the translation speed increased.

Sukeshini et al. studied the effect of varying the nozzle stand-off distance and virtual impactor exhaust flow rate values (Sukeshini, 2010). It was observed that for the YSZ ink used in the study, the amount of material deposited increased to a maximum; and then, decreased as virtual impactor exhaust flow rate was increased. Several studies determined a process parameter window that influences the line quality, electrical properties and adhesion of AJ printed silver lines (Verheecke, 2012; Mahajan, 2013).

### 1.1.2 Current Aerosol Jet Challenges

For AJ printing to be a viable production tool, run-time stability will depend on a consistent ink composition. Many inks are colloidal dispersions in a solvent (single solvent or co-solvent). Surfactants are optionally included to lower the ink surface tension, and dispersants are often used to prevent particle coagulation. During atomization, nitrogen gas flow over the ink surface causes preferential loss of high volatile components through evaporation. Preferential component loss will create changes in the physical ink properties. The high vapor pressure (low boiling point) solvent removal rate would depend on the dry atomizing gas flow rate (nitrogen gas flow rate) over the solvent, and the component fractional vapor pressure as illustrated in Equation 1.

$$Q_v = Q_{N_2} \cdot (P_v / (P_T - P_v)) \quad [1]$$

where  $Q_v$  is the flow rate of solvent vapors (ccm),  $Q_{N_2}$  is the flow rate of atomizing gas (ccm),  $P_T$  is the total pressure (kPa), and  $P_v$  is the vapor pressure (kPa) of volatile solvent component.

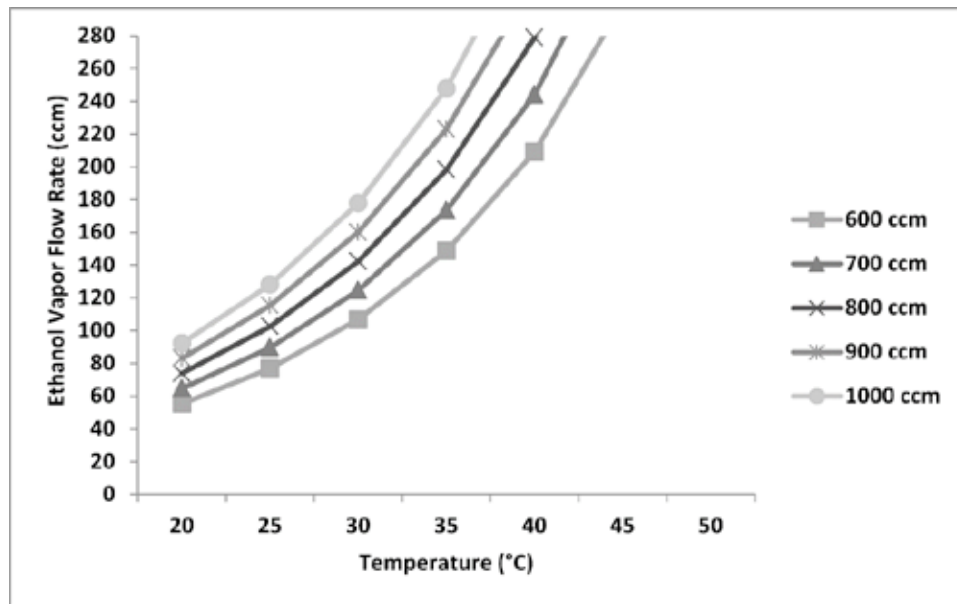


Figure 2: Ethanol flow rate versus temperature curve at different atomization flow rates.

With a 69 Kpa (10 psi) atomization cup pressure, Figure 2 illustrates the simulated loss of ethanol ( $P_v$ ) from the atomizing cup via evaporation at different nitrogen flow rates and temperatures using Equation 1.

Antoine's equation was used to calculate the partial pressure due to ethanol as a function of temperature. To illustrate a common solvent blend used in aerosol jet printing, ethylene glycol is another commonly used co-solvent in ink systems. Ethylene glycol loss, however, during atomization is approximately 1 % that of ethanol due to significantly higher boiling point. In co-solvent inks, therefore, with both low and high vapor pressure constituents, one can effectively focus on the high vapor pressure solvent composition when trying to control ink stability. As shown in Figure 2, the expected rate of solvent transfer with the atomization gas, and therefore solvent loss in the atomization cup, increases significantly with both carrier gas flow rate and temperature.

We propose to control solvent loss by feeding the atomizing gas through a bubbler system prior to the atomizing cup as seen in Figure 1. The idea is that moist atomizing gas will “add back” solvent into the atomizing cup. We are not aware of any research using such an add-back method. The aim of this paper is to study the impact of this solvent add-back approach by monitoring the solvent blend composition during atomization over time and temperature.

## 2. Materials and Methods

All experiments were conducted using an Optomec Aerosol Jet system equipped with two pneumatic atomizers. A bubbler add back system as seen in Figure 1 contains the more volatile solvent of a co-solvent blend. Nitrogen gas was bubbled through the solvent, thereby transferring solvent vapor. The saturation state, of the more volatile component, in the atomization cup will depend on flow rate and cup temperature. In this study, atomization cup temperature was kept constant at approximately 23 °C.

In order to study AJ ink stability as a function of process parameter values, two types of neat co-solvent solutions of ethylene glycol (higher boiling point, lower vapor pressure) and ethanol (lower boiling point, higher vapor pressure) were prepared. No pigment components were added in this study. The co-solvent blend is used in a number of commercial nano-inks, and is therefore a representative co-solvent system of practical significance. The less volatile ink blend consisted of 30 wt. % ethanol and 70 wt. % ethylene glycol. The more volatile ink blend consisted of 85 wt. % ethanol and 15 wt. % ethylene glycol. These two inks were AJ printed over an extended period of time at different atomization flow rates ranging from 600 ccm to 1000 ccm. Experiments were conducted without the solvent add-back system and then again with the solvent add-back system. Samples of the neat solutions were extracted from the atomization cup at 30 minute time intervals in order to determine the stability of the neat solution as measured by the relative proportions of the two co-solvents.

The relative ethanol and ethylene glycol proportions in a given sample were determined by measuring the refractive indices on an Abbe Refractometer. Using the rule of mixtures, the percentage of ethanol in any sample can be determined using Equation 2 in order to quantitatively determine the rate at which the more volatile ethanol solvent is being lost during atomization.

$$\% \text{ Ethanol} = \frac{RI_{EG} - RI_S}{RI_{EG} - RI_{Eth}} \quad [2]$$

where  $RI_{EG}$  is the refractive index of ethylene glycol (measured value = 1.4293),  $RI_S$  is the refractive index of the extracted ink sample, and  $RI_{Eth}$  is the refractive index of ethanol (measured value = 1.3616).



### 3. Results and Discussion

#### 3.1 Ink stability without solvent add-back

Figures 3 and 4 show results of experiments for the low volatility and high volatility inks respectively run without the solvent add-back system.

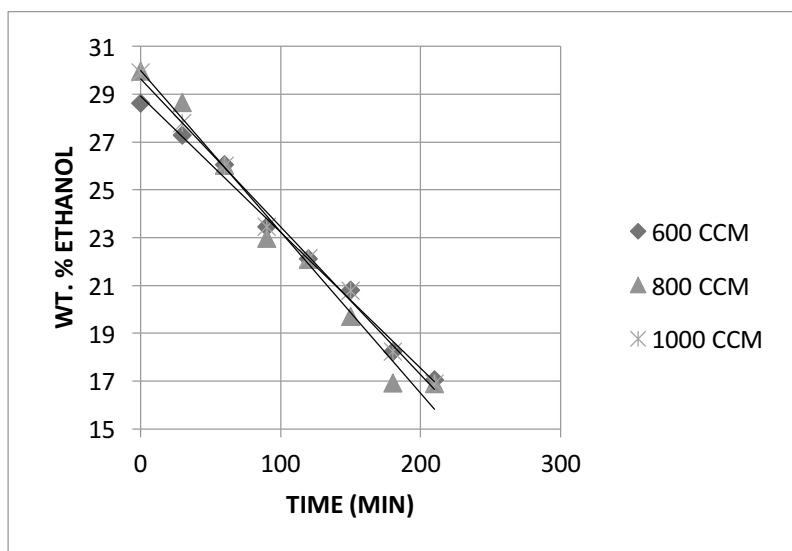


Figure 3: Weight percent of ethanol versus time plot for atomization of a 30 % ethanol 70 % ethylene glycol co-solvent mixture without bubbler add-back.

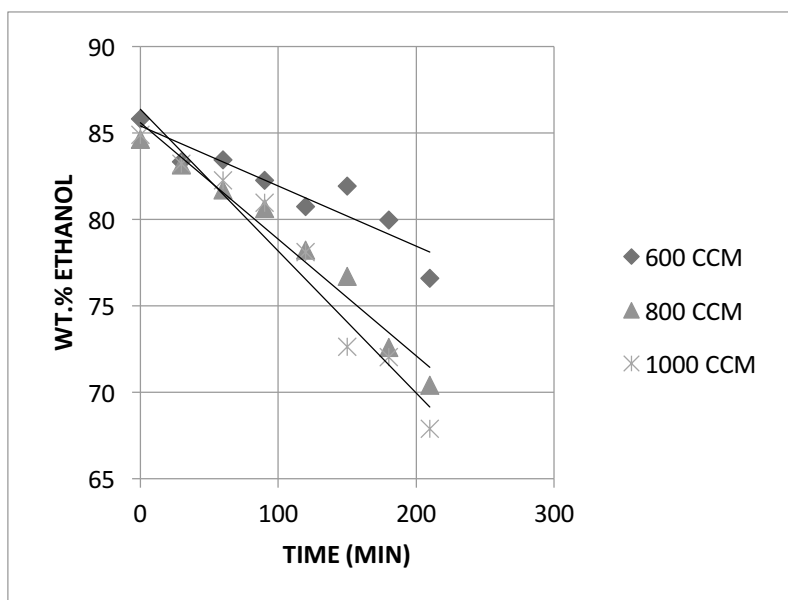


Figure 4: Weight percent of ethanol versus time plot for atomization of 85 % ethanol 15 % ethylene glycol co-solvent mixture without bubbler add-back.

Figures 3 and 4 clearly demonstrate a substantial ethanol loss in a relatively short amount of time (3 ½ hours) when atomization was done with dry nitrogen gas. For the 30 % ethanol ink, nearly half of the ethanol was lost in just three hours of printing. The high vapor pressure solvents (e.g. ethanol) allow aerosol ink droplets to rapidly dry on the substrate. As high vapor pressure co-solvent is depleted in the ink, the drying speed and surface energy of the ink changes – sometimes dramatically. As the drying time of printed lines increases due to loss of high vapor pressure co-solvents in the atomizing cup, the printed

lines have time to both (1) spread out and form wider traces, and (2) to retract into discontinuous beads resulting from a surface tension increase. Practically speaking, this means that the quality of the printed lines, as indicated by line width, thickness, and overspray, will change as the high vapor pressure solvent is depleted. Figures 3 and 4 point towards a strong need for an alternative approach to atomization with high vapor pressure co-solvent blends. The aforementioned solvent add-back system was a relatively simple low-cost approach.

### 3.2 Ink stability with solvent add-back

In order to quantitatively assess effectiveness of the solvent add-back system on ink stability, a second set of experiments were run using the solvent add-back system (see Figure 1). The bubbler contained the more volatile ethanol since the rate of evaporation of ethylene glycol at room temperature is substantially lower than that of ethanol. Figures 5 and 6 show results of experiments for the 30 % and 85 % ethanol inks respectively at 600 (low flow) and 1000 (high flow) ccm nitrogen atomization flow rates respectively. The dry nitrogen (no solvent add-back) results are also plotted for comparison.

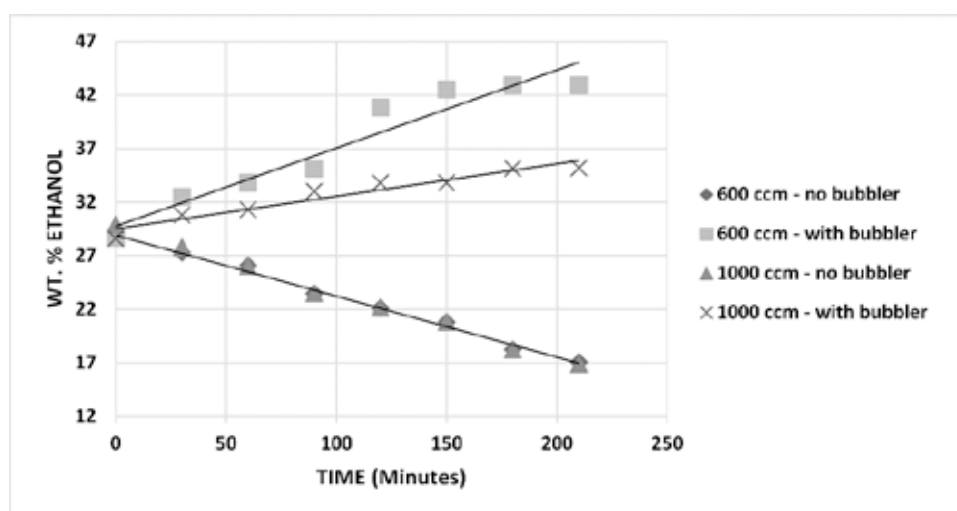


Figure 5: Weight percent of ethanol versus time plot for atomization of 30 % ethanol 70 % ethylene glycol co-solvent mixture with solvent add-back.

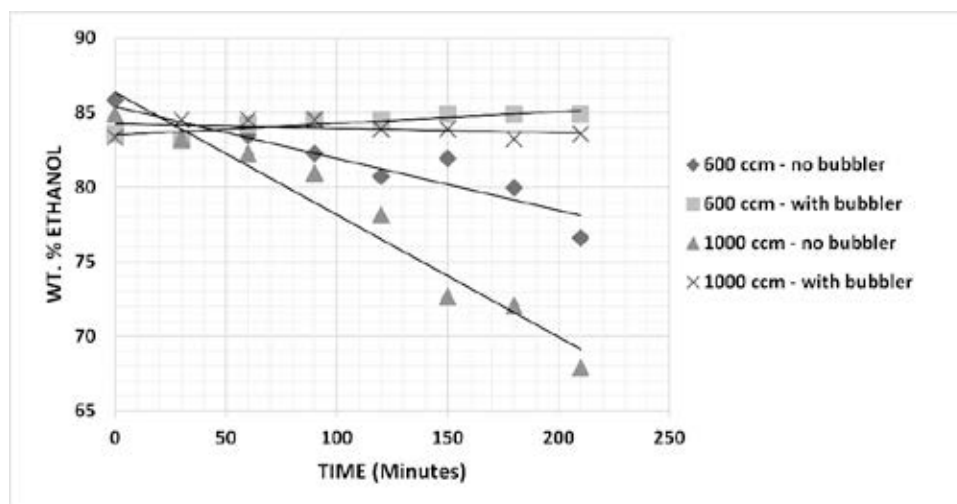


Figure 6: Weight percent of Ethanol versus time plot for atomization of 85 % ethanol 15 % ethylene glycol co-solvent mixture with solvent add-back.

Figure 5 shows ethanol concentration for the low ethanol (30 wt. %) solution. The ideal outcome would be a horizontal line indicating that the ethanol concentration remains constant over the 3 ½ hours of atomization. As opposed to the trends observed without an add-back system, Figure 5 illustrates that the ethanol concentration actually increased with each flow condition using a bubbler. Clearly, the rate of ethanol addition to the atomization cup was greater than ethanol loss from the cup. Possibilities to be explored further are differences in the ethanol evaporation rates, in the two cups, due to differential flow rate anomalies or ethanol partial pressure depression created by the mixed solvent system used in the atomization cup.

Figure 6 illustrates a similar trend for the high (85 %) ethanol ink solution. As expected, the ethanol loss rate with dry nitrogen was greatest at high atomization flow rates (1000 ccm). When the solvent add-back bubbler technique was used, the ethanol concentration was nearly consistent with run-time.

Since it appears that a simple solvent add-back technique was able to compensate for the loss of low boiling point solvent during atomization is promising. Figure 5, however, points to the need for further development work to overcome excessive solvent add-back.

#### 4. Conclusions

Many ink formulations used in AJ printing use blends of low and high boiling point co-solvents. In some applications, slow drying inks that flow out and form a continuous coating are desired, whereas other applications call for fast drying inks used to print narrow lines and/or features with high aspect ratios. Depending upon the application, the low boiling point solvent composition may range from just a few percent up to nearly 100 %. This paper has demonstrated that AJ printing with dry nitrogen gas leads to rapid loss of low boiling point, high evaporation rate, solvent(s). As the ink concentrates, the nanoparticle loading fraction increases, and the wetting and spreading behavior of the ink may dramatically change. Ultimately, inks with high concentrations of low boiling point solvents may become unprintable due to a rapid shift in the higher boiling point solvent concentration. A potential solution to this problem is to add solvent back into the atomizing cup through the use of a bubbler.

The solvent add-back method uses a bubbler to moisten the nitrogen gas before it enters the atomizing cup. This study has shown that the bubbler solvent add-back approach has the potential to overcome the loss of low boiling point solvents under certain conditions such as those shown in Figure 6 where the concentration of a comparatively low boiling point solvent, ethanol, was high. It is, however, also possible to add back an excessive amount of solvent when the concentration of low boiling point solvent is relatively low.

In studying Figure 5, one can envision that a blend of dry and moist nitrogen gas in the correct ratios will lead to continuous printing with a constant ethanol concentration. We will present new results demonstrating the effects of mixing two mass flow conditions – dry and vapor flows. Two mass flow controllers are used to independently control the ratios of dry and wet nitrogen in order to maintain equilibrium.

#### Acknowledgments

The Authors would like to thank the contribution of Optomec Inc. for donation of the Aerosol Jet Printing Platform. This work was also supported by a grant from the National Science Foundation (USA) (NSF-PFI 12-511).

## References

- Deffenbaugh, P., Goldfarb, J., Chen, X., and Church, K., 2013. Fully 3D Printed 2.4 GHz Bluetooth/Wi-Fi Antenna. In: *IMAPS, 46<sup>th</sup> International Symposium on Microelectronics 2013*.
- Goth, C., Putzo, S., and Franke, J., 2011. Aerosol Jet printing on rapid prototyping materials for fine pitch electronic applications. In: *IEEE Electronic Components and Technology Conference (ECTC) 2011*, pp. 1211–1216.
- Grunwald, I., Groth, E., Wirth, I., Schumacher, J., Maiwald, M., Zoellmer, V., and Busse, M., 2010. Surface biofunctionalization and production of miniaturized sensor structures using aerosol printing technologies. *Biofabrication*, 2(1), p. 014106.
- Ha, M., Seo, J.W., Prabhumirashi, P., Zhang, W., Geier, M., Renn, M., Kim, C., Hersam, M., and Frisbie, D., 2013. Aerosol jet printed, low voltage, electrolyte gated carbon nanotube ring oscillators with sub-5  $\mu$ s stage delays. *Nano letters*, 13(3), pp. 954–960.
- Hon, K.K.B., Li, L., and Hutchings, I.M., 2008. Direct writing technology—Advances and developments. *CIRP Annals-Manufacturing Technology*, 57(2), pp. 601–620.
- Hoerber, J., Goth, C., Franke, J., and Hedges, M., 2011. Electrical functionalization of thermoplastic materials by Aerosol Jet Printing. In: *IEEE Electronics Packaging Technology Conference (EPTC) 2011*, pp. 813–818.
- Jones, C., Lu, X., Renn, M., Stroder, M., and Shih, W.S., 2010. Aerosol-jet-printed, high-speed, flexible thin-film transistor made using single-walled carbon nanotube solution. *Microelectronic Engineering*, 87(3), pp. 434–437.
- Kessler, S.S., Dunn, C.T., Borgen, M., Raghavan, A., Duce, J., & Banks, D.L., 2009. A cable-free digital sensor-bus for structural health monitoring of large area composite structures. In: *Annual Conference of the Prognostics and Health Management Society 2009*.
- Kim, S.H., Hong, K., Lee, K.H., and Frisbie, D., 2013. Performance and stability of aerosol-jet-printed electrolyte-gated transistors based on poly (3-hexylthiophene). *ACS applied materials & interfaces*, 5(14), pp. 6580–6585.
- Liu, R., Ding, H., Lin, J., Shen, F., Cui, Z., and Zhang, T., 2012. Fabrication of platinum-decorated single-walled carbon nanotube based hydrogen sensors by aerosol jet printing. *Nanotechnology*, 23(50): p. 505301.
- Mahajan, A., Frisbie, C.D., & Francis, L.F., 2013. Optimization of aerosol jet printing for high-resolution, high-aspect ratio silver lines. *ACS applied materials & interfaces*, 5(11), pp. 4856–4864.
- Mahmud, Z., Hoey, J.M., Lutfurakhmanov, A., Daus, J., Swenson, O.F., Schulz, D.L., and Akhatov, I.S., 2010. Experimental characterization of aerosol flow through a micro-capillary. In: *ASME 2010 8<sup>th</sup> International Conference on Nanochannels, Microchannels, and Minichannels collocated with 3<sup>rd</sup> Joint US-European Fluids Engineering Summer Meeting 2010*, pp. 949–958.
- Sukeshini, A.M., Jenkins, T., Gardner, P., Miller, R.M., and Reitz, T.L., 2010. Investigation of Aerosol Jet Deposition Parameters for Printing SOFC Layers. In: *ASME 2010 8<sup>th</sup> International Conference on Fuel Cell Science, Engineering and Technology 2010*, pp. 325–332.
- Sukeshini, M., Meisenkothen, F., Gardner, P., and Reitz, T., 2012. Aerosol Jet printing of functionally graded SOFC anode interlayer and microstructural investigation by low voltage scanning electron microscopy. *Journal of Power Sources*, 224, pp. 295–303.
- Verheecke, W., Van Dyck, M., Vogeler, F., Voet, A., Valkenaers, H., 2012. Optimizing Aerosol Jet printing of silver interconnects on polyimide for embedded electronics applications. In: *8<sup>th</sup> International DAAAM Baltic Conference 2012*.

## Optimized inking for cardboard food packaging

*Fons Put*

Flemish innovation center for graphic communication

E-mail: fons.put@vigc.be

### Short Abstract

In the print-production of full-colored packaging, cyan, magenta and yellow process colors are coded to construct a color gamut. Coding is done in such a way that the produced color gamut fits with the customer expectations. Important variables in this color-coding process are:

- Use of black ink. Darker colors have a large degree of freedom regarding the use of black ink. Identical colors can be produced with different amounts of black ink.
- Maximum ink limit. A maximum ink limit is set for the color gamut. The total area coverage can vary from 200 to 330 %.

In this research an optimized amount of black ink and maximal ink coverage is determined in order to:

- Fulfil the customer demand for color quality
- Ensure the best process stability in printing
- Minimize the risk for set-off
- Minimize ink costs

**Keywords:** packaging, color

## 1. Introduction and background

Food packaging printing is a challenge. Use of proper materials and appropriate manufacturing processes are necessary to produce regulatory food safe printed packaging. The 'good manufacturing practice'-regulation (Regulation EC 2023/2006) states that there is no contact or migration from the printed side towards the food contact side! The biggest risk for this type of migration, known as "set-off" in offset printing, is logically to be found at printed areas with the highest ink coverage. In order to minimize the risk for set-off, a minimum needed amount of ink has to be defined and used during printing. For this purpose a specific test form was developed and printed in a production packaging company. Analyses of the printed results returns information about the use of black ink and maximum ink limit in the construction of separation profiles. The results are applied on "proof-of-concept" print runs in commercial packaging companies.

## 2. Materials and Methods

A printing test form is developed for standardized printing on coated paper substrates, as defined in ISO 12647-2:2004. The test form exist of following elements:

- "Colormatch" print target: used to determine the degree of color standardization of the printing process.

- “Dark colors” print target: used to determine the influence of the maximum ink coverage on the color gamut.
- “Black curve” print target: used to determine the influence of grey component replacement on print accuracy and stability.
- “set-off” print target: used to determine the level of visual set-off during the printing process.

## 2.1 Colormatch

Starting point is a standardized printing process with colors that can be predicted, proofed and verified. The packaging company uses the FOGRA39 dataset, based on ISO12647-2:2004 type 1, as the reference color gamut for their workflows and printed products. Process colors, halftones and grey-balances are evaluated against their standardized aim values.

## 2.2 Dark colors

This chart is used to investigate the impact of the maximum ink limit on the size (loss) of the color gamut. Colors from all hue directions that are positioned on the gamut borders, are selected. For every selected CIE  $L^*a^*b^*$  color of the list, 3 different CMYK-separations are calculated and grouped into the dark colors chart (Figure 1). The maximum ink limits of the 3 separation types are 320 % (basic industry profile), 260 % and 220 % (chosen limit). The lower limit is determined on basis of the color errors that are introduced by limiting the amount of maximum ink in the separation type. Table 1 shows a number of industry color profiles with their maximum ink limit and amount of color and black in the separation. The VIGC-profiles are calculated from the FOGRA39 dataset through X-rite i1Profiler software. For every profile the introduced color error by the corresponding maximum ink limit is calculated on basis of the dark colors chart.

*Table 1: Differences in ink consumption of ICC profiles with different maximum ink limits., where the differences are based on the 80 darkest colors of the FOGRA39 color gamut; in separation types with less than 220 % maximum coverage, the maximum color error becomes significant.*

ICC-profile	maximum ink limit	Color deviation (DE2000)		ink consumption difference			
		average	maximum	Cyan	Magenta	Yellow	Black
ISOcoated_v2_eci	330 %	0	0	reference	reference	reference	reference
Coated Fogra 39 (Adobe)	330 %	2	4	8 %	9 %	9 %	-10 %
Coated_Fogra39L_VIGC_320	320 %	1	2	-15 %	-16 %	-20 %	7 %
ISOcoated_v2_300_eci	300 %	0	1	-4 %	-4 %	-5 %	2 %
Coated_Fogra39L_VIGC_300	300 %	1	1	-17 %	-18 %	-22 %	7 %
Coated_Fogra39L_VIGC_280	280 %	1	1	-18 %	-18 %	-23 %	8 %
Coated_Fogra39L_VIGC_260	260 %	1	1	-20 %	-20 %	-26 %	8 %
Coated_Fogra39L_VIGC_240	240 %	1	2	-24 %	-24 %	-30 %	9 %
Coated_Fogra39L_VIGC_230	230 %	1	2	-27 %	-26 %	-34 %	10 %
Coated_Fogra39L_VIGC_220	220 %	1	3	-30 %	-29 %	-38 %	10 %
Coated_Fogra39L_VIGC_210	210 %	2	4	-35 %	-33 %	-43 %	11 %
Coated_Fogra39L_VIGC_200	200 %	2	6	-40 %	-37 %	-48 %	12 %

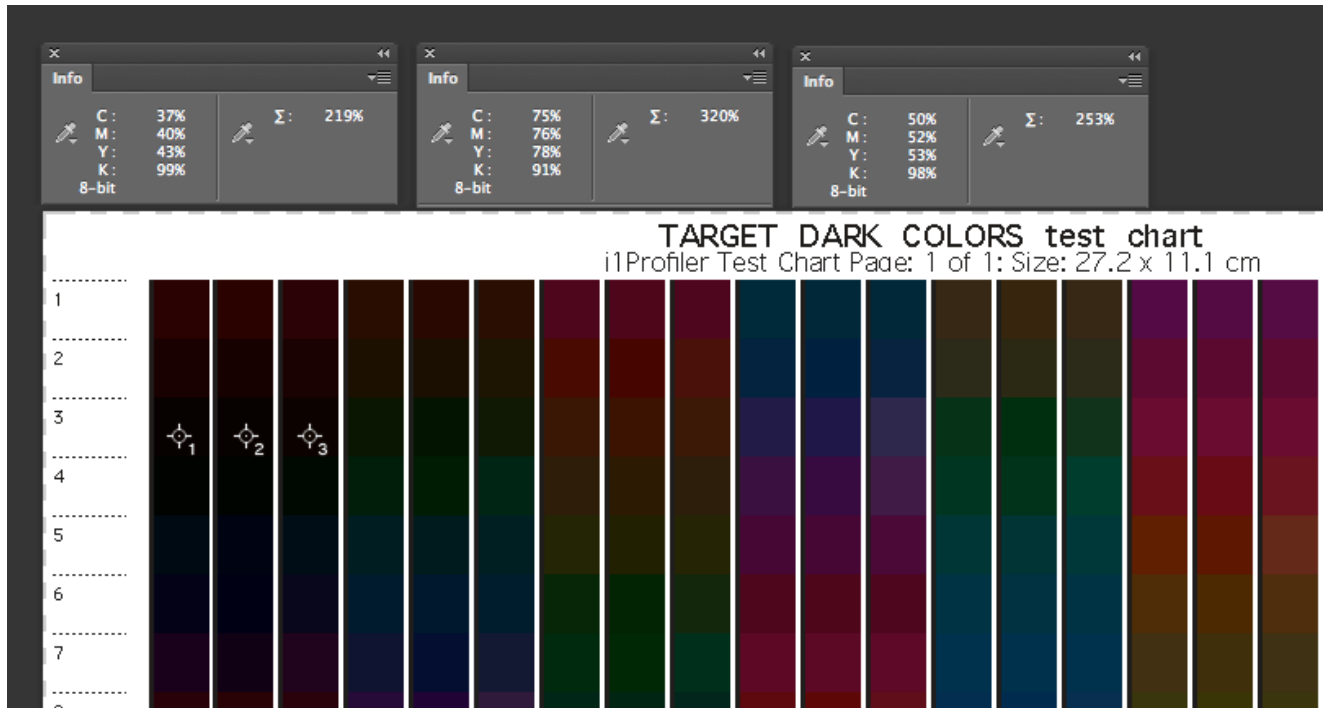


Figure 1: The dark color chart with 3 separation types, where the samples colors (1–2–3) have identical Lab values but different CMYK values (inkcoverage 219 % – 320 % – 253 %).

### 2.3 Black curve

By building up a large black separation the total ink amount can be further reduced. 80 midtone CIE L\*a\*b\* defined colors are selected out of the FOGRA39 color gamut to investigate more in detail the influence of a large black separation. In this case the colors are selected closer towards the L-axis, here the effects on ink consumption will become more obvious. In Table 2 the differences in ink consumption are calculated for a number of industry color profiles. The test chart uses 3 different types of separation: separation with only color ink (no black), medium black ink and maximum black ink (Figure 2).

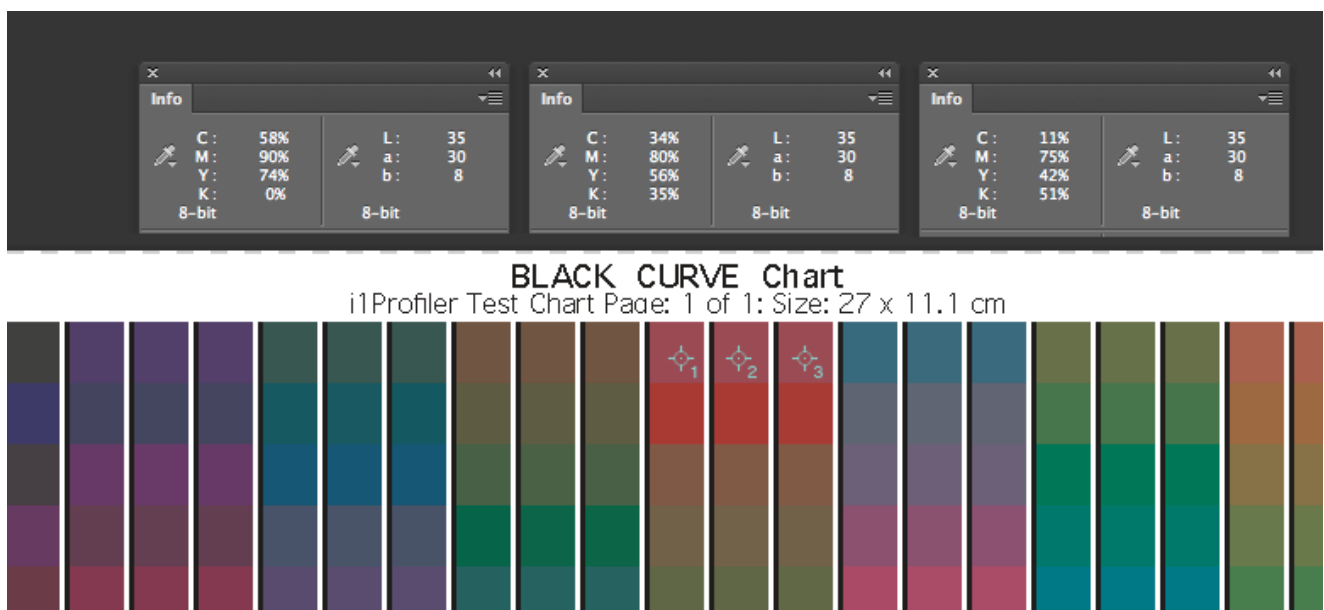


Figure 2: Black curve print target with 80 midtone color combinations, where the sampled colors have the same Lab values but different separations values: without black ink, medium black and maximum black.

Table 2: Differences in ink consumption of ICC profiles, based on the black curve chart, where the ink consumption of the profile “ISOcoated\_v2\_eci” is set as a reference; it is clear which profiles are using more black ink, replacing color inks, the maximum ink limit has no effect on these midtone colors.

ICC-profile	% ink consumption difference			
	Cyan	Magenta	Yellow	Black
ISOcoated_v2_eci	reference	reference	reference	reference
ISOcoated_v2_300_eci	-5 %	-5 %	-5 %	7 %
Coated Fogra 39 (Adobe)	7 %	9 %	8 %	-17 %
Coated_Fogra39L_VIGC_320	-19 %	-19 %	-19 %	27 %
Coated_Fogra39L_VIGC_260	-20 %	-20 %	-21 %	28 %
Coated_Fogra39L_VIGC_220	-22 %	-21 %	-22 %	30 %

## 2.4 Set-off print target

This target enables to check how the ink drying speed is related to the maximum ink limit. In Figure 3. The maximum ink coverage of industry color profiles is shown. The ink amounts are the result of relative colorimetric rendering with black point compensation of a Lab color with coordinates 0,0,0. Most popular maximum ink limits were printed and analysed in an IGT drying tester. In this tester the wet printed strokes (dark black color) are brought slowly into contact with an unprinted back side. This will cause set-off that will become less visible in time because of the drying of the ink layer.

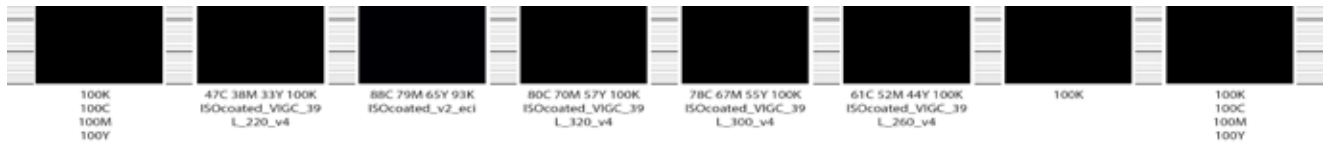


Figure 3: Construction of the set-off print target, where each combination consists of a solid dark black that after printing will be transferred through an IGT set-off tester.

## 3. Results and Discussion

### 3.1 Evaluation of the maximum ink limit

Figure 4 and Figure 5 show what happens when different maximum ink limits are put under pressure in the IGT drying tester. Inks for food packaging have a long drying time (the inks are almost only dried by absorption in the coating). To overcome this, the print is covered with a water-based lacquer (fast drying).



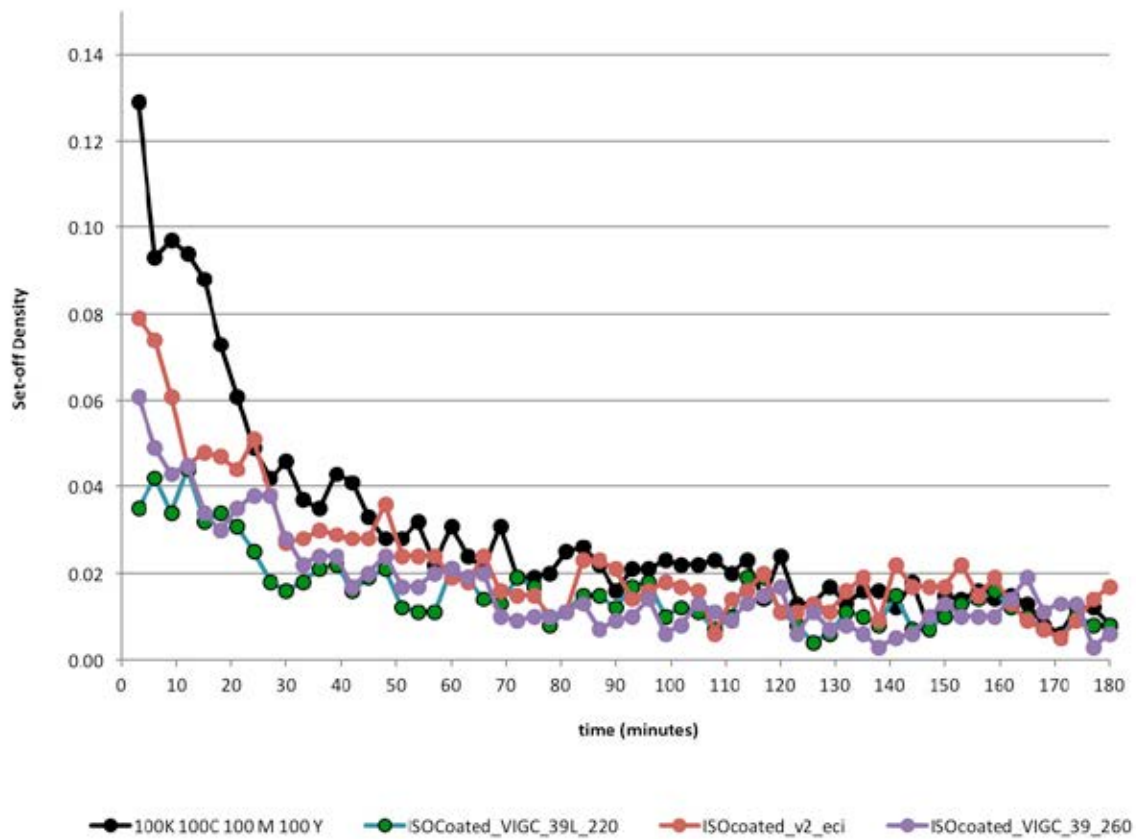


Figure 4: The risk for set-off is significantly lower for a 220 % ink limit than the widely used 320 % limit of the ISOcoated\_v2\_eci-color profile.

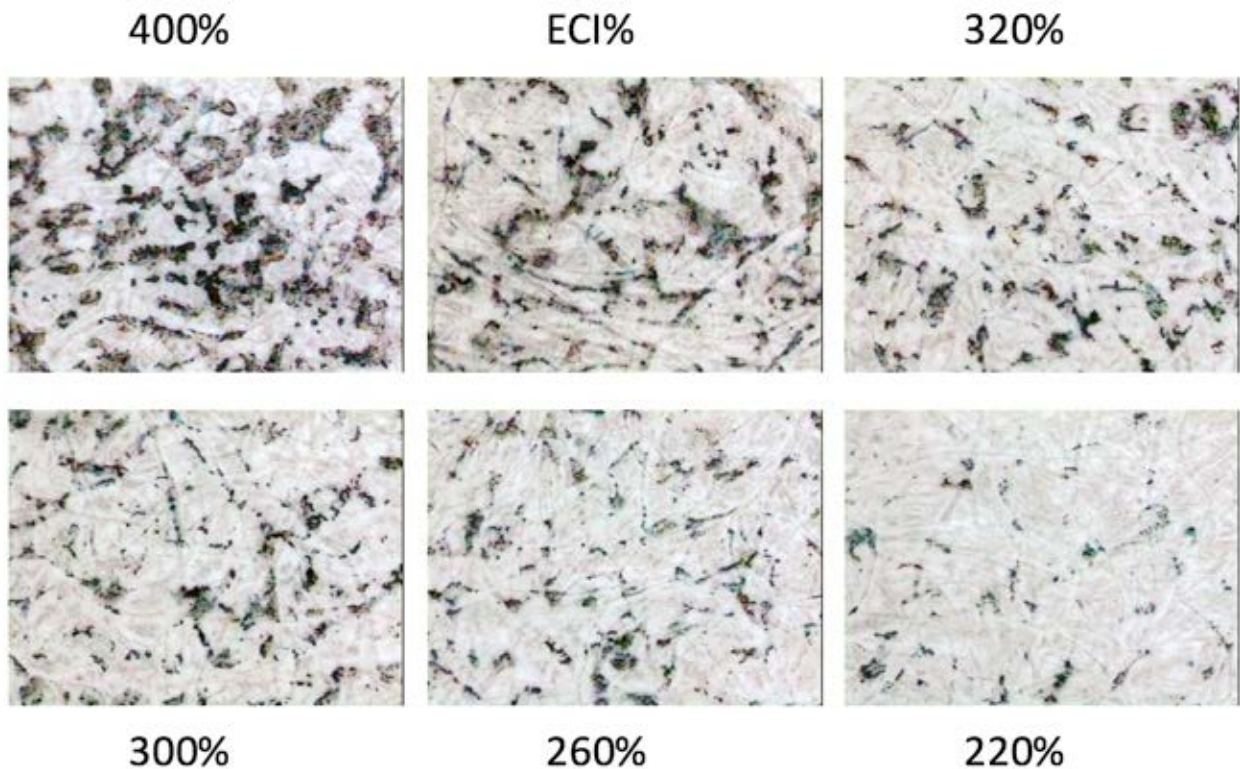


Figure 5: Microscopic images of the set-off directly after printing; the risk is lowered as a function of the maximum ink limit of the used color profile.

### 3.2 Evaluation of black in separation

The color differences between the measured printed charts and the target values are illustrated in a CIE  $L^*a^*b^*$  graph in Figure 6. This chart shows the color differences for the 80 patches of the black curve chart. The separation without the black has the largest errors, the separation with the maximum use of black ink the smallest.

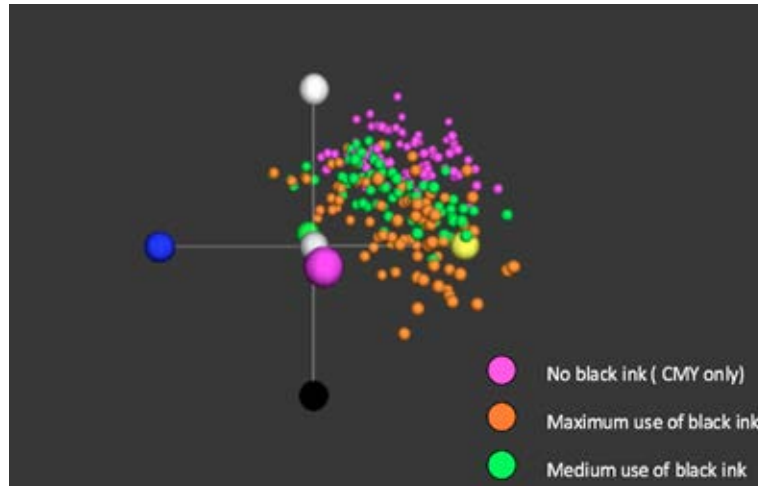


Figure 6: Lab chart containing the color differences between print and target, where each axis shows the color difference, a plot in the middle is the “perfect print”, and the distribution shows the best result for the separation with maximum use of black ink!

Main reason for the better black reproduction is the presence of a finishing glossy lacquer layer. Gloss lacquer causes printed black ink to look darker (lower  $L^*$  values). Substitution with black ink makes use of this advantage. Figure 7 shows the measurement results of the separation with maximum black, with and without a finishing glossy lacquer. The presence of the glossy lacquer lowers the  $L^*$  value of the printed colors.

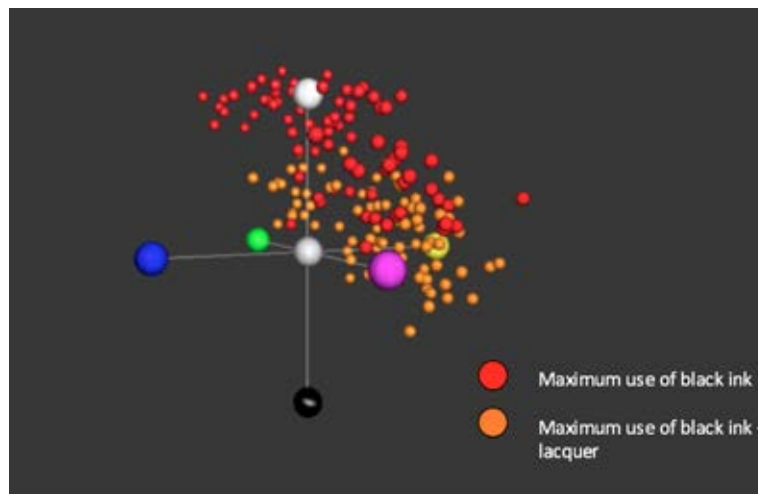


Figure 7: Lab chart showing the cause of the better results with maximum use of black, and the presence of a glossy lacquer over the printed black lowers the  $L^*$  values significantly.

To measure the color stability of the different separation types, 20 samples were taken out of a print run of 3000 copies. From every sample the average deviation of the 80 colors of the black curve chart is calculated (expressed as a CIE2000 number). Figure 8 shows the average and maximum result for the 3 different separation types. The maximum black separation shows the smallest variation in color.

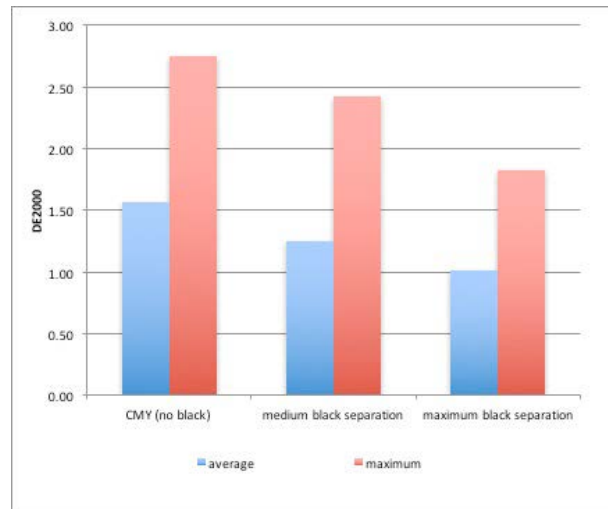


Figure 8: Color stability of different black separations in a print run.

As a proof-of-concept a “chocolate” packaging design (Figure 9) was printed in 2 versions: One with the traditionally ink limit of 320 % and low/medium black, and one with a maximum ink limit of 220 % and maximum black separation. Design colors were samples and compared by the CIE2000-formula. The result of this is shown in Figure 10.



Figure 9: Proof of concept with a real-life chocolate design.

nr	Kleur	originele separatie: druk versus target										separatie ViGC 220: druk versus target										separatie 1/2	
		C	M	Y	K	L*	a*	b*	ΔCIE2000	ΔL	ΔC	ΔH	C	M	Y	K	ΔCIE2000	ΔL	ΔC	ΔH	ΔCIE2000		
1		10	70	52	2	56.0	41.8	19.8	3	2.5	-1.0	-1.5	1	68	48	10	3	3.0	-0.5	0.8	1		
2		44	62	67	64	27.5	8.1	9.3	3	2.5	0.0	-2.2	23	51	57	74	3	3.0	0.7	1.6	1		
3		35	85	64	57	26.1	23.1	8.6	2	2.6	-1.7	-0.8	13	78	51	68	2	2.8	-2.0	0.4	0		
4		63	68	56	78	18.8	3.8	-0.1	3	3.5	-0.7	-1.2	37	48	35	88	3	3.2	-0.2	-1.4	1		
5		59	77	64	86	14.6	5.2	2.0	3	3.5	0.2	-1.2	29	55	40	94	2	3.4	0.4	0.8	0		
6		60	62	57	67	23.5	3.3	1.1	2	2.5	-0.4	-1.1	35	44	38	82	3	3.1	0.0	0.8	1		
7		62	72	62	91	11.8	-0.6	-1.0	3	3.6	-0.8	-1.4	47	38	33	100	4	3.5	0.6	-3.0	2		
8		69	80	61	89	12.6	3.5	0.0	3	4.0	0.0	-1.1	37	51	33	97	3	3.9	0.4	-1.9	1		
9		35	80	63	45	31.3	24.9	10.1	4	3.9	-1.9	-1.9	12	74	51	90	3	3.6	-2.0	0.2	1		
10		46	70	63	70	22.9	9.6	5.4	3	3.6	-0.3	-2.2	24	59	49	80	3	3.7	-0.3	1.0	1		
11		53	60	60	63	27.1	4.8	4.2	1	1.2	0.4	-0.5	31	46	45	76	2	1.9	0.6	0.2	1		
12		50	56	51	55	31.8	5.8	2.4	1	1.3	0.0	-0.5	31	45	38	68	1	1.1	0.0	0.1	1		

Figure 10: Proof-of-concept of a chocolate design, where the CIE2000 color differences between the 2 versions almost never exceed 1!

## 4. Conclusions

The results of the print trials show that packaging printers can significantly lower the amount of ink without sacrificing visual design aspects. Use of appropriate color profiles enables designers and prepress to work with the best suitable combination of maximum ink limit and black separation. In this specific proof-of-concept, a maximum ink limit of 220 % was sufficient to reproduce the needed color gamut. In the upcoming months more proof-of-concept print runs are planned to check these findings.

## References

- 2011-11-14\_EuPIA\_Guideline\_for\_Food\_Packaging\_Inks\_-\_November\_2011\_corr\_July\_2012.
- Balasubramanian, R. and Eschbach, R., 2001. Reducing Multi-Separation Color Moiré by a Variable Undercolor Removal and Gray Component Replacement Strategy. *Journal of Imaging Science and Technology*, 45(2), pp. 152–160.
- Graindourze, M., 2014. Low Migration Inkjet Ink Technology for Printing of Food Packaging, *RTE Food Packaging Seminar Stuttgart*, 24<sup>th</sup> September 2014.
- ISO12647-2:2004, Graphic technology: *Process control for the production of half-tone colour separations, proof and production prints Part 2: Offset lithographic processes*.
- Ivory, N., 2014. Safe Use of Radiation Cured Inks and Varnishes. *RTE Food Packaging Seminar Stuttgart*, 24<sup>th</sup> September 2014.
- Kang, B.-H., Cho, M.-K., Choh H.-K. and Kim C.-Y., 2005. Black Color Replacement using Gamut Extension Method, NIP & Digital Fabrication Conference. *2005 International Conference on Digital Printing Technologies*. pp. 384–386.
- Kisilev P., Sivan Y., Aharon M., Keshet R., Staelin C., Braverman G. and Harush S., 2011. Local Gray Component Replacement Using Image Analysis. *19<sup>th</sup> Color and Imaging Conference Proceedings*, pp. 234–238.
- Klump, S., 2014. Head of Packaging Quality and Safety Nestlé, Nestlé Food Packaging Safety “Managing Risk”, *RTE Food Packaging Seminar Stuttgart*, 24<sup>th</sup> September 2014.
- PrintIP Research Report (FOGRA, PTS, VIGC, AIDO, CELABOR), 2013.
- Qiao, Y., Ernst, L., 2013. (RICOH), Printer Ink Limit Optimization, (ICC-meeting, Frankfurt).
- Whitehead, C., 2014. Migration of Chemicals from Food Packaging and the Printing Inks used. *Proceedings of the 41<sup>st</sup> International Research Conference of IARIGAI*, 7–10 September 2014, Swansea, Wales, UK: *Advances in Printing and Media Technology*, Vol. XLI(I), Ed. by Nils Enlund and Mladen Lovreč, ISBN 978\_3\_9870704\_0\_3, ISSN 2409\_4201, Darmstadt MMXIV.
- Wu, T.-L., Wu, Y.-H. and Huang Y.-C., 2004. A Table-Based Ink-Reducing Approach with Estimating Ink Limitation of Media and Gray Component Replacement for Printing Devices. *NIP20: International Conference on Digital Printing Technologies*, pp. 483–486.

## Colour Management of Tablet Devices

*Daniel Langsford, Reem El Asaleh, Richard Adams*

Ryerson University, 350 Victoria Street, Toronto, ON M5B 2K3

E-mail: daniel.langsford@ryerson.ca; reem.elasaleh@ryerson.ca; richard.adams@ryerson.ca

### Short Abstract

As of now, the creation and use of tabular devices in society has been strictly focused on the benefits for commercial use. While other device such as monitors or cameras are capable of device-specific colour management, tabular devices have been left behind with only manufactured colour adjustments available. This has resulted in a limited use for tabular devices such as the Windows Surface, Apple's iPads and Samsung's Galaxy Tabs, in the professional/printing industry. In particular, the use of these tablets have had limited integration with an already existing and functioning colour management workflow. This study has analyzed and identified the colour reproduction capabilities of specific tabular devices so that possible workflow or industry integrations can be established. This tested evaluated each device through the creation of a ICC profile using i1Profiler. The profiles were then compared to Macbeth ColorChecker Classic Chart for colour difference values ( $\Delta E_{2000}$ ) and amongst themselves for general colour gamut using ColorThink Pro software. The outcome of the tests has shown that each device tested thoroughly resulted in acceptable industry set  $\Delta E_{2000}$  standards with average well below 2. It was also seen that each device consists of various roadblocks or concerns when looking for future integration into industry workflows. Overall, while technically usable, the use of tabular devices in the industry is limited by the progress towards acceptable hardware for the industry.

**Keywords:** Windows Surface, iPad, Samsung Galaxy, tablets, colour management

### 1. Introduction and background

In the commercial setting of electronic displays, it is evident that a difference in colour exist between various brands and specific devices including televisions, cameras, monitors, mobile, and tablets. While some of these devices such as monitors and cameras can undergo device-wide colour management, others including tabular devices are left behind with only manufactured colour adjustments being made available. These adjustments cannot be changed creating limited control over colour accuracy especially if the purpose of the device requires specific colour management. From an average consumers stand point, colour management capabilities is not a dire necessity with many being accustomed to middling colour accuracy. With basic technology consumers are capable of viewing devices that are comparable to the best electronic displays of the past and as such manufacturers as of now do not see the importance of incorporating the feature of expanded colour management inclusion. From a professionally related stand point, specifically with regards to the printing industry, tabular colour management is a promising integration to the practical production workflow. This when related to commercial monitors used for average viewing and respectively targeted colour managed monitors. With colour management not only would these devices be capable of mediocre comparisons, but would be capable of absolute colour accuracy for soft proofing, beyond simply content.

Display Mate Technologies conducted a set of lab experiments to understand display technologies of various tabular devices (Soneira, 2015). In doing so, the analyzed absolute colour accuracy, where reference



points were devised from four sub-categories including full colour gamut accuracy, facial skin tone colour accuracy, organic colour accuracy, and blue region (cyan to magenta range) colour accuracy. In light of this, Display Mates research was limited to the commercial use of tabular devices, particularly aiming at home photography rather than professional work. As such, identifying and understanding factors brought upon by the printing industry would be beneficial. Additional research was conducted by the University of Novi Sad with backing from Acta Graphica performed experiments regarding tabular colour management as it relates directly for their use in colour soft proofing or other colour accurate dependent applications (Zorić, 2014). The devices were tested using digital versions of the Macbeth ColorChecker card (calibrated tiff files use on the device) as well as of Datacolour's SpyderGallery application, which allowed for colour management calibration. It searched the possibility of in-application colour management, but identified the limitations to using specific device software for viewing rather than expanding hardware capabilities.

While in-application colour management would benefit particular industries, the inability to connect with our devices limits integration with print. With this belief, there resides a need for research and experimentation on various tabular devices to examine existing colour reproduction capabilities of hardware and identify future industry possibilities.

## 2. Materials and Methods

In order to study the colour reproduction capability and identify possible future uses of tabular devices in the printing industry, a set of quality reports were produced for each tablet. The tabular devices employed and tested in this study were the Windows Surface Pro 3, Apple's iPad 2, Apple's iPad Mini 4 and Samsung's Galaxy Tab S. Each tablet was measured using the i1Profiler software and i1Pro 2 to calibrate and identify an ICC profile. Measurement conditions for each device used a CCT white point of D65, a Native luminance, a gamma of 2.2 and a Native contrast ratio. All these settings were used to best simulate standard device conditions. To perform the measurements, an additional Duet Display software was used to simulate the iPads as second monitors. The Surface Pro 3 was capable of installing i1Profiler directly on the device. The Samsung device required the use of Splashtop's remote desktop software both on the tablet and a secondary computer. The Samsung device was then set to view the secondary computer, allowing the tablet to be measured while the i1Profiler ran on the desktop monitor. The Samsung/Splashtop measurement method was later scrapped due to inaccuracies later discussed. After initial measurement and possible ICC profile integration (unavailable on iPads), a quality measurement was performed. The measurement compared to the 24-patch Macbeth ColorChecker Chart embedded in the i1Profiler software. This was then used to identify and evaluate the colour difference ( $\Delta E_{2000}$ ) in CIELAB colour space. The  $\Delta E_{2000}$  equation ( $CIEDE2000, \Delta E_{00}$ ) was used, despite other options as it is an accepted method seen in standards such as ISO12647. In addition, this equation has been found to better correlate with small differences of colour in a human observer (Habekost, 2013). The ICC profiles gathered during the measurement process were also compared for general colour gamut using ColorThink Pro 3.0.3 software.

## 3. Results and Discussion

When analyzing the results of this study, two major categories were considered. These included the device-specific colour gamut and general colour reproduction capabilities. Beginning with gamut, as demonstrated in Figures 1 to 3, the iPad Mini produced the widest colour gamut volume when compared iPad and Surface (which had the lowest). When examining and comparing each device gamut, it was seen that the Apple-based devices were capable of achieving an expanded gamut within red to green range. In particular, the iPad Mini was able to produce an extended amount of warmer colours, specifically yellows. This outcome could be attributed to the manufactured screen characteristics which aim for a warmer white point;

thus allowing for more vibrant colours. This is done for commercial photo viewing purposes. The Surface Pro produced a gamut with an expanded blue to magenta range when compared to the iPad Mini, but was ultimately overcome by the iPad's gamut. The Surface Pro is aimed towards traditional desktop computer use and as such has limited manufactured screen adjustments for colour. In addition to device-specific gamut, it can also be seen that each of the colours tested using the Macbeth ColorChecker Chart sat within gamut allowing for accurate colour reproduction measurements. Ultimately by examining colour gamut, it was possible to identify how the hardware of each device influenced its capability to display a range of colour. Notably, it determined how the white point of each device affected a further function for colour management purposes.

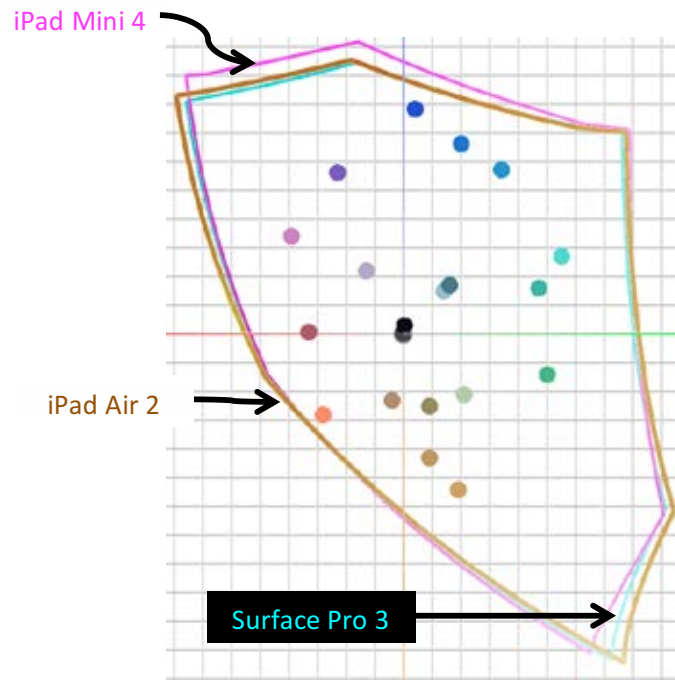


Figure 1: 2D graphs of all device gamut tested

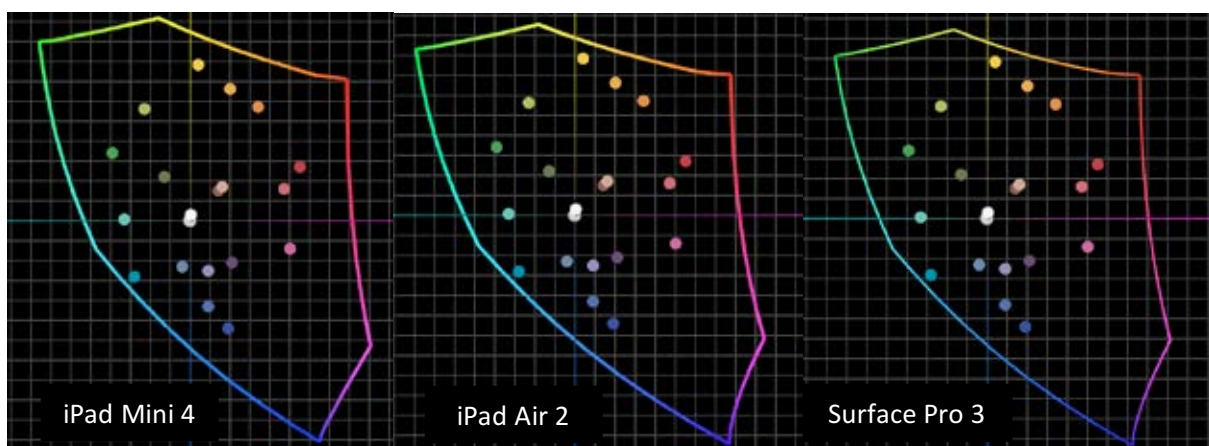


Figure 2: 2D graphs of individual device gamut

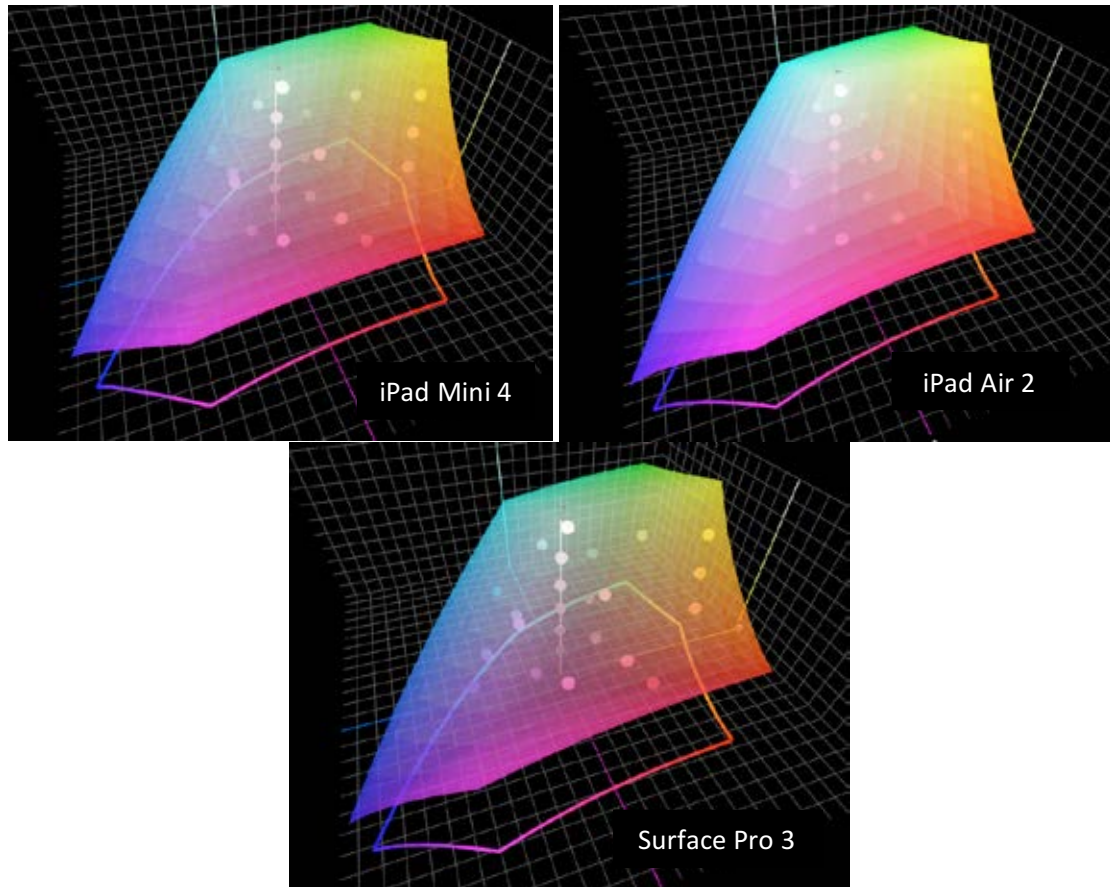


Figure 3: 3D graphs of individual device gamut tested

Table 1 summarizes the  $\Delta E_{2000}$  comparison between the tested tabular devices and the Macbeth ColorChecker Chart. The average  $\Delta E_{2000}$  values were 1.26 for Surface Pro 3, 1.44 for iPad 2 and 1.71 for iPad Mini 4. A significant comparison can be seen as the Surface Pro consisted of the smallest gamut volume, but ultimately achieved better colour reproduction capabilities. This associated to the Surface Pro's ability to incorporate ICC profiles as to improve colour reproduction. This proficiency is unachievable using the Apple-based devices. A significant statistic identified was that for all devices, 90 % values measured resulted in a  $\Delta E_{2000}$  of less than 2. From this it can be expected that regardless of device, it is possible to achieve a colour difference that is not significantly noticeable to the human eye. In addition, industry soft proofing tolerances would consider these results acceptable (IDEAlliance, 2016). With this in mind, it was also made apparent that the maximum  $\Delta E_{2000}$  measured for all devices would be considered noticeable, but continues to fall under maximum tolerance expected for soft proofing. While the soft proofing tolerances do not necessarily match the tabular device conditions, it does provide a strong baseline for comparison. When further examining the maximum  $\Delta E_{2000}$  measured, it was determined that for all devices the cyan patch was culpable. From analyzing each device gamut, it can be recognized that the cyan patch falls extremely close to the edge of the available gamut. This would explain why each device has trouble reproducing the specific colour. It is interesting to note, that the iPad 2 surpassed the capabilities of the iPad Mini 4 despite its age. This may be a result of the manufactured adjustments made to the iPad Mini 4 which aimed for an improved or more pleasing photo device, rather than achieve accurate colour.



Table 1: Summary of  $\Delta E_{2000}$  comparison for tested tabular devices

	Average $\Delta E_{2000}$	Average of Lowest 90 % $\Delta E_{2000}$	Average of Highest 10 % $\Delta E_{2000}$	Min. $\Delta E_{2000}$	Max. $\Delta E_{2000}$
Surface Pro 3	1.26	1.09	3.17	0.33	3.71
iPad 2	1.44	1.32	2.74	0.69	3.53
iPad Mini 4	1.71	1.56	3.33	0.95	4.40

#### 4. Conclusions

It is evident that manufactured colour accuracy and external colour management on tabular devices will improve in the future, but this is dependent on various impacting factors that need to be considered both in the hardware and software. The screens available today that are used in various tabular devices are targeted for commercial and practical consumer use, which do not meet standard lighting conditions used in the printing industry. In particular, commercial devices traditionally target the sRGB colour space by using a white point close to D65. The purpose relies on the profiles broad use across digital media. For each device tested, the colour temperatures exceed 7 000 K CCT as to better orient consumer activities. The use of higher values of 7 000 K and above result in bluer screens thus producing inaccurate colour, regardless of the  $\Delta E$  measured (Monoyios, 2012). This could be further looked upon by examining possible subjective tendency with relation to viewing device choice. This could ultimately alter image/photo choice despite the specific devices colour accuracy.

It is indisputable that as screen technologies such as LED, OLED, and LCD continue to advance colour accuracy will improve, but this can only go so far with regards to colour management for industry applications. Due to this the need for colour adjustment capabilities within the devices operating system is vital in allowing colour accuracy to spread across the entire device. As of now colour management is only available on tabular devices through specific software applications and limit the viewing space to inside the application. An example such applications includes the previously mentioned SpiderGallery and X-Rite's ColorTRUE applications. While applications such as these do allow for the illusion of available colour soft proofing options, the main purpose and fundamental reason for colour management is to provide accurate colour display across numerous devices such as cameras, monitors, proofers, and printers.

That being said, most general image viewing applications do not incorporate extensive colour managed settings. The inability to inject and extract colour profiles such as ICC from individual devices lead to limited connection to the overall color workflow. Those of which are capable, will ultimately be limited by the screen technology used. Overall, the devices tested show a capability of reproducing colour to a standard fitting of the printing industry. In light of this, numerous hardware and software roadblocks limit the functionality of tabular devices for conventional purposes within a workflow. This was particular seen during the testing process for the Samsung Galaxy Tab S. Due to complications in the Samsung's measurement availability and method, the ICC and  $\Delta E_{2000}$  results represented extremely obscure and inaccurate data. As such, the results of the Samsung device were excluded until a functional testing method can be identified. At this time, a suitable method to accurately mirror i1profiler or other CM software to the Samsung device does not exist.

## References

- Habekost, M., 2013. Which color differencing equation should be used? *International Circular of Graphic Education and Research*, pp. 20–32.
- IDEAlliance, 2009. *Proofing Certification Programs*. IDEAlliance, pp. 6–8.
- Lee, M., Son, C., Kim, J., Lee, C. and Ha, Y., 2007. Illumination-Level Adaptive Color Reproduction Method with Lightness Adaptation and Flare Compensation for Mobile Display. *Journal of Imaging Science and Technology*, 51(1), p. 44.
- Monoyios, K., 2012. *Gamma and White Point Explained: How to Calibrate Your Monitor*. [online] Scientific American. Available at: <<http://blogs.scientificamerican.com/symbiartic/how-to-calibrate-your-monitor/>> [Accessed 30 May 2016].
- Soneira, R., 2014. *Surface Pro Display Technology Shoot-Out*. [online] DisplayMate. Available at: <[http://www.displaymate.com/Surface\\_Pro\\_ShootOut\\_1.htm](http://www.displaymate.com/Surface_Pro_ShootOut_1.htm)> [Accessed 30 May 2016].
- Soneira, R., 2015. *iPad 2015 Display Technology Shoot-Out*. [online] DisplayMate. Available at: <[http://www.displaymate.com/iPad\\_2015\\_ShootOut\\_1.htm](http://www.displaymate.com/iPad_2015_ShootOut_1.htm)> [Accessed 30 May 2016].
- Zorić, V. and Karlović, I., 2014. Colour Reproduction on Tablet Devices. *Acta Graphica*, 24(1-2), pp. 31–36.

## Microscale halftone dots analysis: A spatial threshold evaluation method

*Louis Vallat-Evrard, Lionel Chagas, Raphaël Passas, Nadège Reverdy-Bruas*

Univ. Grenoble Alpes, LGP2, F-38000 Grenoble, France

CNRS, LGP2, F-38000 Grenoble, France

Agefpi, LGP2, F-38000 Grenoble, France

E-mail: louis.vallat-evrard@lgp2-grenoble-inp.fr; nadege.reverdy@pagora.grenoble-inp.fr

### Short Abstract

Evaluating threshold algorithms is a necessary step to obtain reliable measurements of halftone dots characteristics at the microscale. Supervised evaluation methods are based on a comparison between a thresholded image and a reference image called the ground truth. However, in most cases the ground truth is defined manually by the experimenter. Generating a synthetic image from a defined ground truth is a solution to obtain an objective evaluation. We propose therefore in this work to present a method to generate synthetic images that reproduce the degradations encountered during printing and imaging, affecting the halftone dots. This method is a combination of two steps: a simulation of the physical dot gain altering the ideal dots shape, and a generation of optical defects resulting in a synthetic degraded grayscale image. These treatments include common mean and median convolution filters and specially developed filters such as a spatial dislocation filter, a pixel aggregate filter and a noise generator filter. Precise tuning and combinations of the filters allow to obtain a synthetic degraded image that reproduces the defects encountered on the microscope visualized reference. Performance of the generation is then analyzed through visual, frequencial, spatial and coupled approaches. Synthetic degraded image and microscope captured image appear to be visually similar, have comparable histograms and have 95.21 % of pixel values matchings after a thresholding by mean value of the histogram. Only 3.01 % of fluctuation is observed when analyzing the mean misplacements of the dots centroids. Coupled spatial and frequency analysis showed a stable number of misclassified pixels in the threshold range of 50–150/255.

**Keywords:** print, dot gain, synthetic defects, objective evaluation

## 1. Introduction and background

Since the introduction of mechanical printing by J. Gutenberg in the 15<sup>th</sup> century, multiple processes and techniques were invented to improve print quality and productivity. One major achievement was the development, in the 19<sup>th</sup> century, of the halftoning method allowing to print continuous tone graphics. Today that method, although improved, remains the common way to print graphics. In order to print a continuous tones image, dots of primaries are printed separately (i.e. halftone) over a small area. Relying on the property of the human visual system (i.e. averaging the light received under its resolution limit), a halftone printed area is perceived as a continuous tone. Thus many studies (Lau and Arce, 2001) have been conducted to improve relations between the printing parameters (i.e. dots shapes, sizes and organizations) and the print perception. These studies require consequently to measure precisely dots characteristics at the microscale level (Ukishima, 2010), (Lundström and Verikas, 2010). Subsequently, models to predict the output reflectance of a halftone area have been developed and reviewed such as the well-known Murray-Davis, spectral Neugebauer or Yule-Nielsen models (Wyble et al., 2000). Three types of parameters are used in these models: spectral parameters, microscale dimensional parameters and microscale light interactions parameters (i.e. optical dot gain and uniformities of ink thickness over the dot surface).

Although determined traditionally at the macroscale level by the fit of the experimental data and model output, studies are now investigating the direct measure of these parameters at microscale, (Nyström, 2008; Namedanian, 2013; Rahaman et al., 2014). Recently applications in the field of product security and authentication to prevent counterfeiting were developed and relied on singular microscale properties of printed dots. Indeed, dots printed at high resolution present unique shapes, sizes and registrations due to print defects. As these defects are uncontrollable and random, attributes of micro 2D codes constructed from these single dots are unique and not reproducible. The system works through precise measurements of the dots at the microscale level (Nguyen et al., 2014; Reverdy-Bruas et al., 2015).

In order to achieve measurement at the microscale level, a magnification device such as an optical microscope equipped with a digital camera is often adopted. Measuring objects (i.e. dots) on a color or grayscale image is not trivial because there are no direct relations to differentiate pixels belonging to the object from background pixels. An image processing, called thresholding, is then required and allows to differentiate objects and background (Russ, 2016). This process is in two steps: first a threshold value is defined, then pixels having a gray level under the threshold value are assigned to the first level and the remaining pixels are assigned to the second level, thus obtaining a binary image. This binary image has ideally only the object represented by the first level and only the background represented by the second level. Measurements from the thresholded image become then straightforward: measuring the attributes of the first or the second level of pixels.

Multiple threshold algorithms have been developed and evaluated (Sezgin, 2004). However their performances were not tested for microscale halftone dots images. Evaluating objectively threshold algorithms is then a necessary step to obtain reliable measurements and thus improve the accuracy of applications requiring microscale halftone dots characteristics. Multiple threshold evaluations were proposed in the literature, however the approaches taken were either application independent, based on subjective steps or based on supervised methods that compare the thresholded image with an image of reference defined by the experimenter and called the ground truth image (Zhang, 1996; Philipp-Foliguet and Guigues, 2008; Cárdenes et al., 2009; McGuinness and O'Connor, 2011; Johnson and Xie, 2011). In most cases encountered in the literature the ground truth image is defined manually by the experimenter and reduces the objectivity of the evaluation. As explained by Johnson and Xie, (2011), one way of achieving objective evaluation is to generate a synthetic image. The principle of this method is to generate a synthetic image that is similar to the natural image, by degradation of a ground truth image. We propose in this work a novel method to generate synthetic images reproducing degradations encountered during printing and microscope imaging (i.e. simulate degradations that transform ideal halftone dots to the observed dots), in order to perform an objective evaluation of printed dots images threshold algorithms. This evaluation is necessary to control measurements errors and improve the measure accuracy of halftone dots characteristics at the microscale. This allows to improve halftone and color models in relation to the print perception and allows progress in advanced printed applications such as printed product security and authentication to prevent counterfeiting.

## 2. Materials and Methods

To evaluate objectively threshold algorithms processing microscale halftone dots, the strategy described in Figure 1 is adopted. First microscale halftone dots configurations are captured on luminance calibrated optical microscope. These images, called microscope captured image (MCI), are used as reference grayscale images to be thresholded. In a second step, an ideal binary image representing printed halftone dots is generated from transformed ideal dots and called the ground truth image (GTI). This ideal image represents a theoretical perfect threshold of printed dots (i.e. dots presenting mechanical dot gain but having a constant reflectance over the surface). In a third step, the GTI is transformed into a grayscale image by simulating

defects encountered during printing and capture under optical microscope. This gray level image is called the synthetic degraded image (SDI). In a fourth step various thresholding algorithms are applied on the SDI to obtain a new binary image called the thresholded degraded image (TDI). Finally, in a fifth step, the two binary images TDI and GTI are compared allowing to evaluate objectively threshold algorithms.



Figure 1: Strategy to evaluate threshold algorithms, from microscope captured image (MCI), to ground truth image (GTI), synthetic degraded image (SDI) and thresholded degraded image (TDI).

## 2.1 Paper, printing and optical microscope measurements

The test form shown in Figure 2a is generated manually and consists of 30 dots with a pixel binning of  $2 \times 2$  at the resolution of 2 400 dpi, spaced unequally to reduce periodic influence. Each dot is a  $21.17 \mu\text{m}$  width square. The test form is printed on a Seaille & Tison Sprint 2000 conventional offset printer of 480 mm width with a rotating web performing at a native resolution of 2 400 dpi, at a maximum of 130 m/min. Classical offset coated paper of  $85 \mu\text{m} \pm 1 \mu\text{m}$  thickness and  $0.9 \mu\text{m} \pm 0.1 \mu\text{m}$  roughness is employed. A Zeiss Axio Imager M1m optical microscope mounted with a Zeiss MRC5 (RGB 5.0 megapixels CCD camera) is used with an EC Epiplan Neofluar 20X/0.5 HD DIC objective. Total magnification on sensor is  $12.6 \times$  with a physical pixel size on sensor of  $3.4 \mu\text{m}/\text{pixels}$ . Thus the calibrated system captures images of  $0.271 \mu\text{m}/\text{pixels}$ , giving an observation field of  $700 \mu\text{m} \times 525 \mu\text{m}$ . Dark field reflected light microscopy is chosen to capture dots at microscale thus taking into account optical dot gain (Nyström, 2008). A halogen lamp Zeiss Hal 100 is used as light source for the microscope. Let's note that the source used is not a standard illuminant however we consider it close to standard illuminant A. The luminance is calibrated with a photodiode to take into account the ageing of the source and losses on the microscope according to the observation method. The microscope captured image, MCI, is shown in Figure 2b.

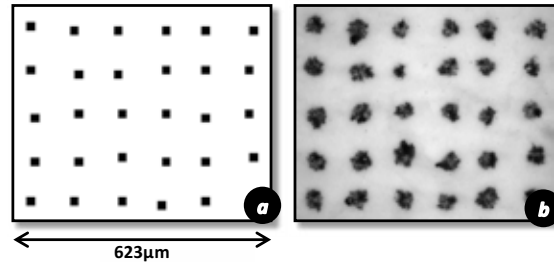


Figure 2: (a) test form, (b) print of (a) on paper observed under optical microscope (MCI).

## 2.2 Image processing transformations

Usual and specially developed image transformations are used to simulate GTI and SDI. Image smoothing is used through usual mean and median blur convolution filters described in equations [1] and [2].

Special filters include a generation of the theoretical dots with a parametrized randomization of the dots sizes shown in equation [3]. A pixel spatial dislocation filter, presented in equation [4], was designed to degrade the regular smooth borders of the theoretical dots. Pixels aggregates were generated using the function described in equation [5]. Finally a noise generator shown in equation [6] was designed to reproduce the sensor induced statistical error.

$$I(x, y) = \sum_{i, j=-m}^m \frac{1}{m^2} \times I(x+i, y+j), \text{ with } m \text{ the kernel size} \quad [1]$$

$$I(x, y) = \text{Median}_{i, j=-m}^m I(x+i, y+j) \quad [2]$$

### 2.3 Synthetic degraded image generation

$$I(x, y) = \begin{cases} K & \text{if } (x - C_x(p))^2 + (y - C_y(p))^2 = R_d(p)^2 \\ 0 & \text{otherwise} \end{cases} \quad [3]$$

with for each dot  $p$   $R_d(p)$ : parametrized random radius  
 $C_{x,y}(p)$ :  $x, y$  centroid coordinates and  $K$  the pixel value

$$\begin{aligned} I(x, y) &= I(x + Rsw_x(x, y), y) \times Rds_x(x, y) \\ I(x, y) &= I(x, y + Rsy_y(x, y)) \times Rds_y(x, y) \end{aligned} \quad [4]$$

with  $Rds_{x,y}(x, y)$ : Parametrized random continuity function  
 $Rsw_{x,y}(x, y)$ : Parametrized random displacement function

$$I(x, y) = \begin{cases} I(x, y) \times K_v & \text{if } C_{x,y}(s) + \sum_0^u Rst_{x,y}(s, u) = (x, y) \\ 0 & \text{otherwise} \end{cases} \quad [5]$$

with for each stain  $s$  of size  $u$   $Rst_{x,y}(s, u)$ : connexion value at size  $u$  and  $K_v$  the pixel intensity variator  
 $C_{x,y}(s)$ :  $x, y$  centroid coordinates

$$I(x, y) = \begin{cases} K_b & \text{if } R_n(x, y) = True \\ K_o & \text{if } R_n(x, y) = False \end{cases} \quad [6]$$

with  $K_{b,o}$ : the pixel value for background ( $K_b$ ) and object ( $K_o$ )  
 $R_n$ : parametrized random Gaussian function

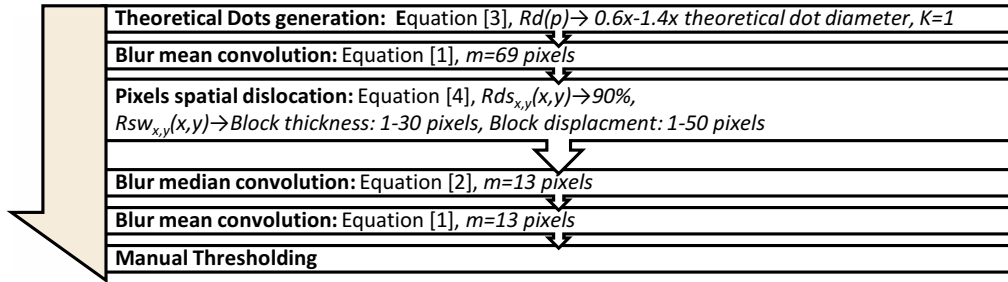


Figure 3: Generation and transformation of ideal dots to obtain the GTI.

Starting from the MCI, the first step is to build the GTI. First a manual thresholding is applied to the MCI, Figure 5b, (controlled visually to discard optical dot gain Figure 5a) and dots centroids are measured. A first GTI is obtained by generating theoretical ideal dots (disks) at each measured centroids, Figure 5d. This result although close from the image before printing doesn't simulate the physical dot gain encountered during printing, Figure 5c. Consequently further treatments are applied on the GTI, Figure 3, such as regeneration of theoretical dots with size randomization, smoothening by a mean convolution filter, centered random spatial dislocations, smoothening by median and mean convolution filters and a final mean thresholding to rebinarize the GTI, Figure 5e. A comparison of the GTI and the thresholded MCI is shown in Figure 5f.

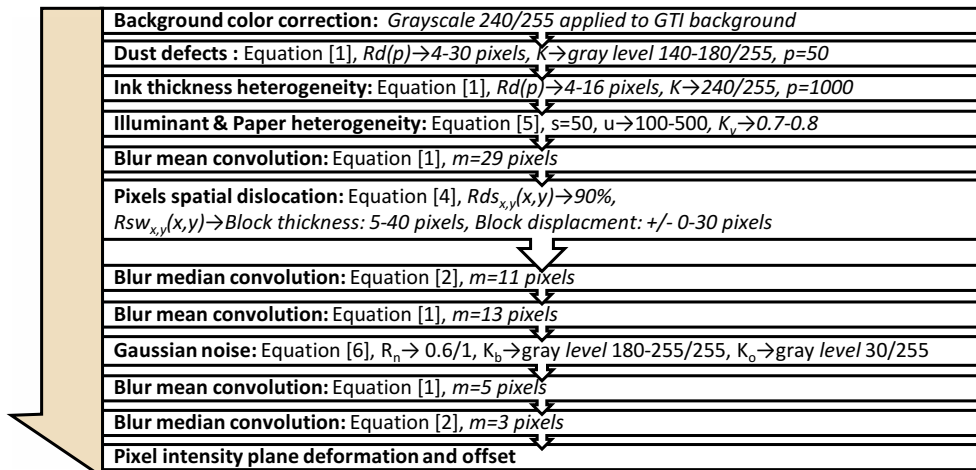


Figure 4: Synthetic defects simulation to obtain the SDI from GTI.

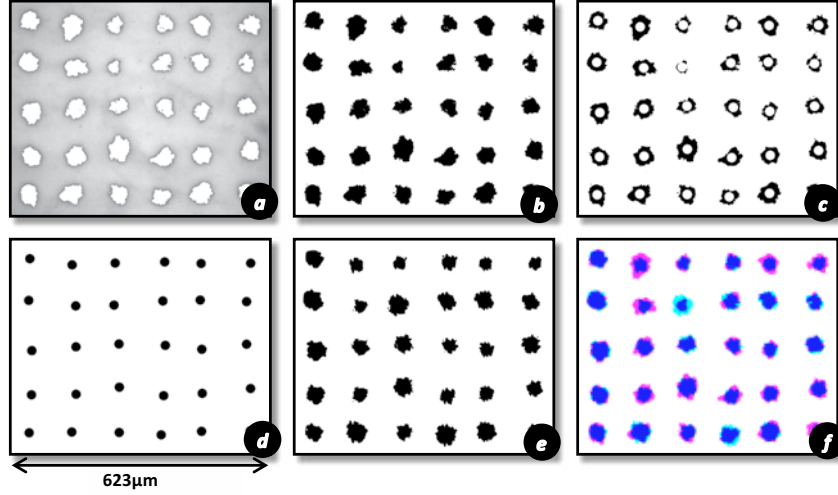


Figure 5: Ideal dots alteration: (a) thresholded dots of the MCI in white on MCI background showing discarded optical dot gain, (b) thresholded dots of the MCI, (c) theoretical dots generation in white at the centroids of the MCI thresholded dots, (d) theoretical dots generation, (e) dots obtained after application of the ideal dot alteration method, (f) comparison between (b) in magenta and (e) in cyan.

Next, synthetic defects are applied on the GTI to obtain the grayscale SDI as shown on Figure 4. First a correction of background color is applied by offsetting the background of the GTI. Then defects are added to the GTI. The first simulates optical defects by generation of dots with parametrized random sizes, centroids and gray levels associated with intensity gradient. The second defect simulates ink thickness heterogeneity by introducing small dots with identical gray level as background and parametrized random sizes and centroids. The third defect simulates the illuminant and paper heterogeneity by generation of pixels aggregates with parametrized random sizes, centroids and gray level. Results of these degradations are showed on Figure 6a. Then treatments to simulate optical dot gain are applied. These treatments can be summarized as a smoothening by a mean convolution filter, centered random spatial dislocations, and others smoothening by median and mean convolution filters. Degradations induced by the sensor are then simulated. These degradations are generated by the application of a parametrized Gaussian noise causing gray value random errors affecting differently background and objects. Smoothening by mean and median convolution filters convolution is then performed. The final deformation takes into account the non-uniformity of the background gray level intensity, due to edge effects (i.e. light scattering), by bending the plane and thus decreasing the pixel intensity on the edges. The SDI generated is shown in Figure 6b.

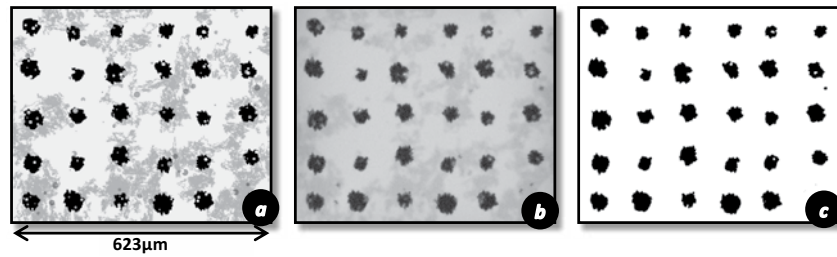


Figure 6: Synthetic defects generation: (a) background correction and simulated degradation added on the GTI, (b) SDI obtained, (c) manual threshold of the SDI.

### 3. Results and Discussions

We propose in this section to investigate the similarities between SDI and MCI from qualitative (i.e. visual comparison) and quantitative (frequential, spatial and coupled measurements) approaches. The MCI, Figure 2b, and the SDI, Figure 6b, (enlarged in Appendix 1) appear visually to be similar. Heterogeneous



background is observed for both images, with darker areas (i.e. shadows), fuzzy edge of halftone dots, random background noise and background defects such as dust in the optical path or ink residues on the paper. Although these last defects seem to be smaller and in a greater number on the MCI. Comparing now the dots, we observe that their shapes and sizes distribution are globally similar. Dark levels seem to be a little more pronounced on the SDI, as we observe bigger varieties of gray levels on the MCI. The missing areas inside the halftone dots appear to be well simulated on the SDI. Looking at the Figure 7, we can evaluate the performance of the SDI focusing on a single dot. Edge sharpness, general shape, size, optical dot gain, shadows, satellite defects and miss-inking appear to be similar. The simulated dot gives an impression of blurrier version of the MCI, which is discarded after thresholding where the two dots seemed to be similar. From this first qualitative analysis, we conclude that SDI seems to simulate correctly the observed MCI. As this first analysis allows to give a global perception, a deeper investigation is necessary to quantify the performance of the SDI.

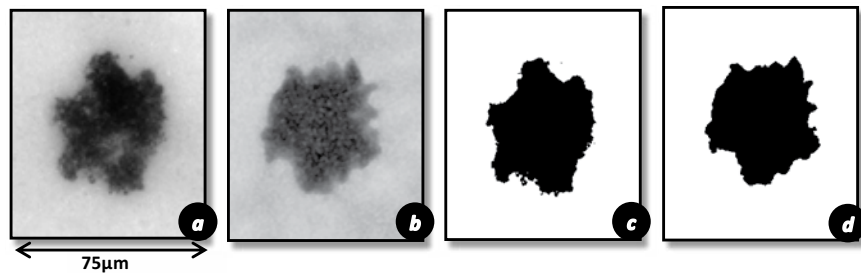


Figure 7 Comparison of the MCI and the SDI at the scale of a single dot. Enlargement of: (a) MCI, (b) SDI, (c) thresholded MCI, (d) thresholded SDI.

### 3.1 Frequency analysis

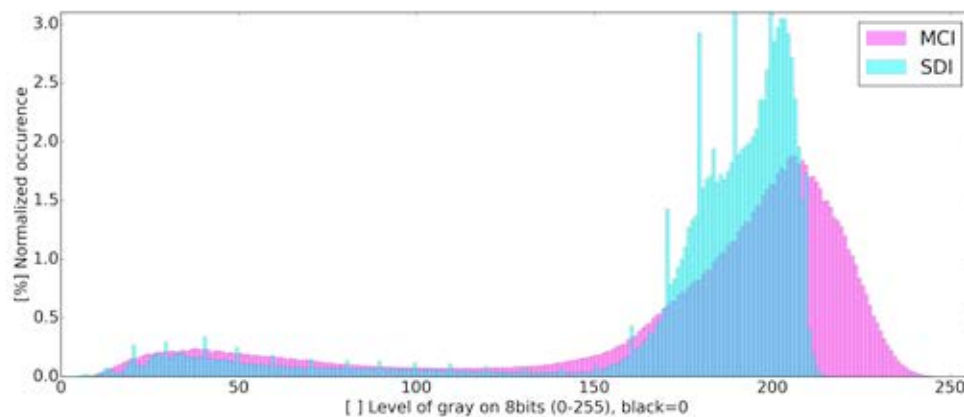


Figure 8: Histograms of the MCI in magenta and of the SDI in cyan.

The frequency analysis (i.e. histogram) allows to determine the gray levels repartition of the pixels. It is interesting to study this property because most thresholding algorithms operate on the histogram. Images that give ideal threshold results show a histogram with two maxima: one located in the low gray levels (i.e. dark areas corresponding to the foreground) and another one located in the high gray levels (i.e. lighter area corresponding to the background). Threshold of this ideal histogram takes place in between these maxima. The results obtained differ from the ideal case, Figure 8, with for MCI and SDI, only one maximum well defined. This shows why thresholding correctly the MCI is difficult. MCI and SDI histograms are similar. The generation simulates then correctly the frequency repartition of the MCI. For both repartitions, maxima are located at the same levels. Let's note that the SDI shows repartitions less similar to Gaussian distributions than the MCI, which can, in some cases, decrease the accuracy of the threshold algorithms. The frequency analyses only rely on global repartition of pixels gray levels, spatial information of pixel is totally ignored. For that reason, a spatial repartition study is required to improve the analysis of the SDI.



### 3.2 Spatial analysis

To conduct a spatial analysis, we first need to threshold MCI and SDI in order to be able to simply compare pixels from one image to another. Thresholds by mean value of the histogram are applied. The threshold level for the MCI is calculated at 105/255 and the SDI at 114/255. The thresholded SDI, called the TDI, and thresholded MCI are then compared with a XOR function modified to take into account separately missing foreground pixels and added foreground pixels. Results are shown in Table 1 and in Figure 9. We can observe, on the TDI, that there is a greater number of missing foreground pixels than added ones: 31.07 % normalized to the number of foreground pixels and 4.32 % normalized to the total number of pixels. As shown on Figure 9, the random parameters of the generation make the comparison dots per dots difficult and it is interesting to introduce indicators. The subtraction of missing and added foreground pixels gives an access to an average differential measurement called DMean. This average indicates the total area difference of dots and is positive if the area is smaller than the reference and negative if the area is larger. A range of misregistered pixels is introduced as well and allows to analyze the total area variation of dots. Finally, the fidelity ratio  $F_{\%}$  is calculated through equation [7] and evaluates the similarity of the dots of the two images. DMean reaches 20.96 % and indicates that the averaged area of dots is smaller on the TDI. The range of misregistered pixels of 41.18 % indicates that the area dispersion of the TDI dots is large compared to the average size of the dots on thresholded SDI. The fidelity ratio  $F_{\%}$  normalized to the number of foreground pixels of the thresholded MCI reaches 65.56 % and respectively 95.21 % when normalized to the total number of pixels, thus we can conclude that the shapes and areas of the TDI dots are globally similar to the reference. Another measure of the spatial similarity investigates the TDI dots centroids misplacements compared to the thresholded MCI centroids. As shown on Figure 10, we can observe that the orientations of the misplacements vectors are distributed in every direction. The eigenvector of the misplacements has a small modulus: 2.4 pixels (i.e. 3.1 % mean misplacement error normalized to the theoretical dot size). This demonstrates that our generation method reproduces globally the spatial distributions of the MCI dots. We conclude that the simulated SDI is spatially similar to the MCI. This analysis relies on the threshold chosen. Coupling spatial and frequency analysis is then the next step to evaluate the SDI.

Table 1: Special XOR to find misregistered pixels on the TDI compared to the thresholded MCI

	Normalized to the number of foreground pixels of thresholded MCI.	Normalized to the total number of pixels.
Added foreground pixels on TDI.	10.11 %	1.41 %
Missing foreground pixels on TDI.	31.07 %	4.32 %
DMean of misregistered pixels on TDI, equation [7].	20.96 %	2.91 %
Range of misregistered pixels on TDI, equation [7].	41.18 %	5.73 %
<b>Fidelity ratio <math>F_{\%}</math> of TDI, equation [7].</b>	<b>65.56 %</b>	<b>95.21 %</b>

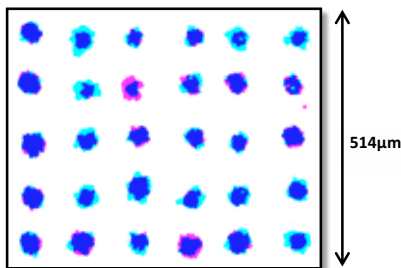


Figure 9: Representation of modified XOR with in cyan the TDI missing foreground pixels, in magenta the TDI added foreground pixels and in blue the shared foreground.

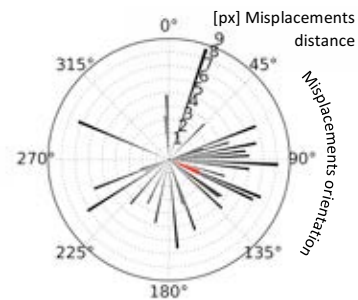


Figure 10: TDI centroids misplacements vectors (MCI reference) in black and eigenvector in red.

### 3.3 Coupled spatial and frequency analysis

Coupled spatial and frequency analysis gives access to misregistered pixels indicators normalized to the total number of pixels in function of the cumulated frequency from 0 to 255. The results are shown in Figure 11. The figure is made less bright on the edges because spatial misregistration is not relevant for small and big threshold values as shown on the two thresholded images of the MCI in Figure 11. We observe on the black curve a plateau of the inverse fidelity ratio going from threshold value 50/255 to 150/255. Minimum of this plateau is found at threshold value of 100, which confirms the choices of threshold for the spatial analysis. Moreover having a plateau implies that thresholds within the plateau interval will result in similar amount of misregistered pixels. We can then conclude that the simulated SDI is stable toward threshold value variations and represent correctly the MCI from frequencial and spatial approaches. The simulated SDI is then relevant and the method can be used to perform threshold evaluation for microscale halftone dots measurements.

$$F_{\%} = 100 - \frac{|DMean| + 2 \cdot Range}{3}; \quad DMean = Mp - Ap; \quad Range = Ap + Mp \quad [7]$$

With  $Ap$ =Added foreground pixels,  $Mp$ =Missing foreground pixels

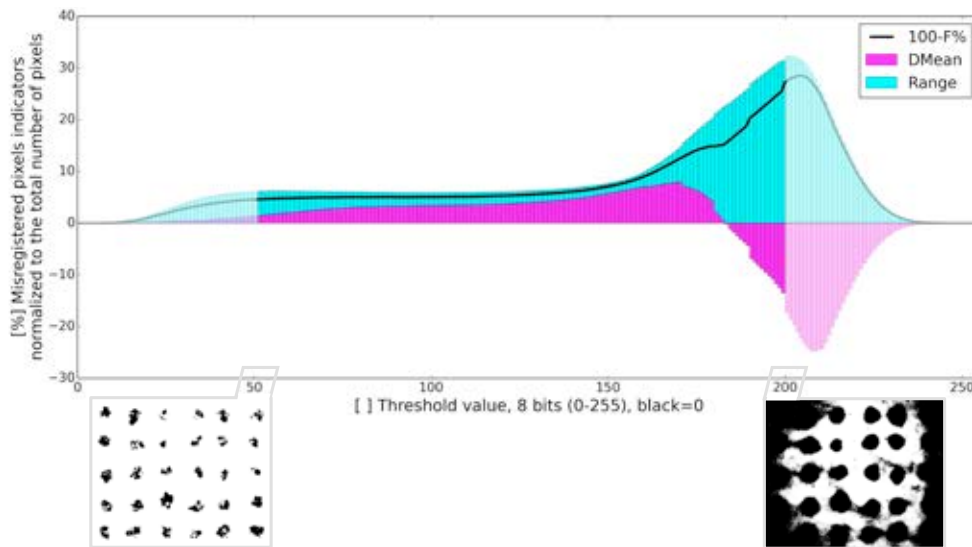


Figure 11: Misregistered pixels indicators normalized to the total number of pixels as a function of the threshold values applied to MCI and SDI and two images of thresholded MCI at threshold values of 50/255 and 200/255.

## 4. Conclusion

The generation method, presented in this work, allowed to generate a grayscale synthetic degraded image. This image was then analyzed to measure the similarity from the microscope captured image. Visual comparison showed that the two images appeared similar. A frequency analysis was conducted and showed that the two image histograms were similar with maxima and minima located at the same levels. The synthetic degraded image shows a repartition less similar to Gaussian distribution. Spatial analysis was investigated after thresholding of both images by mean method. 65.56 % of fidelity ratio  $F_{\%}$  normalized to the number of foreground pixels of the reference was found which showed consequent error from the simulations when comparing single dots. This was explained by the random parameters used in the generation with 41.18 % of missing and added foreground pixel range. 95.21 % of fidelity ratio  $F_{\%}$  normalized to the total number of pixels was found when a global measurement approach was taken. Mean misplacement of centroids was found at  $\pm 3.1$  % of theoretical dots size, which confirmed similarity of dots placement. Coupled spatial and spectral analysis finally showed that the generated synthetic degraded images are stable and behave similarly compared to the reference for thresholding in the 50–150 interval range.

The method developed allowed to obtain reliable synthetic images that reproduce correctly degradation encountered by halftone dots printed on coated paper. As explained, evaluating objectively thresholds algorithms is a necessary step to measure precisely halftone dots characteristics at the microscale. Reliable halftone dots measurements at the microscale allow finally to improve halftone and color models in relation to the print perception and allow progress in advanced printed applications such as product security and authentication to prevent counterfeiting. Another perspective of this work is to reverse the method presented here to develop an improved threshold algorithm specially adapted for printed halftone dots.

### Acknowledgments

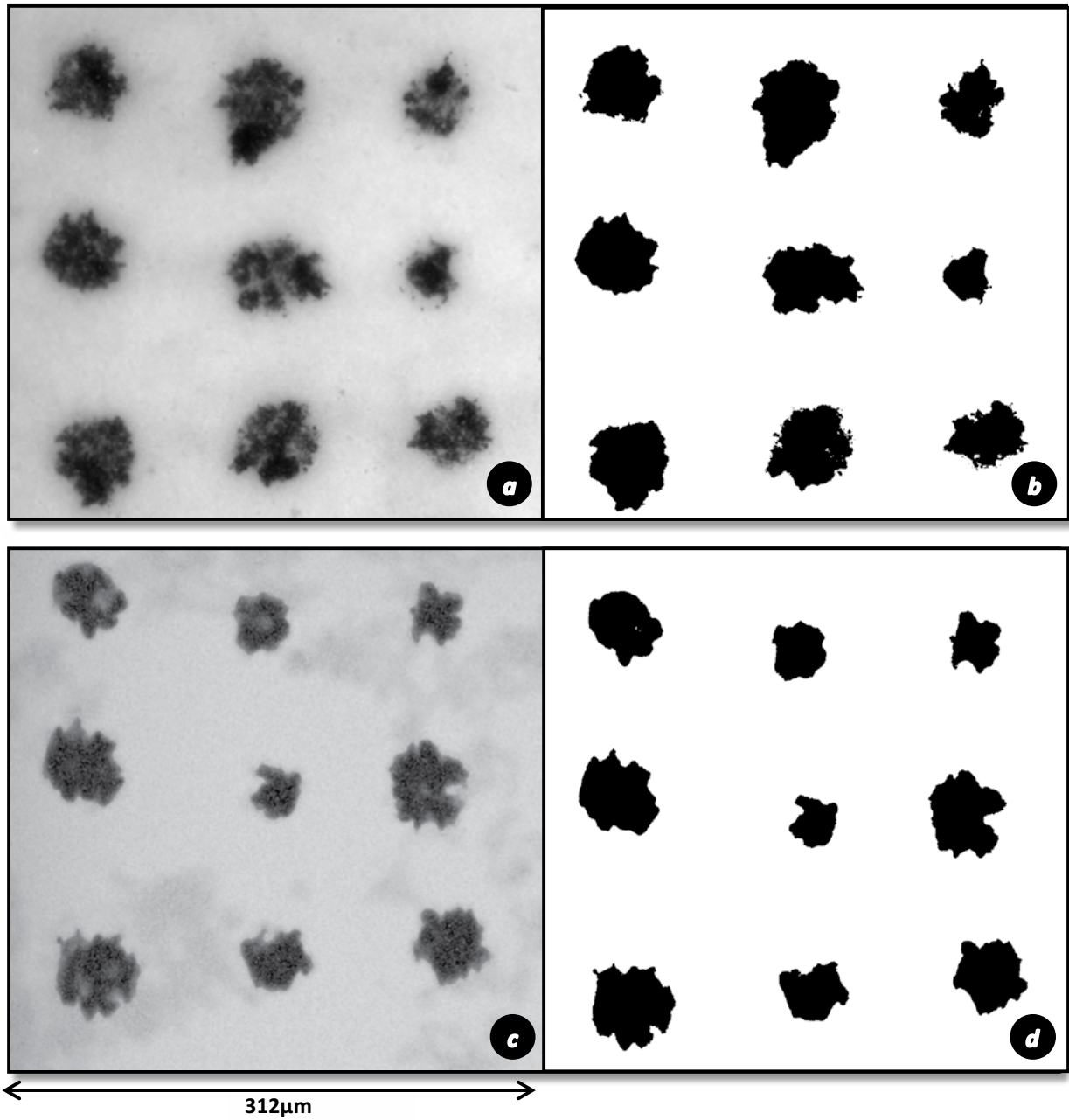
This research was supported by grants from the Agence Nationale pour la Recherche (A.N.R., France – ANR-10-CORD-019), the LabEx Tec 21 (Investissements d’Avenir - grant agreement N° ANR-11-LABX-0030) and of the Énergies du Futur and PolyNat Carnot Institutes (Investissements d’Avenir - grant agreements N° ANR-11-CARN-007-01 and ANR-11-CARN-030-01), TekLiCell platform funded by the Région Rhône-Alpes (ERDF: European regional development fund).

### References

- Cárdenes, R., de Luis-García, R. and Bach-Cuadra, M., 2009. A multidimensional segmentation evaluation for medical image data. *Comput. Methods Programs Biomed.*, 96, pp. 108–124.
- Johnson, B. and Xie, Z., 2011. Unsupervised image segmentation evaluation and refinement using a multi-scale approach. *ISPRS J. Photogramm. Remote Sens.*, 66, pp. 473–483.
- Lau, D.L. and Arce, G.R., 2001. *Modern digital halftoning*. CRC Press.
- Lundström, J. and Verikas, A., 2010. Detecting halftone dots for offset print quality assessment using soft computing. In: *Fuzzy Systems, 2010 IEEE International Conference*, pp. 1–7.
- McGuinness, K. and O’Connor, N.E., 2011. Toward automated evaluation of interactive segmentation. *Comput. Vis. Image Underst.*, 115, pp. 868–884.
- Namedanian, M., 2013. *Characterization of Halftone Prints based on Microscale Image Analysis*. PhD Dissertation. Linköping University Electronic Press.
- Nguyen, T.Q., Delignon, Y., Chagas, L. and Septier, F., 2014. Printer identification from micro-metric scale printing. *Acoustics, Speech and Signal Processing, 2014 IEEE International Conference*, pp. 6236–6239.
- Nyström, D., 2008. *High resolution analysis of halftone prints: a colorimetric and multispectral study*. PhD Dissertation. Linköping University Electronic Press.
- Philipp-Foliguet, S. and Guigues, L., 2008. Multi-scale criteria for the evaluation of image segmentation algorithms. *J. Multimed.*, 3, pp. 42–56.
- Rahaman, G.M.A., Norberg, O. and Edström, P., 2014. Microscale halftone color image analysis: perspective of spectral color prediction modeling. *IS&T/SPIE Electronic Imaging*, pp. 901506–901506.
- Reverdy-Bruas, N., Chagas, L., Poletti, J.-P. and Passas, R., 2015. Image analysis as a tool to discriminate counterfeit from true 2D printed codes. *J. Print Media Technol. Res.*, 4, pp. 205–216.
- Russ, J.C., 2016. *The Image Processing Handbook, Seventh Edition*. CRC Press.
- Sezgin, M., 2004. Survey over image thresholding techniques and quantitative performance evaluation. *J. Electron. Imaging*, 13, pp. 146–168.
- Ukishima, M., 2010. *Prediction and evaluation of color halftone print quality based on microscopic measurement*. PhD Diss. For. Nat. Sci. University of Eastern Finland.
- Wyble, D.R. and Berns, R.S., 2000. A critical review of spectral models applied to binary color printing. *Color Res. Appl.*, 25(1), pp. 4–19.
- Zhang, Y.J., 1996. A survey on evaluation methods for image segmentation. *Pattern Recognit.*, 29, pp. 1335–1346.

**Appendix 1:**

*(a) Microscope captured image of printed halftone dots (MCI), (b) manual threshold of (a), (c) simulation of the MCI by application of synthetic defects, (d) manual threshold of (c).*



## A Case of Beer: A study to determine if the visual design elements of Ontario craft beer packaging communicate their unique flavour profiles

Diana Varma

Ryerson University, Toronto, ON, Canada

E-mail: d7brown@ryerson.ca

### Short Abstract

The North American craft beer industry is expanding at a rapid pace. Revenue growth has been at, or near, the double-digit mark since 2009, while the overall beer industry's sales have remained stagnant. *The Ontario Craft Brewers Association* (OCB) represents over 60 craft breweries across the province of Ontario, declaring the slogan: "Taste. The difference." This research project examines whether or not the unique flavour profiles that differentiate craft beers from their competitors are effectively communicated through the products' packaging, as decoded by target consumers. The current literature on branding, graphic design, and semiotics in the food and beverage industry has not adequately addressed craft beer packaging in this context. This project seeks to address the aspects of visual communication in packaging (typography, colour and imagery) and their effectiveness in connecting to the flavours of Ontario craft beers. Through data gathered by questionnaires distributed to a convenience sample of consumers, this research provides insight to graphic designers and craft beer brand champions as to whether or not their main competitive advantage is effectively communicated. Ultimately, consumers may be able to taste the difference, but this research determines whether or not they are able to see the difference.

**Keywords:** packaging, print, design, typography, semiotics

### 1. Introduction and Background

The *Ontario Craft Brewers Association* (OCB) represents over 60 craft breweries across the province of Ontario and states that: "... it's taste that we're obsessed with, and taste that distinguishes us from other beers, so naturally our slogan is *Taste. The difference*" (Ontario Craft Brewers Association, 2013a). This research examines whether or not the unique flavour profiles that differentiate craft beers from their competitors are communicated effectively to target consumers through the products' packaging.

The North American craft beer industry is expanding at a rapid pace. Revenue growth has been at, or near, the double-digit mark since 2009, while overall beer industry sales have remained stagnant (Koustas, 2012). The craft beer segment continues to grow between 20 %–30 % each year, proving to be fastest area of expansion within the *Liquor Control Board of Ontario's* (LCBO) beer category (Ontario Craft Brewers Association, 2014). The *Ontario Craft Brewers Association* (2013b) defines Ontario craft brewers as small (maximum size of 400,000 hectolitres of total beer production per year), independent (locally-owned and not significantly controlled by a larger company), and traditional (promising to brew innovative beers). Craft breweries' key competitive advantage is small batch brewing resulting in unique tasting notes and creative flavour profiles.

Retailers (namely *The Beer Store* and *LCBO* in Ontario) are embracing the craft beer trend and purchasing product to accommodate the expanded palates of their customers. *The Beer Store* (which is a private

retailer run by three major international breweries) opened up ownership to Ontario craft breweries in January 2015 (Benzie, 2015). The LCBO introduced beer descriptors on their in-store shelf tags and provided supplementary printed material to educate customers on various flavour profiles. In the short printed publication released by the LCBO entitled *Beer World: Tap into the Adventure* (shown in Figure 1), the inside front cover sets the stage for the revolution in craft brewing: “Like wine or whisky, beer is complex. It ranges from light to full, malty to spicy, and everything in between. Knowing about beer styles and tastes is the first step to choosing a beer that you’ll love. So enjoy the variety and tap into the adventure!” (*Beer world: Tap into the adventure*, n.d., p.1). Customers are then presented with a decision tree, encouraging them to use a three-step system: pick the body (mouthfeel, texture, weight), pick the flavour/aroma (malty, roasted, fruity, floral, hoppy, spicy), and the retailer then encourages consumers to find their favourite beer using the body and flavour/aroma descriptors on the in-store shelf tag (i.e. light and fruity) (*Beer world: Tap into the adventure*, n.d.).



Figure 1: Beer decision tree and in-store shelf tag example  
(Beer world: Tap into the adventure, n.d., p.2)

In his book entitled *Synesthetic design: Handbook for a multisensory approach*, Haverkamp (2012) discusses design elements such as colour, typography, and imagery and ways in which they impact olfactory and gustatory sensory modalities. Colour strongly influences perceived smells; therefore colour is an important factor not only in the perception of the beverage product itself, but also the packaging containing the items. Sales are directly affected by the dissonance between expectation and reality of the colour of food and beverage products. Although the perception of colour, smell, and other sensory experiences are unique to individuals, colour systems have been developed, namely a colour circle for scents, created by perfume designer, Karl-Heinz Bork (shown in Figure 2) (Haverkamp, 2012). In the middle of the circle there are four categories of senses described: two cross-sensory (light and heavy) and two that make reference to specific smells (green refers to fresh, while floral notes refers to flowery scents). In studies conducted using this framework, the results are fairly consistent regarding smells associated to specific colours (Haverkamp, 2012).





Figure 2: Circle of scents representing the allocation of characteristic smells to colours  
(Luckner, 2002)

Furthermore, in this study, visual communication will be examined through a semiotic lens (including typography, imagery and colour). The semiotic tradition is most relevant to this topic because it explores sign systems, meanings, and the overall medium to achieve common understanding (therefore clear communication) between individuals (Craig & Muller, 2007). Although the field of semiotics includes words and language, the focus will remain on non-linguistic, visual semiotics. This research is important because distinctive flavour profiles are craft breweries' primary differentiator; therefore this research will be informative to craft brewers, as well as food and beverage marketers in general, to see if their packaging designs (including typography, colours and imagery) communicate unique flavours to target consumers.

## 2. Materials and Methods

The research design method selected for this study was cross-sectional, as it examines a single point in time. This research falls into the discovery paradigm, as the nature of the findings attempt to classify objects and the process will be systematic and repeatable. Furthermore, this study is considered exploratory, as there is currently little research in this area.

Participants in this research study were of legal drinking age when they participated in the study and they were provided with an electronic survey. Surveys were distributed to a convenience sample of friends, family, colleagues, and students within the School of Graphic Communications Management at Ryerson University in Toronto, Ontario. Participants were asked to complete a short survey questionnaire available via *GoogleForms*. A total of 148 respondents completed the questionnaire in its entirety.

Both quantitative and qualitative information was gathered through a questionnaire and participants' answers remained confidential. The questionnaire took under 10 minutes to complete and it was designed in a visually pleasing way to reduce the likelihood of respondent fatigue resulting in non-completion. The questionnaire was comprised of two sections. In the first section, participants were asked questions related to demographics (age and gender), beer purchasing habits, the participant's level of expertise regarding craft beer, as well as questions about what participants believe beer tastes like in general. In the second section, participants were asked about their understanding of the flavours represented in seven craft beer

packaging designs. Participants were asked to select all of the flavours that they felt were communicated through the label displayed from a list of 20 flavours. The flavours on this list were chosen because each one is a flavour contained within one or more of the seven craft beer examples. In this study, participants were then asked two multiple choice questions about the most important visual cue they used to make their flavour choices (fonts, colours, images/graphics, beer name, additional words, other), as well as the least important visual cue they used to make their flavour choices (using the same list as the previous question).

The specific packaging examples used were chosen either because they were seasonal brews or less common craft beers that most consumers would not have seen or tried. The specific examples were also selected because they did not outwardly state the flavour of the beer in their title. Furthermore, these beers were chosen because their flavour profile and tasting notes were available to the researcher, helping to increase the validity of information for this study. A range of craft beer products (all from different Ontario craft brewers) was chosen to provide a more representative sampling of products. Open-ended questions were used sparingly and only for “additional comments”, which allowed the participant to enter free-form text with no character limit. The “additional comments” section was the only part of the questionnaire that was optional to answer.

The list of flavors for each of the seven packaging examples was imported into a word cloud generating site ([www.wordle.net](http://www.wordle.net)) where patterns regarding the most frequently selected flavours began to emerge visually. Word clouds provide graphical representation of the data and are suited to exploratory qualitative analysis, but are also helpful in identifying trends in a closed-format quantitative study where participants are asked to select from a series of keywords (BetterEvaluation, 2014). A consistent typeface and orientation was used for all word clouds in this study, however the colour scheme was modified for each one to best represent the most commonly selected flavours for each packaging example. For instance, for the packaging examples that have “cinnamon” as one of the top flavours selected, a brown color scheme was used to coincide with this popular flavour. This helps to visually communicate the common flavor profiles.

### 3. Results and Discussion

#### 3.1 Results of Two of the Seven Craft Beer Samples with the Most Significant Findings (n = 148)

##### 3.1.1 Beau’s All Natural Brewing Company’s Channel Ocho Mexican Spiced Ale (Figure 3)



*Figure 3: Beau's All Natural Brewing Company's Channel Ocho Mexican Spiced Ale label*  
(Channel Ocho Mexican Spiced Ale, n.d.)





Figure 4: Channel Ocho word cloud of flavours selected by participants

As visually communicated (Figure 4) through the word cloud for *Channel Ocho* craft beer, the most commonly selected correct flavour was chilies with over three-quarters of participants (75.7 %) identifying this flavour correctly. Notably, chipotle was also correctly identified by a large number of participants (63.5 %). Cinnamon was correctly identified by a smaller percentage of participants (29.7 %) and fruit, banana, fig, and cocoa were identified by an even smaller percentage, as each of these four flavours was identified correctly by fewer than 10 % of participants (Figure 5). Ginger, nutmeg, citrus, apple wood, orange peel, and smoke were the most commonly selected incorrect flavours, that do not exist in *Channel Ocho* craft beer.

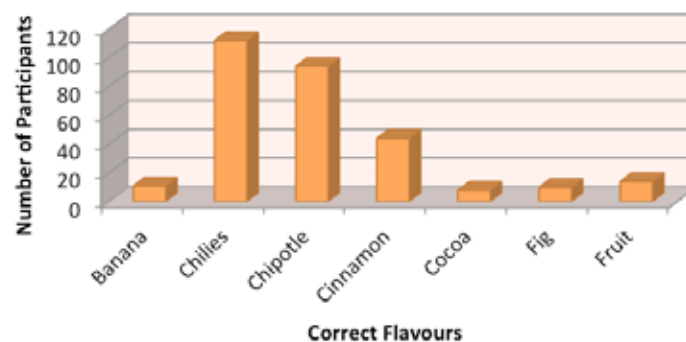


Figure 5: Frequency of participants who selected flavours correctly for Channel Ocho craft beer

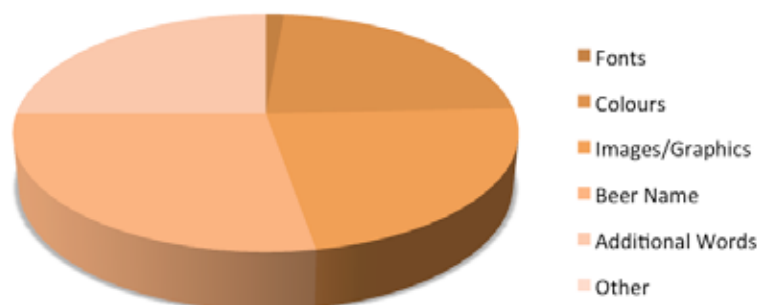


Figure 6: The most important visual cue used to make flavour choices for Channel Ocho craft beer

The distribution of visual elements on the label that participants identified as the most important cue to make flavour choices was fairly even (Figure 6). Colours (23 %), images/graphics (23 %), beer name (27.7 %), and additional words (25 %) on the label were the most common visual cues used to select the flavours in the craft beer.

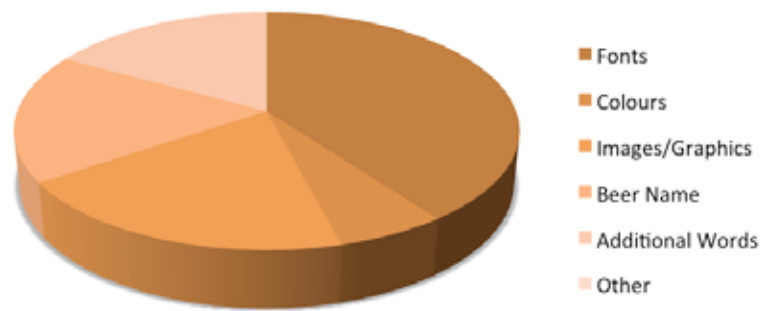


Figure 7: The least important visual cue used to make flavour choices for Channel Ocho craft beer

The least important visual cue (Figure 7) that participants did not use to make flavour choices for this craft beer label was fonts (39.9 %).

### 3.1.2 Railway City Brewing Company's Iron Spike Beer (Figure 8)



Figure 8: Railway City Brewing Company's Iron Spike label  
(Iron Spike, n.d.)



Figure 9: Iron Spike word cloud of flavours selected by participants

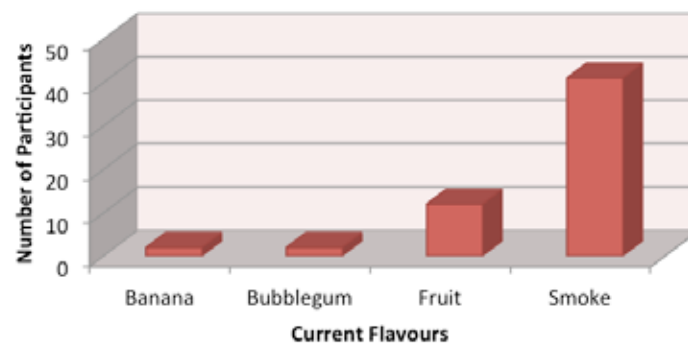


Figure 10: Frequency of participants who selected flavours correctly for Iron Spike craft beer

As visually communicated through the word cloud for *Iron Spike* craft beer, the most commonly selected of the four correct flavours was smoke with approximately one-quarter of participants (27.7 %) identifying this flavour correctly (Figure 9, 10). Fruit was the second most commonly identified correct flavour by 8.1 % of all participants. Banana and bubblegum were the least correctly identified flavours (each identified by only 1.4 % of participants). Cinnamon, caramel, apple wood, and coffee were the most commonly selected incorrect flavours, that do not exist in *Iron Spike* craft beer.

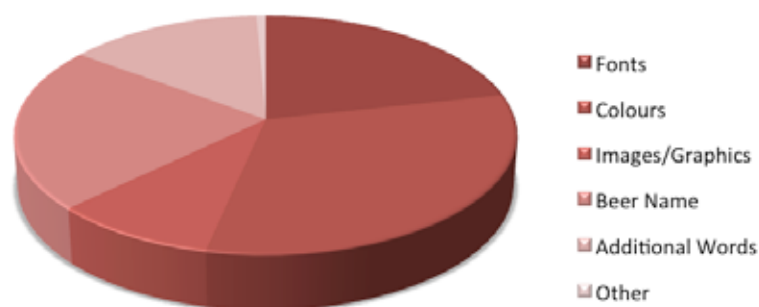


Figure 11: The most important visual cue used to make flavour choices for Iron Spike craft beer

The most important visual cue participants used to make flavour choices (Figure 11) was colours (31.8 %), followed by beer name (22.3 %), fonts (21.6 %), additional words (14.2 %), images/graphics (9.5 %), and other (0.7 %). The one respondent who selected “other” did not enter free-form text.

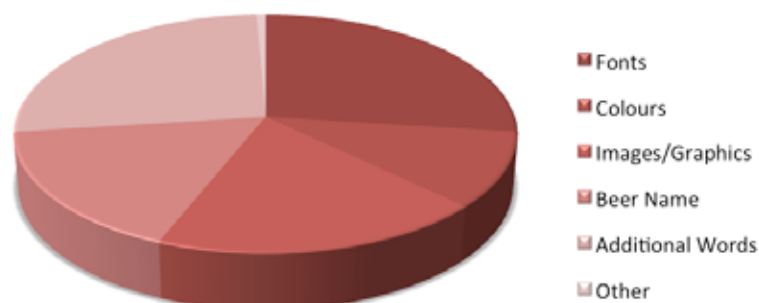


Figure 12: The least important visual cue used to make flavour choices for Iron Spike craft beer

The least important visual cue that participants did not use to make flavour choices (Figure 12) for this craft beer label was fonts (27.0 %), followed by additional words (26.4 %), images/graphics (18.9 %), beer name (16.9 %), colours (10.1 %), and other (0.7 %). The one respondent who selected “other” did not enter free-form text.

### 3.2 Discussion

In analyzing the results, it is clear that identifying flavour correctly based on the visual cues presented on craft beer labels (even when provided with a list to choose from) is very difficult.

There was one main exception where participants had greater success selecting correct flavours, as well as one label where very few participants identified any flavours correctly, which are the two labels explored in the results.

The label examples that were most successful from a flavour identification standpoint was *Beau's All Natural Brewing Company's Channel Ocho* craft beer. This label had the highest percentage of correct responses for any one flavour. Over three-quarters of all participants (75.7 %) identified "chilies" correctly. Interestingly, participants overall did not identify one dominant visual cue as the most important to make flavour choices. In fact, the distribution across the four most frequently selected visual cues was fairly even (colours – 23 %, images/graphics – 23 %, additional words – 25 %, and beer name – 27.7 %). Furthermore, some participants provided qualitative data to help explain their flavour choice, including one participant who stated: "After seeing the word "Mexican Spiced", I started associating Mexican flavours (like chilies, coffee) with the label."

The quantitative and qualitative data for *Channel Ocho* craft beer suggests that it is not just one visual cue that works independently to help identify flavour. The data also suggests that different visual cues work for different people to identify flavour. The different visual cues presented on the label may work together with one another to help the viewer determine what the label is trying to communicate.

Regarding the craft beer that was least successful in communicating specific flavours to consumers (*Railway City's Iron Spike*), almost two-thirds of all participants in the study (63.5 %) identified zero of the four flavours in the craft beer correctly. All participants (100 %) identified two or fewer of the four correct flavours. Some of the flavours in this craft beer were fairly unusual (banana and bubblegum) and a total of 2 participants (1.4 %) identified either of these unusual flavours correctly. These results are logical because there are no visual cues (fonts, colours, images/graphics, beer name, additional words) present on the label to suggest that these flavours would be in this beer. Furthermore, the most important visual cue participants used to make flavour choices was colour (31.8 %), followed by beer name (22.3 %). This supports the results that participants' selected incorrect flavours not present in the beer such as cinnamon, caramel, apple wood, and coffee, which could all be represented by the deep red colour on the label or even through the name "*Iron Spike*".

### 4. Conclusion

The craft beer marketplace is booming, however brand owners have very little formal research available to them about how to communicate key messages through packaging design. Unique flavours are craft brewers' competitive advantage but that doesn't mean that specific flavour nuances are effectively communicated to, or decoded by, consumers. The results of this study showed that it is very difficult to identify specific flavours by examining only the front label of the craft beer product, even when the participant is provided with a list of flavours. However, perhaps it is not through the visual cues on the labels that the unique flavours should be communicated. Instead, by leveraging standardized identification systems already in place (such as in-store shelf tag system used by the *LCBO* in Ontario), flavour can be categorized and communicated to consumers for increased awareness and understanding.

Currently, the *LCBO* uses "beer descriptors" on their in-store shelf tags and they have provided supplementary printed material to educate customers on a variety of standardized flavour categories, as described in

an earlier section of this study. A strong comparison can be made between the colours chosen by the *LCBO* for the six flavour/aroma categories and the “circle of scents” by Karl-Heinz Bork (shown in Figure 2). Below is a chart that describes how these two visual flavour/scent identification systems compare to one another.

*Table 1: LCBO Flavour/Aroma Categories Relative to Bork’s “Circle of Scents”*

<b>LCBO Flavour/Aroma Category</b>	<b>Description of LCBO Flavour/Aroma Category</b>	<b>Colour for LCBO Flavour/Aroma Category</b>	<b>Most Closely Corresponding Scent (and Colour) From Bork’s Chart</b>
Malty	Bread crust, caramel, molasses, chocolate, cereal grains, brown sugar	Gold	Amber (Dark Brown)
Roasted	Coffee, dark chocolate, toasted dark bread, toasted nuts	Dark Brown	Nutty-Dark (Red)
Fruity	Strawberry, plum, pear, ripe banana, orange, lemon, lime	Orange	Fruity-Light (Orange)
Floral	Lavender, white flower, rose petal, spring meadow	Purple/Lilac	Sweet-Aromatic (Pink)
Hoppy	Citrus, grass, herbal, green tea, pine, grapefruit pith, overripe pineapple	Green	Green (Lime Green)
Spicy	Pepper, cinnamon, nutmeg, coriander, ginger, clove	Red	Aromatic-Spicy (Red)

As outlined in the Table 1, four of the six flavour/aroma categories used by the *LBCO* employ the same colours as those depicted in Bork’s “circle of scents” chart when compared to the most closely corresponding category. The remaining two flavour/aroma categories were quite close in colour to those depicted within the “circle of scents”. This consistency is very encouraging and it helps support the idea that colour can be used as a visual indicator to help standardize the communication of flavours and aromas. These colours act as learned sign systems that visually communicate complex beer flavours in an easily understandable format to consumers.

It is in the craft brewers’ best interests to work with retailers (such as the *LCBO* and *The Beer Store* in Ontario) to emphasize, expand, and otherwise more broadly communicate the “beer descriptors” identification system currently used on store shelves by the *LCBO*. Currently, the *LCBO* uses colour to communicate the six flavour/aroma categories in their marketing materials, but they do not use colours on store shelf tags. They only provide the written text of body and flavour/aroma on the in-store tags and do not include the associated colours. The use of colour as a visual cue on the in-store shelf tags would help more effectively communicate flavour to consumers. As the number of craft breweries in Ontario, Canada, and the world increase, these types of standardized flavour identification systems will become more important for both brewers and consumers to aid in a common level of understanding.

## Acknowledgements

Thank you to my project supervisor, Professor Susan Colberg at the University of Alberta, for her guidance, encouragement, and attention to detail throughout the process. Sue, I am extremely lucky to have had the opportunity to work with you and learn from your expertise.

Thank you to the School of Graphic Communications Management at Ryerson University for offering me a wonderful outlet to share what I know with enthusiastic students in the areas of communication, design, and printing technology.

Lastly, thank you to my husband, Adam. I am forever grateful for your on-going support, encouragement, and for listening to me talk about printing and beer far too often.

## References

*Beer world: Tap into the adventure* [Brochure]. (n.d.) Toronto, ON: LCBO.

Benzie, R., 2015. The Beer Store to open up ownership to craft breweries. *The Toronto Star*. Retrieved from: <[http://www.thestar.com/news/queenspark/2015/01/07/the\\_beer\\_store\\_to\\_open\\_up\\_ownership\\_to\\_craft\\_breweries.html](http://www.thestar.com/news/queenspark/2015/01/07/the_beer_store_to_open_up_ownership_to_craft_breweries.html)> [Accessed 7 January 2015].

BetterEvaluation. (2014). *Word cloud*. Retrieved from: <<http://betterevaluation.org/evaluation-options/wordcloud>>.

Craig, R.T. & Muller, H.L., 2007. *Theorizing communication: Readings across traditions*. Thousand Oaks, CA: Sage Publications, Inc.

Haverkamp, M., 2012. *Synesthetic design: Handbook for a multisensory approach*. Basel, Switzerland: Birkhaeuser.

Koustas, A., 2012. *Good time for a beer?* Retrieved from: <<http://www.bmonesbittburns.com/economics/reports/20120815/SR120815.pdf>>.

Luckner, P.E., 2002. Multisensuelles Design [Image]. Retrieved from: <<http://books.google.ca/books?id=NfLTAAAAQBAJ&printsec=frontcover#v=onepage&q=packaging&f=false>>.

Ontario Craft Brewers Association, 2013a. *About the OCB*. Retrieved from: <<http://www.ontariocraftbrewers.com/content.php?nextpage=aboutus>>.

Ontario Craft Brewers Association, 2013b. *Brewing philosophy*. Retrieved from: <<http://www.ontariocraftbrewers.com/content.php?nextpage=brewphilosophy>>.

Ontario Craft Brewers Association, 2014. *Industry fact sheet* [Fact Sheet]. Retrieved from: <[http://www.ontariocraftbrewers.com/pdf/media\\_IndustryFactSheet.pdf](http://www.ontariocraftbrewers.com/pdf/media_IndustryFactSheet.pdf)>.

## Why most Brand Manuals fail when it comes to defining Brand Colors; And how to determine acceptable Color Deviations for specific Brand Colors

*Michael Abildgaard Pedersen*

The Danish School of Media and Journalism (former Graphic Arts Institute of Denmark)  
Department of Media Production and Management, Copenhagen.

E-mail: map@dmjx.dk

### Short Abstract

From top class Universities and governmental organizations to high-end global brands and well-known local brands, a surprising consistency of inattentiveness has been published in these companies' prestigious Brand Manuals and Brand Guides. When it comes to providing technical guidance, defining and describing their Brand Colors, they all fail. By examining and analyzing more than 300 different Brand Colors from 156 Brand Manuals by reputable local and Global Brands including 28 of the 100 Best Global Brands (Interbrand 2015) and by numerous of visits and interviews with responsible professionals from both sides throughout the years it is obvious that there is an alarming lack of communication between technical experts and design experts. 91 % of the Brand Manuals specifies their Brand Colors as either PANTONE or PANTONE C. 90.4 % of the Brand Manuals also specifies their Brand Colors with supplementary CMYK-values even though only 45.8 % of those Brand Colors are achievable by using the process colors CMYK. This will result in unpredicted color differences of up to  $35 \Delta E_{ab}^*$  or  $8.3 \Delta E_{2000}$  when some of those Brand Colors are reproduced. Nevertheless, none of the Brand Manuals has neither any remarks, comments or warnings of color deviations nor indications of acceptable color tolerances. Only 1.3 % of the Brand Manuals also define their Brand Colors with device independent CIELAB-values. It appears that when designers and Brand Owners select and specifies Brand Colors they tend to choose colors which cannot be reproduced by using CMYK process colors and therefore the Brand Color cannot be shown in e.g. magazine ads, newspaper ads, digital print and other print media. They are bound to be disappointed. This Paper will present a practical approach to specifying and communication Brand Colors and to determine acceptable color deviation for specific Brand Colors.

**Keywords:** brand manual, brand color specification, color reproduction, tolerance, graphic design

### 1. Introduction

Brand Owners care deeply about their Brand and their visual identity. They are as committed as they are concerned about how their Brand appears on all types of different media in the society. A Brand should create recognizability in the marked and the Brand Colors symbolize identity, emotions and inner values for that company.

That is why Brand Owners turn to professionals for help when they wish to produce a good and useful Brand Manual. They put all their trust and confidence in the hands of these professionals and the Brand Owners are willing to pay high prices for a useable and professional Brand Manual.

However, it seems that the first priority of the Art Director or the Designer is to produce a pretty and beautiful Brand Book rather than a Brand Manual, which can actually be used as a manual or a guide. In surpris-

ingly many cases the Brand Manuals contains contradictory and absurd information. The responsibility for this rests on the designers (Drew and Meyer, 2006, pp. 147, 193)

Consequently one may wonder what the purpose really is with these Brand Manuals. Is it the intention that the Brand Manual should serve as a nice prestigious tribute to the Brand's visual identity or is it the intention of the Brand Manual that it should actually serve as a MANUAL for future professionals who need to reproduce those Brand Colors?

### 1.1 Ten Reasons why Brand Manuals cause Problems

When a Brand Color has been chosen by the Brand Owner and when an Art Director or Graphic Designer subsequently shall specify and describe this colors' technical specifications in the Brand Manual this will in most cases be done by providing four sets of color specifications as shown in Figure 1.



*Figure 1: A typical description of a Brand Color in a Brand Manual*

However, these simple definitions raise a huge amount of unanswered questions among those professionals who are about to reproduce this Brand Color within their field. Those four color specifications pose more questions and obstructions than helpful guidelines.

For the professional expert who is looking for a precise color recipe or some guidance on how to reproduce this color, this Brand Manual has more the character of an enigmatic book of contradictions than that of a Manual.

Apparently all companies are using the same inexpedient method. All Brand Manuals, Brand Guides, Visual Identity Guidelines and Brand Books are fundamentally designed and structured in the same way, roughly using the same layout and defining and specifying the Brand Colors in the same manner. The design and branding professionals call this "Best Practice".

However, the result is that Brand Colors is being reproduced with unacceptable large color differences while Designers and Brand Owners becomes frustrated and disappointed.

#### 1.1.1 PROBLEM ONE: How are these values derived?

- In none of the Brand Manuals, there is any information on how these color specifications has been generated.
- Since it is typically an Art Director or a Graphic Designer who have read out these values from their Adobe Creative Suite software package then it is crucial to know which Working Space this Art Director have used in his or hers Color Settings.
- The future professionals who shall use this Brand Manual to reproduce this Brand Color must adjust their Working Space and Color Settings to the exact same settings. Otherwise the probability of acceptable color match is minimized. Crucial information on methodology and color management is missing.
- A Brand Manual should contain information on how the displayed values have been found.



### 1.1.2 PROBLEM TWO: Pantone?

- In 91 % of the Brand Manuals, the Brand Color is specified as Pantone Colors. Either as an unspecific Pantone Color (e.g. Pantone 151) or as a Pantone Color specified as printed on gloss Coated paper (Pantone 151 C) or Uncoated paper (Pantone 151 U).
- In 46.2 % of the Brand Manuals, the Brand Color is specified and specifically defined as “C” meaning the way the Brand Color appears on gloss coated paper. This raises questions on how this Brand Color will appear on other substrates like uncoated paper, matte coated paper, plastic foil, textile, corrugated board, metal etc.
- Since it is not possible to obtain a “C color” on a “U paper” or vice versa (Green, 1995) then the Brand Owner will have to accept an unknown color difference if he choose another substrate than coated paper.
- The differences between Pantone 151 C (Coated) and Pantone 151 U (Uncoated) is  $16.7 \Delta E_{ab}^*$  or  $6.4 \Delta E_{2000}$  (according to CIELAB-values from PANTONE Color Manager).
- Will this be regarded as an acceptable color difference for this Brand Color? None of the Brand Manuals has any indications on this issue.
- A Brand Manual should contain information on a Brand Color’s “master values” in CIELAB and comments on acceptable deviation tolerances.

### 1.1.3 PROBLEM THREE: CMYK? – Is this specific Brand Color achievable in CMYK?

- In none of the Brand Manuals, there is any information on whether or not the Brand Colors can be reproduced with an acceptable color match by using the process colors CMYK. However, in 90.4 % of the Brand Manuals specific CMYK values are provided. As shown in Figure 1, the second information tells us that Pantone 151 C can be reproduced by using the CMYK-values: 60 % Magenta + 100 % Yellow.
- Nevertheless, Pantone 151 C is a color, which cannot be reproduced satisfactorily by using the process colors CMYK. This is evidenced by the PANTONE COLOR BRIDGE Coated and in Adobe Creative Suite which gives a gamut warning. If Pantone 151 C is reproduced with the applied CMYK-values from the Brand Manual this would result in a color difference of  $18.6 \Delta E_{ab}^*$  or  $5.5 \Delta E_{2000}$  (according to CIELAB-values from PANTONE Color Manager). So this Brand Color is destined to have a huge color difference if it is reproduced in CMYK. Does the Brand Owner know that?
- Only 45.8 % of the 300 Brand Colors can be achieved by using the process colors CMYK. However, there are no comments on that issue in none of the Brand Manuals. When a Brand Manual display specific CMYK values for a Brand Color this creates an expectation that this Brand Color can be reproduced in CMYK.
- A Brand Manual should contain information on whether or not a Brand Color is achievable in CMYK.

### 1.1.4 PROBLEM FOUR: CMYK? – What kind of CMYK?

- In 90.4 % of the Brand Manuals the Brand Colors is also specified with specific CMYK-values. In addition to the aforementioned example another problem with these CMYK-values is that there is no information on what kind of substrate and print technology this applies to.
- Should the provided CMYK values be understood as if this Brand Color is printed on Gloss Coated paper as Pantone 151 C indicate? And if so, in what kind of print technology is it to be printed? (Sheet fed offset? Web Offset/Heatset? Gravure? Flexo?). The Brand Manuals doesn’t tell. But it is of crucial importance for the outcome. There are as many CMYK’s as there are paper types multiplied with the number of different printing technologies.
- Less than 10 % of the Brand Manuals tries to give some kind of information on this. And in those cases most of them just indicate the same CMYK-values for both Coated and Uncoated paper which makes no sense, unless for example a red Brand Color is specified as 0 100 100 0, which would indicate that screening of this color is not acceptable.

- A Brand Manual should contain information on which print conditions (ICC-profile) the displayed CMYK-values refer to.

#### 1.1.5 PROBLEM FIVE: CMYK? – Why specific CMYK-values?

- Another problem with defining a Brand Color with specific values for C, M, Y and K (like Figure 1; C0, M60, Y100, K0) is that this color only accidentally will be produced with those values – for many reasons.
- It is well known in the Graphic Arts Industry, that if you send the same set of CMYK-combination to different printers and printing presses they would all produce different colors (Sharma, 2004; Adams II, Sharma, and Suffoletto, 2008).
- In a normal Color Managed workflow the Brand Color will be converted by using relevant ICC-profiles with different rendering intents, black generation and tone value increase correction curves. In some cases some sort of Ink Saving processing will also be applied. Thus the CMYK-values will be changed to match the current situation. So, why provide specific CMYK-values?

#### 1.1.6 PROBLEM SIX: Specific CMYK values versus variation tolerances

- According to ISO 12647-2:2013, section 4.3.4.2 the ordinary variation tolerance allows a variation of  $\pm 4$  percentage points. That means that the CMYK values of the intended magenta of 60 % displayed in Figure 1 would be acceptable between 56 % and 64 %.
- The difference between these two extremes will result in a color difference of  $8.6 \Delta E^*_{ab}$ ,  $5.6 \Delta E_{2000}$  and  $7.5 \Delta H^*_{ab}$  (according to CIELAB-values from Adobe Photoshop).
- A Brand Manual should contain information on acceptable variation tolerances.

#### 1.1.7 PROBLEM SEVEN: RGB and Hex Values? – Which Color Space?

- In 81.4 % of the Brand Manuals the Brand Colors is specified with additional RGB values. The Brand Manual's attempt to specify color values for websites, mobile platforms and other screen technologies raises the same unanswered questions. Are the stated RGB-values understood to be sRGB, AdobeRGB, eciRGB, AppleRGB or another RGB? No answer is given. And since the Hexadecimal values are directly connected to the chosen RGB color space, the same questions apply here.
- Since the standard RGB for the Internet is sRGB (Stokes, Chandrasekar and Motta, 1996; IEC, 1999) and since most mobile media displays colors through sRGB, it would be natural to expect that the stated RGB-values is to be understood as sRGB.
- However, since most Art Directors and Graphic Designers work in AdobeRGB and since they are the professionals who have made these Brand Manuals it is more likely that the displayed RGB-values are AdobeRGB. The point is that there is no information on this issue in any of the Brand Manuals. In only 1.3 % of Brand Manuals the Brand Colors is specified as a specific RGB (sRGB).
- A Brand Manual should contain information on which color space the displayed RGB-values refer to.

#### 1.1.8 PROBLEM EIGHT: CIELAB? – Why are there no device-independent values?

- Since all the color code values shown in the Brand Manuals are device-dependent color values it is far too risky to rely on the Brand Manual's Pantone-, RGB, Hex- and CMYK-values unless they are followed by specific information on devices and substrates – which they aren't. Furthermore, less than half of all Brand Colors can be reproduced by using the process colors CMYK and a similar amount of Brand Colors cannot be shown on a sRGB a screen which is a problem since sRGB is the standard for the Internet (Stokes, Chandrasekar and Motta, 1996; IEC, 1999) and most mobile devices.
- A Brand Manual should contain information on device independent CIELAB values for the Brand Color.

### 1.1.9 PROBLEM NINE: Acceptable color deviations?

- In none of the 156 Brand Manuals acceptable deviation tolerances is neither specified nor commented. In spite of all the potential risks of color mismatch described above no guidance on acceptable color difference can be found in any of the Brand Manuals.
- In only two of the 156 Design Manuals (Canon 2015 and Siemens 2008) the Brand Colors was defined with CIELAB-values but not even here were there any indications of acceptable color deviations.
- A Brand Manual should contain information on acceptable deviation tolerances.

### 1.1.10 PROBLEM TEN: The missing Color specifications

- In Figure 1 which represents a typical example of a Brand Manual's Color specifications it is remarkable that the Brand Color only is specified for reproduction on an unknown screen technology and in an unknown print technology using an unknown print substrate.
- In short, the values in Figure 1 only try to meet the needs of the Printer and the Web Designer, even though it fails. There is no color specifications for the use in other industries, technologies or other color systems like RAL, NCS, Textile etc.
- Only 4.5 % of the Brand Manuals provide NCS-values, only 6.4 % provide RAL-values and only 2.6 % of the Brand Manuals provide values for textile.
- A Brand Manual should contain information for other industries, technologies and color systems.
- In the light of all these potential problems it would be relevant to present a proposal on how a useful and professional Brand Manual should specify and communicate Brand Colors and how to determine specific values for acceptable color deviations for each specific Brand Color.

## 2. Methodology

In the search for literature on this subject (*how to specify Brand Colors in a Brand Manual*), the TAGA 2005–2014 Proceedings and the IARIGAI proceedings from the 39<sup>th</sup> to the 42<sup>nd</sup> conferences where consulted. Although it was possible to find some literature that seems relevant for this paper's subject regarding Color Management, Spot Colors and Brand Colors (Chung et al., 2004; Chung, 2005; Chung et al., 2007; Sperry and O'Hara, 2007; Sangmule et al., 2010; Shendye et al., 2011; Seymour, 2013), they all seem to be focusing on subjects that were in the periphery of this paper's subject. However, some useful points and statements from this literature where used.

Other sources on Spot Colors and Brand Colors where consulted (VIGC, 2008; Fogra, 2010; Meittamo, 2010) and so was textbooks aimed for Graphic Arts Designers regarding selecting and specifying colors where conducted (Eisemann, 2000; Drew and Meyer, 2006; Schmidt, 2013).

It has not yet been possible to find any literature that directly describes how to specify Brand Colors in a Brand Manual or how to precisely communicate a color's technical specifications.

Through an Internet research 156 Design Manuals from major recognized Brands where found and downloaded after which 300 Brand Colors were chosen and analyzed.

Throughout this paper Pantone 151 C is used as a representative example of a Brand Color. This Color where chosen because it is out of CMYK gamut like more than half of all Brand Colors examined.

The CMYK-values, RGB-values, Hex-values and CIELAB-values presented in the tables in this paper were found by using PANTONE COLOR BRIDGE Coated (the Plus Series) 2015. After registration of this prod-

uct the PANTONE COLOR MANAGER Software (version 2.1.0.249 for Windows) were downloaded and installed after which the official Pantone CIELAB values from all Pantone Colors were downloaded to Excel.

All calculated  $\Delta H^*_{ab}$ ,  $\Delta E^*_{ab}$  and  $\Delta E^*_{2000}$  values were found by using those official Pantone CIELAB values.

The official iOS apps: “myPANTONE” and “PANTONE X-ref” were used to find corresponding colors from different Pantone Color fan Decks.

The RAL Colors were found through the official RAL COLOUR iOS App “RAL iCOLOURS” while the NCS Color values were found through the online application “NCS NAVIGATOR Premium”.

The color code values from different RGB and CMYK color spaces were found through Adobe Photoshop where the color settings gradually were changed to different RGB and CMYK ICC-profiles using Absolute Colorimetric Rendering Intent and subsequently the CIELAB values for PMS 151C were entered through color picker each time. No measurements have been carried out.

### 3. Results and Discussions

For all existing Brands it applies that they have already chosen their Brand Colors whether they are reproducible or not. But when it's time to produce a new Brand Manual then it is important to initially find the device independent “master values” (CIELAB values) for this specific Brand Color. This can easily be found via Adobe Photoshop, the PANTONE COLOR Manager software or the smartphone app “myPANTONE”. The  $L^*a^*b^*$  details for PANTONE 151C are given in Figure 2.

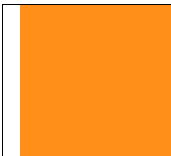
	<b>PANTONE 151 C</b>
	<b>CIELAB:</b>
	$L^*$ 69.68
	$a^*$ 47.28
	$b^*$ 78.51

Figure 2: Specification of a Brand Color's “Master Values”

In principle, a Brand Manual doesn't need to contain much more color specifications than these. However, if the Brand Manual should be helpful to those professionals who are about to reproduce this color within their discipline, within their color system then a Brand Manual should provide much more information.

#### 3.1 Determination of device dependent CMYK values

In Table 1 below five different CMYK value combinations for PMS 151 C is shown for lithographic offset printing on coated paper. This is to illustrate that they are all different and that they only apply to these five print conditions.

Table 1: Five different CMYK interpretations based on the CIELAB values of PMS 151 C

Color Settings: Working Space (Absolut Colorimetric R.I.)	ISO Coated v2 (FOGRA39)	PSO Coated v3 (FOGRA 51)	Euroscale Coated v2	U.S. Web Coated (SWOP) v2	U.S. Sheet fed Coated v2
<b>PANTONE 151 C</b>					
CIELAB $L^*$	69.68	69.68	69.68	69.68	69.68
CIELAB $a^*$	47.28	47.28	47.28	47.28	47.28
CIELAB $b^*$	78.51	78.51	78.51	78.51	78.51
CMYK:	0 56 97 0	0 55 99 0	0 55 96 0	0 54 100 0	0 52 99 0

Color Settings: Working Space (Absolut Colorimetric R.I.)	ISO Coated v2 (FOGRA39)	PSO Coated v3 (FOGRA 51)	Euroscale Coated v2	U.S. Web Coated (SWOP) v2	U.S. Sheet fed Coated v2
CIELAB values for this CMYK combination of PMS151C by using this CMYK profile	64.00 35.00 63.00	64.00 37.00 64.00	63.00 34.00 62.00	62.00 31.00 58.00	64.00 35.00 63.00
Closest CMYK-match to PMS 151 C	$2.8 \Delta H^*_{ab}$ $20.6 \Delta E^*_{ab}$ $7.1 \Delta E_{2000}$	$1.5 \Delta H^*_{ab}$ $18.7 \Delta E^*_{ab}$ $6.0 \Delta E_{2000}$	$3.3 \Delta H^*_{ab}$ $22.2 \Delta E^*_{ab}$ $7.3 \Delta E_{2000}$	$4.0 \Delta H^*_{ab}$ $27.3 \Delta E^*_{ab}$ $8.8 \Delta E_{2000}$	$2.8 \Delta H^*_{ab}$ $20.6 \Delta E^*_{ab}$ $6.4 \Delta E_{2000}$

So, if the Brand Manual should contain specific CMYK values they should be followed by a reference to an ICC-profile. However, any CMYK reproduction of PMS 151 C will still result in a huge color deviation.

### 3.2 Determination of device dependent RGB values

In Table 2 below five different RGB value combinations for PMS 151 C is shown. Also in this case, it is seen that they are all different and that they only apply to one RGB color space (ICC-profile).

Table 2: Five different RGB interpretations based on the CIELAB values of PMS 151 C

Color Settings: Working Space (Absolut Colorimetric R.I.)	AdobeRGB	sRGB	AppleRGB	eciRGB v2	CIE RGB
<b>PANTONE 151 C</b>					
CIELAB $L^*$	69.68	69.68	69.68	69.68	69.68
CIELAB $a^*$	47.28	47.28	47.28	47.28	47.28
CIELAB $b^*$	78.51	78.51	78.51	78.51	78.51
RGB	236 131 23	255 132 0	255 109 0	233 146 43	250 146 57
HTML/Hex #	ec8317	ff8400	ff6d00	e9922b	fa9239
CIELAB values for this RGB combination of PMS 151 C by using this RGB profile	70.00 47.00 79.00	69.00 44.00 75.00	70.00 46.00 73.00	70.00 47.00 79.00	70.00 47.00 80.00
Closest RGB-match to PMS 151 C	$0.5 \Delta H^*_{ab}$ $0.6 \Delta E^*_{ab}$ $0.4 \Delta E_{2000}$	$1.0 \Delta H^*_{ab}$ $4.9 \Delta E^*_{ab}$ $1.2 \Delta E_{2000}$	$1.8 \Delta H^*_{ab}$ $5.7 \Delta E^*_{ab}$ $1.5 \Delta E_{2000}$	$0.5 \Delta H^*_{ab}$ $0.6 \Delta E^*_{ab}$ $0.4 \Delta E_{2000}$	$1.0 \Delta H^*_{ab}$ $1.5 \Delta E^*_{ab}$ $0.6 \Delta E_{2000}$

So, if the Brand Manual should contain specific RGB values they should be followed by a reference to an ICC-profile.

### 3.3 Finding matching colors in other Color Systems

On the basis of the color name “Pantone 151 C” the official Pantone app “PANTONE X-ref” can be used to find corresponding Pantone colors in other Pantone Fan Decks.

On the basis of the CIELAB values of Pantone 151 C the official “RAL iCOLOUR” app can be used to determine the closest RAL color match.

On the basis of the CIELAB values of Pantone 151 C the official online application “NCS NAVIGATOR Premium” can be used to determine the closest NCS color match.

The results can be seen in Table 3 on the following page.

#### 4. Determination of acceptable color deviations

##### 4.1 Closest match within the same process

When measuring Brand Colors and other Spot Colors it is recommendable to use the  $\Delta E_{2000}$  formula since this is created to display a numeric value for the specific color difference that the human eye perceives, independent of the color hue and saturation.

Since there is no official ISO-standard for Brand Colors or Spot Colors and thus no standard for acceptable color deviation tolerances for specific Brand Colors, then the Brand Owner or the Graphic Arts Designer themselves must determine which color deviations can be accepted in each case – for each Brand Color.

However, some of the process standards within the ISO 12647-family specify some informative deviation tolerances. ISO 12647-2:2013 and ISO 12647-3: 2013 specify informative deviation tolerance of  $3.5 \Delta E_{2000}$  for the chromatic solid process colors CMY produced in lithographic offset while ISO 12647-6:2012 specify a variation tolerance of less than  $1.5 \Delta E_{2000}$  for Spot Colors produced in flexographic printing.

It should also be taken into account that the inaccuracy between measuring devices and the differences in paper within the same batch alone can cause a deviation of  $1-2 \Delta E_{ab}^*$  (BVDM, 2003).

Fogra suggests that the uniform deviation tolerance for Spot Colors in offset printing should be  $2.5 \Delta E_{2000}$  (FOGRA, 2010, p. 10).

In Belgium customer demands a maximum  $\Delta E_{ab}^*$  of 2, for quality print jobs (VIGC, 2008).

Thus, based on the above, it should be possible to expect a maximum color difference of  $3 \Delta E_{2000}$  for any Brand Color reproduced within the same process.

##### 4.2 Closest match across substrates and technologies

If the Designer and the Brand Owner only have specified one Brand Color name with no further information and if they expect that this Brand Color is to be reproduced on all substrate types in all reproductive technologies, then the Brand Owner have to accept the closest possible color match between the Brand Color and the chosen substrate and reproduction technology.

In view of the aforementioned studies a method is proposed to determine specific color deviation tolerances for a specific Brand Color.

Table 3: Determination of closest match to the Brand Color Pantone 151 C

	Color Name	CIELAB			Color Differences		
		$L^*$	$a^*$	$b^*$	$\Delta E_{ab}^*$	$\Delta E_{2000}$	$\Delta H_{ab}^*$
PANTONE FORMULA GUIDE Coated	151 C	69.68	47.27	78.51	<b>0</b>	<b>0</b>	<b>0</b>
PANTONE FORMULA GUIDE Uncoated	151 U	72.00	48.07	62.04	16.7	<b>6.4</b>	9.9
PANTONE COLOR BRIDGE Coated	151 CP	67.88	32.91	66.77	18.6	<b>5.5</b>	6.9
PANTONE COLOR BRIDGE Uncoated	151 UP	71.14	30.68	47.58	35.1	<b>8.3</b>	2.2
PANTONE + CMYK Coated	P 24-7 C	66.66	33.70	61.22	22.2	<b>5.6</b>	3.1
PANTONE + CMYK Uncoated	P 17-8 U	69.87	33.02	53.74	28.6	<b>6.4</b>	0.7
PANTONE GoeGuide Coated	13-1-5 C	72.53	44.93	78.49	3.7	<b>2.4</b>	2.0
PANTONE GoeGuide Uncoated	7-1-7 U	74.23	44.39	75.51	6.2	<b>3.6</b>	0.9


	Color Name	CIELAB			Color Differences		
		$L^*$	$a^*$	$b^*$	$\Delta E_{ab}^*$	$\Delta E_{2000}$	$\Delta H_{ab}^*$
PANTONE GoeBridge Coated	13-1-6 CP	64.87	34.15	66.23	18.6	<b>6.1</b>	5.4
PANTONE FASHION+HOME Cotton	15-1263 TCX Autumn Glory	71.60	46.24	76.30	3.1	<b>1.5</b>	0.3
PANTONE FASHION+HOME Nylon Brights	15-1460 TN Orange Clown Fish	74.53	74.18	78.84	27.3	<b>11.8</b>	21.2
PANTONE FASHION+HOME INTERIORS Paper	15-1263 TPX Autumn Glory	71.38	49.05	79.60	2.7	<b>1.4</b>	1.0
RAL Classic For industrial varnish, powder coating and plastics	2003 Pastellorange	64.23	44.09	61.86	17.8	<b>6.6</b>	6.4
NCS For painting	S 0580-Y40R	69.00	43.00	75.00	5.6	<b>1.6</b>	1.9

All color differences are calculated from the CIELAB-values of the reference color Pantone 151 C

## 5. Proposal for future Brand Color specification

Based on the research of this paper the following Brand Color specification guidelines are proposed (Figure 3). This would be useful to most professionals regardless of industry and technology.

[this is ongoing and future work]



**PANTONE 151 C**

**CIELAB:**  $L^*$  69.68  
 $a^*$  47.28  
 $b^*$  78.51

**sRGB** 255 132 0 (Warning out of gamut)

**HTML** #ff8400 (sRGB) Warning out of gamut

**CMYK Coated** 0 55 99 0 (FOGRA51) Gamut Warning

**Textile** 15-1263 TCX

**Interiors** 15-1263 TPX

**RAL** 2003

**NCS** S 0580-Y40R

This Brand Color should be reproduced by using a Pantone 151 spot color printing ink when possible.  
In other cases the following color deviation tolerances apply.

Acceptable deviations when PMS 151C is reproduced

• within the same process (technology and substrate)	3 $\Delta E_{2000}$	(0.0)
• on same substrates (regardless of technology)	3 $\Delta E_{2000}$	(0.0)
• on different substrates	7 $\Delta E_{2000}$	(6.4)
• by using process colors CMYK on coated (CP)	6 $\Delta E_{2000}$	(5.5)
• by using process colors CMYK on uncoated (UP)	9 $\Delta E_{2000}$	(8.3)
• as cotton products	3 $\Delta E_{2000}$	(1.5)
• as nylon products	12 $\Delta E_{2000}$	(11.8)
• as industrial products (RAL)	7 $\Delta E_{2000}$	(6.6)
• as painted surfaces (NCS)	3 $\Delta E_{2000}$	(1.6)

Figure 3: Proposal for future Brand Color specification including acceptable color deviations.

Attention: These values only apply for this specific Brand Color.

All other Brand Colors will have other deviation values.

Values in brackets indicates the calculated values from Table 3

## References

- Adams II, R.M., Sharma, A. and Suffoletto, J.J., 2008. *Color Management Handbook: A Practical Guide*. PIA/GAFT Press.
- BVDM, 2003. *Altona Test Suite – Application Kit*. Wiesbaden: German Printing and Media Industries Federation (bvdm), Print & Media Forum AG.
- Chung, R., Chun, E., Sigg, F., and Costa, T., 2004. *Test Targets 4.0: A Collaborative effort exploring the use of scientific methods for color imaging and process control, RIT Scholar Works 2004*. Rochester Institute of Technology.
- Chung, R., 2005. Color Repeatability of Spot Color Printing. In: *TAGA 2005 Proceedings*, pp. 42–53.
- Chung, R., Hsu, F. and Liu, W., 2007. Achieving Color Agreement: Evaluating the Options. In: *Proceedings of the 34<sup>th</sup> International Research Conference of iarigai, Advances in Printing and Media Technology, September 9–12, 2007*. Grenoble, France. Darmstadt: iarigai.
- Drew, J. and Meyer, S., 2006. *Color Management for Logos – A comprehensive Guide for Graphic Designers*. RotoVision, chapter 7, pp. 147–189.
- Eisemann, L., 2000. *Pantone's Guide to Communicating with Color*. How Books.
- FOGRA, 2010. *Fundamentals for the standardization of spot colours in offset printing: Uwe Bertholdt Fogra Research report no. 32.158*. Fogra.
- Green, P., 1995. *Understanding Digital Color*. Graphic Arts Technical Foundation.
- IEC, 1999. *International Electrotechnical Commission IEC 61966-2-1:1999. Multimedia systems and equipment Colour measurement and management – Part 2-1: Colour management - Default RGB colour space – sRGB*.
- Interbrand, 2015. *Best Global Brands 2015: Creating and managing brand value*. [online] Interbrand. Available at: <<http://interbrand.com/best-brands/best-global-brands/2015/ranking/>>.
- ISO 12647-2:2013 *Graphic technology — Process control for the production of halftone colour separations, proof and production prints Part 2: Offset lithographic processes*.
- ISO 12647-3:2013 *Graphic technology — Process control for the production of halftone colour separations, proof and production prints Part 3: Coldset offset lithography on newsprint*.
- ISO 12647-6:2012 *Graphic technology — Process control for the production of halftone colour separations, proof and production prints Part 6: Flexographic printing*.
- Meittamo, M., 2010. *Colour Management of the Brand Colour*. Helsinki Metropolia University of Applied Sciences, Degree Programme in Media Technology. Final Year Project.
- Sangmule, S.L., Lovell, V., Pekarovicova, A. and Fleming, P.D., 2010. Digital Proofing of Spot Colors for Flexo Packaging. In: *TAGA 2010 Proceedings*, pp. 445–460.
- Schmidt, K.W., 2013. *CMYK GUIDE Composing Colors*. Copenhagen: Grafisk Kommunikation ApS.
- Seymour, J., 2013. Evaluation of Reference Materials for Standardization of Spectrophotometers. In: *TAGA 2013 Proceedings*, pp. 355–379.
- Sharma, A., 2004. *Understanding Color Management*. Thomson Delmar Learning.
- Shendye, A., Fleming, P.D., Pekarovicova, A. and Deshpande, K., 2011. Study of Visual-Instrumental Agreement in Different Color Spaces for Colors Close to Boundary of Quadrants in CIEL\*a\*b\* Color Space. In: *TAGA 2011 Proceedings*, pp. 187–199.
- Sperry, J. and O'Hara, L., 2007. An Evaluation of Generic Output Profiles for n-Color Printing. In: *TAGA 2007 Proceedings*, pp. 257–263.
- Stokes, M., Chandrasekar, S. and Motta, R., 1996. *A Standard Default Color Space for the Internet – sRGB, Version 1.10*. [online] The World Wide Web Consortium (W3C), Available at: <<http://www.w3.org/Graphics/Color/sRGB.html>>.
- VIGC, 2008. *Study on spectrophotometers reveals: instrument accuracy can be a nightmare*, Turnhout, Belgium: VIGC (Vlaams Innocatiecentrum voor Grafische Communicatie, Flemish Innovation Center for Graphic Communication).



## Influence of drying temperature on inkjet printed droplets and lines morphology by using silver nanoparticles based ink: relation with electrical performances

Vincent Faure<sup>1,2,3,4,5</sup>, Aurore Denneulin<sup>1,2,3</sup>, Yahya Rharbi<sup>4,5</sup>, Albert Magnin<sup>4,5</sup>, Anne Blayo<sup>1,2,3</sup>

<sup>1</sup> Univ. Grenoble Alpes, LGP2, F-38000 Grenoble, France

<sup>2</sup> CNRS, LGP2, F-38000 Grenoble, France

<sup>3</sup> Agefpi, LGP2, F-38000 Grenoble, France

<sup>4</sup> Univ. Grenoble Alpes, LRP, F-38000 Grenoble, France

<sup>5</sup> CNRS, LRP, F-38000 Grenoble, France

E-mail: vincent.faure@lgp2@grenoble-inp.fr; anne.blayo@pagora.grenoble-inp.fr

### Short Abstract

For several years, printed electronics have been a creative sector with the printing of numerous electrical devices such as transistors, capacitors, diodes, transistors, lightings, solar panels, memories, etc. In order to ensure the electrical connection of these different electronic components, the printing of conductive tracks with low resistances and homogeneous properties is essential. Thanks to its main advantages, inkjet printing process was identified as a relevant technology to print these conductive tracks. Indeed, inkjet printing is a direct writing process which offers the possibility to produce fine elements on a large variety of substrate. However, with inkjet process, the printing pattern morphology, i.e. the transversal profile of the printed tracks still remains an important issue to consider. Indeed, it is well-known that the different flows that may arise during the drying phase (Coffee-ring effect, Marangoni ... etc.) can lead to inhomogeneous profile and affect strongly the electrical conductance of the printing patterns. In this work, the piezoelectric inkjet printing of individual droplets and fine lines was performed by using a commercially silver nanoparticles ink.

To complete an accurate printing, the ink compatibility with the inkjet printing requirements was checked thanks to a dimensionless analysis. A set of measures based on four geometrical indexes was defined to precisely characterize the particles distribution within dried printed droplets and lines. The droplet profile variations were monitored over different substrate temperatures. Correlations between droplet profile, line profile and resulting electrical conductance are proposed in the discussion part of this paper. Up to our knowledge, it is the first time that such analysis was conducted with a silver conductive inkjet ink at a picoliter scale.

**Keywords:** printed electronics, silver nanoparticles, inkjet printing process, droplets morphology, conductive tracks

### 1. Introduction and background

Within the last 15 years, printed electronics appears as an attractive growing sector. The main benefits of printed electronics are: (i) the possibility to implement flexible substrates, (ii) the promise to achieve high productivity level with large area production and (iii) the reduction of production costs. Nowadays, numerous electrical devices can be printed: capacitors (Chang et al., 2014), diodes (Heljo et al., 2013), transistors, lightings, solar panels, memories (Singh et al., 2010), etc. In order to ensure the electrical connection of these different devices, the printing of conductive tracks with low resistances and homogeneous properties are crucial. Among printing processes, inkjet printing was identified as a promising and relevant technology for printed electronics. It is a non-contact and direct writing process, with a large variety of printable substrates and the capacity to reproduce fine elements. Regarding inkjet printing process, three

phases need to be finely controlled to allow the production of precise and homogeneous patterns: (i) the droplet ejection, (ii) the droplet impact on the substrate and (iii) the drying phase (Derby, 2010). For each phase, process parameters, ink physico-chemical properties and substrate properties are crucial criteria to consider. Up to now, conductive inkjet inks based on silver nanoparticles are those which provide the highest electrical conductivity, which explains their large implementation. However, like any colloidal suspensions, silver nanoparticle inks are prone to “coffee-ring” effect. This effect results of flows occurring within the droplets during the drying phase: particles move from the center to the edge of the droplet resulting in a non-homogeneous profile of drying droplets. This phenomenon is largely reported in literature at a microliter scale but very few data are available on the inkjet printing scale (i.e. the picoliter) and this is particularly true regarding conductive ink materials. This effect is all the more important to explore with conductive patterns as the resulting non-homogeneous repartition of conductive material within the printed pattern may have a strong impact on electrical performances. According to literature on microliter droplets, several options can be suggested to reduce or eliminate the coffee ring effect: Lim et al. proposed the addition in the ink of a co-solvent presenting a lower evaporation rate than the main solvent (Lim et al., 2008). Hendarto et al. proposed a temperature substrate conditioning in order to take profit of the influence of temperature on coffee ring effect (Hendarto and Gianchandani, 2013; Hu and Larson, 2005; 2006). The latter technique will be explored in the present paper through the following strategy:

- (i) the first part of the study will focus on the morphology analysis of independent droplets inkjet-printed on a polymer film conditioned at different temperatures. Droplet morphologies will be characterized thanks to a set of four geometrical indexes specifically defined for this study;
- (ii) The second part of the study will deal with the printing of fine conductive lines (composed of successive printed droplets) in order to emphasize correlations between their main characteristics (morphology, print quality, electrical conductance, etc.) and their related droplet profiles.

## 2. Materials and Methods

### 2.1 Silver nanoparticles inkjet ink and printing process

A commercially available silver nanoparticle inkjet inks (Tradename: Sicrys™ I30G-1) was purchased from PvnanoCell Ltd. The ink is composed of ethylene glycol as solvent and contains spherical silver nanoparticles as conductive fillers (30 % wt, D50 = 70 nm, D90 = 115 nm, density = 1.81 g.cm<sup>-3</sup>). It consists in a light grey suspension which presents a nearly Newtonian behavior with a viscosity of 26.3 mPa·s (corresponding to a shear rate of 1 s<sup>-1</sup>) and a surface tension of 46.3 mN·m<sup>-1</sup> at 20 °C. The ink was agitated on a roller apparatus during one hour and then filtered through a 0.45 µm syringe filter before printing.

A laboratory piezoelectric inkjet printing machine (Fujifilm – Dimatix DMP 2831 with 10 pL nominal drop size cartridge) was used for this study. It allows the loading of disposable piezoelectric inkjet print heads including 16 nozzles measuring 21,5 µm each (square shape) and distanced at 254 µm from each other. Printing parameters such as drop spacing, nozzle temperature and print height, as well as ejection parameters (voltage and waveform design) were optimized in preliminary adjustments. The resulting print quality is strongly dependent on those printing parameters given in Table 1. In order to achieve comparable line profile, lines with one drop width were printed with a unique active nozzle whereas lines with two drops width were printed with two active nozzles. Therefore, the time needed to print a pattern remains equivalent whatever the line width. To print lines, the drop spacing was set at 20 µm (distance between two subsequent droplet centers, see Figure 1). As the average droplet diameter after printing on the substrate was estimated by microscopy observation to 40 µm, an overlapping of droplets occurs, as illustrated in Figure 1.

A substrate matching the typical requirements of printed electronics, i.e. a substrate presenting a smooth and closed surface with a relatively high dimensional stability over temperature was selected for this study. A polyethylene naphthalate (PEN) film (tradename: TEONEX - 125 from Dupont Teijin Film. The selected substrate has a surface energy of  $40.2 \text{ mJ}\cdot\text{m}^{-2}$ , an average surface roughness  $R_a$  of 4.3 nm and a coefficient of dimensional stability of 0.09 % at 150 °C.

A specific drying protocol was established to allow the monitoring of droplet profile over drying conditions: (i) first, the substrate was heated thanks to a Peltier plate from 30 to 120 °C during 20 minutes. (ii) Droplets were then ejected according to the parameters described in Table 1. (iii) Samples were maintained after printing on the Peltier plate during 20 min. This time scale was determined to be sufficient to allow the suspended particles movement induced by the drying flows. The complete drying of the droplet was checked thanks to an ‘absorption method’: a blotting paper was applied onto the printed droplets during a few seconds to check the drying progress (if ink traces appear on the wipe, the sample was considered as partially dried whereas a clean wipe indicates a sample completely dried). (iv) Printed substrates were put in an oven at 120 °C during 1 hour in order to ensure a through drying of the printed droplets.

For conductive printed lines, a first set of experiments were performed with a protocol similar to the droplet one in order to identify potential correlations between printed droplet and line morphologies. A second set of experimentation was performed by modifying the fourth step of the protocol: the oven temperature was increased to 150 °C during 1 hour in order to ensure the silver nanoparticles sintering and to minimize the impact induced by the substrate temperature conditioning (protocol phase (i) and (iii)) on the resulting conductance.

*Table 1: Inkjet printing and drying parameters*

Voltage applied	20 V
Inkjet head temperature	35 °C
Substrate (Peltier plate) temperature	30 °C to 120 °C
Gap between two droplets for lines printing	20 $\mu\text{m}$
Drying protocol for droplets	20 minutes on the Peltier plate + 1 hour at 120 °C in an oven
Drying protocol for lines	20 minutes on the Peltier plate + 1 hour at 150 °C in an oven

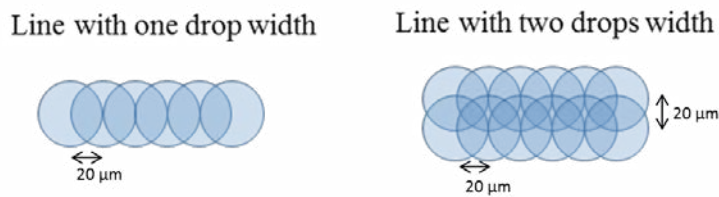


*Figure 1: Overlapping of droplets composing a line with one and two drops width*

## 2.2 Morphological characterization of droplets

3D profile of independent droplets and lines were obtained with a focus variation optical microscope (Alicona InfiniteFocus). 3D data were collected by using a focus variation microscopy technology illuminated with a specular reflection lighting mode. To visualize the morphology of printed patterns, a magnification of  $100\times$  was selected for independent droplets whereas magnifications of  $20\times$  and  $50\times$  were sufficient for printed lines. With the focus variation technology, it is very difficult to achieve relevant 3D mapping with transparent and bright surfaces. In order to overcome undesired optical reflections, gold or

carbon metallizations were performed on the printing samples in order to opacify their surface and therefore allow the 3D data capture.

To characterize and compare droplet profiles, four indexes were specifically defined for this study:

(i)  $R_{c/e}$  was defined as the amplitude ratio between the droplet center and edge.  $R_{c/e} = 100 \cdot \frac{h_c}{h_e}$  with  $h_c$  the height at the center of the drop and  $h_e$  the height at the drop edge (Cf. Figure 2a). For each drying configuration,  $R_{c/e}$  was averaged on twenty profiles (five droplets with four different profiles).

(ii)  $R_{0.5}$  was defined as the radial distance delimitating a distribution of 50 % of material.  $R_{0.5}$  corresponds to the position from the droplet center where there is the same quantity of matter before and after this position. For each characterized droplet, the  $R_{0.5}$  index was averaged on thirty-six droplet profiles captured every  $10^\circ$ . Each droplet profile was normalized so that the center of the drop became the origin and the droplet radius was equal to 1. A Matlab program was developed to determine the radial position corresponding to the half of the profile area (Cf. Figure 2b).

(iii)  $S_a$ , which corresponds to an average arithmetic height, was defined as the droplet internal surface roughness (Cf. Figure 2c1 and 2c2).  $S_a$  represents the average height delimitating an equal repartition of matter above and below it.

(iv)  $S_{max}$  corresponds to the maximum profile height (Cf. Figure 2c1 and 2c2).  $S_{max}$  is the difference between the higher and the lower height of the droplet 3D profile.

$S_{max}$  and  $S_a$  were both calculated on the droplet internal surface (area delimited by the droplet crown – Cf. Figure 2c1 and 2c2) by using the Alicona InfiniteFocus software.

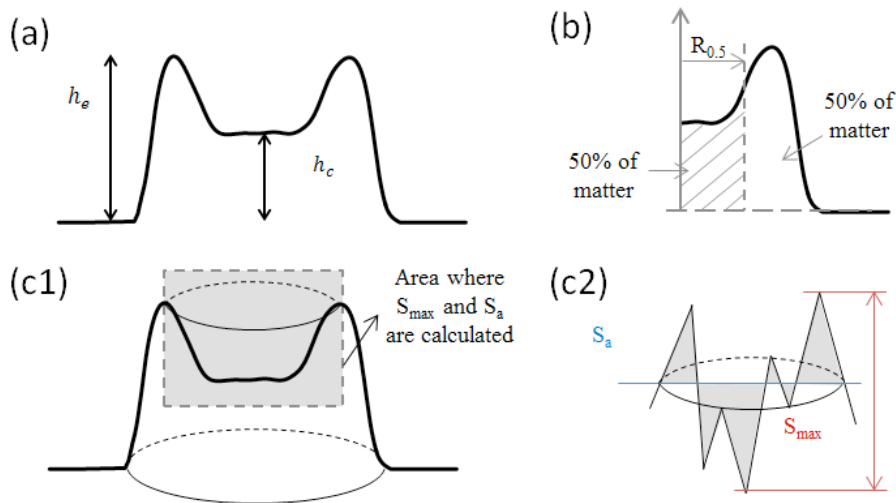


Figure 2: Schematic representation of geometrical indexes: (a) Ratio center/side, (b)  $R_{0.5}$ , (c1 and c2)  $S_{max}$  and  $S_a$

### 2.3 Electrical characterization of tracks

The electrical resistance ( $R$ ) of conductive lines was measured by using a multimeter (Hewlett Packard 34401A). Measurements were performed on conductive tracks having a length of 1 cm. The measured resistance corresponds therefore directly to a linear resistance expressed in  $\Omega \cdot \text{cm}^{-1}$ . In this study, the conductance which corresponds to the inverse of the resistance ( $G = 1/R$ ) was implemented. Considering the following formula  $G = \sigma \cdot \frac{S}{l}$  with  $\sigma$  the conductivity of dried ink,  $S$  the cross-sectional area of the track and  $l$  the length of the track, it is interesting to see that  $G$  is proportional to the cross section of conductive tracks.

### 3. Results and discussion

#### 3.1 Droplet ink-jettability

To achieve a high level of print quality, the ink properties associated to the process characteristics must fulfil the Derby jettability requirements (Derby, 2010). In piezoelectric inkjet printing process, the ink droplet is ejected thanks to a pressure wave based on electromechanically impulsions induced by the piezoelectric element. The ink is jetted only if its kinetic energy overcomes interactions linked to surface energy and viscous forces. Both conditions are formulated through a dimensionless analysis using Reynolds and Weber number defined in equation (1) and (2).

$$\text{Reynolds : } Re = \frac{\rho v d}{\eta} = \frac{\text{Inertial effects}}{\text{Viscous effects}} \quad [1]$$

$$\text{Weber : } We = \frac{\rho v^2 d}{\gamma} = \frac{\text{Inertial effects}}{\text{Capillary effects}} \quad [2]$$

where  $d$  is the nozzle diameter (m),  $v$  is its velocity (m/s),  $\rho$  is the ink density (kg/m<sup>3</sup>),  $\gamma$  is the surface tension of the liquid (N · m<sup>-1</sup>) and  $\eta$  is the dynamic viscosity of the ink (Pa · s).  $We$  number describes the kinetic-surface energy conversion governed by the speed of the jet and the surface tension.  $Re$  number takes into account the viscosity effects. An approach combining these two dimensionless numbers was firstly proposed by Fromm (Fromm, 1984) in which fluid properties are described by the  $Z$  number which is the inverse of Ohnesorge number ( $Oh$ ).  $Oh$  characterizes the propagation of the pressure wave and its attenuation by viscous dissipation.

$$\text{Ohnesorge : } Oh = \frac{\sqrt{We}}{Re} = \frac{\eta}{\sqrt{\rho \gamma d}} = \frac{1}{Z} = \frac{\text{Viscous effects}}{\sqrt{\text{Inertial effects}} \sqrt{\text{Capillary effects}}} \quad [3]$$

As predicted by Fromm, the drop formation in a DOD inkjet printer is possible only for  $Z > 2$ . Reis et al. (2005) refined this prediction and found that the processability of an inkjet ink is given for  $1 < Z < 10$ .  $Z > 10$  corresponds to a situation where droplet formation is improbable or subjected to satellite drops formation. Jang et al. (2009) considered additional characteristics of printing, including droplet generation and position accuracy, and found the printable range as  $4 \leq Z \leq 14$ . Printing using an ink with  $Z < 4$  will lead to a droplet formation with a long-lived filament, resulting in degradation of the position accuracy and printing resolution. Inks with  $Z > 14$  are also inappropriate for inkjet printing because of their inability to form a single droplet without the formation of undesired satellites. However, even with  $Z$  comprised in the right range, the jettability is not guaranteed. Derby (2010) highlighted that drop formation is impossible for a fluid with a  $We < 4$  because the inkjet process does not supply enough energy to overcome surface interactions in the fluid. In the same way, droplets splash the substrate if they are ejected with an excess of energy. For this condition, Derby used the work of Stow and Hadfield (1980) and Bhola and Chandra (1999) and defined a criteria which avoids the splashing:  $We^{1/2} Re^{1/4} < 50$ .

Depending on the voltage applied to the piezoelectric element of the inkjet print head,  $Re$ ,  $We$  and  $Z$  were calculated for the ink selected in the present study. Ink characteristics, as well as calculated dimensionless numbers were resumed in Table 2. The jettability window covered by the selected ink was drawn in Figure 3. It emphasizes that the selected ink fulfills all the requirements to achieve a stable and accurate printing.

Table 2: Calculated dimensionless numbers (Reynolds, Weber and Z) corresponding to the implemented system at different voltage values

Voltage	Re	We	Z
30 V	5.7	5.8	2.4
35 V	11.9	22.8	2.5

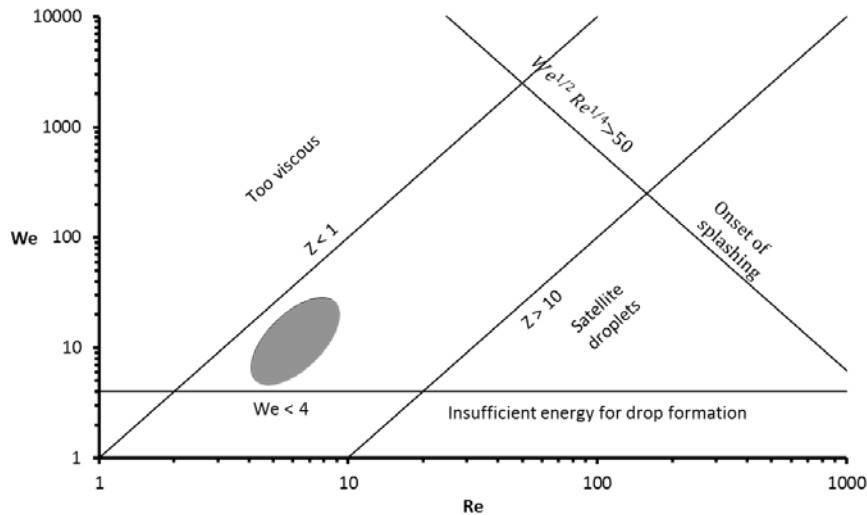


Figure 3: Jettability windows defined by Derby (2010), where the grey area emphasizes the jettability window covered the system implemented in this study (Ink: Sycris I30EG-1, PvnanoCell / Printed: Dimatix DPM 2800)

### 3.2 Influence of substrate temperature on droplet profile

Inkjet printing is constituted of four phases: ejection, impact, spreading and drying. During the last phase, silver nanoparticles contained in the ink move inside the droplet. At the end of drying, most particles are accumulated at the periphery of the deposit. This effect called *coffee ring* was first described by Deegan et al. (1997). It is induced by the combination of two phenomena: (i) solvent evaporation is more important at the edge of drops and (ii) the surface contact area between ink and substrate is pinned for the major part of the drying. A flow takes place to compensate the solvent removal by evaporation at the edge of droplet. The solvent can be totally or partially transferred to the contact line by this flow and thus generate a ring shape to the dried droplet. The *coffee ring* effect can be reduced by heating the substrate in order to generate a temperature gradient, which induces particle recirculation (Hendarto and Gianchandani, 2013). 2D and 3D profiles of independent droplets dried at different temperature are shown Figure 4. Variations in silver particles distribution as a function of printed substrate temperatures are observed. For each drying conditions, diameter and volume of dried droplets were measured and are presented in Figure 4. A deviation of 10 % and 20 % was respectively recorded for diameter and for volumes. These deviations remain relatively low and may be acceptable in the framework of our study (microliter and picoliter scale). Figure 4 emphasizes that the coffee ring effect occurs for all studied temperatures. With substrate temperature rising from 30 °C to 60 °C, the crown shape induced by the coffee ring becomes more and more accentuated. For these temperature levels, most of particles are located at the droplet edge while a very fine thickness of particles remains in the droplet center area. From 60 °C to 90 °C, the droplet edge height decreases from approximately 40 % (from 830 nm to 540 nm) whereas the center height remains relatively stable (from 110 nm to 120 nm). Over 100 °C, the droplet edges thicken and the internal droplet surface revealed a stressed relief.

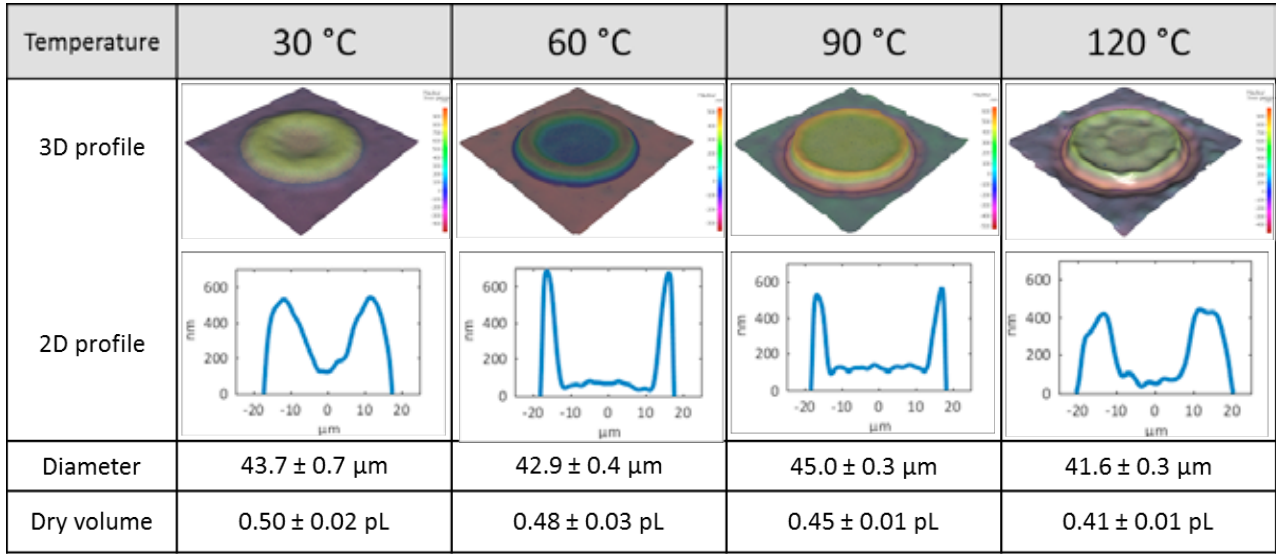


Figure 4: 3D and 2D profiles printed droplets on PEN at different substrate temperatures; 2D profiles are one of the numerous profile constituent droplets in this temperature; the diameter of the dry drop and its volume are noticed under the profiles.

Different indexes were defined to characterize precisely and compare the particle distribution within the different printed droplets. As droplet profiles are ring-shaped, the ratio between the heights at the droplet center and edge  $R_{c/e}$  appears relevant for quantify coffee ring effect. The evolution of  $R_{c/e}$  as a function of substrate temperature is shown on Figure 5a. Theoretically, the closer the index gets to 100 %, more the repartition of nanoparticles within the droplet became homogeneous. As expected in comparison with 3D droplet profiles,  $R_{c/e}$  decreases between 30 °C and 50 °C and rises for temperature ranging from 50 °C to 90 °C. As emphasized on figure 4, particles repartition seems to be more homogeneous for temperature superior to 90 °C. However,  $R_{c/e}$  does not allow identifying this trend. Indeed,  $R_{c/e}$  does not take into account the droplet edge thickening.  $R_{c/e}$  alone is inadequate to qualify the droplet morphology.  $R_{0.5}$ , which corresponds to the radial distance delimitating a distribution of 50 % of material, was then used to take into account the droplet edge thickening. Theoretically,  $R_{0.5}$  value approximate 100 % when all particles are located at the droplet edge and 0 % when all particles are located at the droplet center. The evolution of  $R_{0.5}$  with the substrate temperature is given in Figure 5b. The graph reveals profiles with high particles concentration at the droplet edge for temperature comprised between 50 °C and 70 °C, which corresponds to a  $R_{0.5}$  index superior to 70 %. The graph allows to reflect with a relative accuracy the observations made on the droplets 3D mapping. The  $R_{0.5}$  index appears therefore as a relevant index to quantify the coffee-ring effect but information about surface morphology is missing. Indeed, no distinction between the profile obtained at 30 °C and 120 °C, which show different droplet profiles but similar  $R_{0.5}$  index, is possible. In order to complete the information supplied by the  $R_{c/e}$  and  $R_{0.5}$  indexes, a combination with indexes relating to the internal droplet surface roughness was envisaged. The evolution of  $S_{\text{max}}$  and  $S_a$  over temperature is represented in Figure 5c–d. Finally,  $R_{c/e}$  and  $S_{\text{max}}$  appear to be complementary indexes to describe the vertical particles repartition. For example, droplet profiles at 90 °C and 120 °C present the same  $S_{\text{max}}$  ( $\approx 500 \text{ nm}$ ) but  $R_{c/e}$  at 90 °C ( $\approx 20 \%$ ) is twice higher than at 120 °C ( $\approx 10 \%$ ) which means that the solid content of the drop at 90 °C is higher at the droplet center than at 120 °C. Furthermore, the combination of  $S_a$  and  $R_{0.5}$  appears relevant to describe the radial particles repartition. Indeed,  $S_a$  allow to specify  $R_{0.5}$  by giving information about the surface ruggedness. For intermediate  $R_{0.5}$  value,  $S_a$  allows to know if particles shows an homogeneous or heterogeneous repartition.



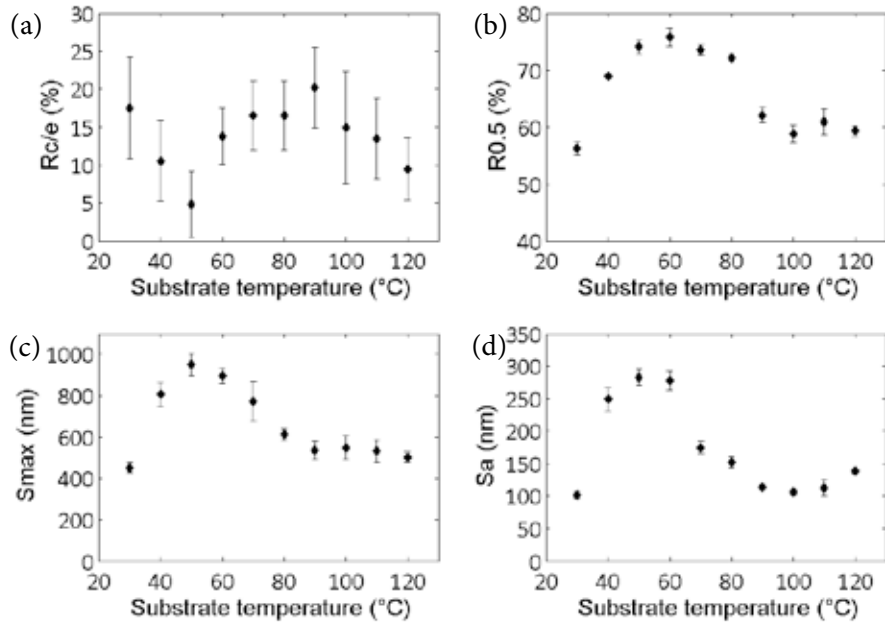


Figure 5: Evolution of (a)  $R_{c/e}$ , (b)  $R_{0.5}$ , (c)  $S_{max}$  and (d)  $S_a$  with temperature substrate.

### 3.3 Correlation between particles distribution and printed line conductance

Inkjet conductive lines are composed of adjacent printed droplets. In this work, silver lines were printed with droplets of 40  $\mu\text{m}$  of diameter after impact and spaced of 20  $\mu\text{m}$ . Therefore, a superimposition of droplets occurs and allows the continuity of lines. As shown in Figure 6, lines show a different silver particles transversal distribution than individual droplets. However, the transversal distributions between line with one and two drops width appear similar. These observations prove that the particles distribution is impacted by the superimposition of droplets. The particles pinned line continuously evolves with the addition of successive droplets until a complete drying.

The electrical conductance of printed tracks is proportional to their cross section surface. Therefore, the transversal distribution of silver particles is expected to have a strong influence on line conductance. In this work, the particles distribution evolution is due to a variation of the substrate temperature (Figure 7). As conductance is directly impacting by the conditions of the sintering step, the substrate temperature conditioning may interfere and impact the resulting conductance independently to the particles distribution. A protocol minimizing the influence of this perturbation was therefore established. The linear electrical conductances of printed lines, presented in Figure 8, increase with the substrate temperature. Regarding the droplet profiles, this trend was not truly expected and it seems that the substrate temperature conditioning influences much more the electrical conductance by a sintering effect than by the transversal distribution of conductive particles. Future work will be focused on the quantification of the particle distribution impact on line conductance.

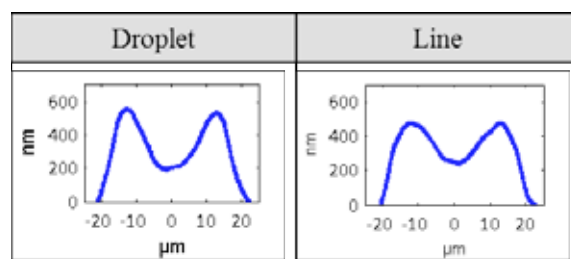


Figure 6: 2D profiles comparison between an individual droplet and one droplet wide conductive line for a substrate temperature of 30 °C.



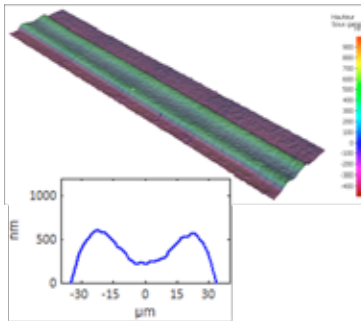
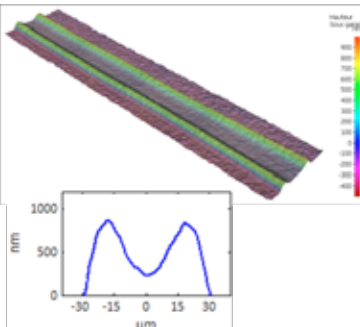
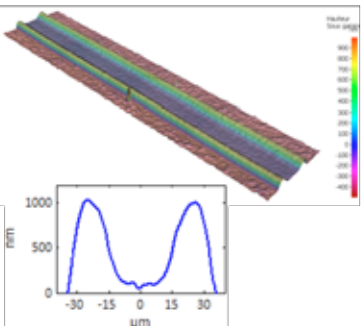
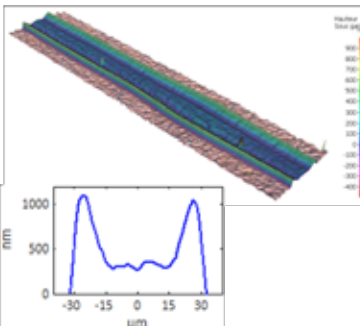
Temperature	30 °C	60 °C
3D and 2D profiles		
Width	$66 \pm 6 \mu\text{m}$	$61 \pm 1 \mu\text{m}$
$R_{c/e}$	$46 \% \pm 12 \%$	$24 \% \pm 10\%$
$S_{\text{max}}$	466 nm	900 nm
Temperature	90 °C	120 °C
3D profile		
Width	$67 \pm 1 \mu\text{m}$	$85 \pm 3 \mu\text{m}$
$R_{c/e}$	$14 \% \pm 1 \%$	$36 \% \pm 15 \%$
$S_{\text{max}}$	1086 nm	952 nm

Figure 7: 3D profiles of two drops wide inkjet-printed tracks as a function of temperature substrate.

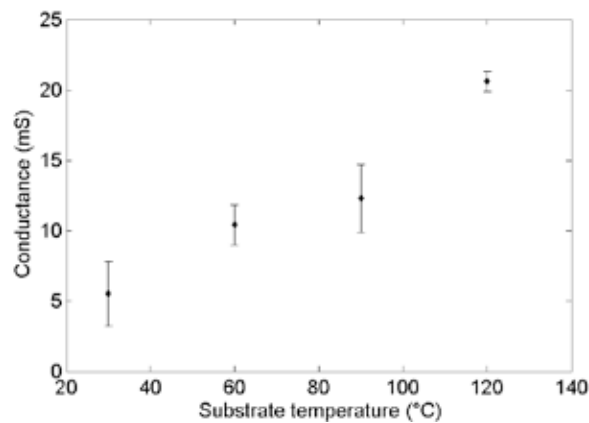


Figure 8: Electrical conductance of 1 cm length tracks as a function of substrate temperature.

#### 4. Conclusions

Inkjet printing process is a relevant technology to print conductive tracks. Inkjet process was used in this work to eject a commercial conductive ink composed of silver nanoparticles which verifies all process requirements. A set of four geometrical indexes specifically designed for this study was set up in order to precisely qualify and compare the particles distribution within dried printed individual droplets and lines. The combination of  $R_{0.5}$  and  $S_a$  gives information about the radial or transversal particle distribution

whereas the combination of  $R_{c/e}$  and  $S_{max}$  gives information about the vertical distribution. Differences between printed individual droplet and line profiles achieved for different substrate temperature were examined. Similar profiles were achieved for lines with one and two drops width whereas significant differences were recorded between individual droplet and line profiles. Conductance measurements were performed on printed lines and with the established protocol, the resulting conductance seems to be more impacted by the sintering effect induced by the substrate temperature conditioning than by the transversal particles distribution. Further experiments will be performed to examine more precisely the impact of each phenomenon. Our future works will focus on a more thorough understanding of the flows occurring within the droplets and lines during the drying step to find potential solutions to reduce the coffee ring. The influence of process parameters (waveform, flight distance, etc.) as well as substrate surface properties (absorption, roughness, surface energy, etc.) on printed pattern profile is also planned to be studied.

### Acknowledgments

LGP2 is part of the LabEx Tec 21 (Investissements d'Avenir – grant agreement n°ANR-11-LABX-0030) and of the Energies du Futur and PolyNat Carnot Institutes. This research was made possible thanks to the facilities of the TecLiCell platform funded by the Région Rhône-Alpes (ERDF: European regional development fund). The Laboratoire Rhéologie et Procédés is part of the Labex Tec 21 (Investissement d'Avenir – grant agreement n°ANR-11-LABX-0033) and of the Polynat Carnot Institut (Investissement d'Avenir – grant agreement n°ANR-11-CARN-030-01)

### References

- Chang, J., Zhang, X., Ge, T., and Zhou, J., 2014. Fully printed electronics on flexible substrates: High gain amplifiers and DAC. *Organic Electronic*, 15, pp. 701–710.
- Deegan, R.D., Bakajin, O., Dupont, T.F., Huber, G., Nagel, S.R. and Witten, T.A., 1997. Capillary flow as the cause of ring stains from dried liquid drops. *Nature*, 389, pp. 827–829.
- Derby, B., 2010. Inkjet Printing of Functional and Structural Materials: Fluid Property Requirements, Feature Stability, and Resolution. *Annual Review of Materials Research*, 40, pp 395–414.
- Fromm, J.E., 1984. Numerical calculation of the fluid dynamics of drop-on-demand jets. *IBM Journal of Research and Development*, 28, pp. 322–333.
- Heljo, P.S., Li, M., Lilja, K.E., Majumdar, H.S., and Lupo, D., 2013. Printed Half-Wave and Full-Wave Rectifier Circuits Based on Organic Diodes. *IEEE Transactions on Electron Devices*, 60, pp. 870–874.
- Hendarto, E., and Gianchandani, Y.B., 2013. Size sorting of floating spheres based on Marangoni forces in evaporating droplets. *Journal of Micromechanics and Microengineering*, 23.
- Hu, H., and Larson, R.G., 2005. Analysis of the effects of Marangoni stresses on the microflow in an evaporating sessile droplet. *Langmuir*, 21, pp. 3972–3980.
- Hu, H., and Larson, R.G., 2006. Marangoni Effect Reverses Coffee-Ring Depositions. *The Journal of Physical Chemistry B*, 110, pp. 7090–7094.
- Jang, D., Kim, D., and Moon, J., 2009. Influence of Fluid Physical Properties on Ink-Jet Printability. *Langmuir*, 25, pp. 2629–2635.
- Lim, J.A., Lee, W.H., Lee, H.S., Lee, J.H., Park, Y.D., and Cho, K., 2008. Self-Organization of Ink-jet-Printed Triisopropylsilyl ethynyl Pentacene via Evaporation-Induced Flows in a Drying Droplet. *Advanced Functional Materials*, 18, pp. 229–234.
- Reis, N., Ainsley, C., and Derby, B., 2005. Ink-jet delivery of particle suspensions by piezoelectric droplet ejectors. *Journal of Applied Physics*, 97.
- Singh, M., Haverinen, H.M., Dhagat, P., and Jabbour, G.E. 2010. Inkjet Printing-Process and Its Applications. *Advanced Materials*, 22, pp. 673–685.
- Stow, C.D. and Hadfield, M.G., 1980. An experimental investigation of fluid flow resulting from the impact of a water drop with an unyielding dry surface. *Proceedings of the Royal Society of London*, 373.

## Influence of the Background Color on the Quality of Embossed Holograms

Pauline Brumm<sup>1</sup>, Edgar Dörsam<sup>1</sup>, Duy Linh Nguyen<sup>1</sup>, Martin Schmitt-Lewen<sup>2</sup>

<sup>1</sup> Technische Universität Darmstadt, Institute of Printing Science and Technology,  
Magdalenenstr. 2, 4289 Darmstadt, Germany

<sup>2</sup> Heidelberger Druckmaschinen AG, Alte Eppelheimer Str. 26, 69115 Heidelberg, Germany

E-mail: pauline.brumm@stud.tu-darmstadt.de; doersam@idd.tu-darmstadt.de;  
nguyen@idd.tu-darmstadt.de; martin.schmitt-lewen@heidelberg.com

### Abstract

Embossed holograms are increasingly often used for the decorative refinement of printed products. So far, there has not been much scientific research about the influence of the background color on the quality of embossed holograms. For this purpose, we produced hologram samples with different background colors in a manual experiment, using the principle of UV embossing. At first, the quality of the samples was evaluated through a visual experiment. The conceptual design of that experiment was part of this research. Second, measurements of color values with an X-Rite MA98 multi-angle spectrophotometer were conducted. The comparison of the results leads to the conclusion that conventional hand-held color measuring instruments used by the graphics industry can evaluate the influence of the background color. We found out that calculating the color difference  $\Delta E^*_{ab}$  between background color and sample can be used to recreate the results of the visual experiment, whereas the samples' chroma  $C^*_{ab}$  is not suitable for evaluating the influence of the background color. Moreover, the number of provided measuring geometries is a limitation of this approach.

**Keywords:** micro embossing, UV curing, multi-angle measurement, visual experiment

### 1. Introduction and background

Embossed holograms are well known from banknotes, identification cards or other security documents where they serve as complex anti-counterfeit elements, but they are also used for decorative refinement, i.e. for the refinement of product packagings.

For some years, a new scope for design is available through the production process UV embossing, which allows the choice of an arbitrary background color for the embossed hologram (Masuda, 2006). Before this, only metallic background colors were possible, which provide the desired brilliant effect of the classical embossed hologram. The free choice of the background color opens up new possibilities but also new challenges. Which background color can be used to achieve a strong holographic effect? How can the quality of an embossed hologram be measured?

So far, there has not been much scientific research about quality control of embossed holograms and the influence of the background color. In general, one can say that quality control of holograms is difficult because of the great angle-dependency of the holographic effect. Similar difficulties can be found when investigating effect coatings (Hupp and Dörsam, 2007; Kehren, Dörsam and Hupp, 2009).

The goal of this research is to find out, if conventional hand-held color measuring instruments used by the graphic industry can evaluate the influence of the background color on the quality of embossed holograms.

For this purpose, we prepare hologram samples with different background colors in Section 2 and conduct a visual experiment, which has the aim to evaluate the samples' quality, in Section 3. The development of the visual experiment is also part of this research. In Section 4, we conduct color measurements and in Section 5, the results of the visual experiment and the color measurements are presented and compared to each other. Finally, conclusions are drawn in Section 6.

## 2. Sample preparation

### 2.1 Pre-printed substrates

Five types of pre-printed substrates in the colors blue, red, black, white and silver with a size of approximately 135 mm × 330 mm were used (Figure 1).

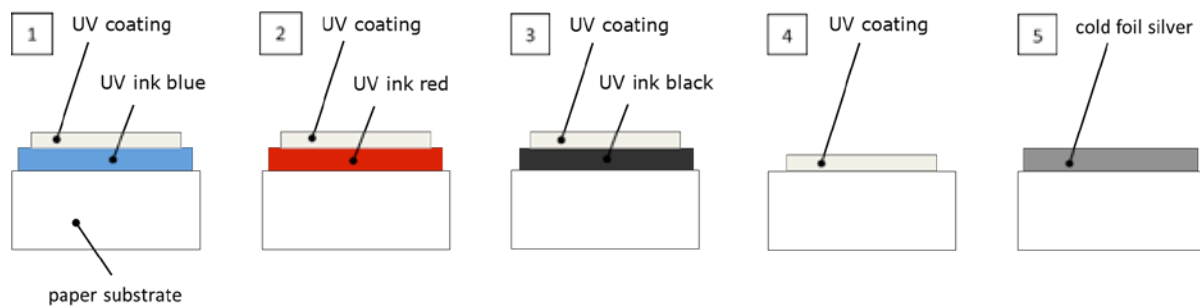


Figure 1: Types of pre-printed substrates. 1 – Blue, 2 – Red, 3 – Black, 4 – White, 5 – Silver

For the blue, red, black and white pre-printed substrates, Fasson MC Offset 2S-90 (SV4565) with a thickness of 71  $\mu\text{m}$  and grammage of 90  $\text{g}/\text{m}^2$  was used as paper substrate. For the UV coating, Saphira UV-Coating U8730 (Heidelberger Druckmaschinen AG) was used. The silver pre-printed substrate differs from the others, because it is produced by cold foil transfer using silver cold foil. Moreover, another paper substrate with a grammage around 180  $\text{g}/\text{m}^2$  was used. Table 1 shows CIELAB color values and gloss values of the five types of pre-printed substrates.

Table 1: CIELAB color values  $L^*$ ,  $a^*$  and  $b^*$  of pre-printed substrates (X-Rite MA98, measuring geometry  $45^\circ/0^\circ$ , illumination D65,  $10^\circ$  observer,  $n = 10$ ) and gloss values of pre-printed substrates (BYK micro-TRI-gloss,  $20^\circ$  measuring angle,  $n = 10$ ) measured on one pre-printed substrate

Pre-printed substrate	$L^*$	$a^*$	$b^*$	Gloss in gloss units
Red	31.3	61.9	40.2	57.3
Blue	31.2	-15.2	-44.9	45.2
Black	7.4	-0.1	-1.8	49.6
Silver	12.8	-0.6	-3.4	1056.7
White	88.1	-0.2	-0.9	60.1

### 2.2 Embossing master

To produce an embossing master, we poured a conventional transparent silicone onto a nickel shim (Iliescu, Necsoiu and Comanescu, 2011) and then hardened it in an oven (Vötsch Industrietechnik VTL 60/90) at  $42^\circ\text{C}$  for about three hours. Afterwards, we left it at room temperature for about 60 hours, before gently peeling of the replica (Figure 2). Thus, we produced a transparent silicone shim (thickness approximately 3 mm), which we later used as an embossing master for the UV embossing of our hologram samples.

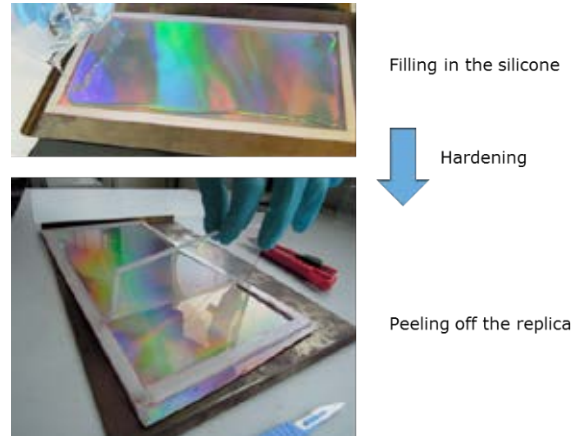


Figure 2: Production of transparent silicone shim

The nickel shim is a commercially available one. It has a double sine wave surface structure that creates a rainbow effect due to light diffraction. The term ‘rainbow effect’ means that in different viewing angles different colors of the rainbow appear. We chose the rainbow effect, because it is a simple holographic effect, which is the base of many complex embossed holograms.

### 2.3 UV embossing

For the production of our hologram samples, we used the principle of UV embossing (Figure 3). To produce one hologram sample, we coated one of the pre-printed substrates with UV lacquer (holographic lacquer from Heidelberger Druckmaschinen AG) using an automatic film applicator coater (Zehntner ZAA 2300) and a doctor blade (Zehntner ZUA 2000) with the gap height of 50  $\mu\text{m}$ . Then, our transparent silicone shim was pressed into the still wet UV lacquer and exposed to UV light, using an UV curing system (IST Metz M-40-1-URS-WIR-TR-SLC). Lastly, the transparent silicone shim was removed. Before using the transparent silicone shim again, we cleaned it from UV lacquer remains with a strip of strong adhesive tape.

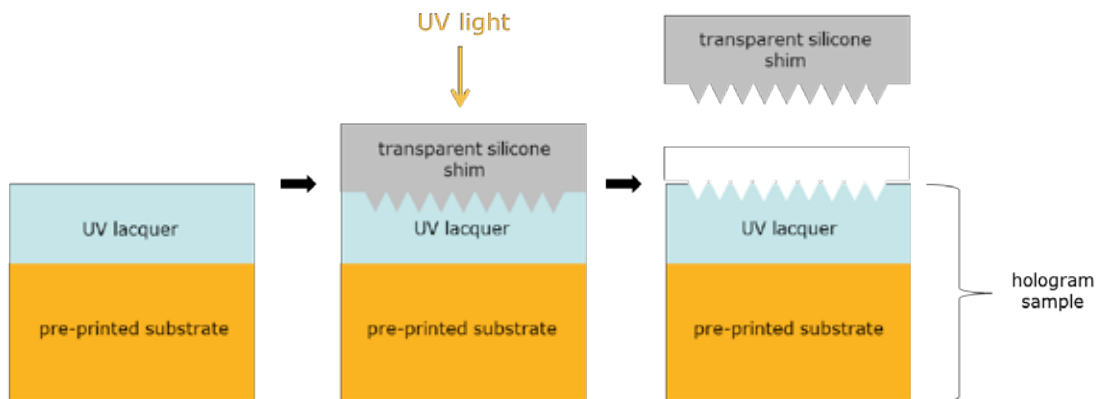


Figure 3: UV embossing of hologram samples

For each type of pre-printed substrate (background color blue, red, black, white and silver), ten hologram samples were produced and numbered in the order of their production (sample #1, #2, #3, ... #10). Preliminary tests had shown that each silicone shim could only be used 12 times on average for UV embossing before it becomes brittle and eventually gets torn. A similar behavior is known from (Theopold et al., 2012) where the influence of solvents on flexo printing forms is investigated. Fine cracks already appeared after approximately eight times of use and could be detected in the sample surface as well (Figure 4). For this reason, we used a new silicone shim (100 mm  $\times$  140 mm) of the same properties for each background color.

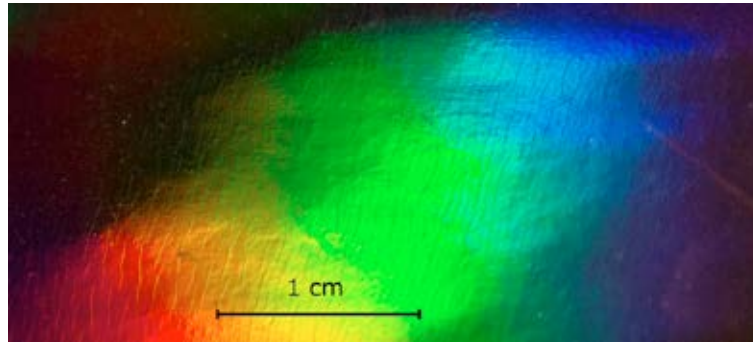


Figure 4: Cracks in the surface of sample #10 with black background color

We would like to emphasize that we prepared the hologram samples in a manual experiment. However, there also exists an industrial process for the UV embossing of holograms, which is commercially referred to as ‘UV Casting’. Other names are ‘UV Film Casting’ or ‘Cast and Cure’. Instead of using a transparent silicone shim as in this research paper, the industrial UV embossing process uses a transparent plastic film, which has a transparent lacquer coating with imprinted micro- or nanostructures on one side (Kaule and Grauvogl, 1999).

### 3. Visual experiment

There hardly exist any scientific approaches for the visual inspection of embossed holograms, yet. For this reason, we developed our own visual experiment.

#### 3.1 Equipment

- Viewing booth Macbeth SpectraLight III, covered with black velvet inside
- Self-made sample display, which can be tilted  $\pm 5^\circ$  around its basic adjustment of  $45^\circ$  to the horizontal (Figure 5)
- Chin rest
- Samples #1 and #10 of each type of pre-printed substrate are used (see chapter 2.3). For better handling and a uniform look, each sample gets a black frame (70 mm  $\times$  70 mm window size) made from cardboard

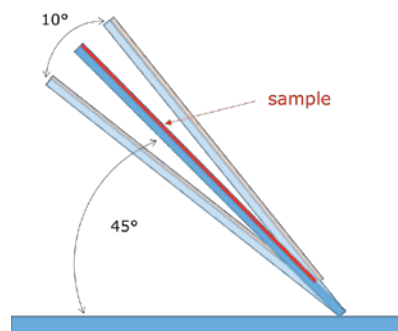


Figure 5: Sample display

#### 3.2 Assessment criteria for the samples' quality

Embossed holograms like our samples are rather used for decorative refinement than for security applications due to their easily damageable open holographic structure. Often, the purpose of decorative refinement is to attract the viewer's attention. Presuming that quality is the fitness for a special purpose

(Teschner, 2010), we therefore assume that the samples' quality depends on certain sample properties that are responsible to attract the viewer's attention, e. g. color properties.

In this research, we choose the sample properties 'intensity' and 'variety of colors' as assessment criteria for our samples' quality, assuming that great intensity and great variety of colors notably attract the viewer's attention. Please note that the visual experiment is conducted in German language, using the German terms 'Leuchtkraft' (intensity) and 'Farbvielfalt' (variety of colors) as assessment criteria, whereby the German and English expressions may have slightly different meanings.

### 3.3 Subjects

Twenty six test persons, 17 male and 9 female, from age 22 to 65 (average 32). All normal or corrected-to-normal sighted. No color vision deficiencies according to the Farnsworth-Munsell 100 Hue Color Vision Test. Ten of the test persons were classified as experts, which have experience in colorimetry or visual experiments.

### 3.4 Procedure

The experiment is part of a broad series of visual experiments, which are conducted in the so-called 'Black Room' at the Institute of Printing Science and Technology, Darmstadt, Germany. This room is almost entirely furnished black, so that as little scattered light as possible gets into the viewing booth. Only the experiment directly relevant to the topic of this research paper is described further. The viewing situation in the viewing booth is shown in Figure 6.

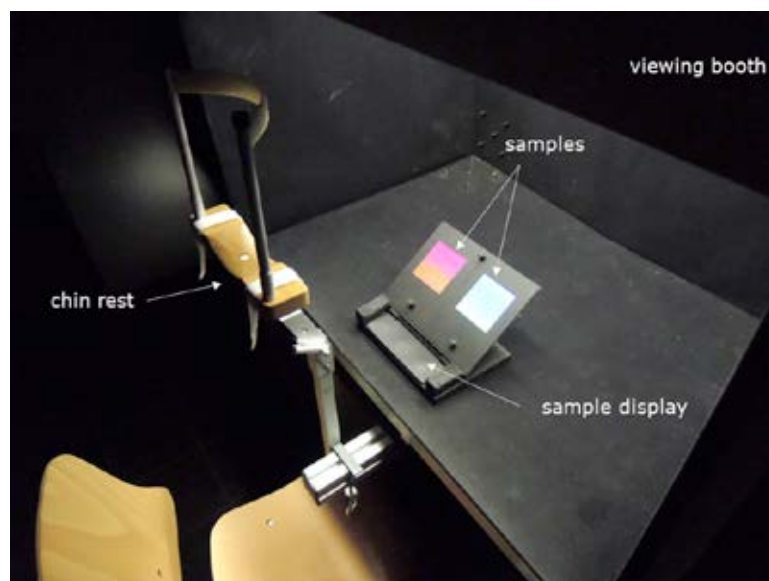


*Figure 6: Viewing situation in the viewing booth*

In the visual experiment, each sample #1 is compared to every other sample #1 with respect to intensity and variety of color (Figure 7). The sample with the higher intensity scores one point and the sample with the higher variety of color scores one as well. The test persons were told to tilt the sample display back and forth several times so that they could see the rainbow effect in its full range.

We want to emphasize that the test persons were always asked to compare solely the samples' rainbow effect and not their background colors, which appear alongside the rainbow effect. Besides, all test persons were told to decide spontaneously and subjectively. All instructions to the test persons were given orally.





*Figure 7: Visual experiment from the view of a test person (exemplary scene);  
Left – Red sample #1, Right – Silver sample #1*

### 3.5 Illumination and geometry

The visual experiment was conducted twice, once with illuminant TL84 and once with illuminant D65 aiming to simulate the viewing conditions in a shopping mall (TL84) and in daylight (D65). Both illuminants are built into the Macbeth SpectraLight III viewing booth by default.

The experimental setup was chosen so that the light of the selected illuminant strikes the sample approximately at an incident angle of  $45^\circ$  from the sample's normal and the emergent angle is approximately  $0^\circ$  from the sample's normal ( $45^\circ/0^\circ$ ). We chose this geometry according to the recommendation of the nickel shim manufacturer. Of course, the viewing geometry changes by the tilting of the sample display. To create a reproducible visual experiment, we preferred this relatively specified geometry to a free geometry.

## 4. Color measurements

For the color measurements, we used an X-Rite MA98 multi-angle spectrophotometer and black cardboard as a measuring underlay. For data handling, we used the software X-Color QC. We measured each sample ten times on random spots and always oriented the measuring instrument longitudinal to the sample to avoid possible anisotropy.

The multi-angle spectrophotometer X-Rite MA98 offers different measuring geometries (Kehren et al., 2011). Due to the angle-dependency of the holographic effect, analyzing several measuring geometries is reasonable. We chose to analyze the measuring geometries  $45^\circ:as25^\circ$ ,  $45^\circ:as45^\circ$  and  $45^\circ:as75^\circ$  because they lie closest to the geometry used for the visual experiment. The first number, 45, represents the incident angle in respect to the surface normal. The second number represents the viewing direction in respect to the specular angle. Accordingly,  $45^\circ:as45^\circ$  represents the geometry used for the visual experiment ( $45^\circ/0^\circ$ ). As illuminant, we chose D65 and as CIE standard photometric observer, we selected the  $10^\circ$  observer because in the visual experiment the samples are regarded at an aperture angle of more than  $4^\circ$  (DIN 5033-1).

## 5. Results and discussion

In this chapter, we present both the results of the visual experiment and the measurements and compare them to each other.

### 5.1 Results of the visual experiment

To begin with, Figure 8 shows the results of the visual experiment at illumination TL84. The silver samples gained the highest score, closely followed by the black samples. On the third and fourth rank are the red and blue samples, which were given rather similar scores for their variety of colors. However, the red samples gained approximately twice the score for their intensity than the blue samples. On the last placing of the ranking, the white samples can be found, which gained no points for intensity and only a few for their variety of colors.

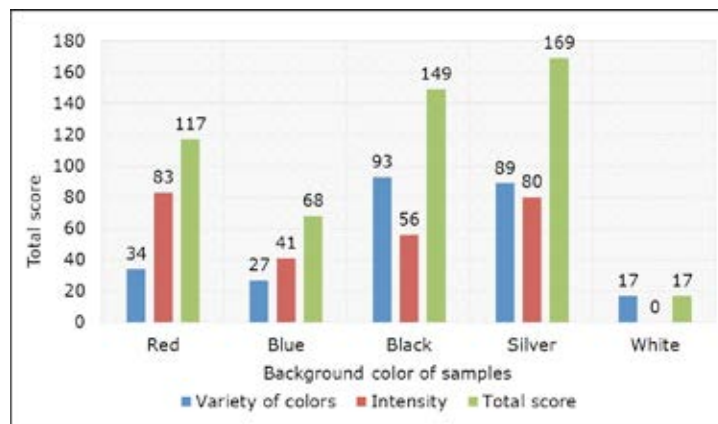


Figure 8: Results of the visual experiment at illumination TL84 and geometry 45°/0°

The results of the visual experiment conducted at illumination D65 are shown in Figure 9. In comparison to the results in Figure 8, similar scores and nearly the same ranking of the samples can be found. Only the first and second placing are inverted. Thereby, we would like to add that those test persons who were considered as experts on average still distributed more points for the silver samples than for the black samples.

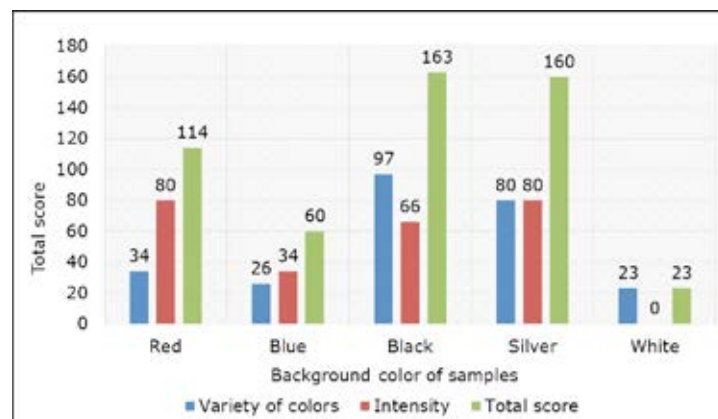


Figure 9: Results of the visual experiment at illumination D65 and geometry 45°/0°

### 5.2 Results of the color measurements

Figure 10 shows three chroma diagrams, one for each of the selected measuring geometries (see chapter 4), where the CIELAB color values  $a^*$  and  $b^*$  of sample #1 to sample #10 of each background color are plotted. The dotted lines between the measuring values serve as a guide for the eye only. Sample #1 is

always marked with the number '1'. As can be seen in all diagrams, samples of different background color show distinctly different color values  $a^*$  and  $b^*$  although they were prepared with the same holographic surface structure. This implies that the background color has influence on the holographic effect.

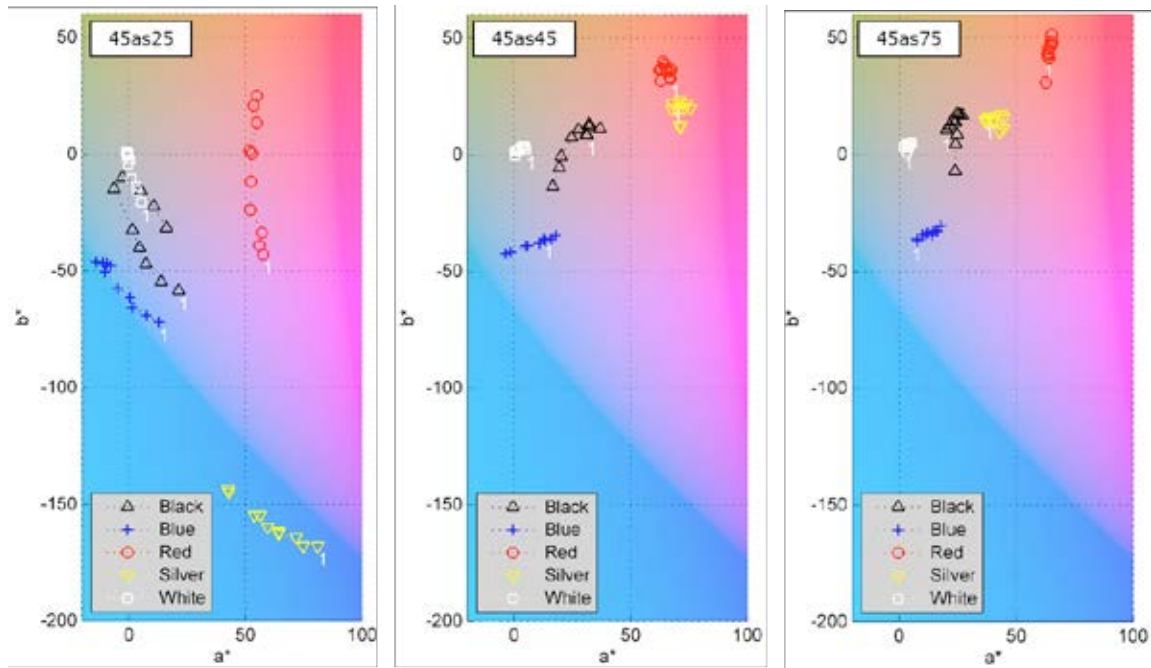


Figure 10: Chroma diagrams of hologram samples at  $L^* = 60$  (illumination D65,  $10^\circ$  observer); measuring geometries from left to right:  $45^\circ:as25^\circ$ ,  $45^\circ:as45^\circ$ ,  $45^\circ:as75^\circ$ ; it is to notice that the displayed colors in the chroma diagrams serve only for visualization purposes and do not conform to the real colors of the samples; this is because the value of the lightness  $L^*$  is chosen as 60 within the chroma diagram but in reality each sample has a different  $L^*$ -value

Taking a closer look at the samples' color locations (Figure 10), it becomes apparent that at all measuring geometries the red samples' color locations lie rather in the red area whereas the blue samples' color locations rather lie in the blue area. In contrast, the silver samples appear rather blue at  $45^\circ:as25^\circ$  and rather red at  $45^\circ:as45^\circ$  and  $45^\circ:as75^\circ$ . This leads to the conclusion that chromatic background colors (blue, red) in contrast to non-chromatic background colors (e.g. silver) overlay with the colors of the rainbow effect so that they shift them into the direction of the background color.

Moreover, Figure 10 shows that the color measurement is not able to characterize the rainbow effect in its full range, since the three selected measuring geometries represent only bluish and reddish parts of the rainbow. However, the rainbow of the applied rainbow effect contains more than these two colors.

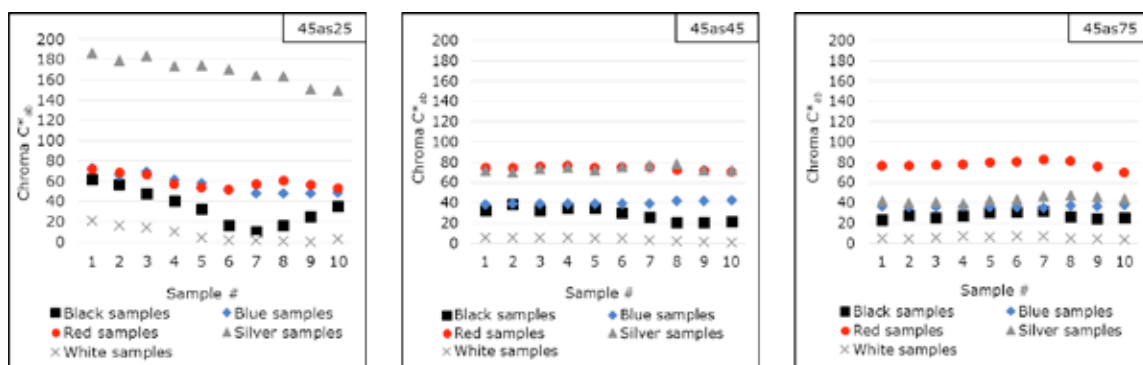


Figure 11: Chroma  $C^*_{ab}$  of all samples at measuring geometries  $45^\circ:as25^\circ$ ,  $45^\circ:as45^\circ$  and  $45^\circ:as75^\circ$  at D65/ $10^\circ$

Investigating the samples' chroma  $C^*_{ab}$  and comparing it to the visual experiment (Figure 11, see chapter 5.1), one could assume that the samples' chroma values represent the samples' quality, since the white samples have the lowest chroma and the silver samples have a rather great chroma at all measuring geometries. However, it contradicts the visual experiment that the black samples have only the second lowest chroma, whereas they gained a rather high scoring at the visual experiment. Consequently, the investigation of chroma values is not a suitable method to evaluate the influence of the background color on the quality of our samples.

In the following, we therefore chose another approach; we calculate the color difference  $\Delta E^*_{ab}$  between the pre-printed substrate and the hologram sample (Figure 12). The consideration behind that approach is that color appears in interaction with its surrounding (Berns, 2000) – in our case the background color, which appears at some viewing angles alongside the rainbow effect. Whereas the chroma  $C^*_{ab}$  is an absolute measurement variable, the color difference  $\Delta E^*_{ab}$  is a relative measurement variable which can consider the background color. Assuming that a greater color difference stands for a stronger holographic effect, Figure 12 clearly states that the black samples have a rather strong holographic effect. This fits better to the results of the visual experiment than the results from Figure 11.

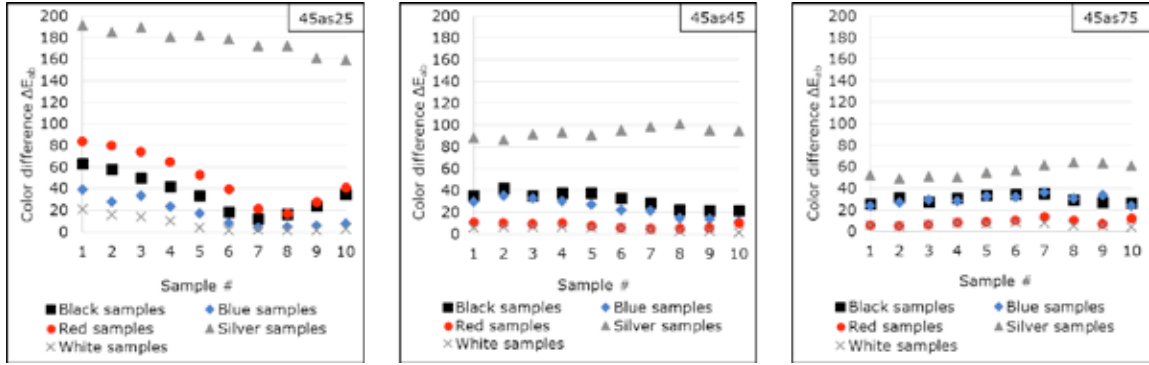


Figure 12: Color difference  $\Delta E^*_{ab}$  between pre-printed substrate and hologram sample at measuring geometries  $45^\circ:as25^\circ$ ,  $45^\circ:as45^\circ$ ,  $45^\circ:as75^\circ$  at  $D65/10^\circ$

To make a combined statement about the color difference, we computed the arithmetic mean of the color differences at all three analyzed measuring geometries (Figure 13). Except the relative positioning of the red and blue samples and the big gap between the silver and black samples, Figure 13 well represents the results of the visual experiment.

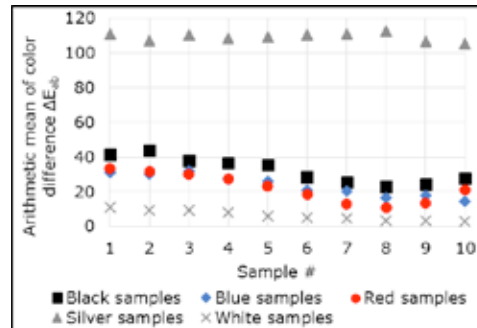


Figure 13: Arithmetic mean of color difference  $\Delta E^*_{ab}$  between pre-printed substrate and hologram sample at measuring geometries  $45^\circ:as25^\circ$ ,  $45^\circ:as45^\circ$ ,  $45^\circ:as75^\circ$  at  $D65/10^\circ$

## 6. Conclusion and outlook

The visual experiment conducted in this research serves as a guideline for the design of UV embossed holograms. We found out that the background colors silver and black achieve the strongest holographic effect. In comparison, red and blue background colors only evoke a mediocre and white background colors evoke the weakest holographic effect.

The comparison of the visual experiment and the color measurements leads to the following conclusions:

- Conventional hand-held color measuring instruments can evaluate the influence of the background color on the quality of embossed holograms
- Calculating the color difference  $\Delta E^*_{ab}$  between pre-printed substrate and sample is a method to recreate the results of the visual experiment
- The number of provided or analyzed measuring geometries is a limitation of color measurements; in this research three measuring geometries ( $45^\circ:as25^\circ$ ,  $45^\circ:as45^\circ$ ,  $45^\circ:as75^\circ$ ) lead to useful results, but other holographic effects may require far more measuring geometries

In future research, the following questions may become important:

- What does the quality of embossed holograms need to look like? Are ‘intensity’ and ‘variety of colors’ useful and sufficient assessment criteria?
- Does the method also work for more complex holographic effects than the rainbow effect?

## Acknowledgement

The authors appreciate the support by the Heidelberger Druckmaschinen AG.

## References

- Berns, R.S., 2000. *Billmeyer and Saltzman's Principles of Color Technology*. 3rd ed. New York: Wiley, p. 24.
- Deutsches Institut für Normung (DIN), 2009. *DIN 5033-1 Grundbegriffe der Farbmetrik*.
- Hupp, H. and Dörsam, E., 2007. Quality control for printed interference colours – investigation for a basic measuring geometry. In: *Proceedings of the 34<sup>th</sup> International Research Conference of IARIGAI*, Grenoble, France, 9–12 September 2007, pp. 257–266.
- Iliescu, M., Necsoiu, T. and Comanescu, B., 2011. Study on holograms laser engraving process. *Recent Researches in Communications, Automation, Signal Processing, Nanotechnology, Astronomy and Nuclear Physics*, pp. 227–230.
- Kaule, W. and Grauvogl, G., 1999. *Verfahren und Vorrichtung zur Herstellung eines Folienmaterials*. German Patent DE000019746268A1.
- Kehren, K., Dörsam, E. and Hupp, H., 2009. Printed interference effect colours – Process control and quality assurance. In: *Proceedings of the 36<sup>th</sup> International Research Conference of IARIGAI*, Stockholm, Sweden, 13–16 September 2009, pp. 329–336.
- Kehren, K., Urban, P., Dörsam, E., Höpe, A. and Wyble, D.R., 2011. Performance of multi-angle spectrophotometers. In: *Proceedings of AIC Midterm Meeting*, pp. 473–476.
- Masuda, S., 2006. *Druckerpresse mit holographischer Endbearbeitungseinheit*. German Patent DE102006021069A1.
- Teschner, H., 2010. *Druck- und Medientechnik: Informationen gestalten, produzieren, verarbeiten*. 13<sup>th</sup> ed. Konstanz: Christiani, p. 762.
- Theopold, A., Neumann, J., Massfelder, D. and Dörsam, E., 2012. Effects of solvent exposure on flexographic printing plates. In: *Proceedings of the 39<sup>th</sup> International Research Conference of IARIGAI*. Ljubljana, Slovenia, 9–12 September 2012.

## TiO<sub>2</sub> nanostructures for dye-sensitized solar cells (DSSCs) on a glass substrate

Jarkko J. Saarinen<sup>1</sup>, Roger Bollström<sup>2</sup>, Björn Törngren<sup>3</sup>, Janne Haapanen<sup>4</sup>, Tommi Kääriäinen<sup>5</sup>, Steven M. George<sup>5</sup>, Jyrki M. Mäkelä<sup>4</sup>, and Martti Toivakka<sup>1</sup>

<sup>1</sup> Abo Akademi University, Center for Functional Materials, Laboratory of Paper Coating and Converting, Faculty of Science and Engineering, Porthansgatan 3, FI-20500 Turku, Finland

<sup>2</sup> Omya International AG, Baslerstrasse 42, CH-4665 Oftringen, Switzerland

<sup>3</sup> Abo Akademi University, Center for Functional Materials, Laboratory of Physical Chemistry, Faculty of Science and Engineering, Porthansgatan 3, FI-20500 Turku, Finland.

<sup>4</sup> Tampere University of Technology, Aerosol Physics Laboratory, Department of Physics, P.O. Box 692, FI-33101 Tampere, Finland

<sup>5</sup> University of Colorado Boulder, Chemistry & Biochemistry, 215 Cristol Chemistry, Boulder CO 80309, United States

E-mail: jarkko.j.saarinen@abo.fi; roger.bollstroem@omya.com; btornngre@abo.fi;  
janne.haapanen@tut.fi; tommi.kaariainen@colorado.edu; steven.george@colorado.edu;  
jyrki.makela@tut.fi; martti.toivakka@abo.fi

### Short Abstract

We report here the manufacturing of a dye-sensitized solar cell (DSSC) by combining roll-to-roll (R2R) liquid flame spray (LFS) deposition of TiO<sub>2</sub> nanoparticles with atomic layer deposition (ALD) of TiO<sub>2</sub> thin films. Three different LFS deposition times and three different ALD film thicknesses were investigated. The best solar energy conversion efficiency of 1.28 % was achieved from a sample with 100 × repeated LFS TiO<sub>2</sub> nanoparticle deposition, subsequently coated with a 10 nm ALD TiO<sub>2</sub> thin film on top. Our results suggest new routes for fabrication of DSSCs that can be expanded into a complete R2R process allowing a significant reduction of the device unit cost.

**Keywords:** dye-sensitized solar cell, TiO<sub>2</sub>, liquid flame spray, atomic layer deposition

### 1. Introduction and background

The late Nobel Laureate Richard E. Smalley postulated *The terawatt challenge* (Smalley, 2005) about the energy generation transformation that is needed to supply energy in a sustainable way for the increasing human population. The current estimate for the energy consumption of the seven billion earth inhabitants is approximately 13 TW, which is expected to grow by at least 10 TW by 2040. Fossil fuel based solutions are the main source of the current energy portfolio, but they contribute to the greenhouse gas charge considered responsible for much of climate change. Nuclear power continues to be strongly questioned, and many national policies were changed in the aftermath of the Tohoku earthquake and the Fukushima Daiichi meltdown in 2011. However, the scientific evidence speaks for expanding, not reducing, the use of nuclear power with significantly reduced mortality compared to fossil fuel based alternatives (Kharecha, 2013). Nevertheless, the most sustainable way to meet the growing energy demand would be to increase the use of solar power.

The amount of solar power reaching the Earth's surface is approximately 120 000 TW. Thus, even a small fraction of this amount would be sufficient to meet the energy demand of the current and future generations. Unfortunately, capturing the solar power cost-efficiently remains a huge challenge. In 1972 Fujishima

and Honda (Fujishima, 1972) published a seminal paper utilizing a semiconductor  $\text{TiO}_2$  for water splitting via *photocatalytic* reaction: the anatase form of  $\text{TiO}_2$  has a bandgap energy of 3.2 eV that corresponds to a photon wavelength of 388 nm (Luttrell, 2014). Hence, ultraviolet (UV) photons from sunlight can excite electrons from the valence band into the conduction band creating electron-hole pairs. In nanostructured media these electron-hole pairs can easily dissociate, diffuse onto the surface, and thus facilitate various reactions via oxidizing or reducing compounds.

The first practical solar panel was established by the Bell Labs already in 1954 with the first cells based on silicon structures (Lanzani, 2012). Recently, a large interest has been directed towards solution processable organic bulk heterojunction (Diao, 2015) and dye-sensitized solar cells (DSSC) (Hashmi, 2015), both of which are suitable for roll-to-roll (R2R) type manufacturing flow.

A DSSC cell consists of a light sensitive dye molecule, a semiconductor photoanode, redox mediator, and a counter electrode as first demonstrated by O'Regan and Grätzel in 1991 (O'Regan, 1991). In the DSSC structure, the solar photon is absorbed by the organic dye that transfers the electron to the  $\text{TiO}_2$  layer with a hole remaining in the dye. The electron transport process is ultrafast, and thus mediates an immediate solar energy conversion into electricity. Various strategies have been implemented to improve the cell efficiency in the DSSC, and today the best DSSC solar conversion efficiency in laboratory scale solar cells has been up to 13 % (Mathew, 2014), whereas in large-area modules ( $> 100 \text{ cm}^2$ ) the highest efficiencies have been around 8.5 %. The DSSC cells have already found commercial applications, for example, in powering the window blinds at the MGM Grand hotel in Las Vegas.

In this work, we utilize two nanoscale surface modification technologies suitable for R2R manufacturing of DSSC. First,  $\text{TiO}_2$  nanoparticles are deposited on the glass surface using a liquid flame spray (LFS) process. LFS is a versatile thermal deposition method that works in ambient conditions. In LFS, an organometallic precursor typically dissolved in isopropanol is fed into a high temperature and high velocity hydrogen-oxygen flame. The precursor evaporates, condenses, nucleates, and forms solid nanoparticles that can be collected on a moving web and whose diameter can easily be controlled from 2 to 200 nm (Mäkelä, 2011). Various metal and metal oxide nanoparticles and their combinations (Keskinen, 2006 and 2007) can be formed. The nanoparticles are loosely bound to the surface by van der Waals forces. Here we utilize an atomic layer deposition (ALD) for having a thin film of  $\text{TiO}_2$  on top of the LFS deposited  $\text{TiO}_2$  nanoparticles, improving the particle adhesion on the substrate. ALD provides a self-limiting thin film deposition technique, in which the layer thickness can be controlled down to a single atomic level (George, 2010) as the used precursors only react with the surface sites. The cross-sections of the fabricated nanostructured samples are cut using broad ion beam milling and imaged using scanning electron microscopy (SEM). Finally, the fabricated  $\text{TiO}_2$  nanostructures are sensitized with a ruthenium based dye for the solar energy harvesting.

## 2. Materials and Methods

All DSSC cells were fabricated on transparent and conductive fluorine doped tin oxide (FTO) glass (TCO30-10/LI, Solaronix SA, CH).

### 2.1 Liquid flame spray (LFS) $\text{TiO}_2$ nanoparticle deposition

$\text{TiO}_2$  nanoparticles were deposited by a liquid flame spray roll-to-roll process. Titanium (IV) isopropoxide (TTIP, 97 % pure, Alfa Aesar) dissolved in isopropanol (IPA, technical grade, Neste) was injected with a feeding rate of 12 ml/min into the hydrogen-oxygen flame with 50/15 l/min gas flow rates, respectively. The track speed was adjusted to 50 m/min with a nozzle to sample surface distance of 6 cm. Three different



nanoparticle coating amounts were fabricated with 50 ×, 100 ×, and 150 × deposited samples *i.e.* samples were passed below the depositing flame the corresponding number of times.

## 2.2 Atomic layer deposition (ALD) of TiO<sub>2</sub> thin film

TiO<sub>2</sub> thin films were deposited on the three different LFS-TiO<sub>2</sub> nanoparticle deposited glass plates at 300 °C by atomic layer deposition (ALD) using a batch type reactor (Beneq TFS-200 ALD, FI). The pressure was approximately 2 mbar in the reaction chamber during the deposition. Nitrogen was used as the precursor carrier gas, as well as for purging between the precursor pulses. TiO<sub>2</sub> thin films were grown from titanium tetrachloride (TiCl<sub>4</sub>) and water. Three different film thicknesses of 1 nm, 3 nm, and 10 nm were applied. A single ALD cycle resulted in a 0.04 nm thick film growth at 300 °C *i.e.* a 10 nm thick film required 250 ALD cycles.

## 2.3 DSSC cell fabrication

TiO<sub>2</sub> semiconductor structures have limited light absorption at visible wavelengths. Therefore, the deposited TiO<sub>2</sub> nanostructures were photosensitized with a widely used ruthenium complex cis-di(thiocyanato)-N-N'-bis(2,2'-bipyridyl-4-carboxylic acid-4'-tetrabutylammonium carboxylate) ruthenium (II) (N-719, Solaronix SA, CH). The used electrolyte in the cell was a commercial iodide based solution (Iodolyte AN-50, Solaronix SA, CH).

## 2.4 Sample imaging

The cross-sectional images of the TiO<sub>2</sub> nanoparticle coated and thin film deposited samples were prepared using an Ilion+ Advantage-Precision Cross-Section System (Model 693, Gatan Inc., US). The cross-sections were milled with an argon broad ion beam (BIB). The samples were platinum coated before the ion milling to improve heat exchange and to reduce heat damage. The cross-sectional samples were imaged using a scanning electron microscope (SEM, LEO 1530 VP Gemini, Carl Zeiss Microscopy GmbH, DE).

## 2.5 DSSC solar cell performance measurements

The photocurrent-voltage (I-V) characteristics of the fabricated LFS/ALD TiO<sub>2</sub> DSSC solar cells were measured under an AM (air mass) 1.5 G (global) condition (Solar Simulator Oriel 150 W, Newport, US) in 1 sun condition that corresponds to an irradiance of 100 mW/cm<sup>2</sup> at AM 1.5 G condition.

## 3. Results and Discussion

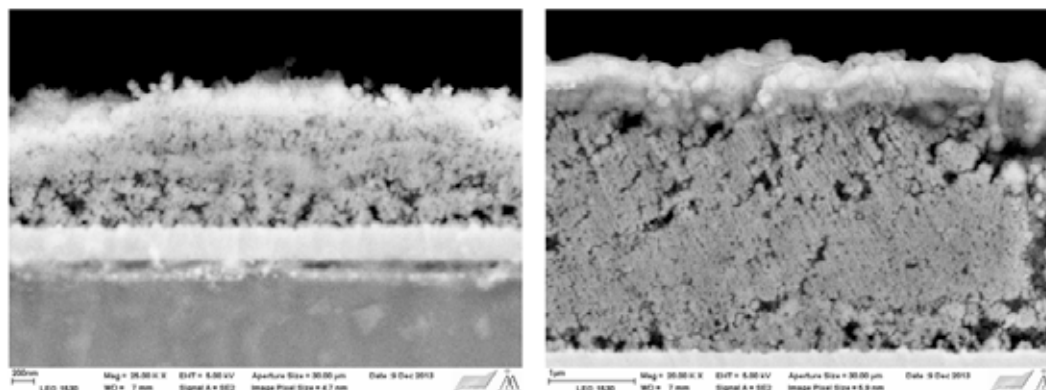


Figure 1: SEM cross-sectional images of (a) 50 × and (b) 100 × LFS deposited TiO<sub>2</sub> nanoparticle coating on a FTO glass.

Figure 1 shows the SEM images of the cross-sections of the  $50 \times$  and  $100 \times$  LFS deposited  $\text{TiO}_2$  nanoparticles without the ALD coating. The average  $\text{TiO}_2$  nanoparticle diameter is approximately 20–40 nm. As clearly seen from the Fig. 1, the number of times the substrate passes below the nozzle correlates well with the observed coating thickness. It can be estimated from the Fig. 1 that  $50 \times$  results in approximately  $1.5 \mu\text{m}$  coating thickness, whereas  $100 \times$  is followed by approximately  $3 \mu\text{m}$  thick porous nanoparticle coating.

Figure 2 presents the corresponding SEM images of the  $100 \times$  deposited LFS sample coated with 1 nm and 10 nm ALD thin film. The subsequent ALD coating results in a more uniform layer on top as the conformal coating fills partially the pores on the surface, and thus smoothens the surface structure.

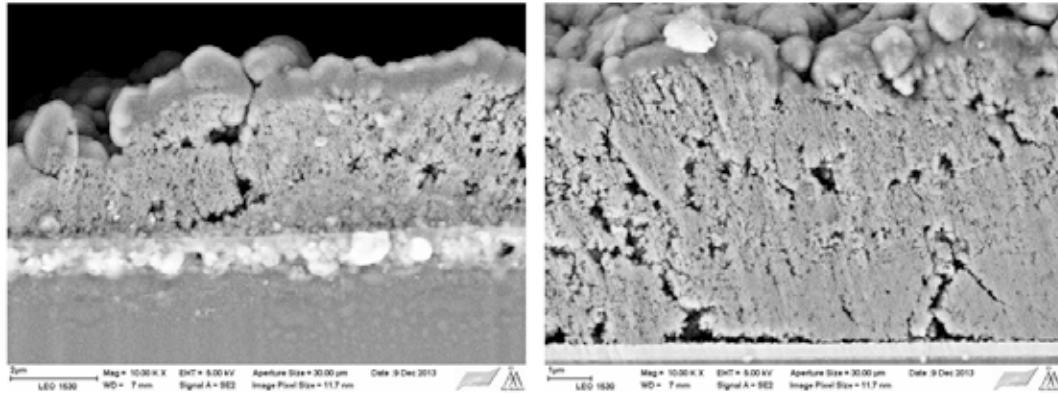


Figure 2: SEM cross-sectional images of  $100 \times$  deposited LFS sample coated with (a) 1 nm and (b) 10 nm  $\text{TiO}_2$  thin film on an FTO glass.

In Table 1 we show the measured solar energy conversion efficiencies for different DSSC cells under normal sunlight. The pure LFS deposited cell has an energy efficiency of only 0.07 % whereas the cells with an ALD deposited thin  $\text{TiO}_2$  film on top have an efficiency from 0.17 % (with 1 nm ALD and  $50 \times$  LFS) to the best of 1.28 % (10 nm ALD and  $100 \times$  LFS).

Table 1: Measured I-V characteristics under sunlight for the DSSC cells with cell area of  $0.64 \text{ cm}^2$ .

	50 LFS	1 nm ALD $\text{TiO}_2$ on top of				3 nm ALD $\text{TiO}_2$ on top of			10 nm ALD $\text{TiO}_2$ on top of		
	50 LFS	50 LFS	100 LFS	150 LFS	50 LFS	100 LFS	150 LFS	50 LFS	100 LFS	150 LFS	50 LFS
Jsc [ $\text{mA}/\text{cm}^2$ ]	0.22	0.53	2.53	2.49	0.88	1.62	1.39	2.45	3.23	1.97	
Voc [V]	0.69	0.76	0.77	0.74	0.71	0.81	0.72	0.78	0.78	0.75	
Fill Factor	0.46	0.42	0.55	0.56	0.47	0.55	0.59	0.48	0.51	0.54	
Efficiency [%]	0.07	0.17	1.06	1.03	0.30	0.73	0.59	0.93	1.28	0.79	

Finally, Figure 3 presents the measured I-V curvature of the best performing cell with  $100 \times$  LFS depositions followed by a 10 nm ALD  $\text{TiO}_2$  coating.

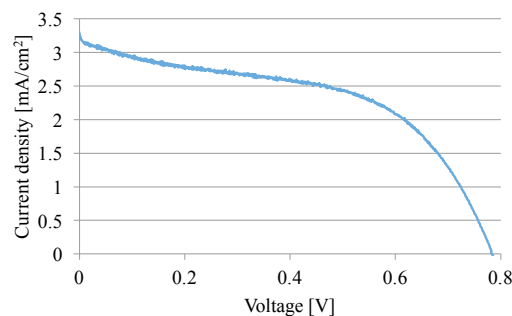


Figure 3: The measured I-V characteristics of the  $100 \times$  LFS with a 10 nm ALD  $\text{TiO}_2$  layer on top.

To summarize our results, we have combined an LFS TiO<sub>2</sub> nanoparticle deposition with ALD TiO<sub>2</sub> thin film deposition for a DSSC solar cell structure. The ALD layer improved the cell efficiency in all cases, and the best efficiency of 1.28 % was observed with a 100 × LFS combined with 10 nm ALD layer.

#### 4. Conclusions

As a summary, we have investigated possibilities to fabricate DSSC structures in a combination of TiO<sub>2</sub> liquid flame spray nanoparticle deposition with atomic layer deposited thin films. Our initial results show that it is possible to extract solar power using such a set-up, although the process parameters are not optimal. The LFS depositions were carried out in a roll-to-roll process flow, whereas ALD was done in a batch-type reactor. However, the ALD has been expanded into roll-to-roll process recently, and commercial R2R ALD systems are available. For example, selective area spatial ALD (SALD) has been shown to produce high quality thin films at a fraction of the time compared to the conventional ALD (Ellinger, 2014). An example of already existing large-scale utilization of DSSCs is powering the remote-controlled electric blinds of the MGM Grand hotel in Las Vegas, US in which DSSCs charge the blind batteries avoiding all extra wiring with significant cost savings (Broadwidth, 2012). A commercial utilization of low-cost ALD-LFS photovoltaic structures on flexible substrates requires improvements in the ALD coating speeds and development of low temperature ALD processes for heat sensitive materials such as paper and plastics. We believe that our results here show avenues towards an R2R deposition of large-scale, cost-effective DSSCs on various substrates ranging from glass to plastics and coated papers.

#### Acknowledgments

JJS wishes to thank the Academy of Finland (grants no 250 122, 256 263 & 283 054) for financial support.

#### References

- Broadwidth, P., 2012. Dyeing for a place in the sun, *Education in Chemistry*, September, pp. 26–29.
- Diao, Y., Zhou, Y., Kurosawa, T., Shaw, L., Wang, C., Park, S., Guo, Y., Reinspach, J. A., Gu, K., Gu, X., Tee, B. C. K., Pang, C., Yan, H., Zhao, D., Toney, M. F., Mannsfeld, S. C. B., Bao, Z., 2015. Flow-enhanced solution printing of all-polymer solar cells, *Nature Communications*, 6, pp. 7955
- Ellinger, C. R., Nelson, S. F., 2014. selective area spatial atomic layer deposition of ZnO, Al<sub>2</sub>O<sub>3</sub>, and aluminum-doped ZnO using poly(vinyl pyrrolidone), *Chemical Materials*, 26, pp. 1514–1522.
- Fujishima, A. and Honda, K., 1972. Electrochemical photolysis of water at a semiconductor electrode. *Nature*, 238, pp. 37–38
- George, S. M., 2010. Atomic layer deposition: An overview, *Chemical Reviews*, 110, pp. 111–131.
- Hashmi, S. G., Ozkan, M., Halme, J., Dimic Misic, K., Zakeeruddin, S. M., Paltakari, J., Grätzel, M., Lund, P. D., 2015. High performance dye-sensitized solar cells with inkjet printed ionic liquid electrolyte, *Nano Energy*, 17, pp. 206–215.
- Keskinen, H., Mäkelä, J. M., Aromaa, M., Keskinen, J., Areva, S., Teixeira, C. V., Rosenholm, J. B., Pore, V., Ritala, M., Leskelä, M., Raulio, M., Salkinoja-Salonen, M., Levänen, E. and Mäntylä, T., 2007. Titania and titania-silver nanoparticle deposits made by liquid flame spray and their functionality as photocatalyst for organic- and biofilm removal, *Catalysis Letters*, 111, pp. 127–132.
- Keskinen, H., Mäkelä, J. M., Heikkinen, R., Suopanki, A. and Keskinen, J., 2007. Synthesis of Pd–alumina and Pd–lanthana suspension for catalytic applications by one-step liquid flame spray, *Catalysis Letters*, 119, pp. 172–178.
- Kharecha, P. A. and Hansen, J. E., 2013. Prevented mortality and greenhouse gas emissions from historical and projected nuclear power. *Environmental Science & Technology*, 47, pp. 4889–4895.

- Lanzani, G., 2012. *The photophysics behind photovoltaics and photonics*. Wiley, Weinheim, Germany.
- Luttrell, T., Halpegamage, S., Tao, J., Kramer, A., Sutter, E., Batzill, M., 2014. Why is anatase a better photocatalyst than rutile? – Model studies on epitaxial TiO<sub>2</sub> films, *Scientific Reports*, 4, pp. 4043
- Mathew, S., Yella, A., Gao, P., Humphry-Baker, R., Curchod, B. F. E., Ashari-Astani, N., Tavernelli, I., Rothlisberger, U., Nazeeruddin, M. K. and Grätzel, M., 2014. Dye-sensitized solar cells with 13 % efficiency achieved through the molecular engineering of porphyrin sensitizers. *Nature Chemistry*, 6, pp. 242–247
- Mäkelä, J. M., Aromaa, M., Teisala, H., Tuominen, M., Stepien, M., Saarinen, J. J., Toivakka, M., Kuusipalo, J., 2011. Nanoparticle deposition from liquid flame spray onto moving roll-to-roll paperboard material, *Aerosol Science and Technology*, 45, pp. 817–827.
- O'Regan, B. and Grätzel, M., 1991. A low-cost, high-efficiency solar cell based on dye-sensitized colloidal TiO<sub>2</sub> films. *Nature*, 353, pp. 737–740.
- Smalley, R. E., 2005. Future global energy prosperity: the terawatt challenge, *MRS Bulletin*, 30, pp. 412–417.

## Challenges in the Fabrication of Optimized Microstructures via Fused Layer Modeling

*Vinzenz Nienhaus, Daniel Laumann, Dieter Spiehl, Edgar Dörsam*

Technische Universität Darmstadt, Institute of Printing Science and Technology,  
Magdalenenstrasse 2, 64289 Darmstadt

E-mail: nienhaus@idd.tu-darmstadt.de

### Short Abstract

Porous structures play a big role in nearly every part of industry and their inner structure is always a key part of their functionality. Unfortunately conventional structures commonly feature random geometric proportions, which can be overcome by the free design opportunities in 3d-printing. For flow optimized structures definition of the shape of small pores and their distribution is a key factor and makes Fused Layer Modeling a recommendable method for producing them. Although offering great opportunities, the processes and software involved are not fully elaborated. The aim of this work is to give an overview over existing capabilities and providing suggestions for future research. To do so, the standard workflow and an exemplary machine are presented and different print parameters are examined. The verification of a linear model for porosity shows the great possibilities in regard of function defined pore distributions. The existing possibilities for porosity percentages are outlined by different parameter studies. Finally, the findings are summed up and promising directions for future research are pointed out.

**Keywords:** 3d-printing, FDM, microstructure

### 1. Introduction

Porous structures are a key component of many chemical, biological and thermodynamic processes, like catalytic converters and heat exchangers, and their effectiveness is highly dependent on internal structures. Common techniques rely on differential construction methods or indirect controllable chemical processes, therefore the freedom of design is highly constrained (Too, 2002). With 3d-printing such limitations can be overcome and an ever more demanding market could be satisfied (Brousseau et al., 2010). Non-random structures with a predefined distribution of pores can be fabricated, following the guiding principle ‘complexity for free’ (Gibson et al., 2014). This leads to major improvements in comparison to conventional manufacturing systems (Neugebauer et al., 2011). Although being an emerging market the processes involved in 3d-printing are not completely understood and the step from a display model to a functional prototype has not fully taken place.

Especially the Fused Layer Modeling (FLM) is regarded as method only for display models, but in fact exhibits some major advantages in contrast to the widely used Selective Laser Sintering (SLS). Due to the layer wise deposition of material through a nozzle it is possible to create porous structures without the need of getting powder out of the cavities and the material can be functionalized with additives that are stable at relatively low temperatures compared to SLS. This makes FLM attractive for chemical and biomedical applications. An additional FLM approach is not to melt a solid and use a solution, dispersion or a sol-gel instead which is printed by the use of bioplotters (Jakus et al., 2015). But the control of the rheological parameters to produce stable 3-dimensional parts is challenging.

Some work has been carried out on porosity of FLM-fabricated structures. They are mainly focused on scaffolds for biomedical applications. Ang et al. (2006) for example investigate the influence of print parameters on porosity and find some basic relations. An extended model is proposed and verified by Too et al. (2002). They relate porosity to raster gaps, which is the void between two parallel material lines (raster lines). One limiting factor for getting smaller structure is the nozzle. Therefore Monzon et al. (2013) use small nozzles with an outlet diameter of 0.05 mm to generate smaller structures. This involves complex simulation and optimization of nozzle designs and shows limits of current system designs. One way to get around the problem is to post-process the layers. Malinauskas et al. (2014) experimented with direct laser writing ablation, which means subtraction of material via a laser. This hybrid method can produce higher porosities and adds special attributes to the surface of the material.

All this should lead to a mathematical model, which relates desired structure to the real object. One limiting factor are current processes and software systems themselves. The software is often constrained to basic patterns, optimized for producing rapid prototypes. An example is the definition of small wall structure in a CAD system and dividing it into layers with the common slicer software slic3r, as displayed in Figure 1.

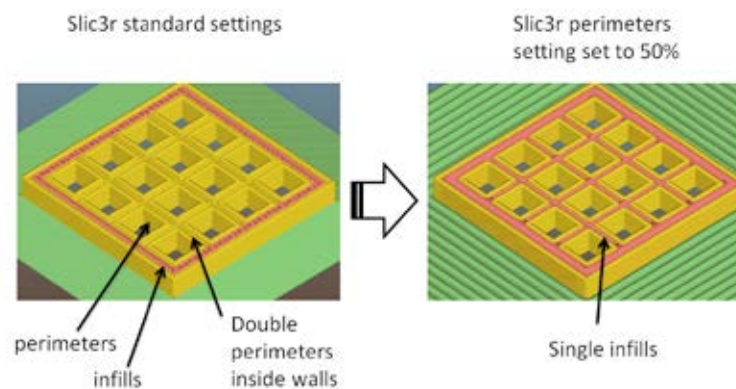


Figure 1: Influence of Slicer software setting on created printing paths; by changing wall thicknesses in a CAD system or alternating print settings, completely different wall structures can be obtained, and this leads to unpredictable results.

The printed structure is influenced by the model and strategy. Therefore, most structures are generated via automatically created infill structures. Common structures are rectangular grids, honeycomb or triangular structures. They show fixed, reproducible patterns, as shown in the next part of this paper, but still lack continuous variable structures governed by functions. It will be part of further work. This paper concentrates on strengths and weaknesses of bulk printer software and hardware and is aimed at providing a basis for finding optimization potentials.

## 2. Materials and Methods

The 3d-printing workflow spans from the virtual CAD to the actual printed part. The virtual part was created in Siemens NX 10.0, a solid block displayed in Figure 2, with dimensions of 30 mm × 30 mm × 3 mm.

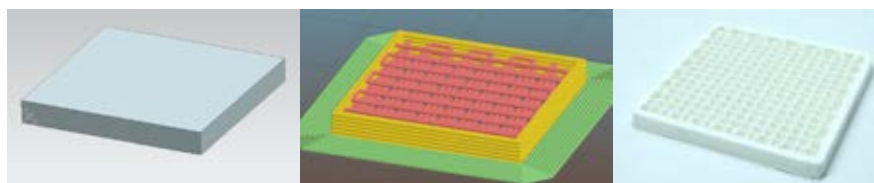


Figure 2: Block with dimensions of 30 mm × 30 mm × 3 mm created in Siemens NX 10.0 on the left, visualisation of print paths in slic3r software in the middle and printed block with inner fill structure on the right.

The block was exported via the STL-Export-extension of NX, which produces a representation of the block by triangulation, and was loaded into Slic3r. There the part is divided into layers (slices). As presented in the previous section, the print strategy is calculated in this part of the workflow. It is based on information about the printer and specific print settings. The most important settings are:

- Nozzle diameter (printer specific)
- Layer height (thickness of each slice)
- Number and width of perimeters (wall thickness)
- Infill density (key factor for controlling porosity)
- Fill pattern
- Number of top and solid layers (set to zero)
- Print speed
- Print temperature (material specific)
- Printbed temperature

With these settings a set of machine data in form of g-code is generated and send to the printer. The FLM printer used is a Hyrel System 30 with a MK1-250 printhead shown in Figure 3. It is a modular system with interchangeable heads, for example syringe based extrusion or Fused Layer Deposition of plastic filaments at up to 410 °C print temperature.

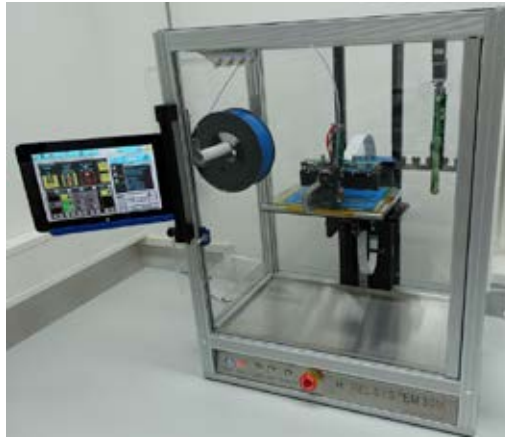


Figure 3: Hyrel System 30M modular Fused Layer Modeling printer

For the experiments PLA (polylactic acid, PLA MAXX Tooth White) polymer was used, due to its good extrusion characteristics like minimal thermal shrinking and low extrusion forces compared to high strength filaments. This feature has a major influence on forces for smaller diameter nozzles, because shear rate increases with a smaller radius to the power of three (Lafleur and Vergnes, 2014). In this study three different nozzle diameters were tested. Their values and the other print parameters are summarized in Table 1.

Table 1: Printing parameters used for PLA printing on Hyrel System 30M printer. Due to a mismatch between nominal and real nozzle diameters the nominal value is given in brackets.

Nozzle diameter (nominal) in mm	Layer thickness in mm	Infill density %	Print speed 1. Layer in mm/s	Print speed in mm/s	Print temperature in °C	Bed temperature in °C
0.45 (0.3)	0,05	10,20,30,40,50,60	10	20	205	55
0.25 (0.1)	0,05	10,20,30,40,50,60	10	20	205	55
0.2	0,05	10,20,30,40,50,60	10	20	205	55



It was found that the nominal size greatly differs from the actual size, measured under an microscope. Hence, the data was corrected with the measured nozzle diameters. The first layer speed is listed here because it is vital for good adhesion to the build plate. Resulting effects are of minor importance. The remaining parameters were kept constant.

Consequently, there are experiments with different temperatures connected with different flow rates. The experiments involve specimens with the print parameters in Table 2.

*Table 2: Printing parameters for investigating the influence of temperature and print speed on porosity.*

Nozzle diameter in mm	Layer thickness in mm	Infill density %	Print speed 1. Layer in mm/s	Print speed in mm/s	Print temperature in °C	Bed temperature in °C
0.3	0.3	30	10	10, 20, 30, 40, 50	195, 200, 205, 210	55

Finally, three different layer thicknesses were investigated with the parameters presented in Table 3.

*Table 3: Printing parameters for investigating the influence of layer thickness on porosity.*

Nozzle diameter (nominal) in mm	Layer thickness in mm	Infill density %	Print speed 1. Layer in mm/s	Print speed in mm/s	Print temperature in °C	Bed temperature in °C
0.45	0.1	10–50	10	20	205	55
0.45	0.2	10–90	10	20	205	55
0.45	0.3	10–50	10	20	205	55

With the experimental parameters being set, the next step is how to define and measure porosity.

## 2.1 Measuring Porosity

The porosity ( $P$ ) is defined as

$$P = \frac{V_{voids}}{V_{total}} \cdot 100 \%$$

using the volume of voids ( $V_{voids}$ ) and the total volume of the specimen ( $V_{total}$ ) and refers to the volumetric density (cf. Ang et al. (2006)). This value is time intensive to measure for high part counts (e. g. using mercury porosimeter), therefore it is more practical to determine the density of the material and weight the specimens. The density (has been determined by measuring the filament before printing, which represents a cylinder (diameter  $d$ , length  $l$ , weight  $m$ ), and it can be derived from the equation:

$$\rho = \frac{4m}{\pi d^2 l}$$

Multiple measurements lead to an average density of PLA ( $\rho_{PLA}$ ) of

$$\rho_{PLA} = 1.22 \pm 0.03 \text{ g/cm}^3.$$

Repeated measurements of the extruded materials deliver the same results. Thus, the material density does not change in the printing process.

## 2.2 Model describing the specimen volume

The model for describing the porosity used here is comparable to the one developed by (Too et al., 2002). It sums up the single lines to a layer and subtracts the outer perimeters. As one can see in Figure 4, the lines are of oval shape.



Figure 4: Cut through layers showing the elliptical shape of the lines.

Thus the area ( $A$ ) cross section is defined as

$$A = \pi ab.$$

The variables  $a$  and  $b$  represent the semimajor and semiminor axis of the ellipse and are set to half of the nozzle diameter ( $d$ ) and half of layer thickness ( $s$ ). With the length ( $l$ ), the equation for the line volume is

$$V_{line} = \pi \frac{d s}{4} l.$$

The total volume of the specimen, being composed of a rectangular perimeter of  $n_{perimeters}$  lines (outer square length:  $l$ ) and the infill (number of lines:  $n_{lines}$ , number of layers:  $n_{layers}$ ) can be described as

$$V_{total} = K * (n_{lines} * n_{layers} * \pi * \frac{d s}{4} (l - 2 * n_{perimeters} * d) + 4 * n_{lines} * s * n_{perimeters} * d (l - n_{perimeters} * d)).$$

The linear factor  $K$  is used to fit the model to measured data.

### 3. Results and Discussion

First, the developed model for volume, which is a basis for the calculation of porosity, is validated. It delivers important information about the linearity of the infill setting. Consequently, the different experimental results regarding the other print parameters are carried out.

#### 3.1 Quality of the model

As one can see in Figure 5, the mass of the specimens linearly rises with increasing infill percentage. This happens in accordance to predicted model based data. With a linear correction factor  $K$  set to 1.1, the model can be fitted exactly to experimental data.

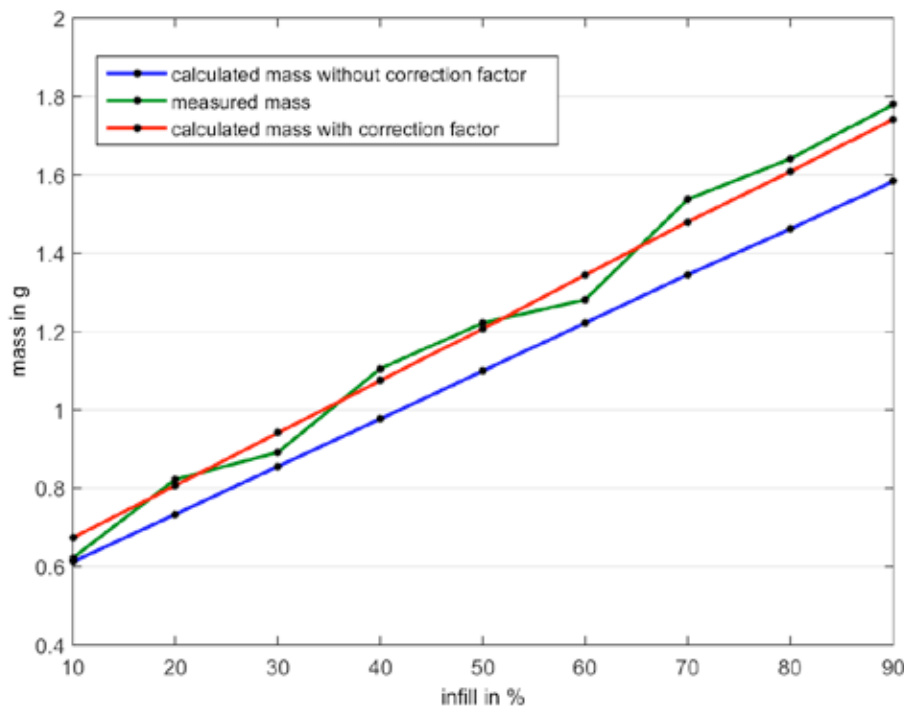


Figure 5: Mass of the specimens compared to defined infill; with print parameters: Nozzle diameter = 0.3 mm, layer height = 0.1 mm,  $K = 1.1$

Thus, the model based on elliptical shapes can be used for estimation of porosity. The fluctuation is within the accuracy of the measurement.

#### 3.2 Influence of nozzle diameter on porosity

Smaller nozzles can be used for creation of higher porosities with smaller cavities. Additionally the porosity can be controlled better due to the higher line count per layer. But there are a few drawbacks. First, the real diameter of the nozzle has to be determined, for example under a microscope. After a few prints, commercially available nozzles show a great divergence between nominal and real diameter and geometric irregularities regarding the cylindrical nozzle outlet.

As stated, the forces rapidly increase with smaller nozzles and as a consequence print speeds or layer thickness has to be reduced. This phenomenon is aggravated by the fact of poor surface quality in the nozzle. These factors limit comparability of different nozzles with equal parameter sets. A practical way to print with different nozzles is to adjust the layer thickness. Obviously, the nozzle diameter limits the width of a line. So a nozzle of 0.3 mm should not be used to create lines, which are broader than 0.3 mm, meaning

a layer thickness of more than 0.3 mm. Going into the other direction, the layer become more and more deformed. As a consequence, even a layer thickness of 0.1 mm cannot create smaller features. Thus, a layer thickness of about half the nozzle diameter is practical and worthwhile to avoid problems with the width and to ensure adhesion to previous layers.

### 3.3 Influence of layer thickness on porosity

The layer thickness has a major influence on the elliptical shape of the filament lines. Experimental data (Figure 6) show this effect in form of different gradients between porosity and infill percentage. The lower the height, the better the porosity can be controlled. Layers of 0.1 mm thickness lead to porosities ranging from 34 to 78 % in opposition to layers of 0.3 mm thickness, where a maximum of only 68 % porosity is possible. More over the gradient is much steeper.

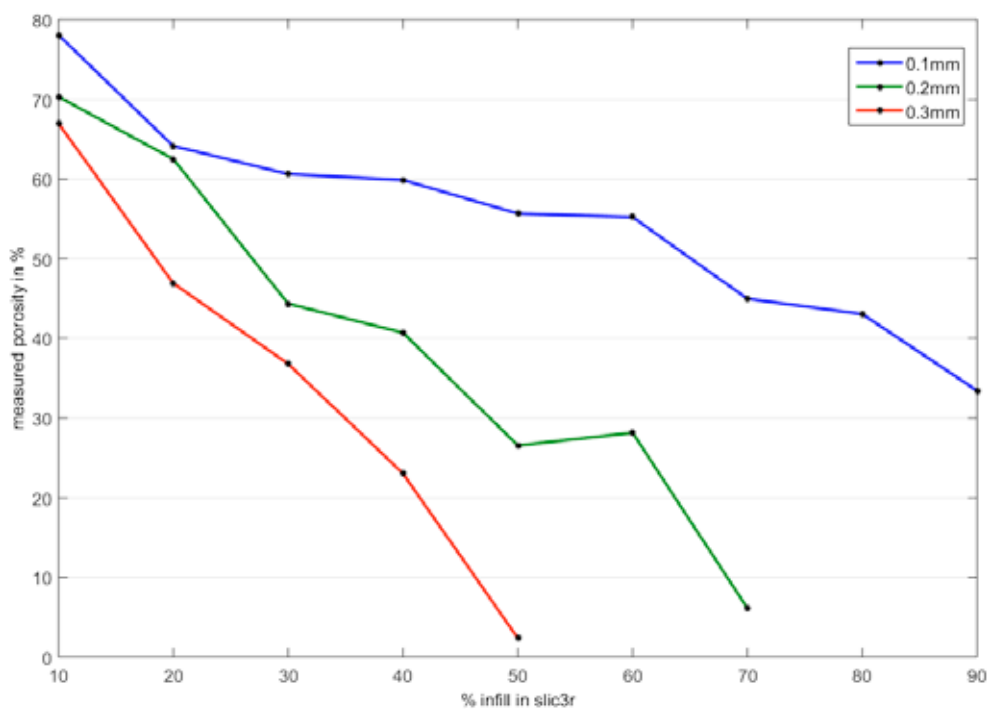


Figure 6: Influence of layer thickness on porosity over infill (as defined in slic3r)

### 3.4 Influence of print speed and temperature on porosity

The influence of print speed versus temperature is highly correlated due to the flow problematics explained in section 3.2. Therefore an interconnected relation can visualize the process limits (Figure 7).

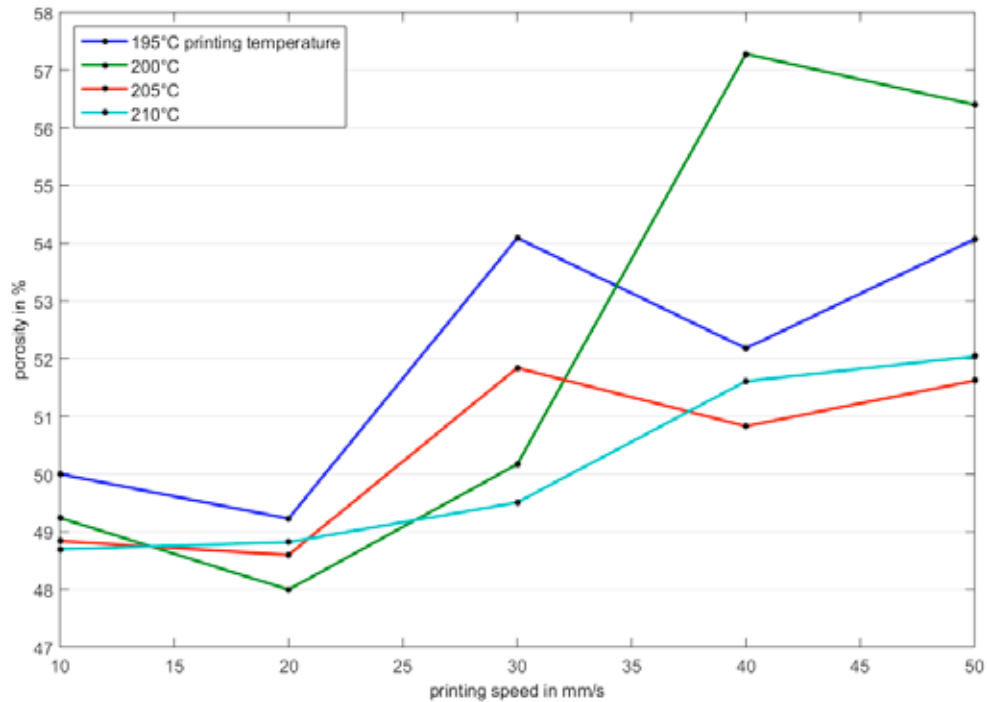


Figure 7: Influence of print speed on porosity at different temperatures.

At low speed the extrusion is stable at all temperatures except 195 °C. The slight rise in porosity is an indicator for badly printed areas. At higher speeds there is a drastic increase in porosity at 195 °C print temperature. The structures get deformed, as seen in Figure 8, and the lines are not printed with a consistent cross section.

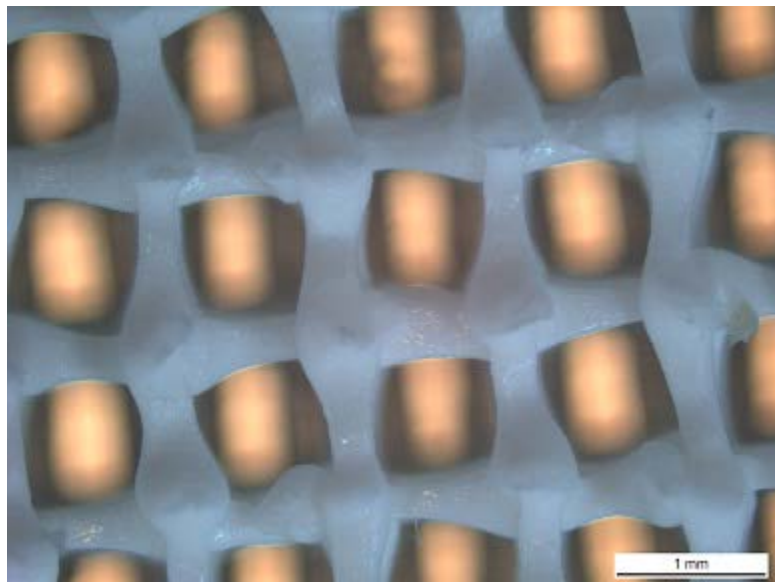


Figure 8: Microscopic image of irregular structure of a rectangular infill structure seen from above, where main influences are the inappropriate print temperature of 195 °C and the print speed of 50 mm/s.

At higher temperatures the influence of higher print speed is lower but still present. The print at 200 °C even shows some special print problems in form of fragmentary lines at higher print speeds. In summary, higher print speeds cannot be used for generation of higher porosities because the structures lack well defined geometry.

#### 4. Conclusions

The results show that the print capabilities are highly constrained to the process and the process parameters. Data generation should be performed by specialized algorithms to create highly regular and reproducible structures. Common slicer software is already capable of varying porosity linearly over a wide range, depending on the parameter sets shown. Experimental results can be fitted to model data, therefore properties can be pre-estimated. This is mandatory for a defined distribution governed by specific functions.

In the realm of software, open structures have to be created to implement complex functions, especially for the implementation of flow optimized structures based on FLM. The workarounds provided here, like deactivation of top and solid layers, and implemented fill structures are no overall solution to more complex models. The focus of common software still lies in prototypes rather than functional parts.

Looking at microstructures, the miniaturization of nozzles may not be the solution, due to the high flow resistance and the lack of advanced feeders with more pushing force and resulting problems with swelling. Instead drawing of lines, as demonstrated by Laput et al. (2015) may be a possible solution.

To refine the results, more work has to be put into control of the extrusion process, the machine design and the software. All of them offer great potential in raising what additive manufacturing is supposed to accomplish, complexity for free.

## Acknowledgments

A special thank goes to the Merck KGaA who provided the funding for the basic research in the field of additive manufacturing.

## References

- Ang, K.C., Leong, K.F., Chua, C.K. and Chandrasekaran, M., 2006. Investigation of the mechanical properties and porosity relationships in fused deposition modelling-fabricated porous structures. *Rapid Prototyping Journal*, 12(2), pp. 100–105.
- Brousseau, E.B., Dimov, S.S. and Pham, D.T., 2010. Some recent advances in multi-material micro- and nano-manufacturing. *International Journal of Advanced Manufacturing Technology*, 47(1–4), pp. 161–180.
- Gibson, I., Rosen, D. and Stucker, B., 2014. Additive Manufacturing Technologies: *3D Printing, Rapid Prototyping, and Direct Digital Manufacturing*. New York: Springer.
- Jakus, A.E., Taylor, S.L., Geisendorfer, N.R., Dunand, D.C. and Shah, R.N., 2015. Metallic Architectures from 3D-Printed Powder-Based Liquid Inks. *Advanced Functional Materials*, 25(45), pp. 6985–6995.
- Lafleur, P.G. and Vergnes, B., 2014. *Polymer extrusion*. Chichester, UK: John Wiley & Sons, Ltd.
- Laput, G., Chen, X.A. and Harrison, C., 2015. 3D Printed Hair: Fused Deposition Modeling of Soft Strands, Fibers, and Bristles. In: *Proceedings of the 28<sup>th</sup> Annual ACM Symposium on User Interface Software & Technology*. Daegu, Kyungpook, Republic of Korea.
- Malinauskas, M., Rekštyte, S., Lukosevicius, L., Butkus, S., Balciunas, E., Peciukaityte, M. and Juodkazis, S., 2014. 3D Microporous Scaffolds Manufactured via Combination of Fused Filament Fabrication and Direct Laser Writing Ablation. *Micromachines*, 5(4), pp. 839–858.
- Monzón, M.D., Gibson, I., Benítez, A.N., Lorenzo, L., Hernández, P.M. and Marrero, M.D., 2013. Process and material behavior modeling for a new design of micro-additive fused deposition. *The International Journal of Advanced Manufacturing Technology*, 67(9–12), pp. 2717–2726.
- Neugebauer, R., Müller, B., Gebauer, M. and Töppel, T., 2011. Additive manufacturing boosts efficiency of heat transfer components. *Assembly Automation*, 31(4), pp. 344–347.
- Too, M.H., Leong, K.F., Chua, C.K., Du, Z.H., Yang, S.F., Cheah, C.M. and Ho, S.L., 2002. Investigation of 3D Non-Random Porous Structures by Fused Deposition Modelling. *The International Journal of Advanced Manufacturing Technology*, 19(3), pp. 217–223.



## 3D Printing of Model Polymeric Resins for Medical Applications

*Azem Yahamed<sup>1</sup>, Pavel Ikononov<sup>2</sup>, Paul D. Fleming<sup>1</sup>, Alexandra Pekarovicova<sup>1</sup>, and Peter Gustafson<sup>3</sup>*

<sup>1</sup>Department of Chemical and Paper Engineering, Western Michigan University, Kalamazoo, MI 49008

<sup>2</sup>Department of Engineering Design Manufacturing and Management Systems,  
Western Michigan University, Kalamazoo, MI 49008

<sup>3</sup>Department of Mechanical Engineering, Western Michigan University, Kalamazoo, MI 49008

E-mail: azemkhalifa.yahamed@wmich.edu, pavel.ikononov@wmich.edu,  
dan.fleming@wmich.edu, a.pekarovicova@wmich.edu, peter.gustafson@wmich.edu

### Short Abstract

Polymeric materials were used for 3D printing of model trabecular human bone substitutes. Acrylate Butadiene Styrene (ABS), an acrylic prepolymer (Digital ABS™), polylactic acid (PLA), polyetherimide (ULTEM 9085) and polyamide (PA 2200) were 3D printed at 100 % of infill or with a designed geometric structure mimicking a honeycomb pattern, triangular or square internal structure (ABSTM, PA2200, and ULTEM 9085). The tensile strength of 100 % infill structures were highest with PLA, followed by digital ABSTM. If the polymer was printed with a designed geometric structure, the highest tensile strength was obtained with PA2200 using square internal geometry, having a tensile strength of 43 MPa, which was 91 % of that found when using 100 % infill. The weakest geometric structures were obtained when using Digital ABS™, which exhibited 45–58 % of the original tensile strength at 100 % infill. The tensile strength of the designed geometric structures exceed the criteria for trabecular bone.

**Keywords:** 3D printing, polymers, trabecular bone, mechanical properties

## 1. Introduction and Background

The development of additive manufacturing techniques, particularly 3D printing, has reached application potential in very many industrial disciplines, and rapidly made its move into the medical field. One particular medical area, bone replacement, is regularly needed to help repair or substitute damaged or diseased tissues ranging from trauma and degenerative disease to cancer. 3D prototyping of particular tissue or organ structures needs a scaffold to direct the general shape and three-dimensional grouping of several cell types (Sun, 2002; Gomi, 1993). The inner architecture of a bone scaffold construct is not trivial and different properties need to be considered, such as porosity, pore size, and interconnectivity of the tissue scaffold structure (Martin, 1991; Hutmacher, 2000; Hollister, 2000). The scaffolds must be precisely built from specific designs that have mechanical characteristics with suitable physiological parameters to be used successfully for bone tissue replacement (Williams, 2005). The development of suitable biocompatible polymeric materials for 3D printers is crucial. Silicone chemistry, in addition to copolymers with polymethylmethacrylate (PMMA), has been used in various materials with high oxygen permeability, and high rigidity. Methacrylates have been successfully employed in medical applications for dental structures (Ligon-Auer, 2016). However, their polymer network is inhomogeneous, which causes brittleness. Thus, these multifunctional acrylate monomers were modified in order to increase their toughness for 3D printing applications (Ligon-Auer, 2016). Toughening of polymers may be achieved by filling with sub-micrometer particle size inorganic fillers, such as calcium carbonate (Ligon-Auer, 2016). It was found that the impact strength of polypropylene at high loadings of calcium carbonate was increased from 2 kJ/m<sup>2</sup>

to  $50 \text{ kJ/m}^2$  (Ligon-Auer, 2016). Polycaprolactone (PCL) has been identified as a biodegradable polymer suitable for bone and cartilage repair, because it is stable at ambient temperature, inexpensive and widely available (Rutherford, 2003; Azevedo, 2003; Fromstein, 2002; Guan, 2004; Mano, 2003). Polycaprolactone (PCL) scaffolds manufactured via selective laser sintering (SLS) have been successfully used to provide the scaffold design for bone tissue.

Various 3D printing methods can in principle be applied for bone tissue engineering. However, SLS is considered to be advantageous for making bone tissue engineering builds for sites such as the temporomandibular joint (TMJ) in the jaw, since it provides a technique to build scaffolds to match the anatomical geometry of periodontal structure. SLS constructs the scaffolds from 3D digital data layer by layer, using computer controlled 3D scanning. A thin layer of powder of thermoplastic material is distributed and leveled by a roller above the flat surface. Applying laser sintering technology, the powder biomaterial binds from the heat of the laser beam. To make room for the new layer of powder, the piston in the cylinder shifts by one layer thickness. Next, the powder supply piston is activated to provide a fresh amount of powder for the next layer. The powder is distributed again on the flat surface to build the next layer of bone scaffold, and so on.

Fused Deposition Modeling (FDM) is able to produce 3D printed objects for medical applications employing thermoplastics polymers such as acrylonitrile butadiene styrene (ABS), polycarbonate (PC), polylactic Acid (PLA) and some other specially engineered thermoplastics. The working mechanism of the FDM technique is using a plastic filament from a coil, which is driven through an extruder. The plastic is heated and melted by the heat extrusion nozzle; the molten filament flows through the nozzles, and is deposited on the building plate to form a layer. The delivery heads move along the X-Y axes to follow a predefined path to form a specific shape on each layer. Then, the platform moves vertically in the Z direction to produce the next layer (Hutmacher et al., 2001). 3D printing with thermoplastics is one of the most common methods to create 3D structures in the medical field.

Stratasys PolyJet technology works in a manner similar to inkjet printing. A print head with multiple nozzles, Figure 1, (Gibson et al., 2015) jets photopolymer onto the substrate table surface, and simultaneously with the movement of the head the ink droplets are flattened by a small roller to make the surface even. An ultraviolet strip source follows the head and cures the material instantaneously. Two materials can be jetted simultaneously, the main model material and the supporting material. The supporting material provides a base for the main material, especially when there is a cavity or overhand structure. The supporting material can be easily removed mechanically or by water jetting.

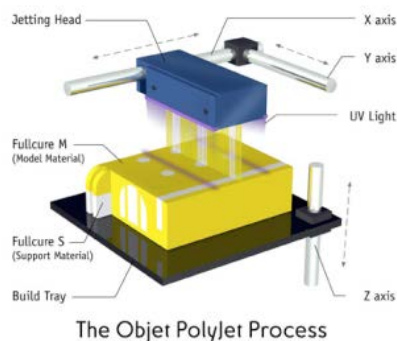


Figure 1: 3D printing principle used by Stratasys PolyJet technology (Gibson et al., 2015)

Fabrication of scaffolds by the stereolithography technique is made by using photosensitive polymers (Husár, 2014). Stereolithography employs a liquid UV-curable monomer and UV laser curing to construct layers. The laser ray hits the surface of the liquid monomer, it in turn polymerizes to create the photopolymer, which then rapidly hardens. After one layer is finished, the stage is lowered one step down and the

second layer is sketched on top of the first one. For each layer, the laser ray draws a cross-section of the part model on the surface of the liquid resin.

The aim of the work reported here is to employ various chemistries, mostly thermoplastic polymers, for printing 3D structures with or without porous interiors, which can be potentially applied as a trabecular bone tissue replacement.

## 2. Materials and Methods

### 2.1 Materials

ABS (Acrylonitrile-Butadiene-Styrene), PLA (Polylactic Acid), ULTEM9085 (polyetherimide), PA 2200 (Polyamide), and Digital ABSTM, an acrylic prepolymer, were used for printing.

### 2.2 3D printing of test samples

SOLIDWORKS® 3D CAD software (Waltham, Massachusetts, USA – Dassault Systèmes S.A., France) software was applied to design the internal engineered structure with various solid and internal porous geometries (solid print, hexagonal, triangular, and square porous structure). The internal pores are closed volumes where the sizes of cavity, side, top and bottom walls are the same as typical trabecular bone structure, as shown at Figure 2. 3D test samples were printed, which followed specified dimensions to comply with the ASTM D695 standard for mechanical properties testing. In order to test various materials for bone replacement, different printers were employed, because it was not possible to change the set up designed by the individual equipment manufacturer. The Fused Deposition Modeling (FDM) technique was used to print ULTEM9085 with Stratasys printer Fortus 400 MC. Selective Laser Sintering (SLS) was employed to print PA2200 (Polyamide) with an EOSP 396 print machine. PolyJet technology was used to print digital ABS™ with a Stratasys Objet 500 Connex3 printer (Stratasys, 2016). Samples were printed as 100 % infill, or with designed internal structure. Hexagonal, triangular and square cross-section pores were designed (Figure 2), mimicking the trabecular bone structure with the average pore size of the real bones (400  $\mu\text{m}$ ). Designed pores are closed cells with lengths and heights of the cross section geometry equal to 400  $\mu\text{m}$ . The walls thickness in all directions is 160  $\mu\text{m}$ . Five samples were printed for each geometric structure and polymer type.

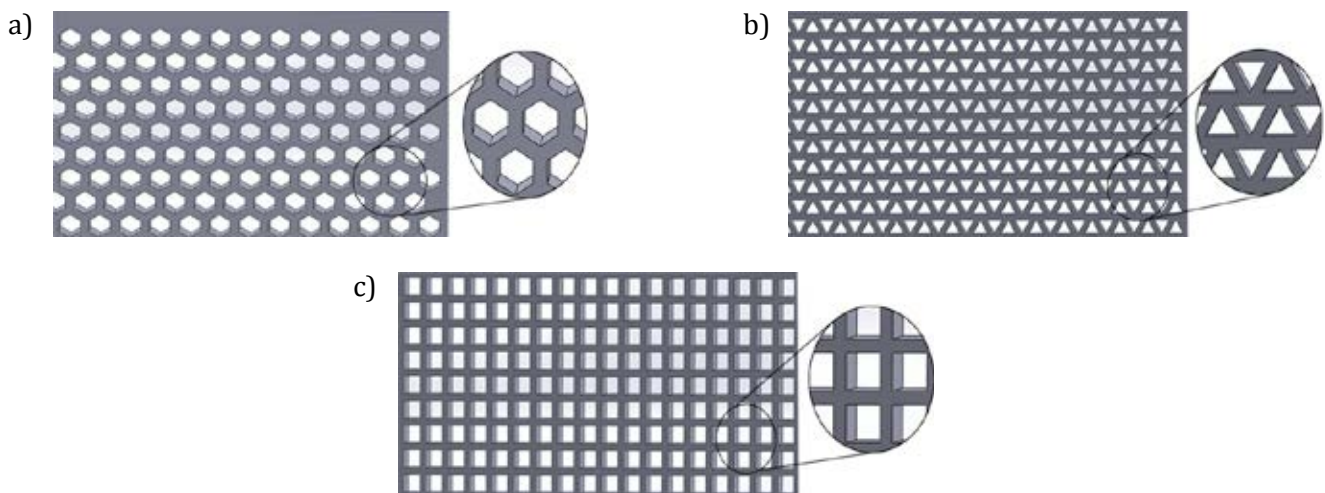


Figure 2: Three different geometric structures: hexagonal (a), triangular (b) and rectangular (c), where the “pores” have length equal the thickness of one printed layer

### 2.3 Mechanical properties

An MTS Bionix Servohydraulic Test Systems-Model 370.02 instrument was employed for testing the tensile strength of the 3D printed test samples according to the ASTM D695 standard. The speed of deformation was 0.2 mm/s. Testing was done at an ambient temperature of 25 °C. Stress strain curves for each test specimen were measured from five replicates. From the measured tensile strength Young's modulus was determined for the different geometric structures. A standard deviation (SD) of Young's modulus was calculated from the standard error of the coefficient of the linear term in a quadratic fit to the tensile test data. The calculated stress-strain curves formed by a least squares regression fit of the experimental data, using a quadratic polynomial, at 100 % infill, with honeycomb, triangular or rectangular internal geometry were constructed.

### 3. Results and Discussion

The calculated stress-strain curves for ABS (Acrylonitrile-Butadiene-Styrene), PLA (Polylactic Acid), ULTEM9085 (polyetherimide), PA 2200 (Polyamide) and Digital ABSTM, the acrylic prepolymer, at 100 % infill are illustrated in Figure 3. The stress-strain curves are concave in shape, pinpointing brittle structures (Figure 3), which do not exhibit any dramatic change in elongation prior to rupture. Again, the brittle material is a characteristic shown by rupturing without any obvious prior change in the rate of elongation, or neck formation (Beer, 2012). These 3D printed materials are mostly thermoplastic, which means they are composed of linear macromolecules, creating inhomogeneous internal structure, thus contributing to brittleness.

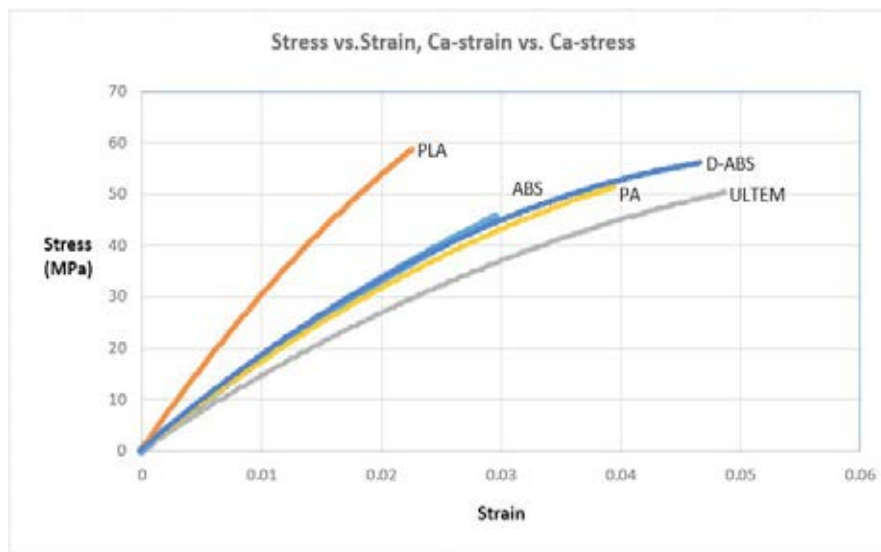


Figure 3: Calculated ("Ca") Stress-Strain curves at 100 % infill for model plastic materials.

PLA has the highest values of both Young's modulus and tensile strength (Table 1). Digital ABSTM has the second highest values of both Young's modulus and tensile strength. ULTEM9085 has the lowest value for Young's modulus and ABS has the lowest tensile strength. Cortical bones have a compressive strength in the range of 131–224 MPa, and a Young's modulus ranging from 17 000–20 000 MPa, while strength and Young's modulus for trabecular bones are in the range of 5–10 MPa and 50–100 MPa, respectively (Razak, 2012). The results of the polymers are less than the required mechanical strength of the compact bone, but they exceed the criteria of the trabecular bone.

*Table 1: Tensile strength of model polymers at 100 % infill*

Material	Tensile Strength [MPa]	Young's Modulus [MPa]	Young's Modulus SD [MPa]
ABS	43	1 925	29
PLA	57	3 333	18
ULTEM9085	50	1 540	3
PA2200	47	1 699	12
Digital ABS™	55	2 013	12

ULTEM9085 printed with three different geometries, hexagonal, triangular and square, gave the same values of the tensile strength for all internal geometries, but different Young's modulus values (Table 2). The triangular structure has the highest Young's modulus, followed by the ULTEM9085 square structure, and the lowest Young's modulus was given by the ULTEM9085 hexagonal structure. PA2200 hexagonal structure has the highest tensile strength average and Young's modulus (Table 2), followed by PA2200 adopting the square structure, and PA2200 with the triangular structure. For digital ABS, the square structure has the highest average value for both tensile strength and Young's modulus, followed by digital ABS having the hexagonal structure and digital ABS adopting the triangular structure. Generally, the values are in the same range for all the structures. However, if we look at hexagonal structures the PA2200 resulted in the highest tensile strength (43 MPa) along with the highest Young's modulus (1 508 MPa). Similarly, ULTEM9085 resulted in the strongest triangular structure with Young's modulus of 1 480 MPa and tensile strength of 32 MPa. ULTEM9085 had slightly higher Young's modulus of 1 480 MPa than PA 2200 (1 456 MPa). PA 2200 created also the strongest square structure with 43 MPa tensile strength and highest Young's modulus of 1 487 MPa.

*Table 2: Tensile strength and Young's modulus for different geometric structures.*

Geometric Structure	Tensile Strength [MPa]	Young's Modulus [MPa]	Young's Modulus SD [MPa]
ULTEM9085 Hexagonal	32	1 327	10
ULTEM9085 Triangular	32	1 480	11
ULTEM9085 Square	32	1 347	3
PA2200 Hexagonal	43	1 508	17
PA2200 Triangular	42	1 456	15
PA2200 Square	43	1 487	4
Digital ABS™ Hexagonal	25	1 124	3
Digital ABS™ Triangular	24	1 036	3
Digital ABS™ Square	32	1 414	13

When compared with trabecular bones having tensile strength and Young's modulus in the range of 5–10 MPa and 50–100 MPa, respectively (Razak, 2012), the results of the thermoplastics with designed structures exceed the trabecular bone criteria. These results show that our structures may serve as trabecular bone replacement in respect to their appropriate tensile strength.

#### 4. Conclusions

Several polymeric materials were 3D printed as a 100 % infill or with designed geometric internal structure. SOLIDWORKS® software was employed to design additional special 3D structures having closed cells pores with lengths and heights of the cross section geometry equal to 400 µm and the walls thickness in all directions is 160 µm. Five samples were printed for each geometric structure and polymer type. The

geometry of the honeycomb reduces the amount of material, therefore minimizing the weight, cost and construct density. Tensile strength was measured and Young's modulus was calculated. The stress-strain curves displayed near linear trends, portraying that the rupture occurs without any dramatic change in elongation, which is typical for brittle assemblies. Designed geometric structures showed 45–91 % less tensile strength, than structures printed with 100 % infill, depending on the polymer used. The least strength loss was found when using PA 2200, exhibiting 91 % of the original tensile strength of the 100 % infill construct. Further research is needed to develop deeper understanding of the mechanical properties and biocompatibility of the 3D printed bone replacement structures. Future design will include interconnected pores similar to trabecular bone structure.

## References

- Azevedo, M.C., Reis, R.L., Claase, M.B., Grijpma, D.W. and Feijen, J., 2003. Development of polycaprolactone/hydroxyapatite composite biomaterials. *J. Mater. Sci.: Mater Med.*, 14, pp. 103–107.
- Beer, F., Johnston, R., Dewolf, J., & Mazurek, D., 2012. *Mechanics of Materials*. New York : McGraw Hill Companies. [online] Retrieved from: <[http://www.pwut.ac.ir/FA/Colleges/Coll1/Files/Mechanics of materials, Ferdinand Beer et al. — 6<sup>th</sup> ed \(2012\).pdf](http://www.pwut.ac.ir/FA/Colleges/Coll1/Files/Mechanics%20of%20materials,%20Ferdinand%20Beer%20et%20al.%20-%206th%20ed%20(2012).pdf)> [Accessed January 2016].
- Fromstein, J.D. and Woodhouse, K.A., 2002. Elastomeric biodegradable polyurethane blends for soft tissue applications, *J. Biomater. Sci. Polym. Ed.*, 13(4), pp. 391–406.
- Gibson, I., Rosen, D. and Stucker, B., 2015. *Additive Manufacturing Technologies 3D Printing, Rapid Prototyping, and Direct Digital Manufacturing*, 2<sup>nd</sup> ed. Springer, 495pp.
- Gomi, K. and Davies, J.E., 1993. Guided bone tissue elaboration by osteogenic cells in vitro. *J. Biomed. Mater. Res.*, 4, pp. 429–43.
- Guan, J., Sacks, M.S., Beckman, E.J. and Wagner, W.R., 2004. Biodegradable poly (ether ester urethane) urea elastomers based on poly (ether ester) triblock copolymers and putrescine: synthesis, characterization and cytocompatibility. *Biomaterials*, 25(1), pp. 85–96.
- Hollister, S.J. Levy, R.A., Chu, T.W., Halloran, J.W. and Feinberg, S.E., 2000. An image based approach for designing and manufacturing craniofacial scaffolds. *Int. J. of Oral and Maxillofacial surgery*, 29(1), pp. 67–71.
- Husár, B., Hatzenbichler, M., Mironov, V., Liska, R., Stampfl, J. and Ovsianikov, A., 2014. *Photopolymerization-based additive manufacturing for the development of 3D porous scaffolds*. In: *Biomaterials for Bone Regeneration: Novel Techniques and Applications*, Woodhead Publishing, pp. 141–201.
- Hutmacher, D.W., 2000. Scaffolds in tissue engineering bone and cartilage, *Biomaterials*, 21, pp. 2529–2543.
- Ligon-Auer, S.C., Schwentenwein, M., Gorsche, C., Stampfl, J. and Liska, R., 2016. Toughening of photo-curable polymer networks: A Review. *Polymer Chemistry*, 7, pp. 257–286.
- Mano, J.F., Koniarova, D. and Reis, R.L., 2003. Thermal properties of thermoplastic/starch synthetic polymer blends with potential biomedical applicability. *J. Material. Sci., Mater.: Medicine*, 14, pp. 127–35.
- Martin, R.B., 1991. Determinants of the Mechanical Properties of Bones. *J. Biomech.*, 24, pp. 79–88.
- Razak, S.I.A., Sharif, N. & Rahman, W.A.W.A., 2012. Biodegradable polymers and their bone applications: A review. *Int. J. Basic Appl. Sci.*, pp. 31–49.
- Rutherford, R.B., Gu, K., Racenis, P. and Krebsbach P.H., 2003. Early events: The in vitro conversion of BMP transduced fibroblasts to chondroblasts. *Connect Tissue Res.*, 44, pp. 117–123.
- Stratsys, 2016. *Polyjet Technology: Stratasys 3d printers technologies*. [online] Retrieved from: <<http://www.stratasys.com/3d-printers/technologies/polyjet-technology>>, [Accessed January 2016].
- Sun, W. and Lal, P., 2002. Recent Development on Computer-Aided Tissue Engineering: A Review, *Journal of Computer Methods and Programs in Biomedicine*, 67(2), pp. 85–103.
- Williams, J.M., Adewunmi, A., Schek, R.M., Flanagan, C.L., Krebsbach, P.H., Feinberg, S.E., Hollister, S.J. and Das, S., 2005. Bone tissue engineering using polycaprolactone scaffolds fabricated via selective laser sintering, *Biomaterials*, 26(23), pp. 4817–27.



## Inkjet Printed Polyelectrolyte Patterns for Analyte Separation on Microfluidic Paper-based Analytical Devices

Risto Koivunen<sup>1</sup>, Eveliina Jutila<sup>1</sup>, Roger Bollström<sup>2</sup>, Patrick Gane<sup>1,2</sup>

<sup>1</sup> School of Chemical Technology, Department of Forest Products Technology, Aalto University, FI-00076 Aalto, Helsinki, Finland

<sup>2</sup> Omya International AG, Baslerstrasse 42, CH-4665 Oftringen, Switzerland

E-mail: risto.koivunen@aalto.fi; eveliina.jutila@aalto.fi; roger.bollstroem@omya.com; patrick.gane@omya.com

### Short Abstract

Paper-based microfluidic devices can provide practical analytics platforms for applications such as point-of-care medical diagnostics. However, immobilisation or separation of analytes on such devices has received limited attention so far. This study introduces inkjet printed polyelectrolyte patterns as possible platforms for immobilisation of cationic and anionic compounds through surface charge interaction. Both anionic (sodium polyacrylate) and cationic (polydiallyldimethylammonium chloride) polyelectrolytes were inkjet printed on a custom designed pigment coating, having fine particle internal pore structure to ensure close proximity between the analytical sample and modified pore walls. Printed polyelectrolyte patterns were themselves poorly visible both under ordinary and UV light. In a proof of principle test, a controllable degree of separation of anionic dyes from aqueous solution passing through a printed cationic polyelectrolyte region could be observed.

**Keywords:** polyelectrolyte, inkjet printing, functional printing, functional pigment coating, paperfluidics

### 1. Introduction and background

Paper-based analytical devices provide possibilities for easily transportable, inexpensive and disposable sensors in various fields of analytics, including point-of-care medical diagnostics or environmental monitoring. One major research field of such analytical devices is paperfluidics or paper-based microfluidics. On paperfluidic devices, aqueous liquid is transported in porous hydrophilic medium by capillary wicking without external pumping, while hydrophobic patterns are used to direct the flow.

Liquid travelling on a paperfluidic device may pass through a number of reaction areas, where analytes of interest may react with pre-applied reagents, before arriving at a detection zone where the final result is analysed. Some examples of demonstrated reactions are detection of nitrite levels from saliva (Cassano and Fan, 2013), detection of liver enzyme alanine aminotransferase from blood (Pollock et al., 2013) and detection of glucose or ketones from urine (Klasner et al., 2010). Detection methods can vary from colorimetric analysis, either with the unaided eye or by external reader, to more sophisticated instrumental methods such as fluorescence microscopy or electrochemical detection (Nery and Kubota, 2013). Sensitivity of detection can be improved by concentrating samples by means of evaporation (Yu and White, 2013).

Despite the wide interest in paperfluidic devices, separation or immobilisation of analytes in such naturally porous matrix has received limited attention. With the ability to separate, components that could interfere with detection can be removed from the sample. An example of such is size-based separation of agglutinated red blood cells from blood plasma, required for colorimetric analysis of plasma content (Yang



et al., 2012). By employing an immobilisation mechanism, the analyte of interest is captured on a small test region for analysis. Immobilisation is common in lateral flow tests, such as the commercial early pregnancy test based on lateral flow and detection of human chorionic gonadotropin in urine (Ngom et al., 2010).

This study investigates the application of a well-known phenomenon in colloidal chemistry in a possible new environment for the immobilisation and separation of analytes from liquid samples travelling on a paperfluidic device, namely the charge or hydrophobic destabilisation in aqueous dispersion of colloidal particulates or macromolecules, and/or the adsorption thereof, by local modification of pore surface chemistry. Two polyelectrolytes, cationic polydiallyldimethylammonium chloride (polyDADMAC) and anionic sodium polyacrylate (SPA), were inkjet printed in aqueous solution on a speciality designed porous coating material in order to adjust the surface charge of the pore walls selectively. These polyelectrolytes are commercially used in industrial applications, for example as additives in paper making and paper coatings to provide dispersion, or in wastewater purification as thickeners to provide flocculation. Previously inkjet printed cationic poly(vinylamine) polyelectrolyte has been applied in paper-based diagnostics to produce a layer for reducing the spreading and promoting storage stability of an anionic reaction outcome (Hossain et al., 2009).

Inkjet printing of polyelectrolytes has been previously studied for a variety of applications, such as formation of self-assembling hydrogels by printing alternating layers of anionic and cationic polyelectrolytes (Limem et al., 2011). Like other polymers, polyelectrolytes are affected by the high shear rates present in inkjet printheads, which limit jettable polymer content within an ink as increasing polymer molecular weight increases the viscoelastic behaviour.

In order to form a working printed polyelectrolyte separation or immobilisation zone, the following requirements should be met:

1. polyelectrolyte ink has to be reliably inkjettable with sufficient dry solids content,
2. polyelectrolyte ink has to penetrate the full depth of the porous substrate,
3. deposited polyelectrolyte has to remain immobile on the surfaces of the porous substrate when re-wetted – a renowned problem in some cases if adsorption is not supported by charge (Coulombic) attraction with the surface or by van der Waals forces,
4. deposited polyelectrolyte has to be able to capture analytes of interest by surface charge, and
5. polyelectrolyte surfaces should not become fully saturated by the adsorbed analytes from sample.

In order to ensure close interaction between the modified pore walls and liquid samples, a custom pigment coating consisting of functionalised calcium carbonate (FCC) and micro-fibrillated cellulose (MFC), inspired by earlier studies on functional coatings by the authors (Jutila, Koivunen and Gane, 2015) was utilised as the porous base material. This custom material has finer pore dimensions than the cellulose filter and chromatography papers most commonly used in paperfluidic studies. Although MFC itself is swellable in water, its fine particle nature, with little to no long range structure, together with the particulate inorganic pigment avoids problems with swelling and warping of the fibre sheet, which is likely to happen to cellulose papers when subjected to the large volumes of aqueous ink required for full-depth ink coverage of the porous substrate.

While printing of hydrophobic barriers, demonstrated also by the authors for cellulosic papers (Koivunen, Jutila and Gane, 2015) and functional pigment coatings (Koivunen et al., 2016), is the most common way of patterning paperfluidic devices, this work uses cutting, a method capable of forming quite complex patterns (Fenton et al., 2009), to produce simple channels for the initial study. However, in the longer term, polyelectrolyte patterns and hydrophobic patterns are intended to be integrated into the same devices.

## 2. Materials and Methods

### 2.1 Functional pigment coating

The speciality coating consists of:

- i. porous functionalised calcium carbonate (FCC) pigment (Omya International AG, Oftringen, Switzerland), formed to contain 11.9 % calcium carbonate and 88.1 % hydroxylapatite, having a specific surface area of  $160 \text{ m}^2\text{g}^{-1}$ , and
- ii. microfibrillated cellulose (MFC) Arbocel MF-40-7 (J. Rettenmaier & Söhne GmbH + Co KG, Rosenberg, Germany), added at a level of 20 pph, based on 100 parts by weight of pigment, as a binder.

The coating slurry was prepared to a dry solids content of 13.8 w/w % and coated on impermeable SuperYUPO pigmented polypropylene film (Yupo Corporation, Tokyo, Japan), formerly known as Synteape®, with a mechanical drawdown K202 Control Coater (RK PrintCoat Instruments Ltd., Herts, UK) using the orange labelled wire-wound rod, applying a  $60 \mu\text{m}$  thick wet film onto the substrate, with a speed setting of  $6 \text{ m} \cdot \text{min}^{-1}$ . Coated substrates were allowed to dry at room temperature overnight. Dried coating layers had a basis weight of  $7.8 \pm 1.3 \text{ g} \cdot \text{m}^{-2}$  and thickness of  $24 \pm 6 \mu\text{m}$ .

### 2.2 Functional inks and printing

The two inks, referred from here on as polyDADMAC ink and SPA ink, consisted of 1.0 w/w % polyelectrolyte, either polyDADMAC with average molecular weight  $< 100 \text{ kDa}$  (Sigma-Aldrich, St. Louis, USA, product code 522376, supplied at 35 % dry solids content) or SPA with minimal molecular weight  $> 1 \text{ kDa}$ , available under the commercial tradename Topsperse G XN (Coatex, Genay, France, supplied at 70.2 % dry solids content), respectively, in aqueous solution with 25 w/w % ethanol to decrease surface tension. Easily evaporating organic solvent was preferred over surfactants for reducing surface tension, since the latter can stay on the printed device and be dissolved when the coating is re-wetted. On a paperfluidic device with hydrophobic barriers, such free surfactant molecules could subsequently adsorb onto the hydrophobised surfaces and cause leaks.

The ink surface tension was measured with a CAM200 contact angle measurement system (KSV, Espoo, Finland) employing the pendant drop method, in a laboratory room maintained at  $22^\circ\text{C}$ . Viscosity was measured with MCR-300 rheometer (Paar-Physica, Graz, Austria) at a shear rate of  $100 \text{ s}^{-1}$  at  $30^\circ\text{C}$ . Jettability of inks was studied and patterns printed with a DMP-2831 inkjet printer (Fujifilm Dimatix, Santa Clara, USA) employing DMC-11610 ink cartridges with 10 pl nominal drop volume. The printhead was maintained at  $30^\circ\text{C}$  while the printer mounting plate was heated to  $40^\circ\text{C}$  to promote drying of the inks. Printing was performed with 15 out of 16 available nozzles.

For the pattern testing, rectangles of nominally  $4 \text{ mm} \times 180 \text{ mm}$  were printed with both polyelectrolyte inks, adopting a  $10 \mu\text{m}$  drop space setting and applying 1, 3 or 5 layers of ink on top of each other. When applying multiple layers, the previously printed layer was allowed to dry for 1 min before printing the subsequent layer.

### 2.3 Separation tests

Printed substrates were cut with scissors into approximately  $3 \text{ mm} \times 50 \text{ mm}$  strips, so that a polyelectrolyte printed region was to be found between 18 mm and 22 mm from the bottom of the strip. These strips were then attached onto  $90 \text{ mm} \times 85 \text{ mm}$  sheets of SuperYupo, marked at 10 mm intervals, using double-sided

tape so that the bottoms of the strips matched with the bottom of the sheet. Each sheet contained seven strips, one with native coating, three with SPA ink (1, 3 and 5 layers) and three with polyDADMAC ink (1, 3 and 5 layers). These SuperYupo sheets were then attached with masking tape to a 100 mm × 100 mm glass slide to provide solid backing.

The following water-soluble dyes were chosen as model compounds for separation tests - each dyestuff was dissolved in deionised water at 0.1 w/w %:

1. Crystal violet (Merck KGaA, Darmstadt, Germany, product number 1.15940.0025)
2. Rhodamine B (Kremer Pigmente GmbH & Co. KG, Aichstetten, Germany, product number 94900)
3. Uranine (Kremer Pigmente GmbH & Co. KG, Aichstetten, Germany, product number 94236)
4. Tartrazine 85 (Kremer Pigmente GmbH & Co. KG, Aichstetten, Germany, product number 94175)

Crystal violet is a cationic colourant, Rhodamine B is weakly cationic, while Uranine and Tartrazine 85 are anionic. Single 0.5 µl drops of the chosen solution were applied with Microcaps micropipettes (Drummond Scientific Company, Broomall, USA) to the coating strips, centred approximately 10 mm from the bottom of the strip. Further 0.5 µl drops of non-ionic 1 w/w % Ferroin solution (Merck KGaA, Darmstadt, Germany, product number 1.09193.0100), for highlighting the water wicking front, were applied approximately 30 mm from the bottom of the strip. The drops were allowed to dry in air for at least 30 min.

Separation of the colourants on the strips was observed in a thin layer chromatography chamber (Camag, Muttenz, Switzerland). Approximately 5 mm of deionised water was placed in the bottom of the chamber, with the atmosphere inside the closed chamber being allowed to saturate for approximately 15 min before placing the first set of samples. The samples were placed inside the chamber so that the bottoms of the coating strips were in contact with the water, allowing it to absorb into the highly wicking speciality coating. Water then travelled along the coating, dissolved the dye from the coating at its position of application and carried it to the polyelectrolyte treated region. Figure 1 shows a schematic of the experimental design to identify the elution and trapping of the dyestuff whilst recording the position of the advancing water front. The samples were observed for 8 min inside the chamber.

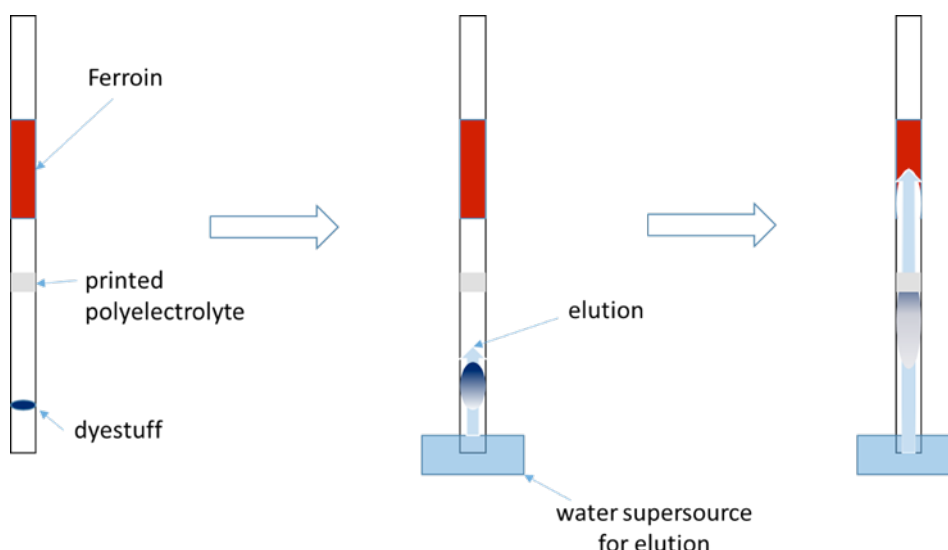


Figure 1: Schematic of the elution and water front identifying technique.

### 3. Results and Discussion

#### 3.1 Ink jettability

Both the anionic and cationic polyelectrolyte inks were found to be jettable with the printer used. Experimentally determined jetting settings and custom waveforms for the two polyelectrolyte inks are listed in Tables 1 and 2. Long term reliability of the chosen jetting settings and ink formulations will be studied as part of future work.

Table 1: Ink characteristics and jetting settings.

Ink	PolyDADMAC ink	SPA ink
Surface tension ( $\text{mN}\cdot\text{m}^{-1}$ )	$35.98 \pm 0.75$	$35.91 \pm 1.59$
Viscosity ( $\text{mPa}\cdot\text{s}$ )	$2.50 \pm 0.08$	$1.62 \pm 0.12$
Jetting frequency (kHz)	6	6
Jetting voltage (V)	18	18
Jetting speed ( $\text{m}\cdot\text{s}^{-1}$ )	10	5

Table 2: Custom waveforms for the inks.

Ink	Segment	Level (%)	Slew	Duration ( $\mu\text{s}$ )
PolyDADMAC	Jetting 1	0	0.65	3.392
	Jetting 2	100	1.20	4.672
	Jetting 3	67	2.00	2.944
	Jetting 4	13	2.00	0.512
	Non-jetting 1	40	1.00	3.712
	Non-jetting 2	27	1.00	6.976
	Non-jetting 3	13	1.00	0.832
PSA	Jetting 1	100	0.35	5.632
	Jetting 2	0	0.06	21.248
	Non-jetting 1	27	0.35	5.632
	Non-jetting 2	0	0.06	21.248

#### 3.2 Detection of printed patterns

Polyelectrolyte rectangles printed on the coating were difficult to detect with the unaided eye. When applied at  $10\text{ }\mu\text{m}$  drop spacing, a single layer of either ink could be detected when the substrate was observed against a light table, but not under ordinary office lighting. When 3 or 5 layers of either ink were applied, the pattern could also be detected with care under office lighting. The nominally  $4\text{ mm}$  wide rectangle was measured as actually being approximately  $5\text{ mm}$  wide. This amount of line spreading suggests that the deposited inks likely travelled the whole depth of the coating, though this does not guarantee that the contained polyelectrolyte was also carried the whole depth or that the whole internal surface is treated due to the selective liquid pore transport mechanisms.

To evaluate the visual detection of the inks, single layer test rectangles were also printed with both inks at drop spacing settings of  $12\text{ }\mu\text{m}$ ,  $15\text{ }\mu\text{m}$  and  $20\text{ }\mu\text{m}$ , resulting in lower applied ink volumes per unit surface area. When printed with SPA ink, none of these patterns were visible when examined against a light table. With polyDADMAC ink, a pattern printed at  $12\text{ }\mu\text{m}$  drop spacing was faintly visible against a light table, while patterns printed at  $15\text{ }\mu\text{m}$  and  $20\text{ }\mu\text{m}$  drop spacing were not.

The patterns were also observed under 365 nm wavelength UV light. In this case, 3 or 5 layers of either ink applied at 10  $\mu\text{m}$  drop spacing could be faintly detected, while the others were not observable. Low background fluorescence from the coating and polyelectrolytes is beneficial when a detection method based on fluorescence, such as fluorescence microscopy, is used for detection of analytes.

### 3.3 Separation of cationic compounds on polyelectrolyte printed coating

Figure 2(a) displays the results of pilot tests conducted with strongly cationic Crystal Violet, on samples featuring either no polyelectrolyte region or 1, 3 or 5 layers of SPA or polyDADMAC ink, with the image taken after 8 minutes of elution. Figure 2(b) displays the same for the very weakly cationic Rhodamine B.

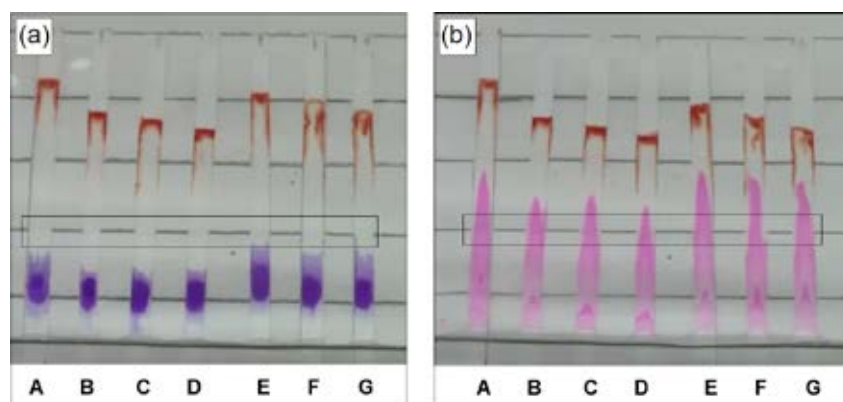


Figure 2: (a) Crystal Violet dye (violet) after 8 min of elution on samples featuring either plain coating (A), 1/3/5 layers of SPA ink (B–D) or 1/3/5 layers of PolyDADMAC ink (E–G), with the approximate location of the polyelectrolyte printed areas marked with the black rectangle; Ferroin colourant (red) on top indicates the water front, (b) Rhodamine B dye (magenta) after 8 min of elution using the same patterning as in (a).

Crystal Violet dye transported very slowly on the coating compared to the water front, and never reached the printed polyelectrolyte zones within the observed period. This is presumably due to interaction between the cationic dye and anionic charge on the partly zwitterionic FCC and anionic MFC binder in the coating. Rhodamine B, being only very weakly cationic, transported faster but did not exhibit immobilisation on the polyelectrolyte regions, presumably due to low charge-to-mass ratio.

### 3.4 Separation of anionic compounds on polyelectrolyte printed coating

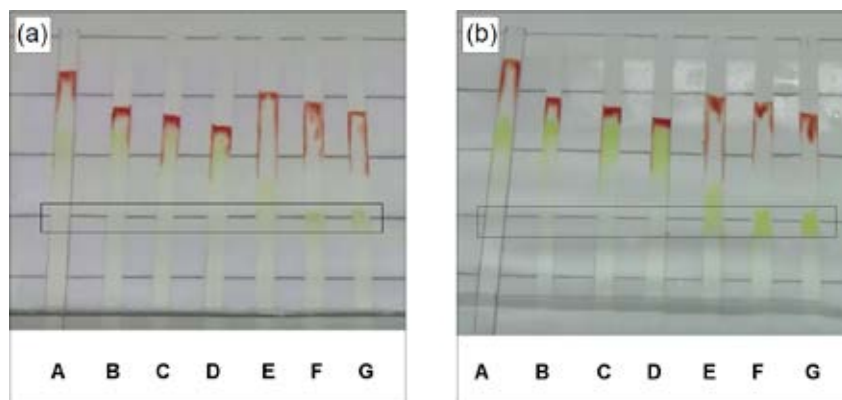


Figure 3: (a) Uranine dye (yellow) after 8 min of elution, with UV illumination applied to enhance visibility, on samples featuring either plain coating (A), 1/3/5 layers of SPA ink (B–D) or 1/3/5 layers of PolyDADMAC ink (E–G), with the approximate location of the polyelectrolyte printed areas marked with the black rectangle; Ferroin colourant (red) on top indicates the water front, (b) Tartrazine 85 dye (yellow) after 8 min of elution using the same patterning as in (a).

Figure 3(a) displays the results of tests conducted with anionic Uranine, on samples featuring either no polyelectrolyte region or 1, 3 or 5 layers of SPA or polyDADMAC ink, with the image taken after 8 minutes of elution. Figure 3(b) displays the same for anionic Tartrazine 85.

Uranine dye is light yellow in colour, and thus not very strongly visible in Figure 3, even though additional 365 nm UV illumination has been applied to take advantage of its fluorescence. Imaging of Uranine was also attempted under UV light only, for stronger contrast, but this did not produce pictures of sufficient quality. Nonetheless, careful examination of B–D shows that there is little separation of Uranine from the water front when the sample has passed through the anionic SPA region. On E, featuring a single layer of printed cationic polyDADMAC, part of Uranine has passed through the printed region, though having been slowed down significantly in the process. On F and G, featuring 3 and 5 printed layers of polyDADMAC respectively, the Uranine dye has been completely captured by the polyelectrolyte region.

As can be seen from Figure 3(b), Tartrazine 85 has a stronger yellow colour and is thus more visible on the coating. Furthermore, it can be seen to behave in a very similar fashion to Uranine, confirming the ability of the printed cationic polyDADMAC region to slow down or capture anionic molecules.

#### 4. Conclusions

This first stage study demonstrates that polyelectrolyte solutions can be inkjet printed on pigment coating. Furthermore, it has shown that printed cationic polyelectrolyte regions impart a chromatographic effect on anionic analytes passing through them, with the magnitude of effect depending on the number of printed polyelectrolyte layers. This immobilisation also indicates that the cationic polyelectrolyte itself must have formed a water-fast layer on the coating, and so has adsorbed onto the partial zwitterionic anionic sites of the FCC, and/or on the anionic MFC binder.

With printed anionic polyelectrolytes, results were limited. Cationic Crystal Violet dye transported so slowly on this coating that it never reached the printed region, again related to the strong anionic charge of the components in the coating. Thus, anionic polyelectrolyte regions on this coating design might be redundant, due to strong capture of the dye by the coating, but on less anionic coatings they will probably be useful. No clearly observable effect was achieved in the case of Rhodamine B, displaying the limitations of the method when applied to only weakly charged or charge-hidden molecules.

While the concept is demonstrated here only for simple colourants, the principles should be applicable to any compounds exhibiting surface charge in solution, which themselves do not undergo size exclusion.

#### 5. Future work

The concept will be explored with further sample analytes. Furthermore, methods to measure whether the polyelectrolytes are permanently immobilised on the coating or to some extent carried away by the wicking water front will be investigated. In the longer term the study will be extended to cover other polyelectrolytes, especially such that could be reliably jetted at higher concentrations than the 1 w/w % illustrated in this study – likely an important requirement for upscaling.

The effect of different quantities of analyte reaching the polyelectrolyte regions may be studied to characterise possible saturation of the polyelectrolyte surfaces by the analyte. To this purpose, the pipetting method of colourant application may prove unsatisfactory for applying controllably small amounts. As an alternative method, inkjet printing could also be employed as a method for applying fine and precise amounts of the test analyte on the samples, thus providing better control and coherence. Combining polyelectrolyte patterns with printed hydrophobic barriers will also provide opportunities for more complex test patterns.

## Acknowledgments

Funding for the project was solely supported by Omya International AG.

## References

- Cassano, C.L. and Fan, Z.H., 2013. Laminated paper-based analytical device (LPAD): fabrication, characterisation and assays. *Microfluidics and Nanofluidics*, 15(2), pp. 173–181.
- Fenton, E.M., Mascarenas, M.R., Lopez, G.P. and Sibbett, S.S., 2009. Multiplex Lateral-Flow Test Strips Fabricated by Two-Dimensional Shaping. *Applied Materials and Interfaces*, 1(1), pp. 124–129.
- Hossain, S.M.Z., Luckham, R.E., Smith, A.M., Lebert, J.E., Davies, L.M., Pelton, R.H., Filipe, C.D.M. and Brennan, J.D., 2009. Development of a Bioactive Paper Sensor for Detection of Neurotoxins Using Piezoelectric Inkjet Printing of Sol–Gel-Derived Bioinks. *Analytical Chemistry*, 81(13), pp. 5474–5483.
- Jutila, E., Koivunen, R. and Gane, P.A.C., 2015. Effect of coating pigment, binder type and binder amount on planar wicking on coated substrates. *Journal of Print and Media Technology Research*, 4(3), pp. 173–186.
- Klasner, S.A., Price, A.K., Hoeman, K.W., Wilson, R.S., Bell, K.J. and Culbertson, C.T., 2010. Paper-based microfluidic device for analysis of clinically relevant analytes present in urine and saliva. *Analytical and Bioanalytical Chemistry*, 397(5), pp. 1821–1829.
- Koivunen, R., Jutila, E. and Gane, P.A.C., 2015. Inkjet printed hydrophobic microfluidic channelling on porous substrates. *Journal of Print and Media Technology Research*, 4(1), pp. 7–18.
- Koivunen, R., Jutila, E., Bollström, R. and Gane, P.A.C., 2016. Hydrophobic patterning of functional porous pigment coatings by inkjet printing. *Microfluidics and Nanofluidics*, 20(6), pp. 1–21.
- Limem, S., McCallum, D., Wallace, G.G. and Calvert, P., 2011. Inkjet printing of self-assembling polyelectrolyte hydrogels. *Soft Matter*, 7(8), pp. 3818–3826.
- Nery, E.W. and Kubota, L.T., 2013. Sensing approaches on paper-based devices: a review. *Analytical and Bioanalytical Chemistry*, 405(24), pp. 7373–7595.
- Ngom, B., Guo, Y., Wang, X., and Bi, D., 2010. Development and application of lateral flow test strip technology for detection of infectious agents and chemical contaminants: a review. *Analytical and Bioanalytical Chemistry*, 397(3), 1113–1135.
- Pollock, N.R., McGray, S., Colby, D.J., Noubary, F., Nguyen, H., Khormaei, S., Jain, S., Hawkins, K., Kumar, S., Rolland, J.P. and Beattie, P.D., 2013. Field evaluation of a prototype paper-based point-of-care fingerstick transaminase test. *PloS One*, 8(9), p.e75616.
- Yang, X., Forouzan, O., Brown, T.P. and Shevkolyas, S.S., 2012. Integrated separation of blood plasma from whole blood for microfluidic paper-based analytical devices. *Lab on a Chip*, 12(2), pp. 274–280.
- Yu, W.W. and White, I.M., 2013. Inkjet-printed paper-based SERS dipsticks and swabs for trace chemical detection. *Analyst*, 138(4), pp. 1020–1025.



## Index of authors

Adams, Richard	65	Passas, Raphaël	71
Athlan, Éric	3	Pedersen, Michael Abildgaard	91
		Pekarovicova, Alexandra	137
Bircher, Fritz	13	Pirrami, Lorenzo	13
Blayo, Anne	101	Pruneau, Michael	3
Bois, Chloé	3	Put, Fons	57
Bollström, Roger	33, 39, 121, 143		
Brumm, Pauline	111	Reverdy-Bruas, Nadège	71
		Rharbi, Yahya	101
Chagas, Lionel	71		
Cormier, Denis	49	Saarinen, Jarkko J.	121
		Schmitt-Lewen, Martin	111
Demarchi, Danilo	13	Sikanen, Tiina	39
Denneulin, Aurore	101	Spiehl, Dieter	127
Desfontaines, Laurent	3	Steven, M. George	121
Dörsam, Edgar	111, 127		
		Toivakka, Martti	121
El Asaleh, Reem	65	Törngren, Björn	121
Faure, Vincent	101	Vallat-Evrard, Louis	71
Fleming, Paul D.	137	Varma, Diana	81
Gane, Patrick	33, 39, 143	Wadhwa, Arjun	49
Gustafson, Peter	137	Williams, Scott	49
Haapanen, Janne	121	Yahamed, Azem	137
		Yin, Jiayuan	21
Ikonomov, Pavel	137		
Jutila, Eveliina	39, 143		
Kääriäinen, Tommi	121		
Klemetti, Aarne	21		
Koivunen, Risto	39, 143		
Korobkin, Maksim	21		
Langsford, Daniel	65		
Laumann, Daniel	127		
Lecomte, Christiane	3		
Magnin, Albert	101		
Mäkelä, Jyrki M.	121		
Martineau, Michel	3		
Mazza, Marco	13		
Nguyen, Duy Linh	111		
Nienhaus, Vinzenz	127		

